

**SIMULATION OF STRENGTHENED REINFORCED
CONCRETE BEAM DEBONDING BEHAVIOUR USING
GLOBAL ENERGY BALANCE APPROACH**

NUSRAT HOQUE

FACULTY OF ENGINEERING
UNIVERSITY OF MALAYA
KUALA LUMPUR

2018

**SIMULATION OF STRENGTHENED REINFORCED
CONCRETE BEAM DEBONDING BEHAVIOUR USING
GLOBAL ENERGY BALANCE APPROACH**

NUSRAT HOQUE

**THESIS SUBMITTED IN FULFILMENT OF THE
REQUIREMENTS FOR THE DEGREE OF DOCTOR
OF PHILOSOPHY**

**FACULTY OF ENGINEERING
UNIVERSITY OF MALAYA
KUALA LUMPUR**

2018

UNIVERSITY OF MALAYA

ORIGINAL LITERARY WORK DECLARATION

Name of Candidate: Nusrat Hoque

Registration/Matric No: KHA 130047

Name of Degree: Doctor of Philosophy

Title of Thesis: Simulation of strengthened Reinforced concrete beam debonding behaviour using global energy balance approach.

Field of Study: Structural Engineering

I do solemnly and sincerely declare that:

- (1) I am the sole author/writer of this Work;
- (2) This Work is original;
- (3) Any use of any work in which copyright exists was done by way of fair dealing and for permitted purposes and any excerpt or extract from, or reference to or reproduction of any copyright work has been disclosed expressly and sufficiently and the title of the Work and its authorship have been acknowledged in this Work;
- (4) I do not have any actual knowledge nor do I ought reasonably to know that the making of this work constitutes
- (5) an infringement of any copyright work;
- (6) I hereby assign all and every rights in the copyright to this Work to the University of Malaya ("UM"), who henceforth shall be owner of the copyright in this Work and that any reproduction or use in any form or by any means whatsoever is prohibited without the written consent of UM having been first had and obtained;
- (7) I am fully aware that if in the course of making this Work I have infringed any copyright whether intentionally or otherwise, I may be subject to legal action or any other action as may be determined by UM.

Date: 09/04/2018

Subscribed and solemnly declared before,

Witness's Signature

Date:

Name:

Designation:

[SIMULATION OF STRENGTHENED REINFORCED CONCRETE BEAM DEBONDING BEHAVIOUR USING GLOBAL ENERGY BALANCE APPROACH]

ABSTRACT

Flaws and insufficient strength in the concrete-FRP interface normally initiate the debonding failure of FRP strengthened RC beams. Existing strength based model is generally good for predicting local failure of structure but not the overall failure. Hence, is not efficient in predicting the debonding failure. On the other hand, applications of finite element (FE) models require precise detail of the interface which is not always available. Fracture mechanic with global energy balance (GEBA) approaches seem to be more reliable for brittle material like concrete. A number of research works using this method for predicting debonding failure of externally bonded reinforcement (EBR) strengthened RC beams has been reported.

The aim of this research work is to investigate the possibility of using GEBA based fracture mechanics model for beams strengthened using near-surface mounted (NSM) technique, combined NSM and EBR techniques, and prestressed FRP, beams that were precracked before strengthening, and T-beams. In addition, this thesis proposes an optimization design tool for the field applications of the model using the fuzzy approach and dimensional analysis for uncracked EBR-strengthened beams for end failure.

The methodology involves finding available energy for the propagation of interface flaw in a beam using GEBA method. Debonding occurs when the available energy for interface flaw propagation reaches the fracture energy of the weakest material of the concrete-FRP composite system. The limiting fracture energy used for determining the failure state is the mode I fracture energy of the concrete because failure often occurs in the concrete substrate in a peeling nature. Different bond conditions, combination of two types of strengthening techniques, proper material modeling, equilibrium condition and geometry of beam are duly considered in the computation of energy dissipation.

The outcome of the analysis is the critical FRP curtailment location from the beam support for end debonding and the critical debonded zone length debonding that initiates debonding in the vicinity of the highest moment. Parameters influencing debonding are reduced through grouping by dimensional analysis. Then, a fuzzy system is developed using the results of the parametric analysis of the model for the end debonding of EBR-strengthened beams.

The validation using published experimental results demonstrates that the model is capable of predicting all modes of debonding failure for FRP strengthened RC beams, for any material and geometric properties of concrete beam, adhesive, FRP. The overall performance of the model is found to be satisfactory. The mean ratio between simulated to experimental failure loads for NSM strengthened beam are 0.99 and a standard deviation of 0.09. For hybrid strengthened beam the mean ratio and standard deviation are 0.95 and 0.09 respectively. For beams precracked before strengthening the mean ratio and standard deviation are 0.97 and 0.09. For beams strengthened using prestressed FRP the mean ratio and standard deviation are FRP 0.93 and 0.09. The mean ratio and standard deviation for T-beams are 0.94 and 0.07. The developed fuzzy dimensional analysis-based model also provides a good correlation with a coefficient of performance and relative error of 0.96 and 7.9%, respectively.

Keywords: Strengthened RC beams, Debonding, Global energy balance, fracture energy, interface flaw.

[SIMULASI SIFAT NYAH-IKATAN BAGI RASUK BERTETULANG YANG DIPERKUKUHKAN MENGGUNAKAN PENDEKATAN IMBANGAN TENAGA GLOBAL]

ABSTRAK

Kecacatan dan kekurangan kekuatan pada permukaan sambungan di antara konkrit dan polimer bertetulang gentian (FRP) biasanya memulakan kegagalan nyahikatan bagi rasuk konkrit bertetulang (RC) yang diperkuatkan dengan FRP. Model sedia ada yang berasaskan kekuatan biasanya dapat meramalkan kegagalan struktur tempatan dengan baik, tetapi tidak kepada kegagalan keseluruhan. Oleh itu, ianya tidak cekap dalam meramal kegagalan nyahikatan. Dalam masa yang sama, aplikasi model unsur terhingga (FE) memerlukan maklumat yang tepat pada permukaan sambungan di antara konkrit dan FRP yang biasanya sukar diperolehi. Mekanik keretakan bersama kaedah keseimbangan tenaga global (Global energy balance approach, GEBA) adalah lebih sesuai untuk diaplikasikan kepada bahan rapuh seperti konkrit. Beberapa penyelidikan menggunakan kaedah ini untuk meramalkan kegagalan nyahikatan bagi rasuk RC yang diperkuatkan menggunakan teknik tetulang ikatan luaran (EBR) telah dilaporkan.

Tujuan penyelidikan ini adalah untuk mengkaji kemungkinan menggunakan model GEBA berasaskan mekanik keretakan untuk rasuk yang diperkuatkan dengan menggunakan teknik pemasangan pada permukaan (Near surface mounted, NSM), gabungan teknik NSM dan EBR, FRP prategasan, rasuk yang mempunyai retak sebelum penguatan dan rasuk-T. Di samping itu, kajian ini juga mencadangkan satu kaedah rekabentuk optimum untuk aplikasi tapak berasaskan logik kabur (Fuzzy logic, FL) dan analisis dimensi bagi rasuk tiada retak yang diperkuatkan dengan EBR.

Metodologi penyelidikan bermula dengan mencari tenaga yang ada untuk penyebaran kecacatan permukaan dalam rasuk menggunakan kaedah GEBA. Kegagalan nyahikatan berlaku apabila tenaga yang tersedia untuk penyebaran kecacatan permukaan mencapai tenaga keretakan bagi bahan yang terlemah di dalam sistem

konkrit-FRP rencam. Had tenaga keretakan yang digunakan untuk menentukan keadaan kegagalan adalah tenaga keretakan Mod 1 bagi konkrit kerana kegagalan sering berlaku dalam substrat konkrit melalui sifat pengelupasan. Pelbagai keadaan ikatan, gabungan dua jenis teknik pengukuhan, pemodelan bahan yang sesuai, keadaan keseimbangan dan geometri rasuk adalah diambilkira dalam pengiraan pelepasan tenaga. Hasil analisa adalah lokasi pengurangan kritikal FRP dari penyokong rasuk bagi nyahikatan hujung dan panjang zon nyahikatan kritikal yang menyebabkan nyahikatan bermula berhampiran dengan lokasi momen tertinggi. Beberapa parameter yang mempengaruhi nyahikatan dikurangkan melalui pengelompokan menggunakan analisis dimensi. Kemudian, sistem kabur dibangunkan dengan menggunakan hasil analisis parametrik bagi model nyahikatan hujung untuk rasuk yang diperkuatkan EBR.

Pengesahan menggunakan keputusan eksperimen yang telah diterbitkan menunjukkan bahawa model ini mampu meramalkan semua mod kegagalan nyahikatan untuk rasuk RC yang diperkuat menggunakan FRP, untuk sebarang sifat bahan dan sifat geometri rasuk konkrit, pelekat dan FRP. Prestasi keseluruhan model didapati memuaskan. Nisbah purata di antara simulasi dengan beban kegagalan eksperimen untuk rasuk diperkukuhkan NSM adalah 0.99 dan sisihan piawai 0.09. Bagi rasuk dikuatkan secara hibrid, nisbah purata dan sisihan piawai adalah masing-masing 0.92 dan 0.18. Bagi rasuk yang retak sebelum pengukuhan, nisbah purata dan sisihan piawai adalah 0.97 dan 0.09. Bagi rasuk yang diperkukuhkan dengan menggunakan FRP prategasan, nisbah purata dan sisihan piawai adalah 0.93 dan 0.09. Nisbah purata dan sisihan piawai bagi rasuk-T adalah 0.94 dan 0.07. Model berasaskan logik kabur dan analisis dimensi juga memberikan korelasi yang baik dengan pekali prestasi dan ralat relatif masing-masing sebanyak 0.96 dan 7.9%.

Kata Kunci: Rasuk RC yang diperkuat, Nyahikatan, Keseimbangan tenaga global, Tenaga keretakan, Kecacatan permukaan.

ACKNOWLEDGEMENTS

First of all, all praise to Allah the Almighty for giving me the strength and patience to complete this work. I give my sincerest gratitude to my supervisors, Professor Ir. Dr. Mohd. Zamin Jumaat, Associate Professor Dr. Nor Hafizah Ramli and Dr. Mithila Achintha who have supported me throughout my thesis work with their patience and knowledge whilst allowing me space to work under my own direction. Their expertise, understanding, and patience added considerable value to my graduate experience. I am very grateful for the time and effort they dedicated to me. Their technical and editorial was essential to the completion of this thesis and they have given me innumerable lessons and insights into the workings of academic research in general. Acknowledgement is also due to University of Malaya, Department of Civil Engineering, Faculty of Engineering and High Impact Research (HIR) secretariat at University of Malaya for the financial support that made it possible for me to complete my graduate studies.

I would also like to send a special thought to my colleagues and friends in the research group for all their help and support.

Finally, writing a thesis is not possible without an extremely understanding family, so I must thank my mother for her limitless and devoted care, my father for his unbounded confidence in me, and my sisters for helping us all out during my study period. I cannot express in words how grateful I am to my husband Tofael Ahmed for his support and patience and little son's sacrifice during my work, your smile and patience kept me going! May Allah give you all best rewards in the afterlife.

2.3.3	Models for shear failure and debonding.....	18
2.3.4	Models using bond strength	19
2.3.5	Models using Finite Element.....	20
2.4	Fracture mechanics in debonding analysis	21
2.4.1	Fracture mechanics for concrete	22
2.4.2	GEBA and fracture mechanics in FRP strengthened structures.....	23
2.4.3	GEBA and fracture mechanics-based models.....	24
2.5	Determination of fracture energy.....	27
2.5.1	Fracture resistance of pure and mixed mode.....	27
2.5.2	Experimental and analytical work on FRP–strengthened beam.....	28
2.5.3	NSM strengthened beam	29
2.5.4	Hybrid FRP-strengthened beam	31
2.5.5	Precracked EBR FRP-strengthened beam.....	31
2.5.6	Prestressed EBR & NSM FRP-strengthened beam.....	32
2.6	Approaches used for implementing numerical models to design.....	34
2.6.1	Dimensional analysis.....	34
2.6.2	Fuzzy approach	35
2.7	Research gaps	36

CHAPTER 3: DEBONDING ANALYSIS OF DIFFERENT TYPES OF BEAMS 39

3.1	Introduction.....	39
3.2	GEBA with fracture criteria model for debonding.....	39
3.2.1	Why GEBA over other methods of Energy Release Rate (ERR)	40
3.2.2	Energy balance during debonding.....	40
3.2.3	Work done on a beam.....	41
3.2.4	Moment–curvature for FRP strengthened section.....	42

3.2.4.1	Branson's effective moment of inertia model	43
3.2.4.2	Modeling of RC beams with external FRPs.....	43
3.2.4.3	Depth of centroidal axis	45
3.2.4.4	Effective elastic stiffness.....	46
3.2.5	Energy release rate zone.....	49
3.2.5.1	Rate of change of potential energy of the externally applied load.....	50
3.2.5.2	Rate of change of work done on the beam.....	51
3.3	Analysis of NSM strengthened beam	53
3.3.1	Moment-curvature analysis	53
3.3.1.1	Material properties for moment-curvature	53
3.3.1.2	Determination of stress-strain	55
3.3.2	Debonding analysis for NSM strengthened beam.....	59
3.3.2.2	Zone of energy release for end failure in NSM strengthened beam.....	61
3.3.2.3	Intermediate crack induced debonding (IC).....	65
3.3.2.4	Determination of energy release rate	68
3.4	Failure criteria.....	71
3.4.1	Fracture Energy	71
3.4.2	Total Length of debonded zone.....	74
3.5	Analysis of Hybrid strengthened beam.....	75
3.5.1	Moment-curvature of hybrid strengthened beam	75
3.5.2	Debonding failure analysis of hybrid strengthened beam.....	77
3.6	Analysis of beams precracked before strengthening	77
3.6.1	Constituent material properties for precracked beam	77
3.6.2	Moment-curvature of unstrengthened section.....	80

3.6.3	Determination of plastic component	81
3.6.4	Moment-curvature of strengthened section.....	82
3.6.5	Centroidal axis depth.....	84
3.6.6	Computation of ERR.....	84
3.6.7	Debonding analysis	85
3.7	Analysis of beams strengthened using Prestressed FRP.....	87
3.7.1	Moment-curvature of prestressed beam	87
3.8	Analysis of T-beams	97
3.9	Summary.....	99
CHAPTER 4: VALIDATION OF PROPOSED MODEL		101
4.1	Introduction.....	101
4.2	Steps for validation of test beams	101
4.3	Validation of NSM strengthened beam	104
4.3.1	A detailed Example of debonding load prediction for NSM beam.....	107
4.3.2	Study on different strengthening technique: EBR and NSM	112
4.3.3	Study on Beams with different NSM lengths.....	113
4.3.4	Study on beams with different reinforcement percentages	116
4.3.5	Study on beams with different adhesive properties	121
4.3.6	Study on beams with different strengthening materials	122
4.4	Validation of test beams for Hybrid strengthened beam	123
4.4.1	Study on hybrid beam with steel as strengthening material.....	126
4.4.2	Study on hybrid beam with CFRP as strengthening material	126
4.5	Validation of beams precracked before strengthening	127
4.5.1	Study on beams with precracking beyond 80 %	130
4.5.2	Study on beams with precracking less than or equal to 80%.....	131

4.6	Validation of test beams for prestressed FRP strengthened beam.....	136
4.6.1	Study on beams with prestressing in EBR technique.....	139
4.6.2	Comparison of beams with prestressing in EBR and NSM	143
4.7	Validation of test beams for T- Beam.....	144
4.8	Comparison of simulation versus experimental results	147
4.9	Parametric study	151
4.10	Summary.....	160

CHAPTER 5: FUZZY LOGIC APPROACH FOR DETERMINING THE SAFE CURTAILMENT LENGTH USING ENERGY BALANCE.....161

5.1	Introduction.....	161
5.2	Development of the FLES for EBR beam	162
5.2.1	Dimensional analysis.....	164
5.2.2	Dimensional analysis and its application to the present problem	164
5.2.3	Interpretation of numerical results based on dimensional analysis.....	169
5.3	Implementation of Fuzzy.....	171
5.3.1	Fuzzy model development for EBR strengthened beam.....	173
5.3.2	Fuzzify inputs	174
5.3.3	Creating rule base.....	176
5.3.4	Aggregation of truncated conclusions.....	177
5.3.5	Defuzzification	178
5.4	Validation of the proposed model.....	180
5.4.1	Comparison of predicted failure load.....	181
5.4.2	Application of fuzzy model in Design	183
5.5	Summary.....	185

CHAPTER 6: CONCLUSIONS.....	186
6.1 General.....	186
6.2 Development of GEBA based model for strengthened beams using NSM and hybrid technique	186
6.3 Application of the GEBA-based model for precracked and prestressed FRP and T-beams	188
6.4 GEBA based model: Overall performance and parametric study	189
6.5 Fuzzy method and dimensional analysis for practical application	189
6.6 Recommendation for future works	190
References.....	192
List of publications.....	210
Appendix.....	211

LIST OF FIGURES

Figure 1.1 Block diagram of research methodology	6
Figure 2.1: Different strengthening technique	11
Figure 2.2: Debonding failure mechanism.....	13
Figure 2.3: Interfacial stress distribution at the interface of a typical EBR strengthened beam. (After (Täljsten, 1997))	15
Figure 2.4: Design approach in strength based and fracture based approach	23
Figure 2.5: Bilinear softening stress separation law	28
Figure 2.6: Typical failure type in NSM strengthened beam observed in experiment ...	30
Figure 3.1: Flowchart showing the M- κ analysis (After Achintha and Burgoyne)	48
Figure 3.2: Transition zone concept used by Achintha and Burgoyne (2008).....	49
Figure 3.3: Debonding flaw a) before and b) after a small flaw extension of ‘ δa ’	50
Figure 3.4: Load versus deflection plot before and after the extension of interface flaw (After Achintha and Burgoyne 2008)	51
Figure 3.5: Changes in different component of work done on beam (After Achintha and Burgoyne, 2008).....	52
Figure 3.6: Material properties.....	55
Figure 3.7: Stress–strain relationship of RC beam section due to flexure.....	57
Figure 3.8: Load versus deflection and FRP strain versus load plot.....	58
Figure 3.9: ERR versus safe curtailment length for beam SC210 by Al-Mahmoud et al. (2010).....	60
Figure 3.10: Interfacial stress distribution	62
Figure 3.11: Interfacial stress distribution in beams at the NSM cut–off location	65
Figure 3.12: Debonded zone for IC debonding modified from Achintha and Burgoyne (2008).....	68
Figure 3.13: Flowchart showing debonding analysis.....	68

Figure 3.14: Crack propagation in interface	73
Figure 3.15: Load versus deflection curve for Hybrid beam tested by Jumaat et al. (2016)	76
Figure 3.16: Load-deflection and stress-strain curve under repeated loading	78
Figure 3.17: Load versus deflection curve	83
Figure 3.18: Flowchart showing computation procedure	86
Figure 3.19: Flow chart of moment-curvature for prestressed FRP strengthened beam	89
Figure 3.20: Load versus deflection curve for prestressed EBR beam	91
Figure 3.21: Load versus FRP strain curve for prestressed EBR beam	93
Figure 3.22: Load versus deflection curve for prestressed NSM beam	94
Figure 3.23: Load versus FRP strain curve for prestressed NSM beam	96
Figure 3.24: Load versus deflection and Load versus FRP strain plot for T- beam	97
Figure 4.1: Flowchart showing calculating debonding load	103
Figure 4.2: Plotting for the beam configuration by Al-Mahmoud (2010)	109
Figure 4.3: Plotting for the beam configuration by Al-Mahmoud (2010)	111
Figure 4.4: Debonded zone length versus load plot for beam tested Khalifa (2016)....	113
Figure 4.5: Safe curtailment length versus load plot	114
Figure 4.6: Plotting of simulation results for beams tested by Khalifa (2016).....	117
Figure 4.7: Plotting of simulation results for beams tested with different FRP percentage	119
Figure 4.8: Safe curtailment length versus load plot for beams NSM 1, NSM2 and NSM 3 by Hosen et al. (2014)	121
Figure 4.9: Safe curtailment length versus load plot for beam E3 and Beam C3 by Caroline (2003)	122
Figure 4.10: Safe curtailment length versus load plot for beam configuration of Sharaky et al. (2014)	123

Figure 4.11: Safe curtailment length versus load plot for hybrid beam HS1 tested by Rahman et al. (2015).....	126
Figure 4.12: Debonded zone length versus load plot for beam CBC10P2 by Jumaat et al. (2016).....	127
Figure 4.13: Plotting of debonded zone length versus load plot for beams by Zaid (2014).....	130
Figure 4.14: Plotting of debonded zone length versus load plot for beams tested by Sharif et al. (Sharif et al., 1994).....	131
Figure 4.15: Plotting of debonded zone length versus load for beams by Wu et al. (2007).....	132
Figure 4.16: Plotting of simulation results.....	133
Figure 4.17: Plotting of debonded zone length versus load plot for beam SM3 tested by Arduini et al. (1997).....	135
Figure 4.18: Plotting of debonded zone length versus load plot for beam B3 tested Dong (2003).....	136
Figure 4.19: Debonded zone length versus load plot for beam C by Yu et al. (2008)..	139
Figure 4.20: Debonded zone length versus load plot for beams tested by Pelligrino and Modena (2009).....	140
Figure 4.21: Debonded zone length versus load plot for beams tested by Xue et al. (2010).....	141
Figure 4.22: Debonded zone length versus load plot for beams tested by You et al. (2012).....	142
Figure 4.23: Debonded zone length versus load plot for beams tested by Quantrill and Hollaway (1998).....	143
Figure 4.24: Debonded zone length versus load plot for beams tested by Peng et al. (2014).....	144
Figure 4.25: Debonded zone length versus load plot for beam tested by a)Castro (2007) and b) Han Choi (2010).....	146
Figure 4.26: Comparison of simulated and experimental failure load.....	151
Figure 4.27: Geometric details of assumed example beam.....	152

Figure 4.28: ERR versus debonded zone length for prestressed beam a) and b) with different level of prestressing.....	153
Figure 4.29: ERR versus debonded zone length for IC debonding failure for 100 % precracked beam.....	154
Figure 4.30: Plotting of simulated results for NSM strengthened beam.....	154
Figure 4.31: Safe curtailment length from (a) to (d) and debonded zone length versus load of from (e) to (f)	156
Figure 5.1: Types of critical interface flaw at plate end failure (Achintha, 2009).....	163
Figure 5.2: Load versus debonding load comparison for various compressive strengths	167
Figure 5.3: Nondimensional load versus normalized safe curtailment length.....	170
Figure 5.4: Nondimensional load versus normalized safe curtailment length.....	170
Figure 5.5: Beam specification for parametric analysis.....	174
Figure 5.6: Membership functions and rules created in fuzzy inference engine	175
Figure 5.7: Fuzzy rule viewer in MATLAB	180
Figure 5.8: Example of control surfaces of fuzzy inferring system for length	180
Figure 5.9: Comparison of actual and numerically predicted value	182

LIST OF TABLES

Table 4.1: Identification and geometric data of the beams used in the analysis.....	105
Table 4.2: Reinforcement details of the beams used in the analysis.....	106
Table 4.3 Identification and geometric data of the Hybrid beams used in the analysis	124
Table 4.4: Reinforcement Details of the beams used in the analysis.....	124
Table 4.5: Beam property for precracked beams failed due to IC debonding	128
Table 4.6: Reinforcement details for precracked beams failed due to IC debonding ...	129
Table 4.7: Details of EBR strengthened prestressed beam	137
Table 4.8: Reinforcement details of EBR strengthened prestressed beam	138
Table 4.9: Identification and geometric data of the T-beams used in the analysis	144
Table 4.10: Reinforcement details of the beams used in the analysis.....	145
Table 4.11: Summary of results for beams strengthened using different technique.....	148
Table 4.12: Summary of results for different types of strengthened beams	149
Table 5.1 Mechanical and geometric properties of beam characterized by the same dimensionless value	169
Table 5.2 Membership function for different parameter.....	177
Table 5.3 Obtaining safe curtailment length from F-dim analysis	181
Table 5.4: Comparison of safe curtailment length: Actual versus fuzzy	182

LIST OF SYMBOLS AND ABBREVIATIONS

A_p	Area of FRP reinforcement
A_{st}	Area of tension steel
A_{sc}	Area of compression steel
A_v	Area of stirrup leg
ACI	American Concrete Institute
ANFIS	Adaptive neuro fuzzy interface system
b_p	The fracture surface, which is adopted in this research work as the width of the beam
b	Beam width
B_{uc}	Uncracked stiffness
B_{fc}	Cracked stiffness
B_{eff}	The stiffness of partially cracked section.
d	Effective depth of tension steel from the top of the beam
d_c	Effective depth of compression steel from the top of the beam
d_a	Aggregate size
d_p	Diameter of FRP
ϵ_c	Strain at maximum stress
E_c	Modulus of concrete
EBR	Externally bonded reinforcement
ERR	Energy release rate
E_p	Elastic modulus of FRP reinforcement.
f_c'	Compressive strength of concrete
f_p	Force in the debonded zone
f_{y_s}	Yield strength of steel
f_{un}	Reversal envelope stress
f_u	Ultimate capacity of FRP reinforcement
f_{vy}	Yield capacity of stirrup

FRP	Fiber Reinforced Polymer
FPZ	Fracture process zone
FE	Finite element
F_{1p}/F_{2p}	Axial force in the FRP
GEBA	Global energy balance
G_a	Shear modulus of adhesive
h	Beam height
h_f	Height to the center of FRP rebars.
IC	Intermediate crack induced
I_g	Second moment of area of the gross section neglecting steel
I_{cr}	Second moment of area of the cracked transformed section
K_p	Modified interpolation coefficient for determining stiffness.
K_α	Modified interpolation coefficient for determining centroid and neutral axis depth.
l_{span}	Total span of the beam
l_{shear}	Shear span of the beam
L_o	Distance of FRP reinforcement from the beam support
$L_{unbonded}$	Length of debonded zone.
LEFM	Linear elastic fracture mechanics
$M_{1appcen}/$ $M_{2appcen}$	Moments acting on RC section about centroid axis
M_{cr}	Moments at first cracking
M_{app}	Applied moment
M_{A-y}	Moment acting on RC section alone about the axis y
M_{eff}	The moment acting on RC section alone
M_{frp_rup}	Moment corresponding to FRP rupture
M_y	Yield moment
M_{inc_cr}	Increase in first cracking moment due to prestressing
M_{inc_yield}	Increase in yield moment due to prestressing

NLFM	Non-linear fracture mechanics
NSM	Near Surface Mounted Reinforcement
P	The applied load
P_{Exp}	Failure load
P_{pre}	Precracked /prestressing load applied on beam
P_{frp_rup}	Failure load corresponding to FRP rupture
P_{yield}	Load due to steel yielding
P_{shear}	Load due to shear
P_{shear_ACI}	Maximum load capacity according to ACI.
P_{PE}	Failure load found from PE debonding analysis
P_{IC}	Failure load found from IC debonding analysis
PE	Plate end
s	Spacing of the stirrups provided
t_a	Thickness of adhesive
t_p	Thickness /diameter of FRP reinforcement
T_{frp}	Force in FRP
RC	Reinforced Concrete
$U_{bending}$	Strain energy due to bending
w/c	Water cement ratio
w	Crack opening
$W_{bending}$	Work done on the RC beam due to bending
W_{axial}	Work done on the RC beam due to axial force
W_{FRP}	Work done on the FRP plate
x	Depth of neutral axis
x_{eff}	Neutral axis depth
x_g	Neutral axis depth at uncracked section
x_{cr}	Neutral axis depth at fully cracked section
y	Height of the reference axis
V_c	Shear capacity of concrete

V_s	Shear capacity of stirrup
α_o	The coefficient for the aggregate type.
α_f	Normal stress on the FRP
α_{un}	Equivalent centroid for uncracked section
α_{fc}	Equivalent centroid for cracked section
γ	Interfacial shear strain
∂a	The assumed extension of the original debonding crack length 'a'
$\delta \Delta$	Increase in deflection at the loading point
δW_b and δW_a δW_p	Work done on RC beam alone due to bending and axial strain Work done on the FRP plate
$\frac{\partial W_{ext}}{\partial a}$	The rate of change of the work done on the beam by the external force
$\frac{\partial W_{sys}}{\partial a}$	The rate of change of energy dissipated by strengthened beam section due to the work done by moment-curvature, FRP-strain
$\epsilon_{20}/\epsilon_{10}$	Strain at the equivalent centroid
$\epsilon_{2p}/\epsilon_{1p}$	Strain at the FRP level
ϵ_c	Strain at any stage, is the f_c' .
ϵ_{cu}	Concrete crushing strain
ϵ_{c_frp}	Strain at concrete at the level of FRP due to bending only;
ϵ_{fu}	FRP rupture strain
ϵ_{un}	Unloading concrete strain
ϵ_{pl}	Plastic or inelastic strain
ϵ_{pl_bot}	Plastic strain at the tension side of the beam i.e. at the bottom fiber of the beam is the
ϵ_{un_bot}	Unloading strain at the tension steel level of the beam
ϵ_{bot}	Strain at the bottom fiber of beam
ϵ_{top}	Strain at the top fiber of the beam.
ϵ_y	Yield strain of steel

ε_{pre}	Prestressing strain applied to the FRP reinforcement
σ	Stress
σ_c	Stress corresponding to ε_c
Δd	Total extension in debonded zone
κ_2/κ_1	Curvature of the RC section
τ	Interfacial shear stress.

University of Malaya

LIST OF APPENDICES

APPENDIX A: SAMPLE CALCULATION.....	208
APPENDIX B: MATLAB CODE FOR DEBONDING ANALYSIS.....	210
APPENDIX C: ENERGY RELEASE RATE CURVE	216

University of Malaya

CHAPTER 1: INTRODUCTION

1.1 Background

Concrete structures are designed usually for a life period of 50 years or greater. However, even a well-designed, constructed and maintained structure cannot attain this expected lifespan (Matthys, 2000). This situation is primarily due to the steel corrosion of the reinforced elements in the corrosive environment and to the unpredictable change in the usage and functionality of the structure. However, a practical solution to this problem is increasing the capacity of these structures by reinforcing them. Therefore, researchers have been focusing on new reinforcing materials that can strengthen structures, be easily used for repairs, and endure adverse environmental conditions. Thus, FRP is becoming increasingly popular worldwide as a structural reinforcement (Matthys, 2000). FRP can be considered a viable means for strengthening concrete structures through continuous research efforts analogous to engineering practices.

FRP is a composite material made up of a polymer matrix that is reinforced mostly with glass, carbon, aramid, or basalt fibers. The first wide-range application of FRP dates back to the 1940s in the aircraft industry due to its high strength, stiffness, and low density. Over time, FRP has become significant in the concrete industry due to its high strength-to-weight ratio, good corrosion resistance, ease of installation, and high fatigue strength (Matthys, 2000; Oudah, 2011). Different forms of FRP elements, such as bars, tendons, ropes, grids, strips, sheets, and fabrics, are commercially available for use as structural reinforcements in concrete members. FRP can be applied in new and old structures. In new structures, FRP can be used as a traditional reinforcement and can be prestressed. In deteriorated structures, FRP is used to strengthen the existing structures using various techniques, such as external bonding (EBR), internal bonding in the groove (NSM), and hybrid (combination of EBR and NSM) techniques. In the early 1980s, the first experimental work on external strengthening with FRP was initiated at

the Swiss Federal Laboratories for Materials Science and Technology (EMPA). The first reported field application was the repair of a bridge in Switzerland in 1991 (Meier, Deuring, Meier, & Schwegler, 1993). The disadvantages of the EBR method, such as exposure to the external environment and premature failure, led to research on strengthening using groove reinforcement, which is commonly called NSM. However, reinforcing the concrete cover for strengthening is not a novel method in the practical field. The first application of this type of strengthening happened in the 1940s in Sweden, in which a bridge slab was strengthened in the negative moment region (Asplund, 1949; Nordin & Täljsten, 2006). The NSM technique is also used in masonry arch bridges (Chen, Ashour, & Garrity, 2007). To address the serviceability issue of FRP-strengthened members, prestressing has also been used in FRP strengthening (Oudah, 2011).

1.2 Problem statement

As described in the previous section, the use of FRP in strengthening concrete beams using different techniques is realistic and promising. Numerous studies have been conducted worldwide (Gunes, 2004; Oudah & El-Hacha, 2013; Pham & Al-Mahaidi, 2006), thereby giving recognition to the use of FRP for concrete construction. However, using FRP for strengthening has not gained its projected success in the field due to the incomplete understanding of the concrete-FRP interface. An important issue hindering the usefulness and safety of this method from a structural perspective is the possibility of a brittle debonding failure, i.e., failure of the beam before the projected capacity of the beam is reached by the peeling off of the FRP from the beam soffit. If this type of failure is not adequately considered in the design methodology, then it might reduce the efficiency of the strengthening application. Generally, debonding in an FRP-strengthened member happens in the vicinity of high-stress concentration because of material discontinuities and occurrence of cracks. The strength properties of the

materials and the fracture properties of the interface govern the propagation path of debonding, which originates from the stress concentration. Theoretically, debonding follows the path of the least energy and can take place within or in the interface of the materials. However, most of the debonding failures reported in the literature occurred in the concrete substrate. Moreover, other debonding mechanisms are observed depending on the geometric and material properties,

However, FRP reinforcement can only be widely applied through the proper understanding of the structural behavior of concrete structures strengthened with FRP and hence with the availability of design guidelines and code regulations. Guidelines are also required for material selection, detailing, cost estimation, and installation processes. Different related topics associated with FRP-strengthened systems, such as mechanical behavior, design and durability issues, and quality assurance methodologies, have been investigated by many researchers around the world. The mechanical behavior of FRP-strengthened systems and the failure mechanism are clarified through experimental investigations. Several empirical and mechanics-based prediction models have been established for design purposes, thereby helping set the design guidelines proposed by American Concrete Institute (ACI). Column strengthening does not suffer from the debonding problem due to its circumferential wrapping, thereby becoming a frequently used seismic retrofitting method for improving ductility and shear resistance. However, FRP strengthening is still not an effective method for beams, slabs, and walls due to the debonding problem.

Debonding failure is a critical issue in the performance of FRP-strengthened members, and its characterization and modeling are popular areas in interdisciplinary research. The cause and mechanism of debonding failure have been intensively studied since the 1990s. Several models have been developed for predicting debonding failure

by using mechanics-based approaches together with the strength of materials or fracture mechanics properties. Some researchers adopted the energy approach and applied GEBA to find the energy available for debonding. However, no consensus has been reached regarding these failures models. Therefore, a better prediction of failure load and criteria for FRP-strengthened flexure members should be developed. The following goals have been selected for this study with the abovementioned issues in mind.

1.3 Objectives of research work

This thesis aims to develop and apply a GEBA-based model developed for EBR-strengthened fresh RC beams for the debonding prediction of beams strengthened using NSM and hybrid techniques and prestressed FRP, beams precracked before strengthening, and T-beams. Moreover, a dimensional analysis and fuzzy based model is proposed using the results obtained from the proposed debonding model for design purposes. The specific objectives of this study are as follows:

- i. Developing a GEBA-fracture based model for predicting the debonding failure of RC beams strengthened using NSM and hybrid techniques.
- ii. Application of the GEBA-fracture based model in predicting the debonding load of beams precracked before strengthening, those strengthened using prestressed FRP, and T-beams.
- iii. Validating the developed model for beams strengthened using NSM and hybrid techniques and prestressed FRP, beams precracked before strengthening, and T-beams using data gathered from the existing literature.
- iv. Proposing a model using fuzzy concept and dimensional analysis that uses the debonding prediction from GEBA-based fracture mechanics model in field applications.

1.4 Research Methodology

The prior stated objectives are fulfilled by the research methodology shown in Figure 1.1. It can be seen from the flow chart of Figure 1.1 that, comprehensive literature review is carried out to understand state-of-art-works done on understanding the debonding behavior of FRP strengthened RC beams. In order to predict the debonding load for different types of techniques and different types of beams, methodology is developed.

In order to evaluate performances of the model, it is validated using data gathered from literature. Finally, a fuzzy based approach has been proposed together with the dimensional analysis to use the results of GEBA based model in practical application.

University of Malaysia

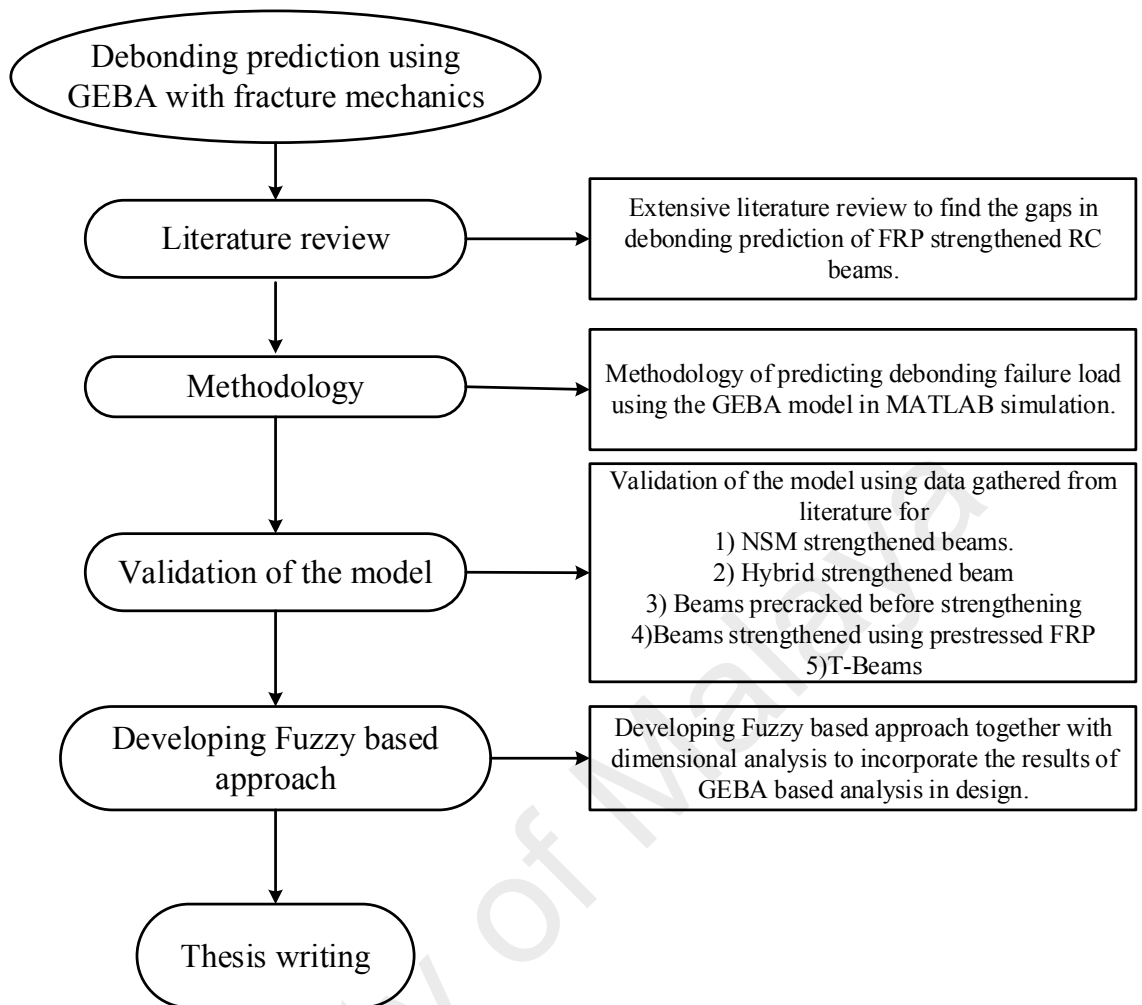


Figure 1.1 Block diagram of research methodology

1.5 Scope of the work

This thesis studies the GEBA for estimating the debonding behavior of RC beams strengthened with CFRP materials using various strengthening techniques, such as NSM and hybrid techniques, strengthening using prestressed FRP, loading before strengthening and subsequent unloading, and strengthening with T-beams. The proposed model is numerical in nature, in which the beam response can be computed for every 1 mm section along the length of the beam. The numerical procedure is coded using MATLAB software. All the material properties of the constituent materials and geometric properties of the beams can be used as inputs in the program. Then, the program can simulate the moment-curvature response of the model and plot moment

versus curvature, load versus deflection, and load versus strain response. Separating FRP and the RC section is one of the novelties of the moment-curvature model presented in this study thesis for the types of beams mentioned beforehand. Another advantage is that the proposed model is independent of any empirical relation or specific material properties, such as bond slip, and can hence be applied in different cases of debonding with different materials.

Debonding analysis follows the moment-curvature response simulation. The model can be run for two types of debonding failures commonly seen in actual beams, namely, plate end (PE) and intermediate crack (IC)-induced debonding. The model can give a safe curtailment length for a certain load in PE-type debonding. By contrast, the model can give the debonded zone length for a certain load in IC debonding. The model proposes a criterion on the basis of analysis and experimental observation to predict the debonding load for PE and IC debonding. For NSM-strengthened beams, the model considers the effect of the transition zone, the length of the transition zone, and length of the fracture surface area. For beams strengthened using the hybrid technique, the combination of EBR and NSM is included and failure analysis is set, assuming that failure will initiate in the EBR layer. For beams precracked before strengthening, the effect of the previous loading, which represents the condition of the unstrengthened beam under service load in the real field, can be simulated through the model. For beams strengthened using prestressed FRP, the model considers the effect of prestressing force on the FRP. The model can run not only for rectangular sections but also for T-shaped cross sections. The validity of the model is checked for all the aforementioned types of beams using data from the literature, and a good agreement is found. The effect of different types of parameters can be analyzed using the model. These parametric studies lead to the development of a fuzzy system. Moreover, dimensional analysis is employed before developing the fuzzy system, thereby reducing

the number of parameters that influence the debonding behavior by grouping the parameter into dimensionless group. The fuzzy program is also run in MATLAB environment. The fuzzy dimensional analysis is also validated against experimental data, and a good correlation is obtained. This fuzzy dimensional model can be an effective tool for using the GEBA model in practical applications.

1.6 Research hypothesis

Predicting failure mode and failure load of strengthened beams is possible using the GEBA analysis and fracture mechanics concepts. The Energy release rate (ERR) associated with an existing interface flaw can be calculated using the moment-curvature model of the beam. During ERR computation a transition zone is assumed where ERR is assumed to take place. If the debonding occurs in the concrete substrate, then the interface fracture energy is assumed to be the fracture energy of the concrete. The failure criteria for different types of failures are assumed accordingly based on the experimental evidences and literatures.

For fuzzy logic approach, the system has been developed based on the results of parametric analysis found from the proposed GEBA model.

1.7 Organization of thesis

The thesis is organized as follows:

Chapter 1 provides an introduction to the use of FRP material as the strengthening reinforcement of reinforced concrete beams. A concise description of FRP in the concrete construction industry, different aspect of repairing and strengthening with FRP reinforcement, the benefits as well as disadvantages of FRP technique is highlighted. Consequently, the problem statement and the aims and outline of this thesis are also presented

Chapter 2 makes a comprehensive review of FRP strengthened beam, with their failure mode, available type of models, their deficiency, experimental observation for a different type of beams and finally the research gaps.

Chapter 3 presents the basic methodology of the numerical work used in this thesis, the debonding models for beams strengthened using NSM and hybrid strengthening, beams precracked before strengthening, beams strengthened using prestressed FRP and beams with T- shape section.

Chapter 4 shows the validation of the model for beams failed by debonding, collected from literature to show the efficiency of the model. It also presents an example of determining debonding load for different types of beams and also provides a brief parametric analysis.

Chapter 5 represents an approach using dimensional analysis and Fuzzy to predict the debonding to be used in the real field. The approach has been presented only for EBR strengthened beam failed due to plate end debonding.

Chapter 6 summarizes the research findings and states the conclusion drawn. Recommendations for future researchers are also presented.

CHAPTER 2: LITERATURE REVIEW

2.1 Introduction

The use of FRP to strengthen RC beams has been in practice since the 1980's (Gunes, 2004). With increasing demand for retrofitting beams in highway and railway bridges, research in this area has been increasing in the context of increasing the efficiency of FRP usage. The primary goal of these researches is to eliminate the various problems associated with the strengthening methods. This chapter summarizes problems associated with FRP strengthening in flexure and provides a brief review of research on the subject. At the end of this chapter, the identified research gaps will be outlined, which will be studied and summarized in the subsequent chapters.

2.2 Use of FRP in flexural strengthening of beams

There are various factors that necessitates the use of flexural strengthening of RC beams in bridge girders, such as increment in traffic load on the bridge girder, decrement of the deformation capacity under live service load, retrofitting of bridge girders to comply with revised building codes, compensating for faulty design or construction, and restoration of the load carrying capacity of the deteriorated beams.

Conventionally, flexural strengthening of the beams can be achieved via three means, i.e. removing the concrete cover, adding extra reinforcement and then replacing concrete cover; increasing the beam cross section, increasing reinforcement area or by applying external post-strengthening to reinforcement; and adding steel plates to the bottom of the beam.

The most convenient amongst them is the addition of steel plates, due to its simplified application, lesser labor, and reduced service disruption cost. However, the use of steel plates in the field is unfavorable, due to transportation and installation problems during the strengthening phase, as well as corrosion problems during service

condition. These problems prompted research to uncover more effective materials and processes. Kaiser (1989) first explored the feasibility of carbon fiber reinforced polymer (CFRP) plates for strengthening techniques. Since then, experimental and analytical methods addressed multiple associated issues pertaining to this field.

2.3 FRP and its development

FRP sheets or reinforcements can be used for strengthening purposes; it can be attached to the tension faces of the beam, which is a method known as EBR. Another commonly used technique is NSM, where the FRP reinforcement is placed in a groove cut at the bottom of the beam. In both cases, FRP is connected to the concrete of the beam through adhesives, as shown in Figure 2.1. The behaviour of NSM can be expected to be similar to that of an EBR strengthened beam; however, allowances should be made for different bond characteristics. The selection of appropriate materials, adequate surface preparation, and proper debonding and curing procedures are keys to the success of an external strengthening application. Since this thesis will address the problem of completed applications, details pertaining to the preparation techniques will not be discussed here.

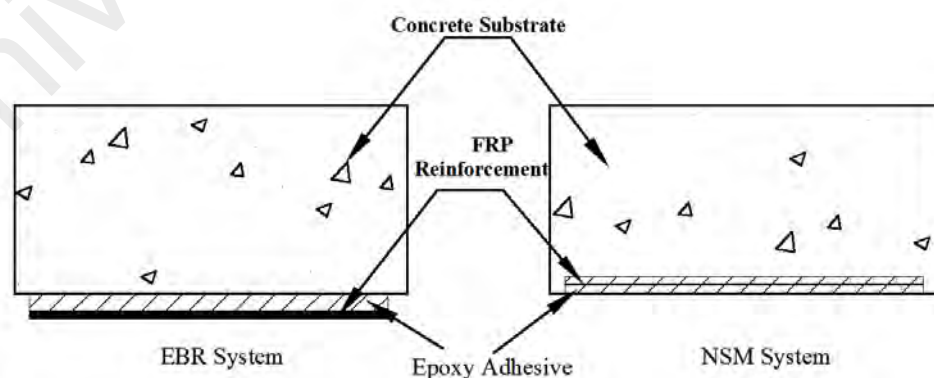


Figure 2.1: Different strengthening technique

2.3.1 Failure mode

When the plate bonding technique was first introduced, it was expected that a strengthened beam would fail either by concrete crushing or by rupture of the FRP layers. Both failure modes are expected at the section with the highest moment. However, in most of the experimental program, both for the EBR and NSM system, some strength enhancement took place, but this was usually less than the expected capacity calculated based on either the concrete crushing or FRP rupture. In most cases, the FRP system (FRP sheet combined with epoxy) debonded at a lower load (Arduini & Nanni, 1997; Gunes, 2004). Premature plate debonding was observed in earlier experimental programs with steel plated bonded beams as well (Jones, Swamy, & Charif, 1988; Ziraba et al., 1994; Zhang et al., 1995). The typical debonding mechanism that might result in premature failure of FRP strengthened beams are shown in Figure 2.2 (Gunes, 2000). The reasons behind these types of failure are briefly summarized below:

- i. Cover separation: Occurs if there are high interfacial stresses, low concrete strength with extensive cracking in the shear span. Figure 2.2a shows this failure mode. These types of failure are the principal failure mode in the case of NSM FRP strengthened beam (De Lorenzis & Teng, 2007).
- ii. FRP debonding from the laminate end: If the concrete strength and shear capacity of the beam are sufficiently high, FRP debonding occurs at the laminate end, and is transferred towards the center of the beam, as shown in Figure 2.2b. Depending on the property of adjoining materials, debonding might occur within the FRP laminate at the concrete–FRP interface or at a few millimeters within the concrete.
- iii. FRP Debonding from flexural-shear crack: If proper bond length is developed or the laminate ends are anchored, debonding might begin at the flexural-shear crack and propagate towards the end of the beam, as illustrated in Figure 2.2c.

iv. FRP Debonding from flexure crack: In the case where the shear capacity of the beam is quite high, debonding might also occur at the flexure crack, as shown in Figure 2.2d, which is rarely seen in the four-point bending test, because in that case, the propagation of debonding within constant moment region is not energetically justified.

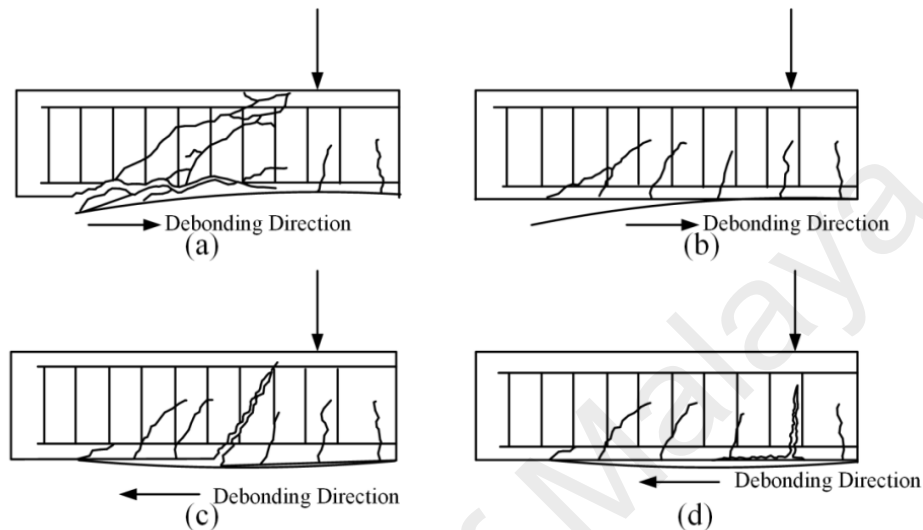


Figure 2.2: Debonding failure mechanism

However, Leung (2001) suggested that high-stress concentration around flexural cracks may initiate debonding. On the other hand, such stress concentration can also be reduced quickly with the propagation of cracks, and result in a small area of debonding.

The failures shown in Figure 2.2a and Figure 2.2c, are commonly known as combined debonding and shear failure. Quite often, distinction could not be made between these failure modes. However, it can be said that if adequate shear reinforcement is provided, the failure due to shear will occur in a ductile manner, while debonding failure will occur suddenly.

2.3.2 Experimental and analytical work on fresh FRP EBR-strengthened beam

Characterizing and modeling debonding in structural members strengthened with FRP has long been a trendy research area. During the last two decades, there has been a considerable research in the field of FRP strengthened flexural members, and significant

progress has been gained in understanding the causes and mechanism of debonding failures via experimental and theoretical studies. A brief review of the various experimental and analytical works addressing debonding include Gunes (2004) and Zhang (2011).

Plate debonding occurs due to the propagation of cracks in the vicinity of the concrete–FRP interface, hence, there is a tendency to study the failure in relation to interface flaws. It is often assumed that the interface flaw initiates when stress at the location exceeds the material strength i.e. tensile strength, implying that when the interfacial stresses exceed the interface strength, plate debonding will take place. This is the basis for strength based approach. The validity of this assumption is doubtful, nevertheless, it is obvious that the beam locations where high interfacial stresses are present are most likely locations for initial debonding. The plate end is the location where the abrupt curtailment of the plate causes a change in geometry and also variation in strength. This is one of the possible locations where high interfacial stress concentration can occur. The presence of flexural or flexural-shear cracks in the concrete beam also results in high interfacial stress concentrations. The failure originating in the plate curtailment location is commonly called plate end (PE) debonding, whereas failure initiating from the flexural and flexural-shear cracks is known as the intermediate crack (IC) induced debonding among the research community, as per Figures 2.2b and d. Debonding starts from the area of stress concentration and traverse along the path that requires the least amount of energy, and when a critical energy state is reached, brittle debonding failure takes place (Gunes, 2004). Among the analytical approaches developed until now, some of the approaches are rigorous; others are relatively simple methods that are either empirical or semi-empirical in nature.

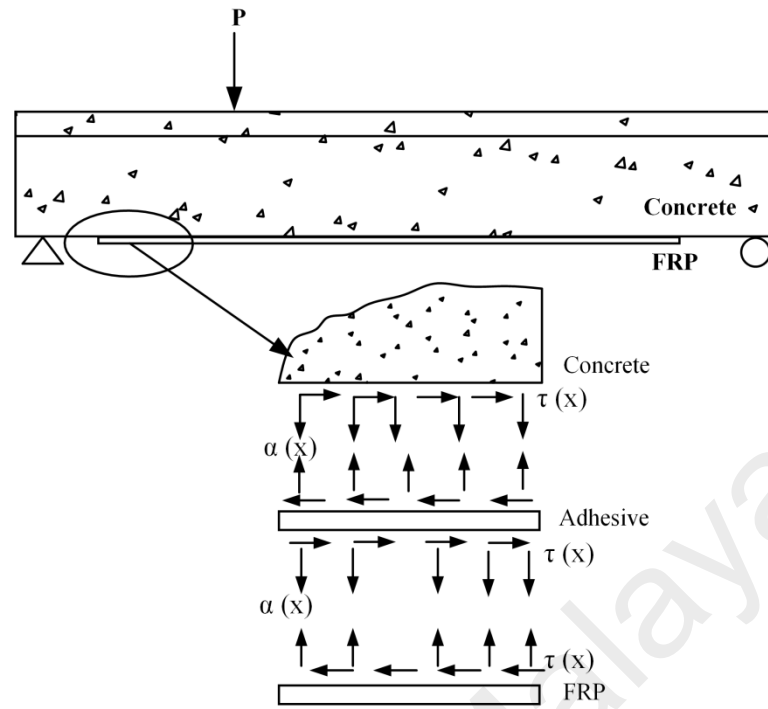


Figure 2.3: Interfacial stress distribution at the interface of a typical EBR strengthened beam. (After (Täljsten, 1997))

The debonding problem leads to the development of several analytical works to predict the debonding load. The stress at the interface is assumed to be as shown in Figure 2.3, where an interface is predicted to have an interfacial stress and a peeling stress. This motivated researchers such as Vilnay (1988), Jones et al.(1988), Robert (1989), Ziraba et al.(1994), Malek et al. (1998), Taljsten (1997), Smith and Teng (2001) to determine the two stress values and correlate it with the debonding load. Vilnay (1988), and Roberts (1989) assumed linear elasticity and simple beam theory. In addition to these assumptions, local variations such as inevitable flaws in concrete, spew-fillets in the adhesive, the compressibility of the adhesive are incompatible with the type of stress analysis used by these researchers. The solution is also dependent on the mechanical and geometric properties of the adhesive layer, which is another parameter that cannot be determined with any certainty. Most of the strength-based models developed later, particularly for FRP plated beams, are an extension of these two models of Vilnay (1988) and Roberts (1989). The solution reported by Malek et al.

(1998) requires the interface flaw location and geometry. Furthermore, the applied moment should be a second order function of the distance to a location under consideration from the beam support. Taljsten's (1997) model is also linear elastic, and according to his solution, the distance to the plate end from beams support greatly influence the plate end stress concentration. Both Taljsten's (1997) and Malek et al.(1998) solution overestimated the load than the experimental values (El-Mihilmy & Tedesco, 2000). In recent studies, researchers also focused on interfacial stress analysis (Daouadji, 2013; Daouadji et al., 2016)

Another issue using interfacial stress analysis is the failure criterion. Failure criterion used for the strength-based methods are empirical values based on a small database of test results, such as in the case of Roberts (1989) and Jones (1988). Contradictory critical stress values are also reported by various researchers. Some researchers used biaxial failure criteria, such as Malek et al. (1998), whereas others proposed maximum tensile stress failure criteria (Pešić & Pilakoutas, 2003). The drawbacks of these two failure criteria are their sensitivity to the accuracy of calculated stress, as well as the reliability of the tensile strength property of concrete. Tensile strength of concrete is dependent on many localized factors such as exact microstructure, stress condition triggering fracture, specimen boundary condition, and also the specimen size (Achintha and Burgoyne, 2013).

Most of the available models are mainly for PE debonding. Very few address the problem of IC debonding. This is due to the fact that in early experimental works, this type of failure was not observed. In strengthened RC beams, once the flaw is initiated at the concrete substrate due to flexural cracks, the tensile stress is transferred to the FRP reinforcement (Ombres, 2010). When the interfacial stresses at the interface exceed the strength of the interface, microcracks develop at the vicinity of the concrete substrate

and epoxy adhesive (Coronado & Lopez, 2006). As the load increases, these microcracks propagate and form macro cracks. Eventually, debonding will occur by propagation of these macro-cracks along the FRP length. Therefore, the development of a flexural crack in the beam soffit resulted in stress development, leading to FRP delamination. IC debonding initiating from flexural or flexural-shear cracks near high moment zone can result in two possible paths; either along the concrete and adhesive interface layer or through the concrete surface adjacent to the bond surface. Generally, if the proper bond condition is assured, the latter mode is encountered in the FRP strengthened RC beams.

Oehlers (1992) first mentioned 'flexural peeling' of steel plate bonded beams when the plates are curtailed within the constant moment zone. Since the moment at the plate end region is too low, it could justify the use of the linear elastic approach in the plate end region; however, this will not be applicable for zones of IC debonding. It is an enormously difficult task to characterize the basic features involved in IC debonding, which is another reason this field remained undeveloped. Some researchers experimented on strengthened beams to determine various features of IC debonding. Some available models of IC debonding are provided by Wang and Li (1998), Sebastian (2001), Teng et al. (2002, 2003, 2004), Malek et al. (1998), Rahimi and Hutchinson (2001), Lu et al. (2007) based on either mechanics or fracture theories or finite element (FE) analysis. Rosenboom and Rizkilla (2008) evaluated some models, and reported poor correlation of the results found from model to the experimental result for a collected database for IC debonding failure. They proposed an analytical model based on the interface shear stress using the concrete shear strength as the failure criteria. However, strength based model can predict the local failure but not the global failure of the beam. So, some researchers (Niu & Wu, 2001) use the fracture energy as the failure criteria for determining the IC debonding failure by limiting the force transferred by the

FRP in strengthened beam by comparing it to the maximum pull force endured by FRP obtained from the simple shear test.

2.3.3 Models for shear failure and debonding

Strengthening a beam for flexure is accompanied by increased shear demand. The strengthened beam must accommodate the shear as well to avoid brittle shear failure. Shear failure in strengthened RC beams was reported by many researchers (Kaiser, 1989; Ritchie et al., 1991; Triantafillou & Plevris, 1992), though initially it was regarded as a debonding problem. Determining the shear capacity of the beam is quite challenging because it is still dependent on the empirical relations provided by different codes. There are several models, but no consensus has yet been reached in the research community. Different shear failure models (Oehlers, 1992; Jansze, 1997; Ahmed, Van Gemert, & Vandewalle, 2001) developed for steel plated beams were assumed to be valid for this type of debonding failure. The interaction between the shear and debonding failure still needs to be characterized in these models. However, this type of failure was later called cover debonding (Gunes, 2000). The shear failure of strengthened RC beams becomes more distinctive due to the application of plate end anchorage methods to prevent debonding failure, as seen in many experimental programs (Baluch et al., 1995; Sharif et al., 1994). In those cases, failure occurred due to shear, outside the plated length at ~60 to 65% of the theoretical shear capacity of the beam. Another type of reported failure is shown in Figure 2.2c (Garden & Hollaway, 1998) within the shear span due to the large shear flexural cracks, consequently ending in debonding of the external FRP reinforcement and shear failure of the beam.

2.3.4 Models using bond strength

In the case of failure via FRP debonding, it is often hard to distinguish between the mechanisms shown in Figure 2.2b to Figure 2.2d due to the brittle nature of the failure.

Therefore, it not easy to tell beforehand in which direction crack propagation will occur. In the case of beams with a short shear span, previous experimental studies suggested that the debonding from the laminate end is generally the governing mechanism, although this is somewhat controversial (Gunes, 2000). On the contrary, for beams with end anchorage or long shear span, this might not very well be the case (Garden & Hollaway, 1998; Hutchinson, 1990; Rahimi & Hutchinson, 2001). This argument makes it necessary to quantitatively characterize the debonding failure originating from both possible regions, as mentioned above, in order to predict the dominant mechanism. The stress-based approach described previously cannot be applied for failure originating from the intermediate crack location. To predict such a failure, a number of researchers used the FRP-concrete bond strength based on the strength or fracture properties and corresponding bond development length. Therefore, the measurement and modeling of concrete-FRP bond strength under various loading conditions is the prerequisite of such failure model.

Different types of bond test for the concrete-FRP interface have been found in the literature. Test setup, such as single shear test by Taljsten (1996) or double shear test by Fukuzawa et al (1997) have been used extensively to determine the bond shear strength in the form of a bond(τ)-slip (s) relationship and anchorage length. Conventionally, the τ - s relationship was measured using strain gauges, while modern techniques incorporate digital image correlation for this purpose (Ali-Ahmad, Subramaniam, & Ghosn, 2006). Fukuzawa et al. (1997) determined bond strength based on mode II fracture toughness, while Kimpara et al. (1999) used the peel test to determine the mode I dominant fracture resistance. To evaluate the bond resistance of FRP-concrete for various phase angles, Karbhari and Engineer (1996) used the mixed mode fracture-peel test setup. Many studies characterized the pull-out behaviour of FRP and concrete (Capozucca, Blasi, & Corina, 2015; de Sena Cruz & Barros, 2004; Khshain, Al-Mahaidi, & Abdouka, 2015;

Mohammed, Al-Saadi, & Al-Mahaidi, 2016; Petersen, Masia, & Seracino, 2009; Seracino et al., 2007).

In most of these experimental works, failure occurs in the concrete substrate a few millimeters away from the concrete-FRP or concrete-steel interface. A few specimens failed due to FRP rupture. However, failure at the concrete-adhesive and FRP–adhesive did not generally occur if proper surface treatment was carried out prior to bonding (Buyukozturk, Gunes & Karaca,2004).

The different bond test methods mentioned above and their respective modified version leads to the development of the bond-strength model, which can predict debonding failure initiated from an intermediate crack at midspan. The use of bond-strength model requires the location of controlling crack beforehand. Different bond-strength models have been developed so far based on either concrete compressive strength or fracture energy (mode II fracture energy). Refer to Gunes (2000) for more details. However, since plate debonding is characterized as a peeling failure, the shear failure that takes place in the bond test cannot simulate the original debonding mechanism. The actual beam force in the FRP varies as debonding progress, but none of the existing bond strength test methods can reproduce this behaviour.

2.3.5 Models using Finite Element

Several FE modeling studies are available for both IC and PE debonding using strength and fracture mechanics approaches. A common problem faced in FE modeling of this type of failure is the difficulties in convergence when modeling concrete cracking behaviour. Chen et al. (2015) utilize a dynamic approach to finite element modeling of FRP strengthened RC beams to eliminate the convergence problem by Newton-Raphson method and the arc method. Although the author reported a successful application of dynamic approach for solving the convergence problem, the method is

dependent on the choice of several factors in modeling, such as appropriate time integration algorithm, loading scheme, loading time, and the damping ratio time increment size. The choice of these parameters is not trivial. Sun et al. (2015) proposed a discrete crack approach to overcome major deficiencies such as computation cost and the complexity of all existing refined FE models. Rami (2012) proposed a 3D nonlinear FE numerical model to predict the load carrying capacity and the response of RC beams strengthened with NSM FRP rods. Bruno et al. (2016) proposed a multilayer formulation applied using a multivariable 1-D finite element technique to calculate the interlaminar stresses and fracture energies. In this case, the results are compared with a continuum FE model only. Al-Saadi et al. (2016) simulate the bond-behavior between NSM-CFRP strips and concrete substrate using an FE model.

2.4 Fracture mechanics in debonding analysis

Based on the previous discussion it can be said that less reliability of the existing model for predicting debonding inspired researchers to look for a more reliable proposition, inclining towards energy concepts.

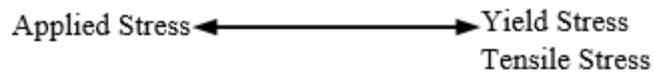
Flaws are unavoidable in materials. However, all of them are not long or weak enough to propagate throughout a structure to cause failures. Fracture mechanics is the study of the propagation of existing flaws (in this case, interface flaws), and can often be used to simulate structural failure more accurately than strength based failure analysis. The strength-based approach, as discussed in the previous section, can predict the flaw initiation from the limiting value of concrete tensile strength, but could not differentiate between the flaws that have sufficient energy to propagate and normal short flaws.

Griffith, as pointed out by Achintha (2009), explained that high-stress concentration that exists in the vicinities of inevitable micro cracks decreases the tensile strength of a

material. Using the energy balance consideration of a structural element, Griffith developed a mathematical formulation to explain the relationship between the sizes of an existing crack to the tensile strength of a linear elastic material. According to Griffith, the comparison of energy released from the system due to the presence of the flaw to the energy required to create new interface flaw surface will determine whether or not a crack will propagate. Later, Griffith's theory was modified by Irwin (1957), taking into account the consideration of the inelasticity of crack tip, which evolved into a branch known as LEFM (linear elastic fracture mechanics).

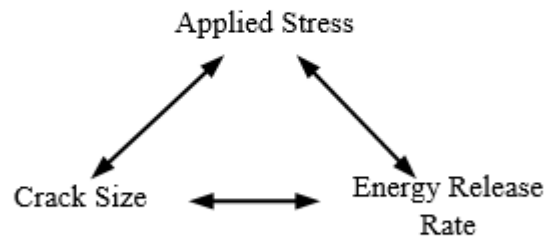
2.4.1 Fracture mechanics for concrete

Concrete structures are also full of cracks. Usually, the failure of concrete structures occurs by the stable growth of large cracking zones and the formation of large fractures prior to the attainment of maximum load. The applicability of the classical theory of fracture mechanics, as mentioned in the previous section, has been explored since the 1950 (Bazant, 1992). However, its application was of dubious validity, because it did not consider the strain softening, crack localization, and bridging stresses. Recent development in this field made it possible to use fracture mechanics in practice. It is believed that the introduction of fracture mechanics into the design of concrete structures will make it possible to achieve more uniform safety margin. Figure 2.4 shows the generalized approach for strength-based and fracture based designs.



Approach Used in Strength Based Analysis

(a)



Approach Used in Fracture Based Analysis

(b)

Figure 2.4: Design approach in strength based and fracture based approach

2.4.2 GEBA and fracture mechanics in FRP strengthened structures

Fracture mechanics can also be used to study the interface failure of composite structures. If there is sufficient energy available for an existing interface flaw to propagate and create new crack surfaces to accommodate crack extension, it will propagate by causing debonding at the interface. Hutchinson and Sue (1990) were the pioneers of the analysis of interface debonding of thin layered elastic material using fracture mechanics. This concept had been extended for debonding analysis in many fields. Since the existing strength-based approach does not provide a satisfactory result for debonding analysis in strengthened RC beams, some researchers expounded upon the idea of fracture mechanics to investigate plate debonding. Most analysis employed the LEFM concept, as per that applied for thin layered materials by Hutchinson et al. However, FRP debonding most often takes place in concrete substrate just above the interface, hence using LEFM results in a conceptual error, as the fracture of concrete cannot be modeled by LEFM. In the case of LEFM, the size of the nonlinear zone is negligible, whereas, in concrete, the nonlinear zone is as high as 300 mm (Achintha,

2009), which absorbs more energy compared to a small plastic zone. This implies the need for the application of nonlinear fracture mechanics (NLFM).

2.4.3 GEBA and fracture mechanics-based models

To accurately predict the behaviour of RC beams with externally bonded FRP, the concrete substrate and both concrete-adhesive and FRP-adhesive interfaces must be considered. Methods dealing with mixed mode fracture of layered materials (Hutchinson, 1990) can account for the fracture properties of the interfaces and substrate materials and can be used to determine the debonding propagation path that may occur along the FRP-concrete interface or within the concrete. A virtual crack propagation path is assumed to evaluate the corresponding ERR via FE modeling. This may be cumbersome for practical applications, so some researchers (Achintha & Burgoyne, 2008; Gunes, 2004; Leung & Yang, 2006) assumed that the debonding crack propagation occurs only along the FRP-concrete interface or within the concrete substrate. The capacity of strengthened beams can be predicted based on energy concepts in lieu of conventional sectional analysis. The energy dissipated during debonding can be associated with the mechanical energy dissipation in terms of concrete cracking, reinforcing steel yielding, and debonding of both the concrete-adhesive and FRP-adhesive interfaces. This section describes the basic features of fracture analysis of layered materials and shows how energy concepts have been used to predict the debonding failure loads.

Hearing (2000) and Gunes (2000) developed solutions for the debonding problem of PE debonding, based on energy balance using fracture energy. Hearing (2000) developed an analytical procedure for the debonding process, assuming that the system is linearly elastic and only considers the fracture contribution. However, experimental validation of the model proved that LEFM was only applicable for test specimens of

moderate compressive strength (34.5 MPa) and steel yield strength (400 MPa) with a small steel ratio, and for beams designed to increase the flexural capacity by only 30% (Hearing, 2000). Hearing acknowledged the need for the inclusion of bulk energy dissipation in the analysis, despite its associated complications. However, the use of LEFM is unreasonable due to the presence of numerous cracks and the fact that the corresponding materials are nonlinear at the time of debonding due to the presence of these cracks.

Buyukozturk et al. (2004) modified the model proposed by Hearing by considering the steel yielding contribution as well but omitting the 'bulk energy dissipation' contribution due to concrete cracking, which was considered to be less significant compared to the other quantities. The hypothesis in the model was that much of the concrete cracking actually takes place prior to debonding. This assumption is quite reasonable, as debonding occurs in a brittle manner, so there is less chance of the propagation of other cracks; which has also been verified experimentally (Gunes, 2004). The final failure might occur either in the materials or at the interface following the path of least resistance. Buyukozturk et al. (2004) assumed that pure mode II fractures governed the debonding process, and pointed out to the lack of research on mixed mode cracking in the FRP–adhesive–concrete interface. Buyukozturk et al. (2004) also assumed that after debonding, the load carrying capacity of the beam section would be equal to its unstrengthened capacity, which is an assumption also made by Hearing (2000).

Although the work by Buyukozturk et al. (2004) is a significant improvement to Hearing (2000), it remains limited in certain areas. The assumption of constant curvature before and after debonding cannot be true if the force acting on the FRP is accounted for because after the FRP detaches from the concrete, the curvature of the

beam will surely increase in the debonded portion. On the other hand, neither of these two models is capable of predicting IC debonding, as pointed out previously, which is another most likely mode of debonding. On the other hand, Gunes's model has the potential for use in design quite easily, because it proposes a simple way of incorporating the model for use to design a strengthened beam.

A further progress to the energy balance based debonding model was proposed by Achintha and Burgoyne (2008, 2012) for the simply supported beam. In this case, the work done on the system has been calculated using Equation (2.1).

$$W_{\text{system}} = W_{\text{bending}} + W_{\text{axial}} + W_{\text{FRP}}, \quad (2.1)$$

Where W_{bending} and W_{axial} are the work done on the RC beam due to bending and axial force and W_{FRP} is the work done on the FRP plate.

The failure criterion of this model is the mode I fracture energy, which is validated via various experimental results collected from literature by Achintha and Burgoyne (2011, 2013). This model differentiates the method of analysis for the two prime debonding failure modes, i.e. PE debonding and IC debonding. Achintha and Burgoyne show that their model can predict the failure load with a tolerance limit of $\pm 10\%$ from the actual experimental failure load by checking the model against a database of beam specimen with a large variety of materials and geometric properties, encompassing both PE and IC debonding. The accuracy of this model is quite acceptable, but a major limitation is its applicability in actual works due to its complexity. Despite a few disadvantages, this model has eliminated other major problems, such as the assumption of constant curvature, linear elasticity, and incapability of predicting IC debonding of the previous models. Therefore, this model can be a prospective way to address and solve the debonding problem.

2.5 Determination of fracture energy

In the energy based solution, the failure criterion is the fracture energy of the concrete material. Therefore, the determination of the fracture energy requires a brief introduction. In LEFM, the critical ERR is the energy required per unit crack extension in a material where there is no process zone, which means that all of the energy is surface energy, and none is dissipated from the crack tip. On the other hand, there is a process zone in concrete, therefore, the total fracture energy includes all of the energy dissipated per unit propagation distance of the fracture process zone as a whole.

2.5.1 Fracture resistance of pure and mixed mode

Different methods are available for the determination of mode I fracture energy value, such as the crack band model, equivalent LEFM model, and cohesive crack model (Hillerborg, 1985; Jenq & Shah, 1985; Petersson, 1981). The crack band model is capable of analyzing the crack distribution in the concrete fracture and consider the tri-axial stress in fracture process zone (FPZ), however, the use of a coarse crack band for accuracy will probably impede the suitability of this method in debonding analysis (Bažant, 2002). The size effect law, effective crack model, and the two parameter model reported by Jenq and Shah (1985) are some of the equivalent LEFM models that are mostly empirical in nature and are usually developed from the statistical and dimensional analysis of the test results. Therefore, it is unreasonable to extrapolate the results from one type of specimen to others without taking the effect of the differential proportion of the FPZ into account and assuming that the original notches are critical notches. It is also unreasonable to consider the maximum load as the sole factor governing fracture behaviour. The cohesive crack model recommended by RILEM (RILEM, 1985) is adopted from Hillerborg's concept (1985), where the stress (σ)-crack opening displacement (w) is a prerequisite for the determination of the fracture energy.

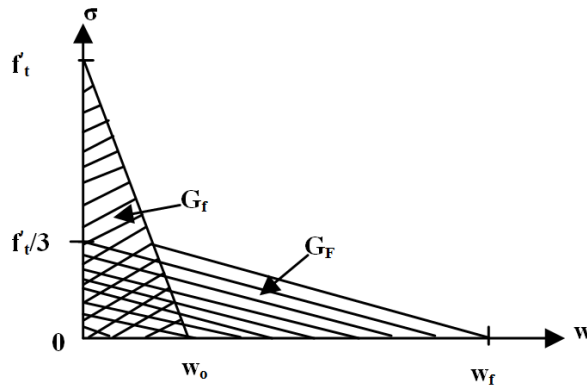


Figure 2.5: Bilinear softening stress separation law

Among the various σ - w models, the bilinear-softening model reported by Petersson et al. (1981), which is shown in Figure 2.5, can be used without too much difficulty. In Figure 2.5, G_F is the area under the entire curve, while G_f is the area under the initial steep segment extended down to the w -axis. G_f can be obtained by the size effect method, while G_F can be obtained by the work of the fracture method. Typically, as per Bazant and Becq (2002); Guinea et al. (1992) and Planas et al. (1992), G_F is ~ 2.5 times that of G_f . The above discussion also implies that during the determination of mode I fracture energy and mode II fracture energy in the case of FRP-concrete joints, precaution has to be taken on which measurement of 'G' is used. Since the determination of G_f , as shown in Figure 2.5, also accounted for the size effects, it is more rational to use this term for debonding analysis. Recent studies by Guan and Burgoyne (2013) reported fracture energy determined from the wedge split peel-off test is within the range of 0.05 to 0.33 N/mm, with a value mostly of 0.15 N/mm, which is quite agreeable with the typical mode I fracture energy value used by Achintha and Burgoyne (2008).

2.5.2 Experimental and analytical work on FRP-strengthened beam

This subsection will discuss the experimental and analytical works on different types of FRP strengthened beams available in the literature.

2.5.3 NSM strengthened beam

Externally bonded FRP faces a major hurdle, which is the debonding of the FRP from the concrete substrate prior to reaching its full capacity (Hawileh, et al. 2015; Mahal, Täljsten, & Blanksvärd, 2016). Several solutions were proposed to avoid debonding failure, however, these solutions render the design of FRP strengthening to be conservative (ACI-4402R-08, 2008; CEB-FIP, 2010). The NSM technique was proposed to compensate for this shortcoming. This technique is better able to resist debonding failures, allowing FRP reinforcement to be utilized with much greater efficiency. Although the use of the NSM technique for strengthening is rather new (Nanni et al., 1999), the first use of NSM steel was reported back in 1949 by Asplund (1949). The experimental study of NSM strengthened beam is an interesting research topic among the research community up till now (Al-Mahmoud, Castel, & François, 2012; Almassri, Kreit, Al-Mahmoud, & Francois, 2014; Capozucca & Magagnini, 2016; Dalfré & Barros, 2013; Ebead & Saeed, 2013; El-Gamal, Al-Nuami, al-Saidy, & Al-Lawati, 2016; Fernandes, Silva, & Sena-Cruz, 2015; Firmo & Correia, 2015; Gopinath, Murthy, & Patrawala, 2016; Hosen, Jumaat, Islam, Darain & Rahman, 2016; Hosen, Jumaat, Alengaram, Islam, & Hashim, 2016; Kim & Khan, 2015; Mahal et al., 2016; Rasheed, 2014; Reda, Sharaky, Ghanem, Seleem, & Sallam, 2016; Rezazadeh, Barros, & Costa, 2015; Rezazadeh, Cholostiakow, Kotynia, & Barros, 2016; Seo, Lee, & Feo, 2016; Sharaky, Torres, Comas, & Barris, 2014; Tang, Balendran, Nadeem, & Leung, 2006; Zhu, Wu, Zhang, Zhan, & Hui, 2014).

Studies (El-Hacha & Rizkalla, 2004; Hassan & Rizkalla, 2004; Teng et al., 2006) on the NSM technique proves that it can still undergo debonding failure, as shown in Figure 2.6. In the case where the NSM reinforcement is curtailed at a significant distance from the support of the beam, the dominant type of debonding failure will be the concrete cover separation failure at the NSM reinforcement cut-off location (Teng et

al., 2006). This ‘Type 1’ failure is termed as end debonding failure in this thesis. Type 1 failures occur due to the peeling force at the location of the NSM curtailment caused by the differences in strain at that location (Sebastian, 2001).

If the NSM reinforcement is provided up to the supports of the beam, debonding failure can occur in two ways. The first is the ‘Type 2’ category, where a localized failure occurs at the maximum moment region (El-Hacha & Rizkalla, 2004; Hassan & Rizkalla, 2004; Teng et al., 2006). This type of failure is caused by the stress from the radial pressure of the NSM reinforcement (Lorenzis, 2004; Hassan & Rizkalla, 2004), which is transferred onto the concrete surrounding the NSM reinforcement. The other type of failure is similar to Type 3, as shown in Figure 2.6, which occurs when there are more than one NSM grooves on the beam, as observed from the experimental results. Type 3 failure propagates from a dominant crack present at or near the mid-span towards the beam’s end (Lorenzis, 2002). Both types 2 and 3 failures can be commonly called IC debonding.

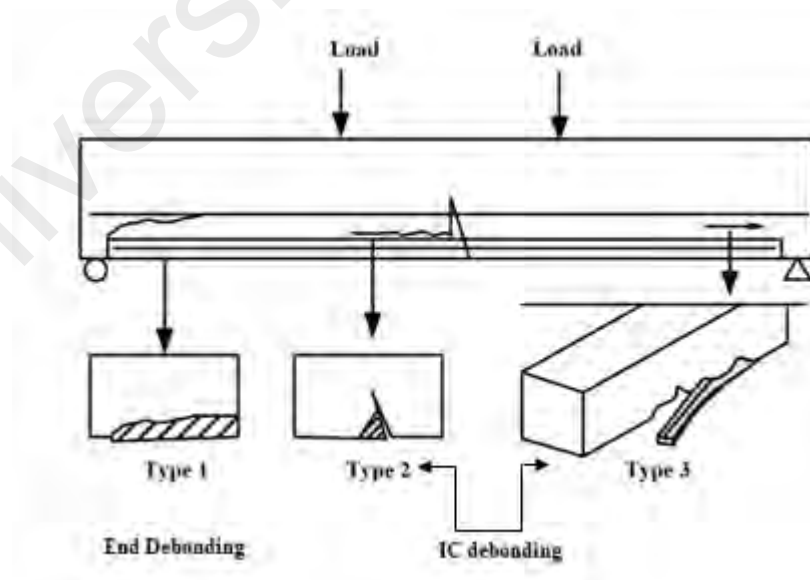


Figure 2.6: Typical failure type in NSM strengthened beam observed in experiment

2.5.4 Hybrid FRP-strengthened beam

The drawbacks of the EBR methods lead to the development of the NSM technique. However, it might be limited in practical applications, such as inadequate edge clearance and higher concrete cover (Rahman, Jumaat, Rahman, & Qeshta, 2015). In order to mitigate the disadvantages of both methods, few researchers assess the behaviour of strengthened beam by combining two techniques and this technique is known as hybrid technique. Very few experimental works report on this technique, such as those reported by Rahman et al. (2015), Jumaat et al. (2016), and Amarasinghe and Gamage (2016).

2.5.5 Precracked EBR FRP-strengthened beam

When FRPs are used to repair or strengthen the deficient RC beams, these beams may exhibit flexural or flexural shear crack as a sign of damage due to the service load. These cracks can be repaired by injecting epoxy; however, the behavior of these beams consequently becomes different from a virgin, uncracked beam, depending on the damage level. These cracks can be simulated in an experimental environment by loading an unstrengthened beam prior to its strengthening. This procedure is commonly known as precracking. The precracking load is represented as a percentage of the flexural or ultimate capacity of the unstrengthened beam. Some researchers use the flexural capacity of the designed beam obtained from code, while others use the ultimate capacity found from the test result of the unstrengthened beam. The behavior of precracked beam strengthened with FRP has been examined to a certain extent. Benjeddou et al. (2007) analyzed the effect of various damage levels for FRP strengthened precracked beams. Similar types of failures, such as PE debonding and IC debonding failures (Smith & Teng, 2002), were reported for those beams (Alfano, De Cicco, & Prota, 2011). However, most significant results observed by Benjeddou et al. (2007) reported that the ultimate load carrying capacity of the beam insignificantly

changes when the precracking level to the flexural capacity of the unstrengthened beam is less than or equal to 80%. On the other hand, if the precracking level is more than 80%, then the load carrying capacity of beam exhibits some changes. The effect of precracking was also studied by some researchers under other conditions, such as under sustained loading, for NSM strengthening (Kim, 2015; Morsy, El-Tony, & El-Naggar, 2015; Wenwei & Guo, 2006). Morsy et al. (2015) tested NSM strengthened beams under precracking using three different precracking levels of 50, 70 and 100 % of the yield capacity of the control beam. All the beams failed in flexure, with an average increase in capacity of ~25%.

The effect of pre-existing cracks should be considered in simulation to correctly predict the behavior of the FRP-repaired beam. Various methods for predicting debonding failure of FRP-strengthened beams are available, but most of them ignore the presence of pre-existing cracks. Very few models are present in literature for precracked beams, such as Zidani et al. (2015), who employed finite element (FE) analysis for predicting debonding of the precracked beam.

2.5.6 Prestressed EBR & NSM FRP-strengthened beam

Flexural tests of strengthened beams show a brittle type of premature debonding of the FRP laminate from the concrete, where the tensile capacity of FRP laminates was well below the ultimate capacity of the FRP laminate. Therefore, the FRP laminate could not be efficiently utilized for strengthening. To address this serviceability issue of FRP strengthened members, in the 1990s, some researchers' proposed a new technique of strengthening by prestressing the FRP laminate prior to attaching the beam, which could obviously utilize the tensile capacity of the FRP more than the unstressed FRP (El-Hacha, Wight, & Green, 2001; Pellegrino & Modena, 2009; Quantrill & Hollaway, 1998; Saadatmanesh & Ehsani, 1991; Shahawy & Beitelman, 1996; Triantafillou &

Deskovic, 1991; Wight, Green, & Erki, 2001; You, Choi, & Kim, 2012; Yu, Silva, & Nanni, 2008). In addition to the utilization of the utmost capacity of the FRP, prestressing the tension reinforcement of the RC beam also reduced the crack formation whilst increasing its capacity. Therefore, failure analysis of prestressed beam is one of the significant research fields in strengthening. Despite significant progress in a prestressed strengthened beam due to the usage of different prestressing technique, prestressing percentage, and so forth, there has been a very little study on predicting the debonding failure of this type of beam. Though FRP rupture is the prominent failure mode for beam strengthening using prestressed FRP, intermediate crack induced (IC) debonding type failure, initiating from the location of major flexure or flexure-shear crack near the load application point and travels towards the end of the beam is mainly observed for prematurely failed beams, whereas PE type failure initiating from the FRP curtailment location and propagating towards the center of the beam is rarely reported.

However, few analytical studies on predicting the ultimate failure of the beams strengthened with prestressed FRP, such as concrete crushing and steel yielding, are available. Barros et al. (2012) developed a design-oriented model to determine the moment-curvature response of a rectangular cross section of FRC members prestressed by longitudinal prestressed steel and FRP bars failed in flexure. Kara et al. (2016) also developed a numerical method for estimating the response of beam strengthened with NSM FRP bars and strips using sectional analysis. Hajihashemi et al. (Hajihashemi, Mostofinejad, & Azhari, 2011) estimated the response using sectional analysis. Woo, Nam, Kim, Han, & Byum (2008), Xue, Tan, & Zeng (2010) and Rezazadeh, Costa, & Barros(2014), simulate the response of prestressed strengthened beam using nonlinear FE approach. Despite these analyses, none of the researchers focus on estimating the premature failure of strengthened beam with prestressed FRP.

2.6 Approaches used for implementing numerical models to design

The application of numerical methods in design is another challenge for researchers. As pointed out previously, the implementation of numerical methods, such as those proposed by Achintha and Burgoyne (2008), cannot be directly applied for design purposes. Hence, this thesis work will develop a model to use the numerical model in a real design application. The various analysis techniques used for developing that method will be briefly introduced in this section.

2.6.1 Dimensional analysis

Dimensional analysis is a standard method in physics. Its underlying assumption is that any equation representing a universal law has to be independent of the unit system. This simple rule frequently makes it possible to develop a form of the equation. The need for dimensional analysis is well recognized in areas where available analytical tools are not capable of yielding an exact solution. For example, the process of non-dimensionalizing Bernoulli's equation can reduce the correlating parameters from five to two. Considering non-dimensional form, in this case, can significantly reduce the experimental works (Bull, 2012).

The application of dimensional analysis in civil engineering is widely reported in Hydraulics. However, the applications of dimensional analysis are also reported in construction engineering, such as in the case of cement (Phatak & Deshpande, 2005) and RC beams (Carpinteri & Corrado, 2010; Fossetti & Papia, 2012; Phatak & Dhonde, 2003), but not for the strengthened beam. Phatak and Dhonde (2003) used dimensional analysis to predict the ultimate torsional strength of the RC beam and showed that the proposed method can be effectively used in this context by comparing the results with the experimental data. Carpinteri and Corrado (2010) used the dimensional analysis approach to determine the plastic rotation capacity of over-reinforced concrete beams. It

has been demonstrated that only two nondimensional numbers can represent the ductility behaviour of the beam, and the results were also validated with experimental findings. Fossetti and Papia (2012) recommended a numerical method to predict the ultimate curvature and moment of rectangular RC sections loaded under combined axial load and biaxial bending using dimensionless terms in order to obtain results that are applicable to different sections. Seko (2014) studied the possibility of applying the ideas of dimensional analysis in optimization problem of building structures. Makris and Black (2004) reported the dynamic nonlinear response of rigid-plastic, elastic-plastic, and bi-linear system of inelastic structures. According to Matuszak (2015), the equations formulated with the use of dimensional analysis are usually clearer and easier to handle. The author reported the application of the dimensional analysis to model and transform equations to be unit independent for multiple cases.

2.6.2 Fuzzy approach

Civil engineering is riddled with many complex and nonlinear problems, such as the behaviour of tall buildings, earthquake effects, wind effects, dynamic systems, uncertainties of tall soil behaviours, and obscure material behaviours. It is therefore inadequate to model this complex system with a simple and crisp solution. Fuzzy mathematics has been extensively used in numerous investigations after Zadeh (1965) published a paper on fuzzy sets. Liang et al.(2000) employed fuzzy mathematics to evaluate the response of existing reinforced concrete bridges. Choi et al. (2015) developed an analytical method based on the fuzzy theory to accurately evaluate the shear strength of the RC beams. Park et al. (2009) reported the application of neuro-fuzzy inference system to predict the compressive strength of concrete. Pakdamar and Guler (2012) used fuzzy logic to evaluate the flexible performance of RC structures using a nonlinear static procedure. Various artificial intelligence techniques, such as an artificial neural network (ANN) and genetic algorithms (GA), have been used in various

FRP strengthened RC structures (2006). However, optimizing parameters with this technique requires extensive experimental results, which is quite challenging, labour intensive, and a time-consuming process (Bashir & Ashour, 2012; Kara, 2011). On the other hand, fuzzy logic expert system (FLES) offers an effective solution, as it utilizes expert appraisal alongside a logical system that resembles human reasoning instead of widespread experimental results (Altun, Tanrıöven, & Dirikgil, 2013; Darain., Shamshirband, Jumaat, & Obaydullah, 2015; Güler, Demir, & Pakdamar, 2012; Shafabakhsh & Tanakizadeh, 2015; Wang, Man, & Jin, 2015). Zheng et al.(2011) predicted the delamination location and the extent of composite laminated beams using a hybrid Fuzzy, neural network, and genetic algorithm technique. The simulation reported promising results in structural health monitoring. Nasrollazadeh and Basiri (Nasrollahzadeh & Basiri, 2014) used Fuzzy interface system to predict the shear strength of FRP reinforced concrete beams for the efficient use of FRP reinforcement. Darain, Jumaat et al. (2015); Darain , Shamshirband et al.(2015) employed the Fuzzy approach and adaptive neuro-fuzzy interface system (ANFIS) to predict the deflection and cracking behaviour of NSM strengthened RC beams. The simulation shows that the ANFIS approach reported better prediction of serviceability over the fuzzy approach. Sobhani and Ramezaninpour (Sobhani & Ramezaninpour, 2009) used the fuzzy system to model the corrosion of reinforced concrete structures. However, no work has been found in literature on the determination of curtailment length of flexural strengthened EBR FRP strengthened RC beams using the fuzzy approach.

2.7 Research gaps

In the last few decades, considerable researches have been done in experimental as well as in analytical fields to understand the performance of FRP-strengthened members. The debonding failure of strengthened beams had been the focus of numerous studies. Various works had also been done to investigate the FRP-concrete interface for

use in the failure model. However, different models vary in their respective capacity to predict the debonding load. Hence, a reliable model is required to predict the debonding, because debonding failure of brittle nature significantly influences the capacity of the strengthened beams.

Analytical, empirical, or numerical works in this area are primarily classified into strength and energy-based approaches. The earlier plate debonding analysis often concentrated on comparing the interface strength with existing interfacial stresses derived from the linear elastic theory. The use of this method cannot be justified due to the presence of crack and other material nonlinearities. Moreover, numerous flaws are expected in concretes, so failure analysis based on strength approaches may not represent the actual failure mechanism. Recently, several fracture mechanics based solutions have been developed. Despite the fact that fracture mechanics-based finite element solution has been applied successfully in interface failure analysis of linear elastic thin layer material, the existing analysis of FRP debonding from concrete beam requires a lot of work.

The review of the energy-based model shows that the model proposed by Achintha and Burgoyne (2009) eliminates the drawbacks of the previous energy-based model proposed by Hearing and Gunes. Thus, the model by Achintha and Burgoyne (2009) could be extended for predicting debonding of strengthened beams, strengthened using NSM technique and hybrid technique, beams precracked before strengthening, beams with prestressed FRP, and T-shaped beams by controlling the moment-curvature relationship, since it is the primary tool of this model. In all of the works, the investigation will be carried out to check if the existing interface flaw can release sufficient energy to propagate, which consequently leads to failure. The developed model can be evaluated against a database of tests results reported in literature.

However, the main drawback of the model proposed by Achintha and Burgoyne (2009) is its difficulty for actual field application. To overcome this drawback, the development of a design methodology for the proposed debonding model is required. Therefore, in this thesis, an approach is proposed by using dimensional analysis alongside the fuzzy approach to use the debonding model in the real field by showing the application of the approach for EBR strengthened beam failing in PE debonding. The objectives of this thesis are set based on the research gaps reported in the literature.

University of Malaya

CHAPTER 3: DEBONDING ANALYSIS OF DIFFERENT TYPES OF BEAMS

3.1 Introduction

Research in the field of strengthened beam is diverse, encompassing various types of strengthening techniques to changes in geometric, as well as material properties and loading schemes. Among the different techniques, the NSM strengthened beam is more popular due to their reported advantages over the EBR strengthened beam. Some researchers also focus on combining NSM with the EBR technique, resulting in a hybrid technique. Moreover, assessing the behaviour of beams strengthened after loading (commonly known as a precracked beam) to simulate the actual cracked condition of the beam in a real field is also an important research parameter. Prestressed FRP has been tested by several researchers for the purpose of increasing the capacity of the strengthened beam since non-prestressed FRP strengthened beams exhibit premature failure at levels far below its estimated capacity. This chapter describes the methodology for predicting the debonding failure load of RC beams strengthened with NSM and hybrid techniques, beams precracked before strengthening, beams strengthened using prestressed FRP using GEBA approach, together with fracture mechanics for rectangular beam section. A brief discussion is also be provided for using the model for beams with T-section.

3.2 GEBA with fracture criteria model for debonding

The high-stress concentration at the concrete-FRP interface can result in the formation of crack, but this crack will not propagate until the energy released by the system exceeds the energy required to form the crack's surface. From this perspective, it is more of a fracture mechanics problem instead of a stress-strain problem. Therefore, addressing this problem using GEBA approach, together with fracture mechanics, have been undertaken by several researchers. The relative advantages and disadvantages of these works have already been highlighted briefly in the previous chapter, and based on

that analyses, the model proposed by Achintha and Burgoyne (2008) has been selected as the basis of this work. This section briefly discusses the hypothesis and methodology of Achintha and Burgoyne's model.

3.2.1 Why GEBA over other methods of Energy Release Rate (ERR)

Fracture mechanics can simulate the mechanism of interface debonding better than any other method, and it actually investigates the possible propagation of the existing crack. In a brittle material such as concrete, numerous cracks may form at the interface; however, not all of them are long enough or weak enough to trigger debonding. Failure can only occur by the propagation of a dominant crack, and the GEBA method estimates that failure. The applicability of analytical method such as stress intensity factor method might not be able to differentiate between the critical flaw able to trigger debonding from a minor flaw. The J -integral method, which is a popular conventional fracture analysis method of computing ERR i.e. G_R at the crack tip is also of dubious validity in beam debonding analysis because of the unidentified microstructure property at the interface. Various types of elements are available in nonlinear FE packages (Achintha & Burgoyne, 2012) for modeling crack tip and FPZ. However, the necessary details required for modeling is not insignificant for a heterogeneous material such as concrete, even for a laboratory specimen. In this context, GEBA can be an easy, though reliable, alternative, with two governing parameters only, namely Energy release rate (ERR), G_R and fracture energy, G_f . These parameters can also be determined with sufficient accuracy for practical purposes.

3.2.2 Energy balance during debonding

In the GEBA model, whether a small potential extension of a given interface flaw will propagate or not can be determined by comparing the G_R associated with that interface flaw to the G_f of the material in which the failure is supposed to occur. The

phenomenon of propagation of interface flaw is associated with stiffness reduction of the beam, which means work is done by the externally applied loads. Simultaneously, the curvature of the beam increases, which means some of the work done is stored in the beam in the form of strain energy, but some energy may still be available for the propagation of interface flaw. Hence, according to the GEBA of the system, the ERR can be expressed as the rate of change in the system's total potential energy and the work done on the beam with respect to the interface flaw length as expressed by Equation (3.1).

$$G_R = \frac{1}{b_p} \left[\left| \frac{\partial W_{ext}}{\partial a} \right| - \left| \frac{\partial W_{sys}}{\partial a} \right| \right], \quad (3.1)$$

Where $\frac{\partial W_{ext}}{\partial a}$ is the rate of change of the work done on the beam by the external force; $\frac{\partial W_{sys}}{\partial a}$ is the rate of change of energy dissipated by strengthened beam section due to the work done by moment-curvature, FRP-strain; ∂a is the length of interface flaw and b_p the fracture surface, which was adopted as the width of the beam for EBR strengthened beam by Achintha & Burgoyne.

Achintha and Burgoyne explained the procedure for simply supported and statically determinate beam.

3.2.3 Work done on a beam

A significant part of the ERR is the strain energy of the beam. The strain energy can be stored due to bending or due to axial force or by both. The strain energy due to bending in a beam can be generally expressed by:

$$U_{bending} = \int \frac{M^2}{2EI} dx, \quad (3.2)$$

Where M is the bending moment, E is the elastic modulus and I is the effective moment of inertia.

The curvature of the beam section can be expressed as

$$\kappa = \frac{M}{EI}, \quad (3.3)$$

So, Equation (3.2) can be expressed as

$$U_{bending} = \int \frac{M\kappa}{2} dx, \quad (3.4)$$

On the other hand, the strain energy due to axial force, F, can be expressed as

$$U_{axial} = \int \frac{F^2}{2EA} dx, \quad (3.5)$$

Where A is the area of the section.

The axial strain due to axial force

$$\varepsilon = \frac{\text{stress}}{\text{young's modulus}} = \frac{\text{force}}{\text{young's modulus} \cdot \text{Area}} = \frac{F}{EA}, \quad (3.6)$$

So, Equation (3.5) can be expressed as

$$U_{axial} = \int \frac{F\varepsilon}{2} dx, \quad (3.7)$$

It is obvious that the knowledge of M- κ , as well as F- ε , is necessary for the evaluation of energy. Since the variation of all these components occurs along the beam's length, dividing the beam length into small segments for numerical analyses renders it convenient.

3.2.4 Moment–curvature for FRP strengthened section

The M- κ analysis of beams began with the assumption of its material properties. The brief review of M- κ model used in this work is adopted from Achintha & Burgoyne (2008) and detailed in the subsequent subsection.

3.2.4.1 Branson's effective moment of inertia model

The moment-curvature of a typical RC beam section can be obtained directly for uncracked and fully cracked section analyses. The effect of tension stiffening makes the analysis of partially cracked section, complicated. The popular Branson's model, as expressed by Equations (3.8) and (3.9), can indirectly incorporate the effects of tension stiffening by defining an effective stiffness. The primary purpose of Branson's model was to predict the deflection of a beam at an acceptable level of accuracy.

$$I_{eff} = KI_{un} + (1 - K)I_{fc}, \quad (3.8)$$

Where I_{eff} , I_{un} and I_{fc} are the moment of inertia for the partially cracked, uncracked and fully cracked section respectively. And K can be expressed as follows:

$$K = \left(\frac{\text{Moment causing 1st flexural cracking}}{\text{Current applied moment due to load}} \right)^4 = \left(\frac{M_{cr}}{M_{app}} \right)^4, \quad (3.9)$$

Hence the curvature of the section

$$\kappa = \frac{M_{app}}{E_c I_{eff}}, \quad (3.10)$$

This model was validated using the experimental results of the deflection of RC beams and with the appropriate modification for the prestressed beam. However, this model was conceived only for conventional RC beams with steel reinforcement, up to steel yield level. Therefore, accounting for the added FRP with different bond characteristics as the second layer of reinforcement is not appropriate. On the other hand, the model has to work beyond steel yield, so Achintha and Burgoyne dealt with these issues when applying Branson's model in the FRP strengthened beam.

3.2.4.2 Modeling of RC beams with external FRPs

A strengthened beam can have three types of sections: uncracked, fully cracked, and partially cracked. In the uncracked type, the applied moment on the beam is less than the cracking moment, M_{cr} , of the section. Thus, the beam does not have any crack in it

at this stage. In the fully cracked type, the applied moment on the section is greater than the yield moment capacity, M_y , of the beam. In other words, the tension steel in the beam yielded. In the partially cracked type, the section is neither uncracked (i.e., the concrete already starts to crack) nor fully cracked (i.e., steel is not yielded). The uncracked and fully cracked sections are solved for the strain at the top and bottom fiber of the beam in this analysis by applying force equilibrium and moment equilibrium conditions using MATLAB code for every 1 mm section along the beam. This strain can then be used to determine the depth of neutral axis, x_{eff} , for the corresponding section.

The contribution of axial force in the FRP has to be included in the analysis. Since this M- κ model separates the FRP force from the analysis, the determination of the FRP force can be obtained via strain compatibility with the extreme tension fiber using trial error process (a sample calculation process is included in Appendix A). For the partially cracked section, the Branson's model needs to be modified. Achintha and Burgoyne suggested that the analysis can be conceptually simplified by incorporating the FRP force as external prestressing force acting on the RC beam alone. However, the analysis is made more complicated due to the fact that the RC section needs to be analyzed for a combined action of compressive force and moment acting about the centroid of the beam. At any given section, the moment applied at any given section will be resisted by the RC section alone and the added FRP reinforcement. The moment acting on the RC section alone (either about the mid-depth axis or centroid axis, M_{eff}) can be separated from the moment resisted by the FRP force, only if the centroid of the beam is known beforehand.

If the FRP is partly debonded, as it is assumed to be in the unbonded zone, then it can be assumed that the extension of the FRP over the unbonded region will be compatible with that of the extreme tension fiber of RC beam over the same region.

3.2.4.3 Depth of centroidal axis

The centroidal axis depth is required to decouple the axial FRP force from the beam (Achintha, 2008). However, the depth in non-homogeneous sections, such as RC, centroid, and neutral axis, continuously changes. To avoid this complexity, the mid-depth axis is chosen as the reference to decouple FRP force instead of the centroidal axis in determining the moment-curvature. And this selection is reported to provide reasonably good results.

Hence the moment that will be acting purely on the RC section, M_{eff} , will be as in Equation (3.11).

$$M_{A-y} = M_{total} - T_{frp}(h_f - y), \quad (3.11)$$

Here, A-y can be used to identify the moment and the axis about which the moment is considered. In that case, A refers to the specific moment that could be applied to moment (*app*), yield (*y*), or cracking (*cr*); M_{total} is the corresponding total moment i.e. M_{app} , M_y or M_{cr} , and y, refers to the axis about which the moment is required. In the case of mid-depth axis, it is the mid-height of the beam, i.e. (h/2), M_{app_mid} refers to the applied moment about the mid-depth axis.

However, the centroid is still required to calculate the ERR. A concept of the equivalent centroid was developed, which will allow for the separation of the M_{eff} and F_p to determine the energy state accurately for debonding analysis. In the case of uncracked and fully cracked section, equivalent centroids (α_{un} and α_{fc}) are computed using equivalent transformed section and secant modulus of the corresponding material.

Since the corresponding materials are nonlinear, the secant modulus varies with stress, and the location of centroid changes with different loads. The equivalent centroid α_{eff} of the partially cracked section can then be obtained by interpolating between α_{un} and α_{fc} using Branson's concept as in Equations (3.12).

$$\alpha_{eff} = K_{\alpha}\alpha_{un} + (1 - K_{\alpha})\alpha_{fc}, \quad (3.12)$$

$$K_{\alpha} = (M_{cr-mid}/M_{app-mid})^{3.5} \left[1 - \left\{ \frac{M_{app-mid} - M_{cr-mid}}{M_{y-mid} - M_{app-mid}} \right\}^{3.5} \right], \quad (3.13)$$

3.2.4.4 Effective elastic stiffness

The interpolation coefficient used by Branson (1968) detailed in Equation (3.9) is such that the section stiffness becomes asymptotic to the fully cracked state, but never reaches that stage, which is valid for conventional RC beams. In case of strengthened RC beams fully cracked state is achieved. Achintha and Burgoyne (2008) assumed that the section will be fully cracked at the moment causing first yielding of steel, and thus adjusted the interpolation coefficient so that the discontinuity in stiffness is avoided at the steel's yielding point. The interpolation coefficient also needs to be computed using the moment acting on the RC section alone by separating the moment using the mid-depth axis. The modified interpolation coefficient becomes:

$$K_p = (M_{cr-mid}/M_{app-mid})^4 \left[1 - \frac{M_{app-mid} - M_{cr-mid}}{M_{y-mid} - M_{app-mid}} \right], \quad (3.14)$$

Once the interpolation coefficient is determined, the stiffness and curvature of the partially cracked section can be computed. However, since the nonlinear behaviour of materials is taken into account in the analyses, the cracked elastic analysis employed in the Branson model is invalid, and since the concrete modulus changes continuously, it makes it irrelevant to define the denominator of Equation (3.10). Rather, an equivalent

elastic stiffness ' B_{eff} ' can be determined by interpolating between the corresponding uncracked and cracked stiffness (B_{uc} and B_{fc}) obtained from the direct sectional analysis.

$$B_{eff} = K_p B_{uc} + (1 - K_p) B_{fc}, \quad (3.15)$$

Once B_{eff} is determined for partially cracked section, the curvature of the section will be

$$\kappa = \frac{M_{eff}}{B_{eff}}, \quad (3.16)$$

Where M_{eff} can be determined using (3.11) by putting α_{eff} as 'y' and M_{total} as the M_{app} .

A Branson-type interpolation coefficient is also used to determine the neutral axis depth, x_{eff} , at partially cracked sections. Given that the partially cracked section in this study remains within the serviceable limit, using the aforementioned equation is justifiable.

$$x_{eff} = K_\alpha x_{un} + (1 - K_\alpha) x_{fc} \quad \text{for } M_{cr} < M_{app} < M_y, \quad (3.17)$$

where x_{un} and x_{fc} are the neutral axis depths at uncracked and fully cracked sections, respectively.

The entire algorithm of computing M- κ is shown in Figure 3.1.

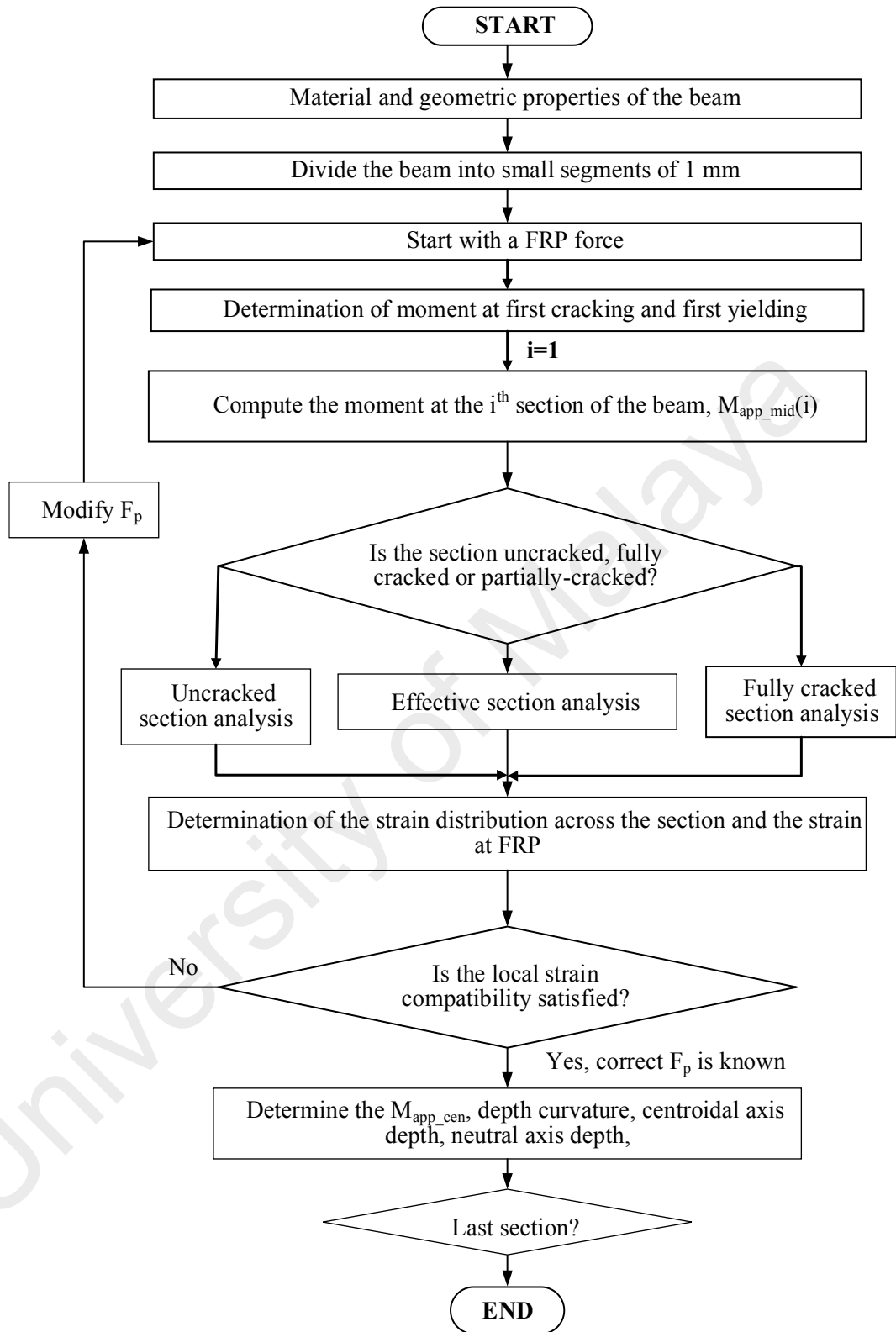


Figure 3.1: Flowchart showing the M-κ analysis (After Achintha and Burgoyne,2008)

3.2.5 Energy release rate zone

After establishing the $M-\kappa$ analysis, the next step is the determination of ERR (G_R). G_R can be defined as the change in system's total potential energy per unit area of a new interface flaw. The extension of this flaw softens some portion of the beam. Along the entire beam length the curvature and stored energy remain unchanged due to debonding. Significant curvature change is expected to occur only near the interface flaw. Achintha and Burgoyne(2008) determined the G_R for PE debonding by considering the curvature and energy changes taking place in the fixed transition zone near the plate end location. On the other hand, in the case of IC debonding, they assumed that energy changes to take place in the debonded zone and two transition zones beside the unbonded zone, as per Figure 3.2.

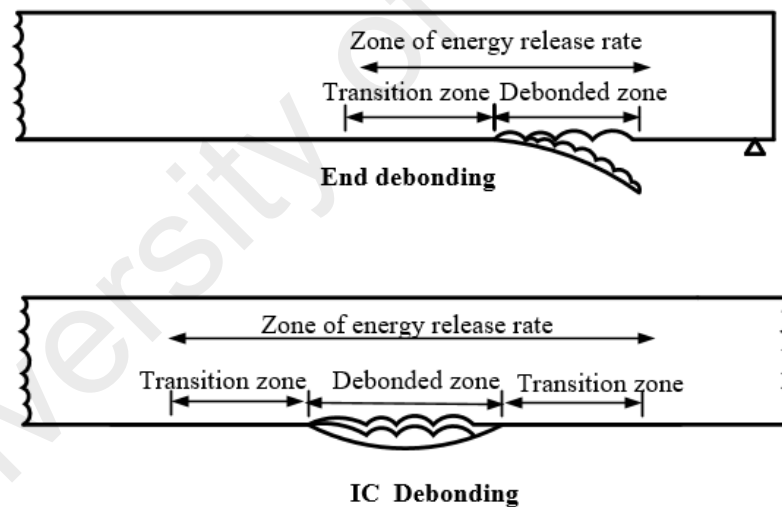


Figure 3.2: Transition zone concept used by Achintha and Burgoyne (2008)

In both cases, a transition zone length that is 30 times the thickness of the FRP was proposed in that study using a simplified analysis based on Taljsten's rigorous interfacial stress analysis. Fully perfect bond was assumed between the concrete and FRP outside this aforementioned zone, and if the load remains constant, the moment and curvature will also be constant in those portions of the beam. Therefore, there will be no change in the energy state in that zone. Once the zone of energy change is

determined, the next step is to determine the two quantities expressed in Equation (3.1). The debonding analysis in the present model starts with the assumption that an interface flaw, either at the FRP end location for PE debonding or at the location near load point for IC debonding is termed ‘state 1’, as shown in Figure 3.3a, after which the flaw is assumed to extend by a small distance of δa , termed as ‘state 2’. The change in the energy state of the beam at both stages can be determined using the $M-\kappa$ relation, which allows to determine the associated G_R .

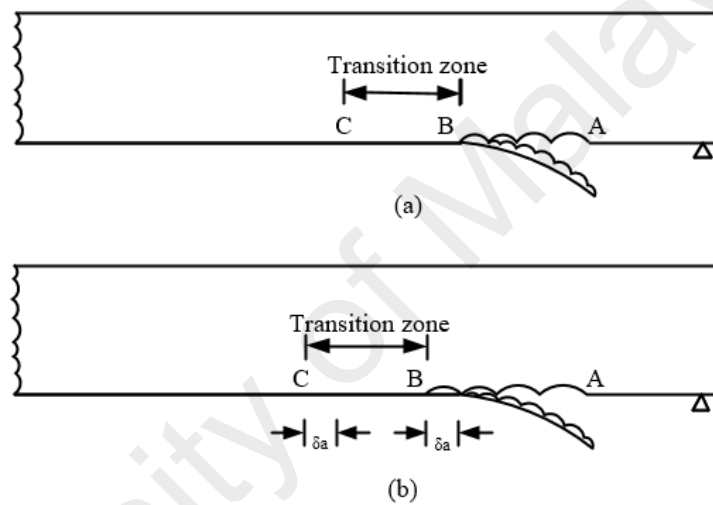


Figure 3.3: Debonding flaw a) before and b) after a small flaw extension of ‘ δa ’

The various component of ERR, as mentioned in Equation (3.1), are described in the following subsections.

3.2.5.1 Rate of change of potential energy of the externally applied load

The graphical presentation of the change in potential energy is shown in Figure 3.4.

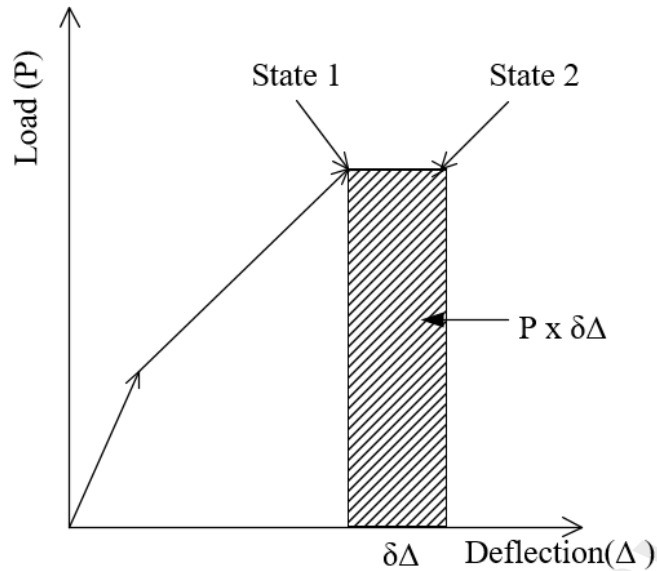


Figure 3.4: Load versus deflection plot before and after the extension of interface flaw (After Achintha and Burgoyne 2008)

The rate of change of work done by an external force can be computed using the relation in Equation (3.18).

$$\frac{\partial W_{ext}}{\partial a} = \frac{P \delta \Delta}{\delta a} \quad (3.18)$$

Where P is the applied load, δa is the assumed extension of the original debonding crack length ' a ' and $\delta \Delta$ is the increase in deflection at the loading point.

The increase in deflection can be determined from the M- κ analysis also.

3.2.5.2 Rate of change of work done on the beam

In the case of an FRP strengthened beam section, Achintha and Burgoyne considered two axial force; one at the centroid of the section, and the other at the axial force due to the FRP alone and one bending moment acting on the RC section alone at the centroid and contributing to strain energy. Based on this, the rate of change of stored elastic energy in the strengthened beam section can be expressed by Equations (3.19) to (3.24) (Achintha & Burgoyne, 2008) . Figure 3.5 illustrates the changes in all three components in a beam section with the extension of the debonding flaw.

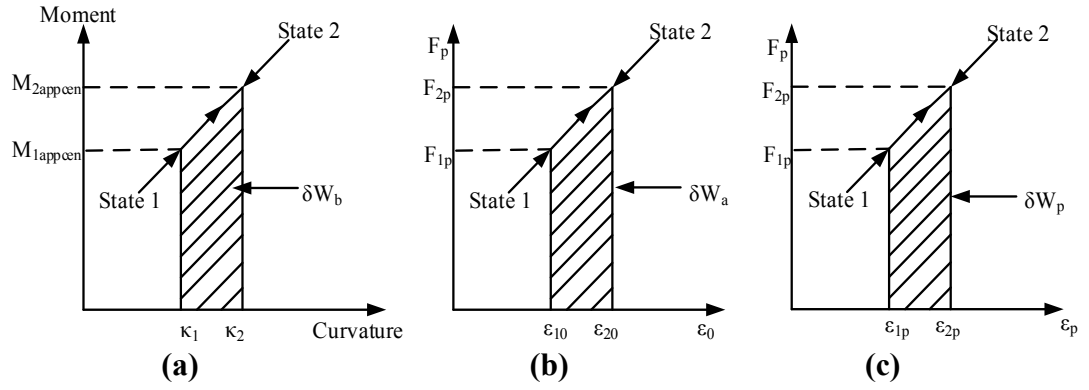


Figure 3.5: Changes in different component of work done on beam (After Achintha and Burgoyne, 2008)

$$\partial W_{sys} = \sum_{critical\ zone} \delta W_{section} \quad , \quad (3.19)$$

$$\delta W_{section} = \delta W_b + \delta W_a + \delta W_p, \quad (3.20)$$

$$\delta W_b = \frac{1}{2} (M_{1appcen} + M_{2appcen}) (\kappa_2 - \kappa_1), \quad (3.21)$$

$$\delta W_a = \frac{1}{2} (F_{1p} + F_{2p}) (\varepsilon_{20} - \varepsilon_{10}), \quad (3.22)$$

$$\delta W_p = \frac{1}{2} (F_{1p} + F_{2p}) (\varepsilon_{2p} - \varepsilon_{1p}), \quad (3.23)$$

$$\frac{\partial W_{sys}}{\partial a} = \frac{\delta W_{section}}{\delta a} \quad , \quad (3.24)$$

δW_b and δW_a are the work done on RC beam alone due to bending and axial strain; δW_p is the Work done on the FRP plate; $M_{1appcen}/M_{2appcen}$ are the moments acting on RC section about centroid axis; κ_2/κ_1 are the curvature of the RC section; $\varepsilon_{20}/\varepsilon_{10}$ are the strain at the equivalent centroid; F_{1p}/F_{2p} are the axial force in the FRP; $\varepsilon_{2p}/\varepsilon_{1p}$ are the Strain at the FRP level. The subscript 1 refers to state '1' i.e. state before infinitesimal debonding crack and subscript 2 refers to state '2' i.e. state after the infinitesimal debonding crack. Equation (3.11) can be used to determine the moment about centroid axis by changing the y in the equation to the depth of centroid.

3.3 Analysis of NSM strengthened beam

In this thesis, GEBA with fracture criteria is used to predict the occurrence of debonding failure in the NSM strengthened beam. The focus of the fracture based solution is to predict Types 1 and 3 failures, as shown in Figure 2.6, where the propagation of the interface flaw is clearly evident. Shukri and Jumaat (2016) employed this GEBA method, incorporating it with the moment-rotation approach for simulating PE debonding of NSM strengthened beam.

This work employs the $M-\kappa$ model adopted by Achintha & Burgoyne (2009) for the NSM strengthened beam and hence employs the debonding analysis. Necessary adjustments are made to the method used for the EBR technique to ensure that it works when applied to the NSM technique for all forms of failure using the approach proposed by Achintha and Burgoyne (2008). The simulation presented in this work is relatively easy to apply, as it requires only the material and geometric properties of the beams and is not dependent on the bond-slip models like in the case of Shukri and Jumaat (2016), though the procedure is numerical in nature and quite complex.

3.3.1 Moment-curvature analysis

The brief description of the moment-curvature model is already mentioned. Details are provided in this section.

3.3.1.1 Material properties for moment-curvature

Parabolic stress-strain relationship proposed by Hognestad (1951) as in Equation (3.25) is used for concrete under compression loading. Under tension, a linear elastic behaviour is assumed with the same modulus as the initial modulus in compression as shown in Figures 3.6a and b.

$$\sigma_c = f \left\{ 2 \left(\frac{\varepsilon_c}{e_c} \right) - \left(\frac{\varepsilon_c}{e_c} \right)^2 \right\}, \text{ when } \varepsilon_c \leq e_c \text{ for loading} \quad (3.25)$$

Where ε_c is the strain at any stage and σ_c is the corresponding stress, e_c is the strain at maximum stress f .

The tensile strength in rupture f_t and modulus of elasticity E_c are determined using relationship provide in Equations (3.26) and (3.27) (ACI-4402R-08, 2008)

$$f_t = 0.62\sqrt{f'_c} \left(\frac{N}{mm^2} \right) \text{ units}, \quad (3.26)$$

$$E_c = 4733\sqrt{f'_c} \left(\frac{N}{mm^2} \right) \text{ units}, \quad (3.27)$$

Where f'_c is the compressive strength of concrete.

Steel and FRP properties adopted in the simulation are shown in Figures 3.6c and d. In the case of beams strengthened with steel instead of FRP, provisions is made for yielding of strengthening steel, as per Figure 3.6c, in the location of strengthening the material.

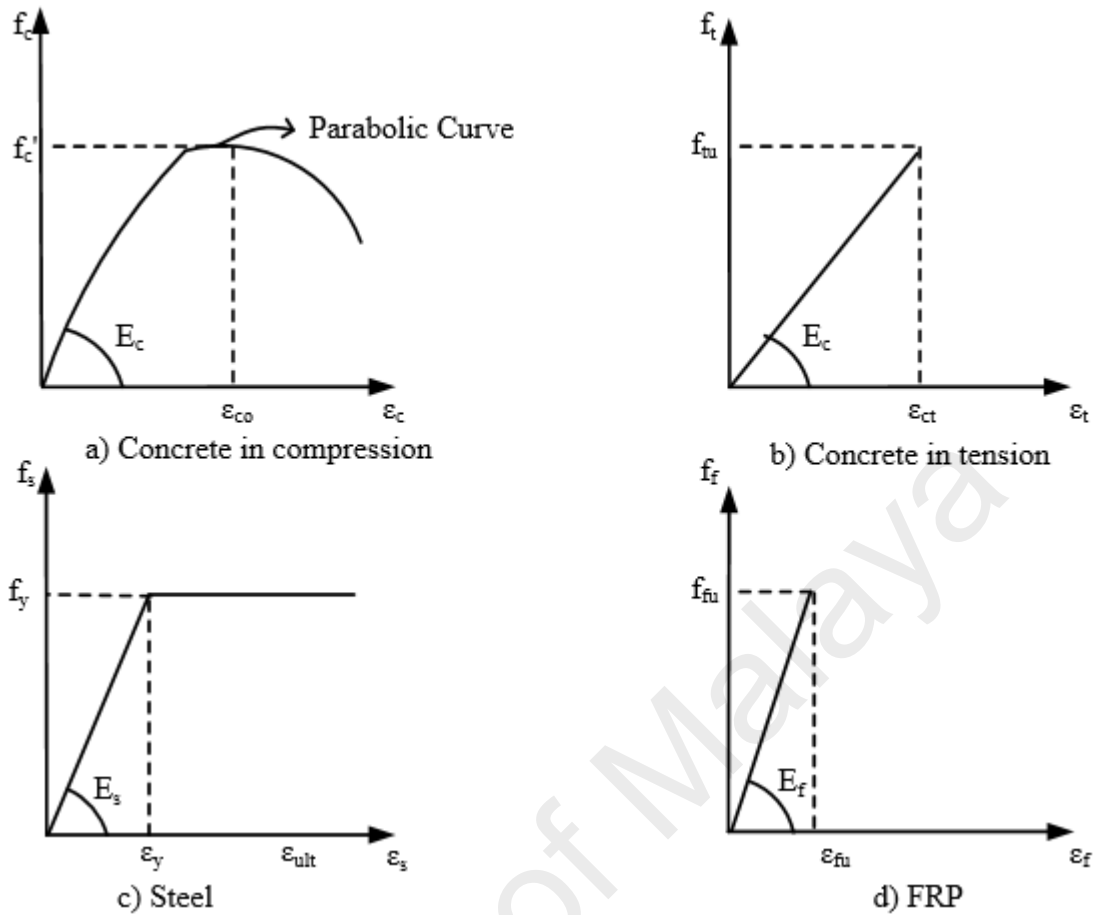


Figure 3.6: Material properties

The steel is modelled with the general elastic-perfectly plastic material, and FRP as elastic material till rupture point, respectively.

3.3.1.2 Determination of stress-strain

Once the material properties are fixed, the moment-curvature of strengthened beam can be determined using MATLAB by solving the force equilibrium and moment equilibrium conditions, taking into consideration the FRP force in MATLAB using the relations given in Equations (3.28) and (3.29). For analysis purposes, the whole beam is divided into small segments of 1 mm along the longitudinal direction.

$$\sum F = C_c + T'_s - C_t - T_s - T_{frp} = 0, \quad (3.28)$$

$$\sum M = C_c(x - \gamma x) + T'_s(x - dc) + C_t(2(h - x)/3) + T_s(d - x) + T_{frp}(h_f - x) = M_{ext}, \quad (3.29)$$

All of the symbols are defined in Figure 3.7, where C_c is the compressive force due to concrete, x is the depth of neutral axis, γx is the depth of concrete compressive force from the top of the beam, T_s' is the compressive force due to top steel, d_c is the depth of compression steel from top fiber, C_t is the tensile force due to concrete below neutral axis, h is the height of the beam, T_s is the tension force due to tension steel, d is the depth of tension steel from top fiber, T_{frp} is the force in FRP, h_f is the depth of FRP from the top fiber, E_c is the elastic modulus of concrete and f_s, f_s' , and f_{frp} are the stress in the tension, compression, and FRP reinforcement, respectively, where stress is the product of elastic modulus of the reinforcement and the strain at any stage. M_{ext} is the moment applied at any section for any load. C_t is considered zero for the fully cracked section because the contribution of concrete at the fully cracked stage will be zero. Decoupling the FRP force for partially cracked section analysis proposed by Achintha and Burgoyne (2009) is also used in the analysis to calculate the stiffness, centroidal axis depth, and corresponding curvature of the partially cracked section using the classical Branson formula (Branson, 1968). Achintha and Burgoyne (2009) introduced the concept of decoupling of the FRP force because the Branson formula is only validated for the RC section up to yield capacity. Therefore, assuming FRP is a second layer of reinforcement, the application of Branson's formula is invalid. The details pertaining to this has already been discussed earlier. On the other hand, the stiffness of the partially cracked section can be determined using classical Branson's formula, as per Equations (3.15) and (3.16).

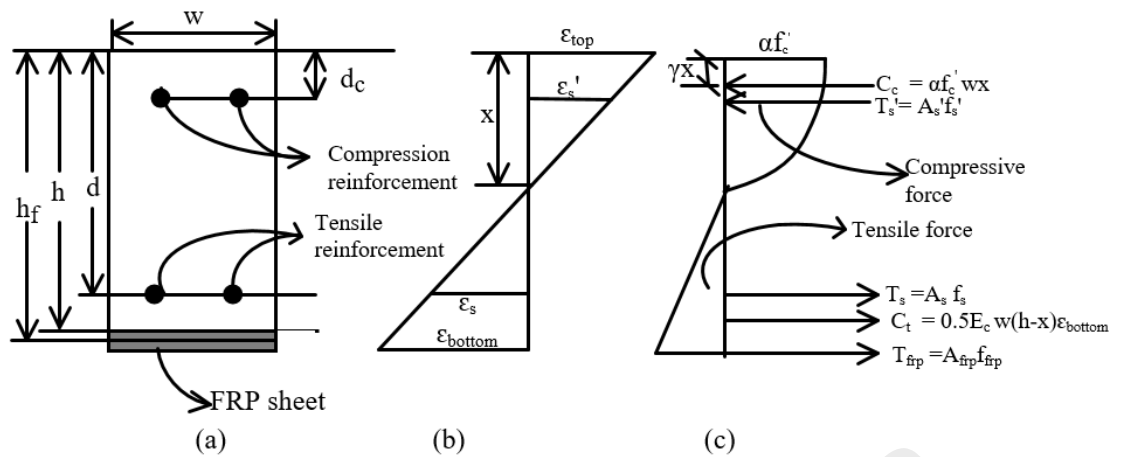
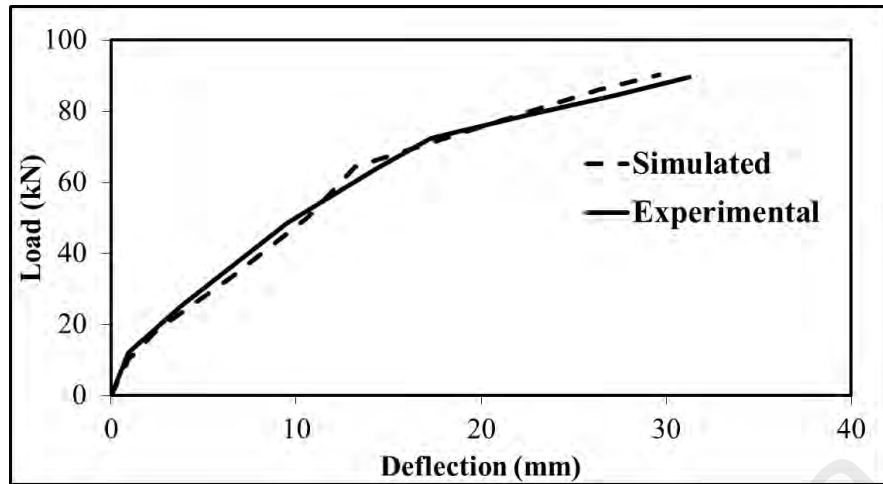


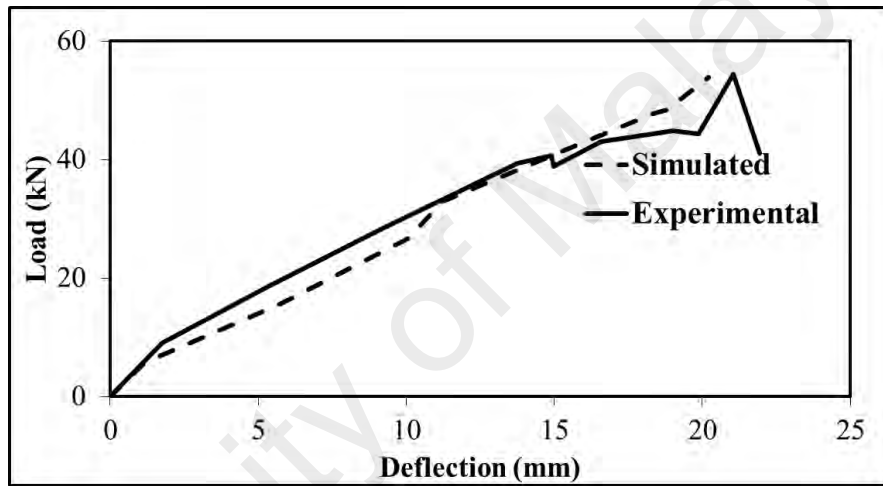
Figure 3.7: Stress–strain relationship of RC beam section due to flexure

Once the strain values are obtained, the deflection value at the midspan can be determined using the classical moment area theorem (Hibbeler, 2012).

The validity of the Achintha and Burgoyne’s moment-curvature model proposed for the EBR strengthened beams has been checked for NSM strengthened beams by comparing load versus deflection and load versus FRP strain curves. Figure 3.8 shows the plots of simulated versus experimental load and deflection, and plotting of the load versus FRP strain for a few beams, the geometric and material details of which are tabulated in chapter 4. Experimental and simulation results show excellent agreement.

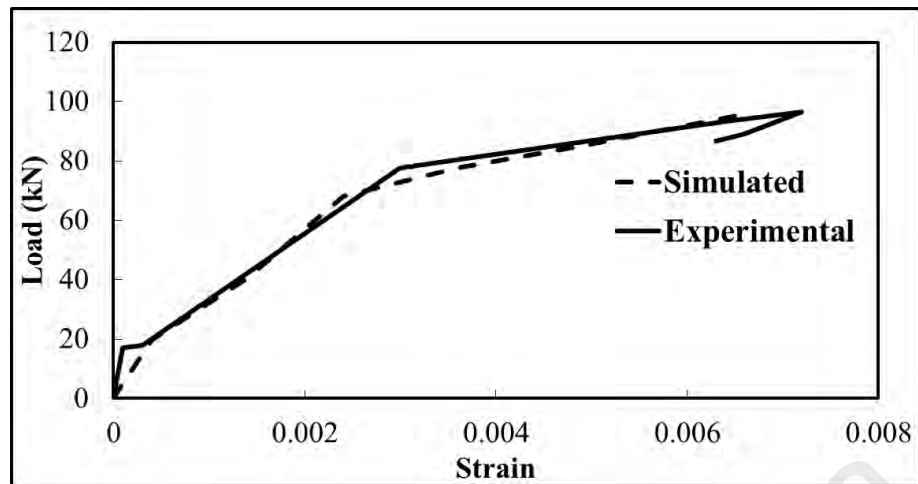


(a) Beam B1800 by Teng et al. (2006)

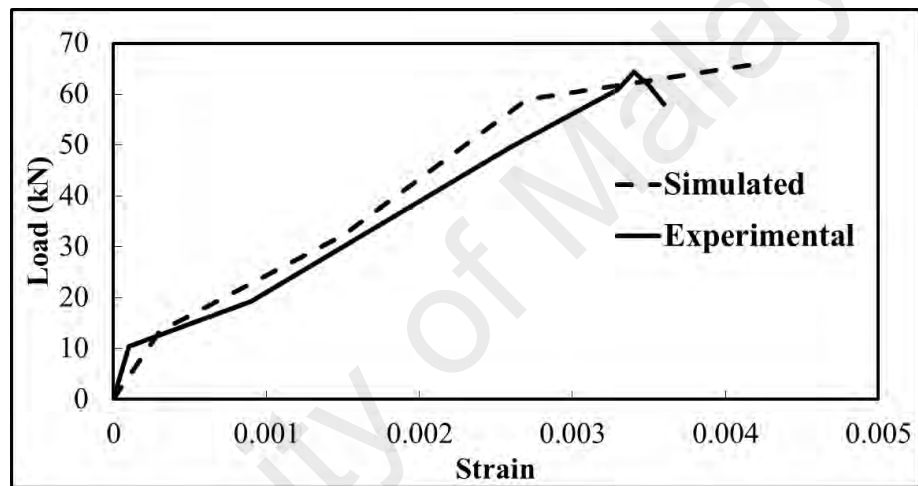


(b) Beam A9 by Ceroni et al. (2009);

Figure 3.8: Load versus deflection and FRP strain versus load plot



(c) Beam BR-2a by Barros & Fortes (2005)



(d) Beam B1200 by Teng et al. (2006)

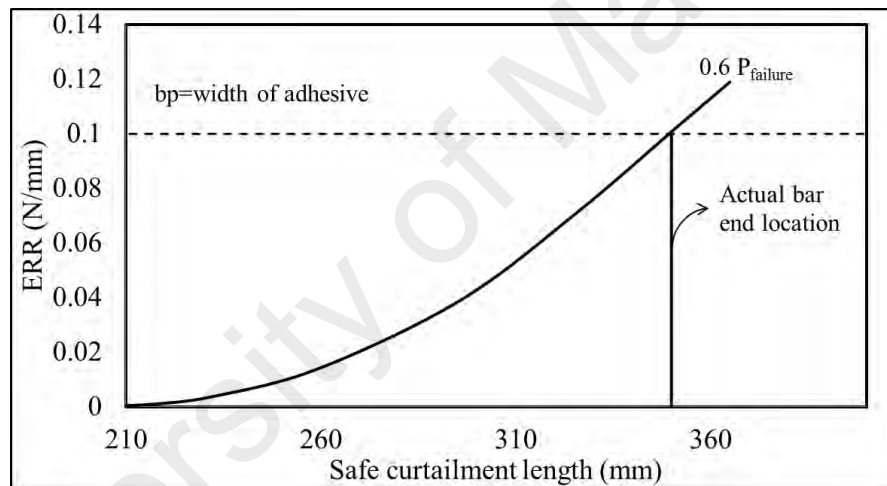
Figure 3.8, Continued

3.3.2 Debonding analysis for NSM strengthened beam

Once the moment-curvature relationship has been established, the strain energy can be computed.

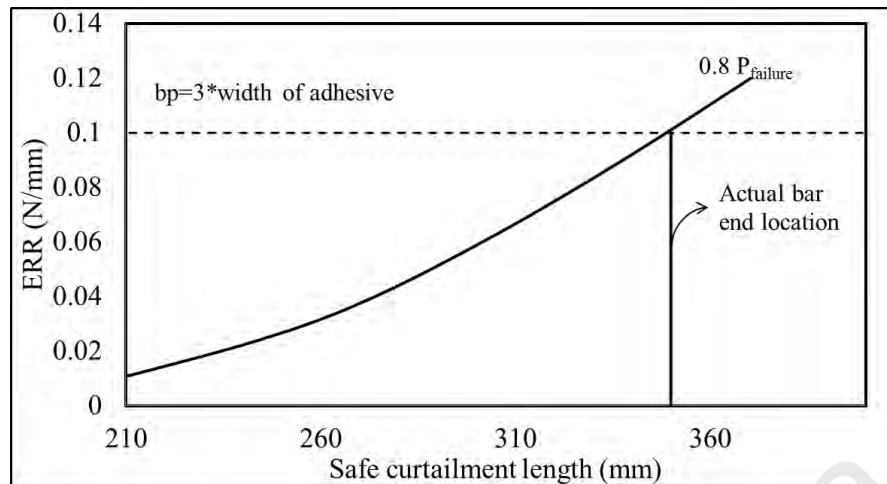
The governing equations have already been described in the preceding sections. ' b_p ' in Equation (3.1) is the fracture surface, which in the NSM analysis is taken as the width of the beam. The assumption of ' b_p ' as the width of the beam is quite reasonable, as the debonding failure of the NSM strengthened beams shows the failure in the whole beam surface along the beam's width. Though the interface flaw is within the epoxy and

the concrete interface along the groove dimension, to avoid complications, it is assumed that energy release takes place along the entire width. The analysis is carried out with different values for ' b_p ', and it is found that the assumption of ' b_p ' value equals to the beam's width reports the most reasonable result. An example of analysis with different length for b_p is shown in Figure 3.9. ERR, by assuming the fracture surface as the width of the groove and thrice the width of the grooves (other details provided later) are as shown in Figures 3.9a and b for the beam by Al-Mahmoud et al. (2010). It confirms that failure will occur at loads lower than the reported failure load (at 60% and 80% of the actual failure load).



(a) Fracture surface is equal to width of adhesive

Figure 3.9: ERR versus safe curtailment length for beam SC210 by Al-Mahmoud et al. (2010)



(b) Fracture surface is equal to three times width of adhesive

Figure 3.9, Continued

3.3.2.2 Zone of energy release for end failure in NSM strengthened beam

This subsection describes the significant modification applied to the ERR methods for NSM strengthened beam. The determination of ERR for the end debonding failure requires a zone in the vicinity of NSM end location, where the FRP force is different due to the detachment of the NSM system from the beam than the zone where FRP is still fully attached to the beam. This zone is called ‘transition zone’ in the remainder of the thesis, and in the case of the NSM end debonding, the energy change is assumed to occur in this zone for any size of interface flaw propagation. For EBR, it was determined to be 30 times the thickness of the strip using the interfacial stress analysis reported by Achintha and Burgoyne (2008). The bond condition in NSM reinforcement is different from that of the EBR. In the case of NSM technique, the reinforcement is completely surrounded by the epoxy, and three faces of the epoxy remain in contact with the concrete, while in the case of EBR, only one face of epoxy is attached to the concrete. This section discusses the determination of the transition zone stress condition for the NSM strengthened beam. The initial guess of the transition zone length can be determined from the interfacial stress distribution (Täljsten, 1997). Instead of the detailed transition zone analysis taking the effect of material nonlinearities and tension

stiffening of a cracked concrete, a simple linear elastic solution, such as that reported Taljsten (1997), Malek et al. (1998), have been used in the current analysis. According to these solutions, the slip at the NSM end is assumed to diminish exponentially.

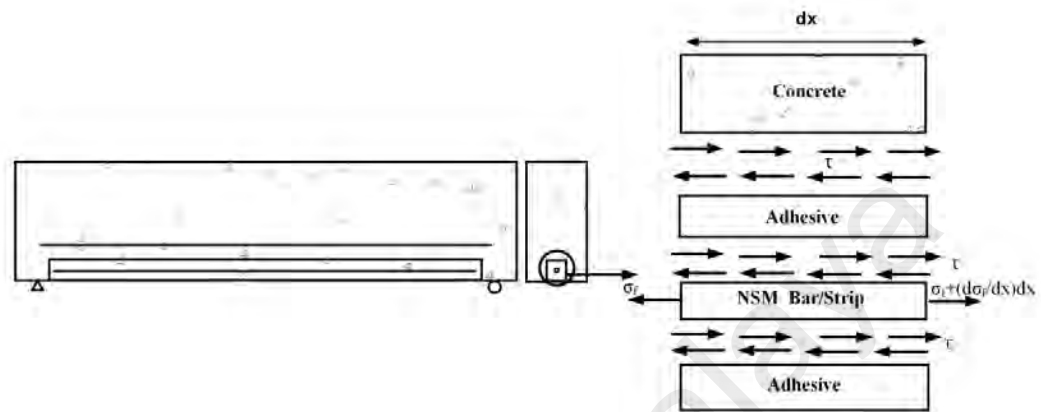


Figure 3.10: Interfacial stress distribution

The following analysis develops an expression for the transition zone FRP force by applying the key features of Taljsten's solution in such a way that it is applicable to the current NSM problem. Taljsten's solution is modified to account for the double bonded area of the near surface mounted strips or rods, as done by Rizkalla for strip reinforcement (Hassan & Rizkalla, 2004). It has been found that the length of transition zone, as shown in Figure 3.2, depends on the initial position of the NSM for end debonding. As the initial position of FRP moves to the center of the beam, the transition zone length increases. From analyzing various beams, no specific value, such as that recommended in the case of the EBR technique by Achintha and Burgoyne (2008), could be recommended for this transition zone lengths; rather, it is suggested that stress analysis be conducted, and estimations be based on these analyses.

The equations required to compute the interfacial shear stress, as shown in Figure 3.10, are as follows:

$$\tau = \frac{d\sigma_f}{dx*(2b_p+t_p)*2} * A_p, \quad \text{for strip} \quad (3.30)$$

$$\tau = \frac{d\sigma_f}{dx*2*\pi*d_p} * A_p, \quad \text{for bar} \quad (3.31)$$

$$\tau = G_a\gamma, \quad (3.32)$$

Where τ is the shear stress, A_p is the area of FRP, b_p , t_p are the width, thickness of rectangular strip respectively; d_p is the diameter of round FRP bar, G_a is the shear modulus and γ is the shear strain

If linear strain-displacement relationship for the adhesive is taken into account, then:

$$\gamma = \frac{du}{dz} + \frac{dw}{dx}, \quad (3.33)$$

Combining Equations (3.30) and (3.31) with (3.32) and hence differentiating with respect to x gives:

$$\frac{d^2\sigma_f}{dx^2} = \frac{2G_a(2b_p+t_p)}{A_p} \left(\frac{d^2u}{dx dz} + \frac{d^2w}{dx^2} \right), \quad \text{for strip} \quad (3.34)$$

$$\frac{d^2\sigma_f}{dx^2} = \frac{8G_a}{d_p} \left(\frac{d^2u}{dx dz} + \frac{d^2w}{dx^2} \right), \quad \text{for bar} \quad (3.35)$$

$$\frac{d^2u}{dx dz} = \frac{d}{dz} \left(\frac{du}{dx} \right) = \frac{1}{t_a} (\varepsilon_p - \varepsilon_{con}) = \frac{1}{t_a} \left(\frac{\sigma_{frp}}{E_p} - \frac{\sigma_{con}}{E_{con}} \right), \quad (3.36)$$

$$\frac{d^2w}{dx^2} = 0, \quad (3.37)$$

Combining Equations (3.34) and (3.35) with Equations (3.36) and (3.37) gives:

$$\frac{d^2\sigma_f}{dx^2} - \omega^2 \sigma_{frp} = -\omega^2 n \sigma_{con}, \quad (3.38)$$

Where

$$\omega^2 = \frac{2 * G_a * (2b_p + t_p)}{A_p * t_a * E_p}, \quad \text{for strip} \quad (3.39)$$

$$\omega^2 = \frac{8 * G_a}{d_p * t_a * E_p}, \quad \text{for bar} \quad (3.40)$$

By modifying Taljsten and Malek's analysis (Malek et al., 1998; Täljsten, 1997), the shear stress distribution for the NSM reinforcement for a simply supported beam under 4 point bending can be defined as:

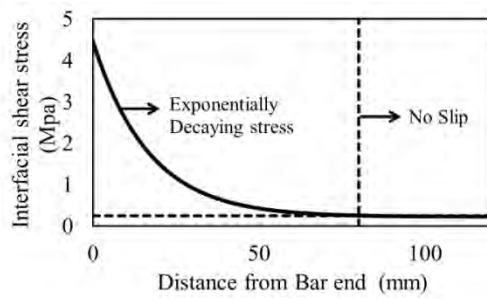
$$\tau(x) = \frac{t_p n P x_{eff}}{32 I_{eff}} [1 + l_o \omega e^{-\omega x}] \quad (3.41)$$

Where n is the modular ratio of FRP to concrete and l_o is the distance from the support to the NSM end. This analysis implies that the difference between the FRP force at the NSM end if the NSM system is fully bonded and the one that actually exists while debonding decays in an exponential manner, at a length scale of $1/\omega$. Assuming these characteristic features to be applicable in the present NSM problem, it can be used to determine the transition zone FRP profile for NSM end debonding.

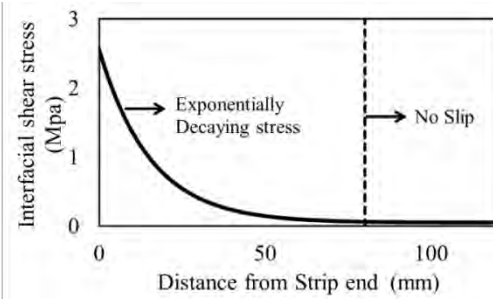
The force in the NSM FRP in the transition zone can then be determined by considering the boundary condition where the force would be zero at the zero location i.e. the location where the FRP is curtailed and would be equal to the fully bonded value at the end of the transition zone.

$$F_p(x) = F_{p-fb}(x) - F_{p-fb}(x=0)e^{-\omega x}, \text{ for bar end failure} \quad (3.42)$$

Figure 3.11 shows the interfacial stress distribution for two beams having short and long NSM end distances from the support (Al-Mahmoud, Castel, François, & Tourneur, 2010; Teng et al., 2006).



(a) Al-Mahmoud et al. (2010)



(b) Teng et al. (2006)

Figure 3.11: Interfacial stress distribution in beams at the NSM cut-off location

3.3.2.3 Intermediate crack induced debonding (IC)

According to Rosenbloom (2008), when flexural cracks occur, the perfect bond assumptions are no longer valid at the crack location. At the toes of the crack, the stress concentration from another set of cracking along the FRP to concrete interface usually occurs within the weak concrete layer. In the case of shear span to depth ratio of 2.5 or greater, the beam exhibit flexural behaviour. In the case of flexural shear cracks away from the maximum moment region, a wide crack opening is possible, which could lead to high peeling stress. The interface shear stress at the toes of the flexural cracks due to stress concentration is related to the fracture energy of the weakest material at the interface. The test results indicate that displacements at the toe of flexural cracks create stress concentrations at the interface of the FRP laminate and the beam, leading to the development of localized interface flaws that typically propagate under the effect of the load to join the original flexural cracks and cause delamination of the FRP system (Rosenboom & Rizkalla, 2008). This concept of interface flaw has been utilized to analyze the IC debonding using GEBA.

Garden & Hollaway (1997) reported two types of IC debonding failures: partial and full. In both cases, flexural or flexural shear cracks around the midspan of the beam cause sliding deformation between the two crack face at that location (Figure 3.12).

This causes the FRP to detach from the beam and hence create an interface flaw. This flaw is termed as critical flaw in this study. The said phenomenon also redistributes the forces caused by energy change, and thus causes crack propagation along the beam to the nearest beam end for most cases. Failure occurs when the ERR reaches the critical value. Thus, the possible debonding location is the maximum moment zone or shear span in the close vicinity of the loading point. The exact location of the critical flaw is one of the prerequisites for analysis. Since debonding analysis using GEBA requires the moment gradient, in the case of the four-point bending, debonding analysis at the constant moment zone is not energetically justifiable. Therefore, the entire constant moment region is assumed to be debonded, and it needs to be checked whether or not debonding will continue in the shear span. The same methodology can be employed for a uniform loaded beam with the location of major flexural or flexural shear cracks as the critical location, and the debonding flowing toward the support. However, this methodology is not validated in this study.

The analysis began by assuming a 1 mm interface flaw at the critical location. Once the FRP is debonded, the FRP force in the whole debonded zone, as shown in Figure 3.2 (for IC debonding), cannot be calculated directly from section analysis due to the lack of bonds. Instead, it is assumed that strain in that zone becomes the average strain of the concrete at the same level of FRP (Achintha & Burgoyne, 2008; Collins & Mitchell, 1987; Shin, 2000). The total deformation of concrete in the unbonded region can be expressed by Equations (3.43) to (3.45)

$$\Delta d = \int_{unbonded} \varepsilon_{c_frp} dx, \quad (3.43)$$

Average strain in concrete will be then

$$\frac{\Delta d}{L_{unbonded}} = \int_{unbonded} \frac{\varepsilon_{c_frp}}{L_{unbonded}} dx, \quad (3.44)$$

As a result, the average stress of FRP due to external load will be

$$f_p = E_f \cdot \frac{\Delta d}{L_{unbonded}}, \quad (3.45)$$

ε_{c_frp} is the strain at concrete at the level of FRP due to bending only; Δd is the total extension in debonded zone and $L_{unbonded}$ is the length of debonded zone.

It is assumed in the analysis that the ERR occurs in that debonded zone due to the changed FRP force. It should be mentioned here that Achintha and Burgoyne (2008) assumed a zone, namely the transition zone which is 30 times the thickness of FRP plate on both sides of the debonded zone. The transition zone, according to their analysis, is the zone where the energy changes occur. The present analysis discards that transition zone for IC debonding analysis, and concentrates on the energy change only in the debonded zone because it is found that the energy change in the transition zone is small with respect to the energy change in the debonded zone. Analysis with this assumption also provides good approximation of debonding load.

After determining the force in the FRP, the strain, curvature, and moment on the section can be determined using sectional analysis, and the rate of change in the stored elastic energy can be determined using Equations(3.19) to (3.24), change in potential energy is determined using Equation (3.18) and the total ERR is determined using Equation (3.1) .

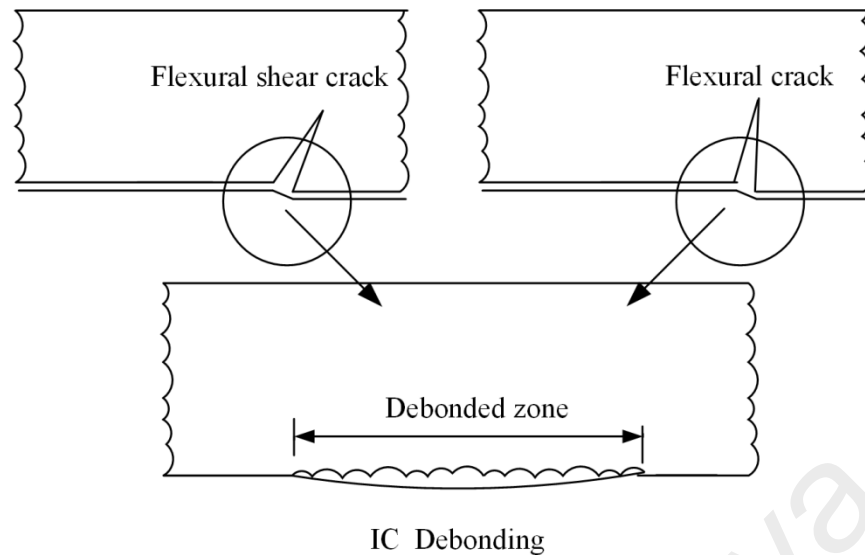


Figure 3.12: Debonded zone for IC debonding modified from Achintha and Burgoyne (2008)

3.3.2.4 Determination of energy release rate

After the zone releasing energy is determined, the next step is determining the ERR itself. The steps for achieving this are:

The analysis starts with a load, P , which is greater than or equal to the steel yield load, P_{yield} of the beam.

Then, the moment-curvature relationship of the beam needs to be determined for the original beam without any debonding, for load P , following the steps outlined in Figure 3.1.

The debonding analysis begins with the assumption of a minute interface flaw of size (1 mm in this case) from the beam end for PE debonding analysis and from the critical location i.e. at the load point in case of IC debonding.

The transition zone's length and FRP profile can be determined using Equations (3.39) to (3.42) for that load combination, together with material and geometric

properties for PE debonding. In the case of IC debonding, the force in the debonded zone can be determined using Equations (3.43) to (3.45).

This change in the FRP force will change the moment-curvature profile of the beam on that particular section. The altered moment versus curvature response and strain versus force profile can be obtained using the methods outlined earlier. The ERR can be determined using Equations (3.19) to (3.24), (3.18), and (3.1).

If the ERR value reaches the value of the critical fracture energy of concrete G_f (details are provided section 3.4), the simulation terminates, otherwise, the flaw size is increased, and the aforementioned procedure is continued till ERR reaches G_f .

The total debonded zone length (caused due to the propagation of the interface flaw), which gives an ERR equal to G_f , is the safe curtailment location (for PE debonding) or critical debonded zone length (for IC debonding) of that beam for that specific load.

A step-by-step debonding analysis procedure is detailed in a flowchart in Figure 3.13.

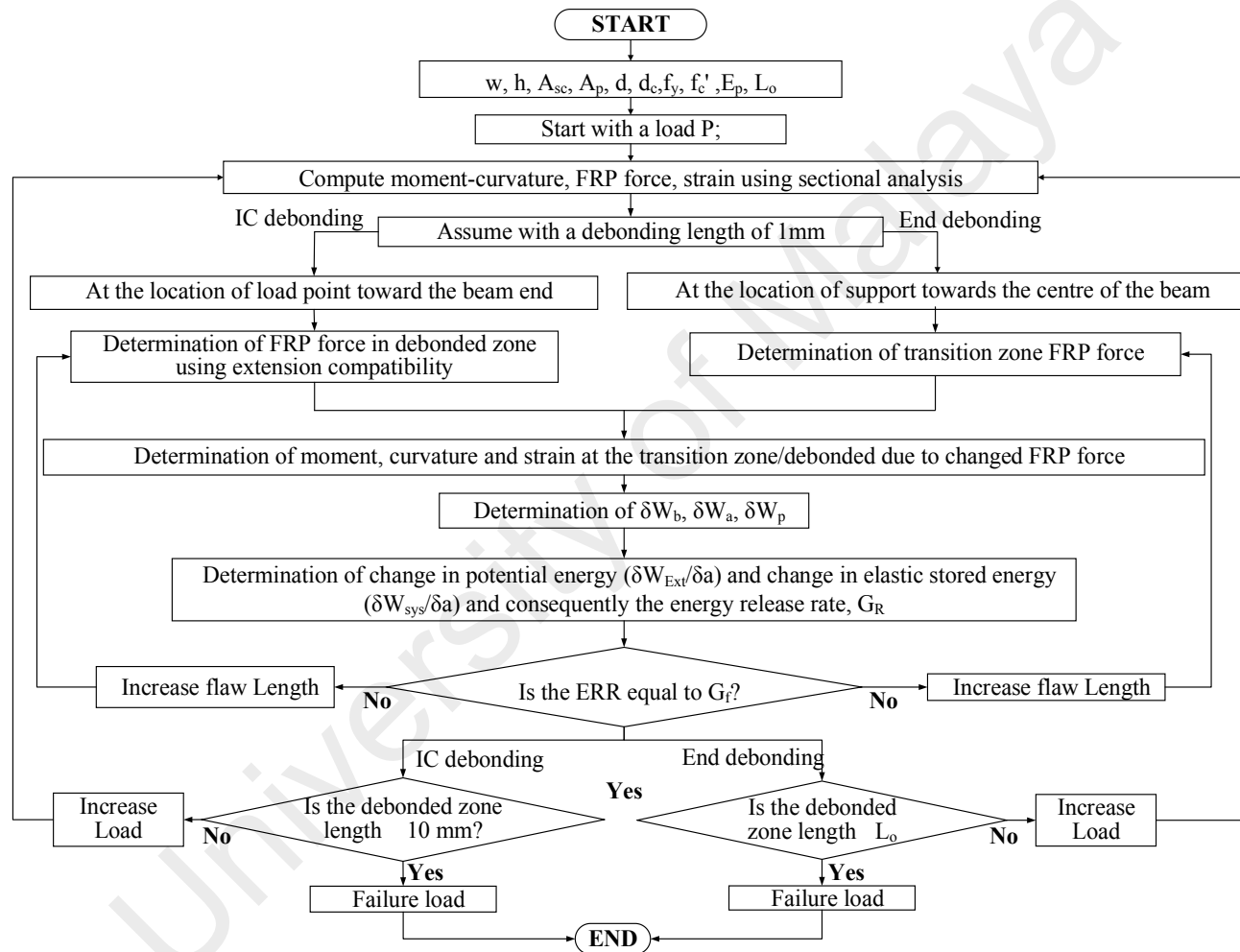


Figure 3.13: Flowchart showing debonding analysis

3.4 Failure criteria

After the ERR, the next step is selecting the failure criteria. Since the fracture based approach is selected to study debonding, by default, it requires an in-depth study of concrete fracture (Guan & Burgoyne, 2013.).

3.4.1 Fracture Energy

Debonding fracture has been categorized as modes I, II and mixed by many researchers. There is currently no consensus amongst reported works on failure mode. Crack propagation in a material can either be opening (mode I) or shearing between two crack faces (mode II), or mixed between modes I and II. The fracture energy depends on these fracture modes, as the stress-displacement field developed near the crack tip area is different for different modes. In an interface with a fracture toughness that is distinct from the adjoining material, the crack propagation usually occurs through the combined action of tensile and shear (i.e., a combination of mode I and mode II deformation). This phenomenon occurs mainly due to the asymmetry in the elastic modulus of the adjoining materials with respect to the interface modulus. Hence it is a great concern what will be limiting value of fracture energy for evaluating the debonding load. It is commonly known that in the case of mode II failure, a crack needs to overcome high shear resistance due to the presence of aggregates in the concrete. Therefore, it is widely assumed that the crack under mixed mode loading propagating by the opening of a crack tip though the propagation direction is dependent of mode mixing. The choice of mode I fracture energy have been discussed elaborately by Achintha and Burgoyne (2013) for an EBR strengthened beam. The observation shows that the 'Type 1' failure for the NSM strengthened beam is similar to the plate end debonding failure in EBR shown in Figure 3.14a. Therefore, the choice of mode I fracture energy for this type failure was already rationalized by Achintha & Burgoyne (2008).

On the other hand, several codes, such as ACI 440.2R-08 (2008) and TR 55 2012 (2012), adopted some guidelines for IC debonding that are solely based on the simple shear test specimen. Although several similarities were observed between IC debonding and failure behavior in a simple shear test, subtle differences were also evident. Rosenboom and Rizkilla (2008) studied a database of beams and slabs that failed due to IC debonding, and their results confirmed that several analytical models provided by the national code documents are inadequate for predicting IC debonding and are primarily based on bond-shear test corresponding to mode II failure. It is further assumed that a crack usually starts to open up when the maximum principal tensile stress (MPTS) reaches the value of concrete tensile strength (f_t'), and the sudden propagation will be in the direction perpendicular to MPTS. As per these assumptions, the mode I fracture energy also seems justifiable for IC debonding of 'Type 3' in the NSM strengthened beam. According to Achintha and Burgoyne, although the debonded zone (i.e., the total length of interface flaw) carries shear, it fails in tension due to the peeling force being more dominant than shear during failure. The approximate crack propagation for this type of failure is shown in Figure 3.14b. The current analysis uses mode I fracture energy as the limiting criteria for IC debonding on average, although the local details in the interface is not purely in mode I (it is in mixed mode).

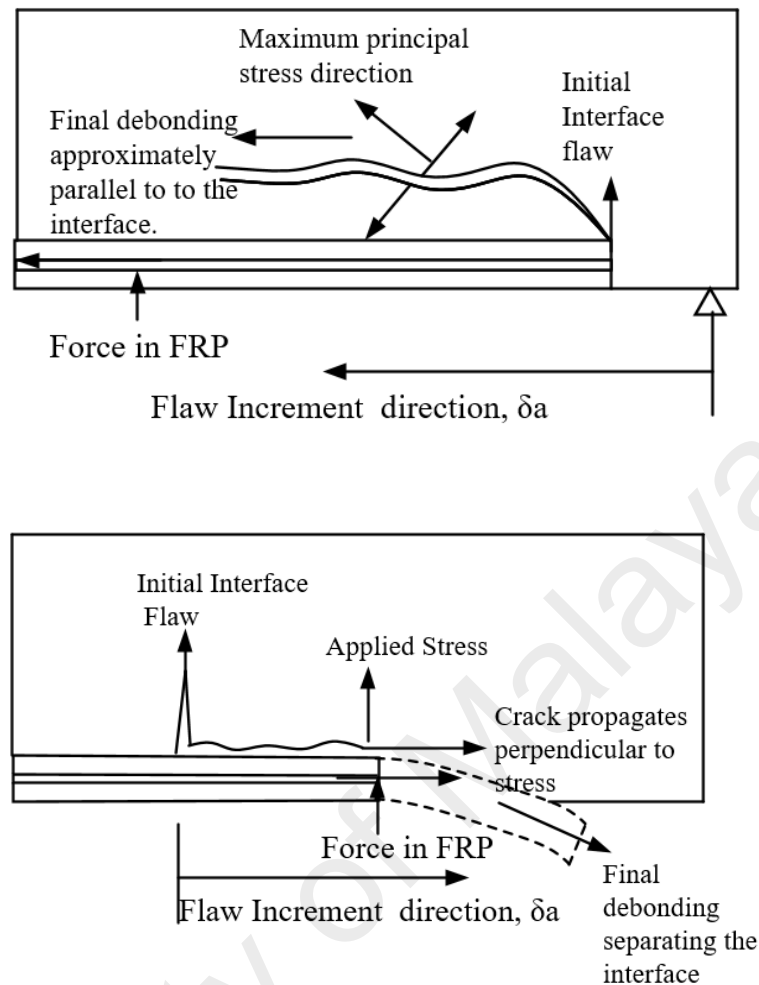


Figure 3.14: Crack propagation in interface

The flaw increment ' δa ', directions are also shown in Figure 3.14 for two types of debonding. When the ERR value for any increment reaches the value of critical energy release rate, the flaw increment is terminated.

Standard fracture test can provide the actual mode I fracture energy of concrete; however, a reliable approximation can only be obtained using simplified tension softening models, such as by Hillerborg's model (1983), or empirical models, such as the two-parameter models by Jenq and Shah (1985). Amongst the models, the empirical relation provided by Bazant and Becq-Giraudon (2002), as shown in Equation (3.46), can be used to estimate the G_f value in this study, owing to its ease of implementation and excellent correlation with tension softening models.

$$G_f = 0.0025\alpha_o \left(\frac{f'_c}{0.051} \right) \left(1 + \frac{d_a}{11.27} \right)^{0.22} \left(\frac{W}{C} \right)^{0.30} \left(\frac{N}{mm} \right), \quad (3.46)$$

where α_o is a coefficient for aggregate type; f'_c is the concrete compressive strength; d_a is the aggregate size, and W/C is the water cement ratio.

3.4.2 Total Length of debonded zone

For any beam, ERR for any load with respect to an assumed debonding crack extension will be compared with the mode I fracture energy of concrete found using the empirical relation or from the estimation based on reported literature if material data is unavailable.

The total length of debonded zone is called the safe curtailment length for the beam for that particular load in the case of NSM end debonding.

However, the nature of the sudden IC debonding in a beam indicates that the failure is triggered by an extremely short undetectable interface flaw or debonded zone, as illustrated in Figure 3.12. This is evident from the experimental results reported by Garden et al. (Garden, Quantrill, Hollaway, Thorne, & Parke, 1998), where they confirmed a vertical displacement of 2 mm prior to failure. On the other hand, Quantrill and Hollaway (Quantrill & Hollaway, 1998) reported a vertical displacement of 5 mm at the base of shear cracks, which leads to failure. Therefore, this concept of short debonded zone is used to predict the failure load in the case of IC debonding. The analysis assumes that the load that can trigger debonding with very short interface flaw would cause failure. However, it is inaccurate to propose a specific critical flaw length for a complicated IC debonding type failure. However, the analysis is checked for the debonded zone lengths of 5 and 10 mm, and a critical debonded zone of 10 mm is selected as the failure criterion due to its conservative estimate of the failure load.

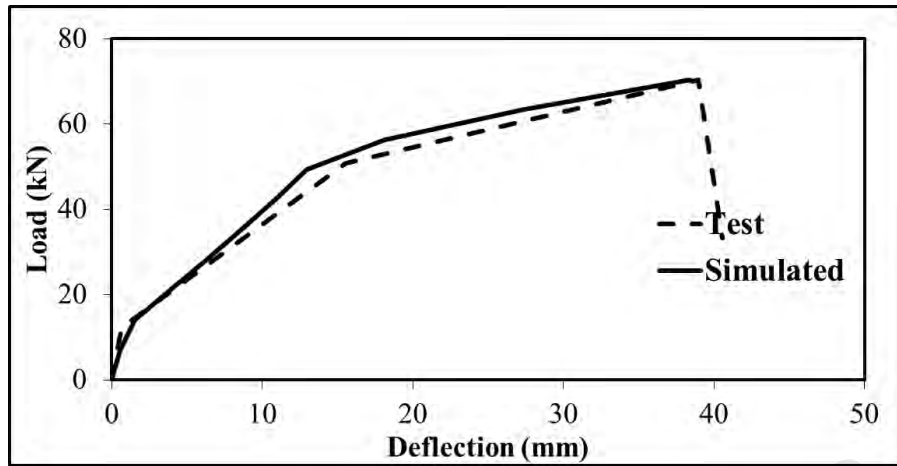
3.5 Analysis of Hybrid strengthened beam

Hybrid strengthening is a combination of the NSM and EBR techniques. Literature on this technique is admittedly scarce (Jumaat et al., 2016; Rahman et al., 2015). This section describes the extension of the GEBA-based method for the hybrid strengthening technique.

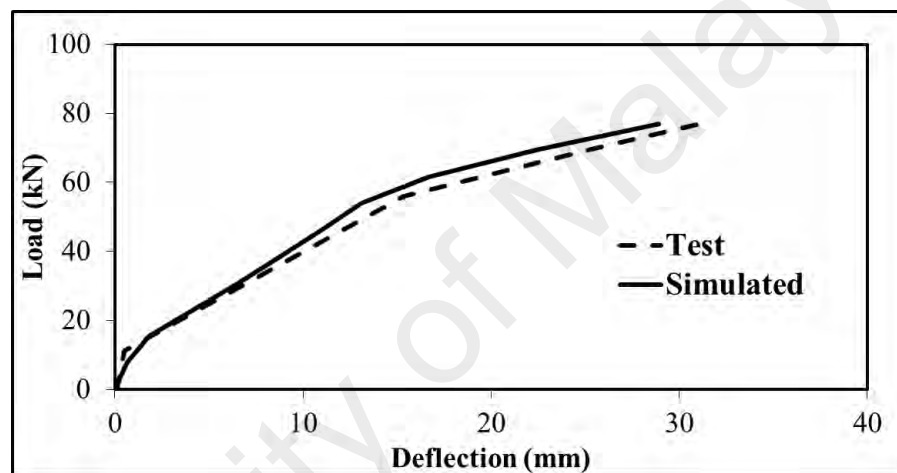
3.5.1 Moment-curvature of hybrid strengthened beam

It is already known that the first step in the GEBA-based method is the determination of moment-curvature for any type of beam. The moment-curvature relationship for hybrid beam is established using the procedure described earlier in the Chapter using Equations (3.28) and (3.29) for uncracked and fully cracked section. The FRP force in that case would have two components; one from NSM rebar and other from EBR with corresponding area, elastic modulus and effective depth. The partially cracked section is analyzed using the modified Branson concept.

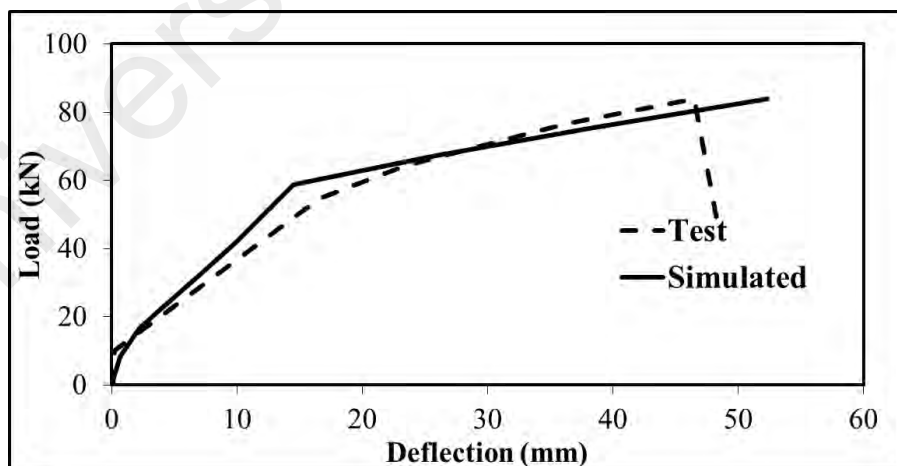
The load versus deflection plot for a few beams, as shown in Figure 3.15 for the hybrid technique shows excellent correlation between the experimental and simulated results, which justifies the applicability of the modified Branson moment-curvature model for the hybrid technique also.



(a) CBC8P1



(b) CBC8P2



(c) CBC10P1

Figure 3.15: Load versus deflection curve for Hybrid beam tested by Jumaat et al. (2016)

3.5.2 Debonding failure analysis of hybrid strengthened beam

Since hybrid strengthening is a combination of EBR and NSM so debonding analysis in this case is computed in the usual manner as for EBR or NSM strengthening. Two types of debonding i.e. both PE and IC have been seen for hybrid strengthened beam. It is assumed that the debonded force will be only the force in the EBR reinforcement because due to the bond condition, detachment of the EBR layer is most likely to happen, earlier than NSM layer. So the analysis used for EBR strengthening is used. The analysis of PE debonding is also done using the same analysis procedure as for EBR assuming that failure will initiate in the EBR layer. The FRP force contribution from NSM layer is assumed to be fixed while debonding analysis.

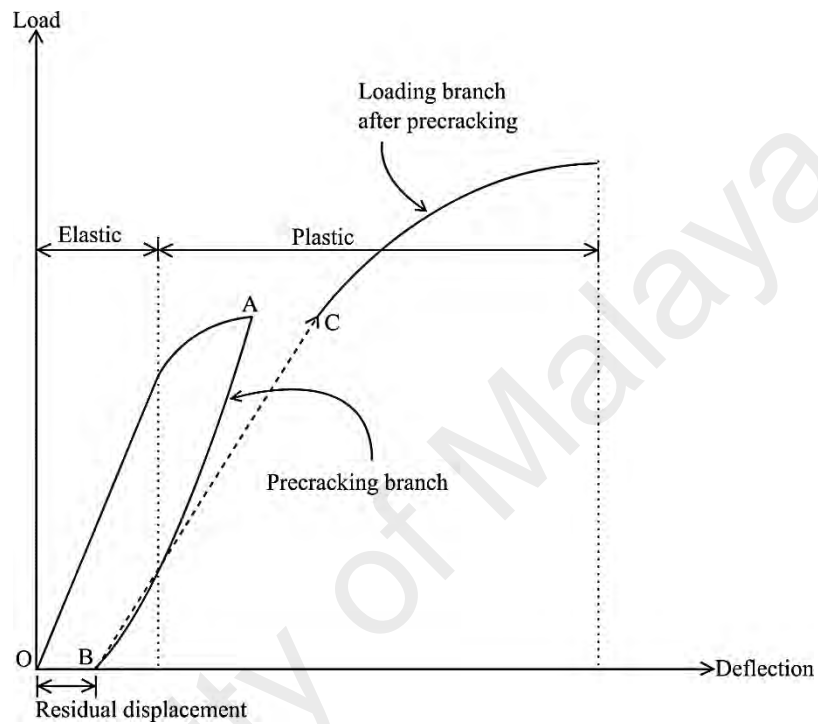
3.6 Analysis of beams precracked before strengthening

The study of debonding failure for the fresh beam remains in its infancy. The purpose of this work is to apply the energy-balance with the fracture energy in the debonding analysis of the different types of strengthened beam. The method is extended in this part of the chapter to check for the efficiency of the method for determining the failure load of strengthened precracked beam with the necessary modification.

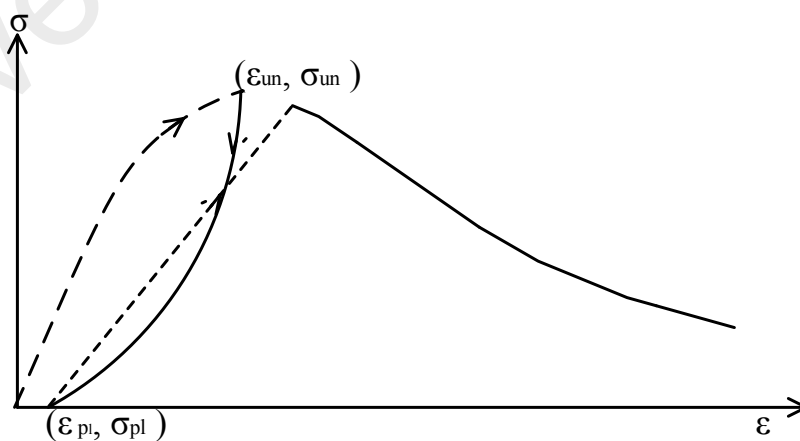
3.6.1 Constituent material properties for precracked beam

The first stage of the model proposed by Achintha and Burgoyne (2008) is the development of moment-curvature for the beam. Since precracking is involved in the precracked beam, it means that unloading the applied load after reaching a certain load on unstrengthened RC beams, and then reloading again after applying strengthening materials, so the constituent materials need to be modeled for both unloading and reloading. The typical load versus deflection curve for a precracked beam is shown in Figure 3.16a, and it can be seen that one of the most important aspects of the precracked beam is the residual deflection OB or residual curvature already present on the beam

prior to strengthening with FRP. Residual deflection will occur in the beam if it exceeds the elastic range of beam during precracking stages. Thus, provisions should be made in the model to account for this residual curvature, and consequently, for deflection. The loading stage after precracking is shown by the branch BC in the figure.



(a) Typical load versus deflection curve after precracking



(b) Stress versus strain curve for concrete under repeated loading

Figure 3.16: Load-deflection and stress-strain curve under repeated loading

Given that the precracking stage involves loading, unloading, and reloading, material models that consider the effect of these stages should be utilized. Several models for simulating concrete behavior under loading, unloading, and reloading conditions have been reported (Aslani & Jowkarmeimandi, 2012; Kent & Park, 1969; Mander, Priestley, & Park, 1988; Martínez-Rueda & Elnashai, 1997; Sima, Roca, & Molins, 2008; Sinha, Gerstle, & Tulin, 1964; Yankelevsky & Reinhardt, 1987). Previous experimental results (Karsan & Jirsa, 1969; Sinha et al., 1964) indicated that the envelope curve for concrete subjected to axial repeated compression can be approximated by the monotonic stress-strain curve. A particular concrete model should be able to analytically model strength and stiffness degradation under the loading-unloading condition. This task can be fulfilled using specific criteria in formulating monotonic or envelope curve, the unloading-reloading branches, and the rules to determine inelastic strain and strength degradation (Martínez-Rueda & Elnashai, 1997). The parabolic stress-strain relationship proposed by Hognestad is used for concrete in compression prior to strengthening.

Martinez and Elnashai (1997) proposed three rules for determining the plastic strain, depending on the damage level (i.e., low, intermediate, and high strain range) and introduced the maximum strain achieved during loading (ϵ_{un}), as shown in Figure 3.16b. The experimental results revealed that precracked beams can have low-intermediate level of concrete damage from the precracking load. Thus, only the equation of plastic strain corresponding to low and intermediate strain range from Martinez and Elnashai (1997), as per Equation (3.47), is adequate for the precracked beam used in this study. However, the debonding load obtained using the plastic strain value at the intermediate range is slightly different from that obtained using the plastic strain value at low range.

$$\begin{aligned}\varepsilon_{pl} &= (\varepsilon_{un} - \frac{f_{un}}{E_c}), & \text{for } 0 \leq \varepsilon_{un} \leq \varepsilon_{35} \\ \varepsilon_{pl} &= (\varepsilon_{un} - \frac{\varepsilon_{un} + \varepsilon_a}{f_{un} + E_c \varepsilon_a}), & \text{for } \varepsilon_{35} \leq \varepsilon_{un} \leq 2.5e_c\end{aligned}\tag{3.47}$$

where ε_{pl} is the plastic or inelastic strain, ε_{un} is the unloading concrete strain, and f_{un} is the reversal envelope stress. E_c is the modulus of concrete, ε_{35} is the strain corresponding to a stress of $0.35f$ in the ascending branch, ε_a is the strain defined by Mander et al.(1988), and e_c is the strain at the maximum concrete strain f (peak stress of confined concrete).

3.6.2 Moment-curvature of unstrengthened section

The first step in the analysis is to determine the residual curvature and residual strain due to an applied load on an unstrengthened RC beam. This requires the moment-curvature of the unstrengthened beam. An unstrengthened beam can have three types of sections: uncracked, fully cracked, and partially cracked. In the uncracked type, the applied moment on the beam is less than the cracking moment, M_{cr} , of the section. Thus, the beam does not have any crack in it at this stage. In the fully cracked type, the applied moment on the section is greater than the yield moment capacity, M_y , of the beam. In other words, the tension steel in the beam yielded. In the partially cracked type, the section is neither uncracked (i.e., the concrete already starts to crack) nor fully cracked (i.e., steel is not yielded). The uncracked and fully cracked sections are solved for the strain at the top and bottom fiber of the beam in this analysis by applying force equilibrium and moment equilibrium conditions using MATLAB for every 1 mm section along the beam using Equations (3.33) and (3.34), but without the contribution of the FRP force. Consequently, the moment-curvature of that part of the beam can be determined. On the other hand, the stiffness of partially cracked section can be determined using classical Branson's (1968) formula, as per Equations (3.8) and (3.9).

Where M_{cr} and M_{app} are the moments at first cracking and the given applied moment, respectively, I_g is the second moment of area of the gross section, neglecting steel and I_{cr} is that of cracked transformed section. A Branson type interpolation coefficient can be used for determining the neutral axis depth, x_{eff} , at partially cracked sections, as per Equation (3.48).

$$x_{eff} = K_{\alpha}x_g + (1 - K_{\alpha})x_{cr}, \quad (3.48)$$

Where x_g and x_{cr} are the neutral axis depth at the uncracked and fully cracked section, and the coefficient K_{α} can be computed using Equation (3.13). Then, the curvature, κ , can be determined using Equation (3.49)

$$\kappa = \frac{M_{app}}{E_c I_{eff}}, \quad (3.49)$$

The strain at the top and bottom fiber can also be determined then using the following relation in Equation (3.50).

$$\text{Strain} = \kappa \times \text{distance of the fiber from the neutral axis location} \quad (3.50)$$

3.6.3 Determination of plastic component

Once the moment-curvature of the unstrengthened section is determined, the plastic strain at the top of beam fiber can be determined using Equation (3.51). The inelastic strain at the tension side of the beam is significant in the analysis, if the strain in the tension steel exceeds the yield strain of steel during precracking stage. Strengthening increases, the capacity of the existing beam, which is deteriorated, due to changes in the load, faulty design or construction, with the course of time. Thus, whether the beam can still be within its previous design flexural capacity or can exceed the yield limit is uncertain. Accordingly, the inelastic strain at the bottom of the beam is accounted for in the modeling precracked beam.

Therefore, the inelastic strain at the bottom of the beam is:

$$\varepsilon_{pl_bot} = \varepsilon_{un_bot} - \varepsilon_y, \quad (3.51)$$

Where ε_{pl_bot} is the plastic strain at the tension side of the beam i.e. at the bottom fiber of the beam, ε_{un_bot} is the unloading strain at the tension steel level of the beam; ε_y is the yield strain of steel.

After the plastic strains at the two extreme fibers of the beams are determined, the neutral axis x_{pl} and curvature k_{pl} at any location for that plastic strain can be computed as per Equations (3.52) and (3.53).

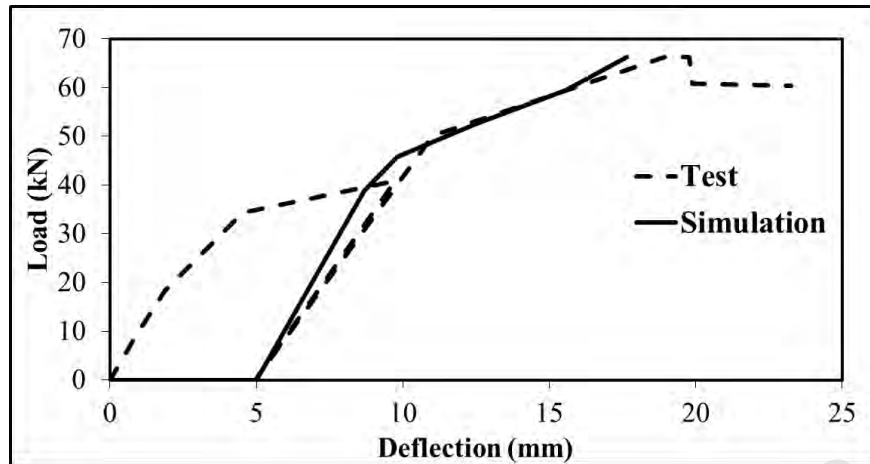
$$x_{pl} = \frac{\varepsilon_{pl} * h}{\varepsilon_{pl} + \varepsilon_{pl_bot}}, \quad (3.52)$$

$$K_{pl} = \frac{\varepsilon_{pl}}{x_{pl}}, \quad (3.53)$$

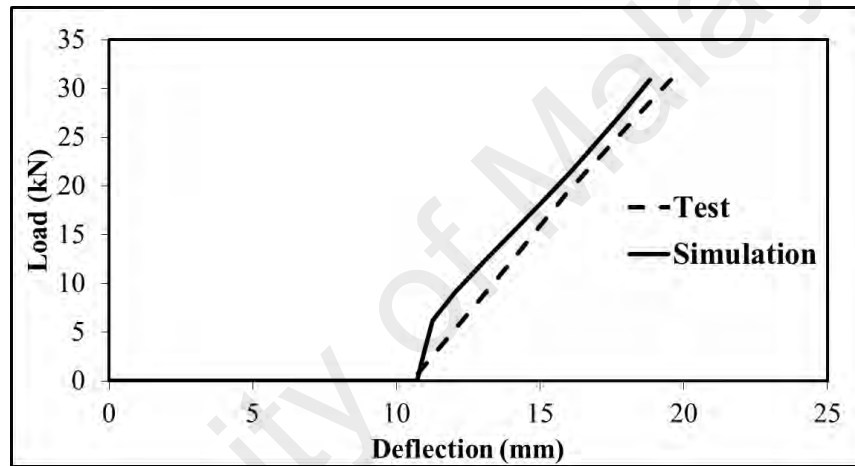
3.6.4 Moment-curvature of strengthened section

After determining the strain values of an unstrengthened section via iteration, the residual plastic strain would be added to that strain to obtain the actual strain profile of the beam.

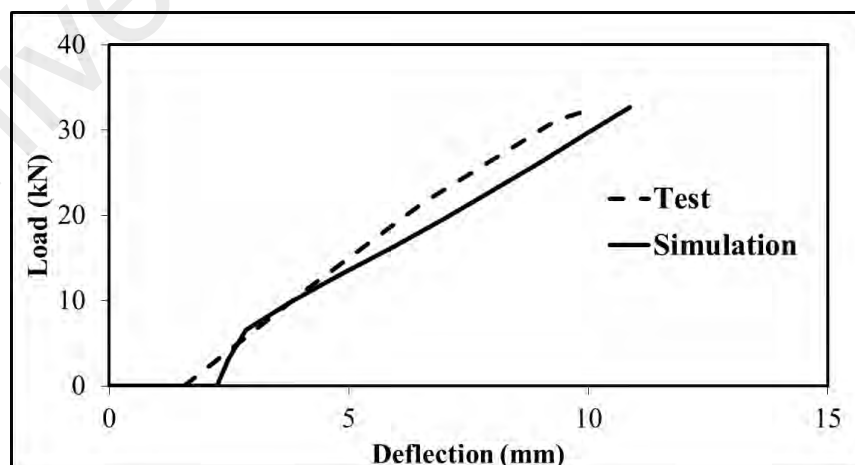
Figure 3.17a and b plots the load versus deflection curve for beam FP2 by Sharif et al. (1994), while beam RB4 was tested by Benjeddou et al. (2007), respectively, where unreinforced beams were loaded to 85% and 100% of their flexural capacity prior to strengthening. The load versus deflection plots of two beams with damage degrees of 90 % are also shown in Figures 3.17 c and d. It shows excellent agreement between experimental and simulation results, implying the suitability of the model for precracked beams.



(a) Beam FP2 by Sharif et al. (1994)

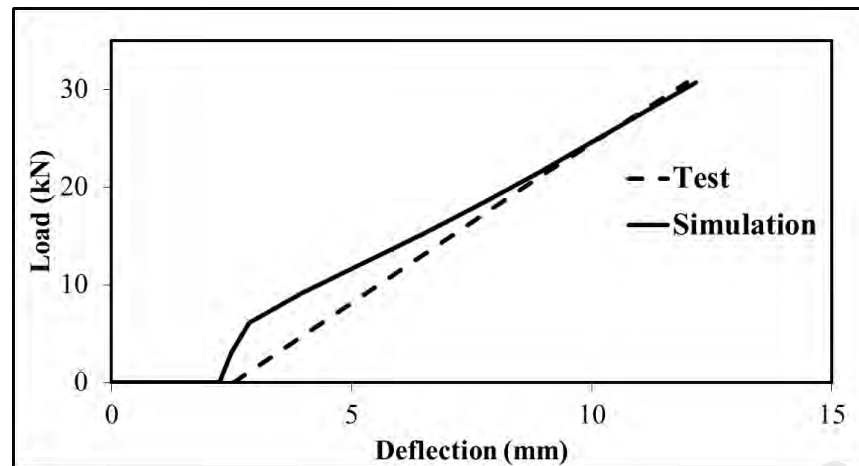


(b) Beam RB4 with a damage degree of 100% by Benjeddou et al. (2007)



(c) Beam RB3 with a damage degree of 90% by Benjeddou et al. (2007)

Figure 3.17: Load versus deflection curve



(d) Beam RB5 with a damage degree of 90% by Benjeddou et al. (2007)

Figure 3.17, Continued

3.6.5 Centroidal axis depth

The determination of the centroidal axis has already been discussed earlier for fresh beam. However, for the precracked beam, some parts of the strengthened beams can be partially cracked, owing to the moment acting on the section but actually reaching a fully cracked stage or being severely damaged during precracking stages. Those sections are analyzed as partially cracked using the modified Branson equation, and their curvature is determined on the basis of the aforementioned analysis. Then, the centroidal axis depth for this type of section is computed for the fully cracked section.

3.6.6 Computation of ERR

The next step after the establishment of the moment-curvature relationship is to employ the GEBA method developed by Achintha and Burgoyne (2008) to calculate the ERR and compare it with the critical fracture energy of concrete.

It should be pointed out that the curvature of precracked beams is composed of the plastic curvature and the curvature due to bending. Therefore, some of the energy will be dissipated via plastic deformation. However, since Equation (3.21) employs the curvature difference in two subsequent debonding states, no further change is required

to include the effect of plastic curvature because this quantity is similar in both states. This argument is also true for Equations (3.22) and (3.23).

3.6.7 Debonding analysis

It is obvious from the moment-curvature analysis of the precracked beam that the zones affected by precracking are only the midspan or the zone near the load point. Therefore, it is less likely that the PE debonding will be affected by precracking. The beams showing IC debonding will be prone to be affected by precracking. The analysis of IC debonding for the precracked beam is the main aim of this work. The debonding analysis has already been discussed in section 3.3.2.3. However, the strain used for determining the FRP force in the debonded zone can be computed by considering the strain due to bending only, i.e. without considering plastic strain component.

The entire debonding analysis procedure is shown in Figure 3.18.

The first step is to apply the precracking load, P_{pre} and hence determine the $M-\kappa$ relationship for that load. Once the $M-\kappa$ relationship is established, the next step is to determine the plastic component of the beam.

The loads will be applied again post-precracking. The steps are similar to the ones detailed in section 3.3.2.4 after the application of the load, P . The end debonding part is not shown in the flowchart as it is similar to the one reported in 3.3.2.3.

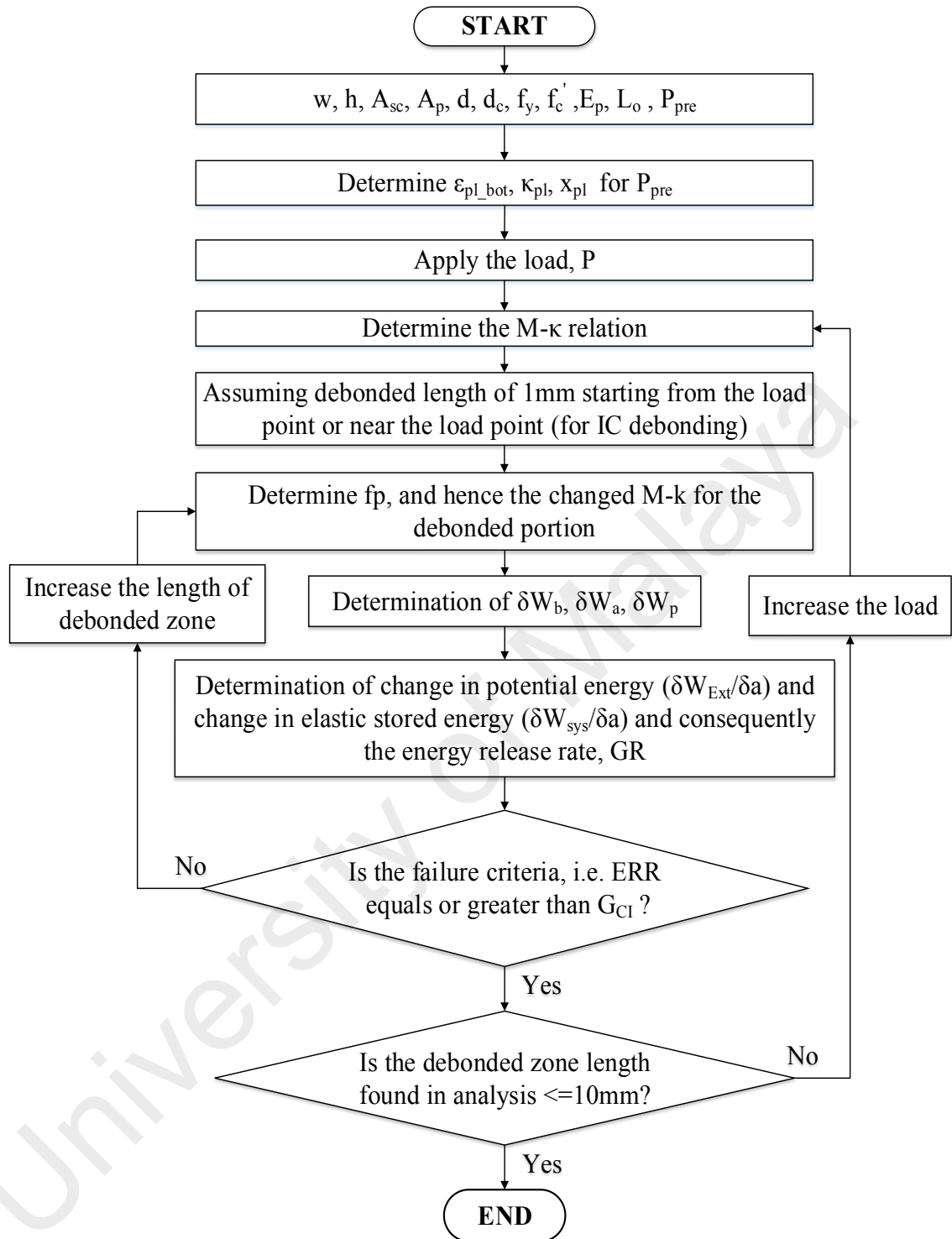


Figure 3.18: Flowchart showing computation procedure

3.7 Analysis of beams strengthened using Prestressed FRP

As discussed in Chapter 2, the failure analysis of the prestressed beam is another research field altogether. This part will concentrate on the analysis of the failure of the prestressed FRP strengthened beam.

3.7.1 Moment-curvature of prestressed beam

The constituent material properties adopted for the moment-curvature analysis of prestressed beam is the same as the one shown in Figure 3.6. Prestressed beam section can be of three types. The section at which the applied moment due to load is less than the cracking capacity of concrete, as expressed by Equation (3.58), or greater than the yield capacity of the section, as expressed by Equation (3.59). These sections are called the uncracked and fully cracked section, respectively. If the moment in any beam section is in between, it will be called a partially cracked section. Once the mechanical properties of materials are selected, the strain at any uncracked or fully cracked section of the beam can be determined by solving the force equilibrium and moment equilibrium conditions given in Equations (3.28) and (3.29). The stress-strain distribution of prestressed beam will be similar to the one shown in Figure 3.7, except that the strain at the bottom fiber would be:

$$\varepsilon_{bottom} = \varepsilon_{frp} - \varepsilon_{pre}, \quad (3.54)$$

The iterative program is executed using MATLAB for every 1 mm section of the beam to solve these equations and to determine the strain at the two extreme fibers. In the case of the prestressed beam, the force in the FRP will be as the one shown in Equation (3.55).

$$f_{frp} = \varepsilon_{frp} E_{frp} = (\varepsilon_{bottom} + \varepsilon_{pre}) E_{frp}, \quad (3.55)$$

ε_{pre} is the prestressing strain applied to the FRP reinforcement for a corresponding force of P_{pre} , ε_{frp} is the total strain in the FRP and E_{frp} is the elastic modulus of FRP.

The prestressing of the FRP sheets in the strengthening of RC beams will increase the cracking, as well as yield moment i.e. it will delay the yielding of steel, and failure load will also increase relative to the non-prestressed strengthened beam. The increase

in the first cracking moment and yielding moment can be calculated using the following relationship espoused by Equations (3.56) and (3.57):

$$M_{inc_cr} = A_{frp} E_{frp} \epsilon_{pre} (h_f - x_{cr}), \quad (3.56)$$

$$M_{inc_y} = A_{frp} E_{frp} \epsilon_{pre} (h_f - x_y), \quad (3.57)$$

x_{cr} and x_y are the depth of compression fiber of beam from the center of the beam for uncracked stage and yield stage.

Therefore, the cracking moment M_{cr} and yield moment M_y for the prestressed beam will be:

$$M_{cr} = \frac{f_r x_{cr}}{I_g} + M_{inc_cr}, \quad (3.58)$$

$$M_y = f \alpha x_y^2 w (1 - \gamma) + A'_s E_s \epsilon'_s (x_y - d_c) + A_s f_y (d - x_y) + A_f E_{frp} \epsilon_{frp} + M_{inc_y} \quad (3.59)$$

The negative curvature of the beam at the uncracked stage will be:

$$k_{pre} = \frac{e_{top_pre}}{x_{pre}}, \quad (3.60)$$

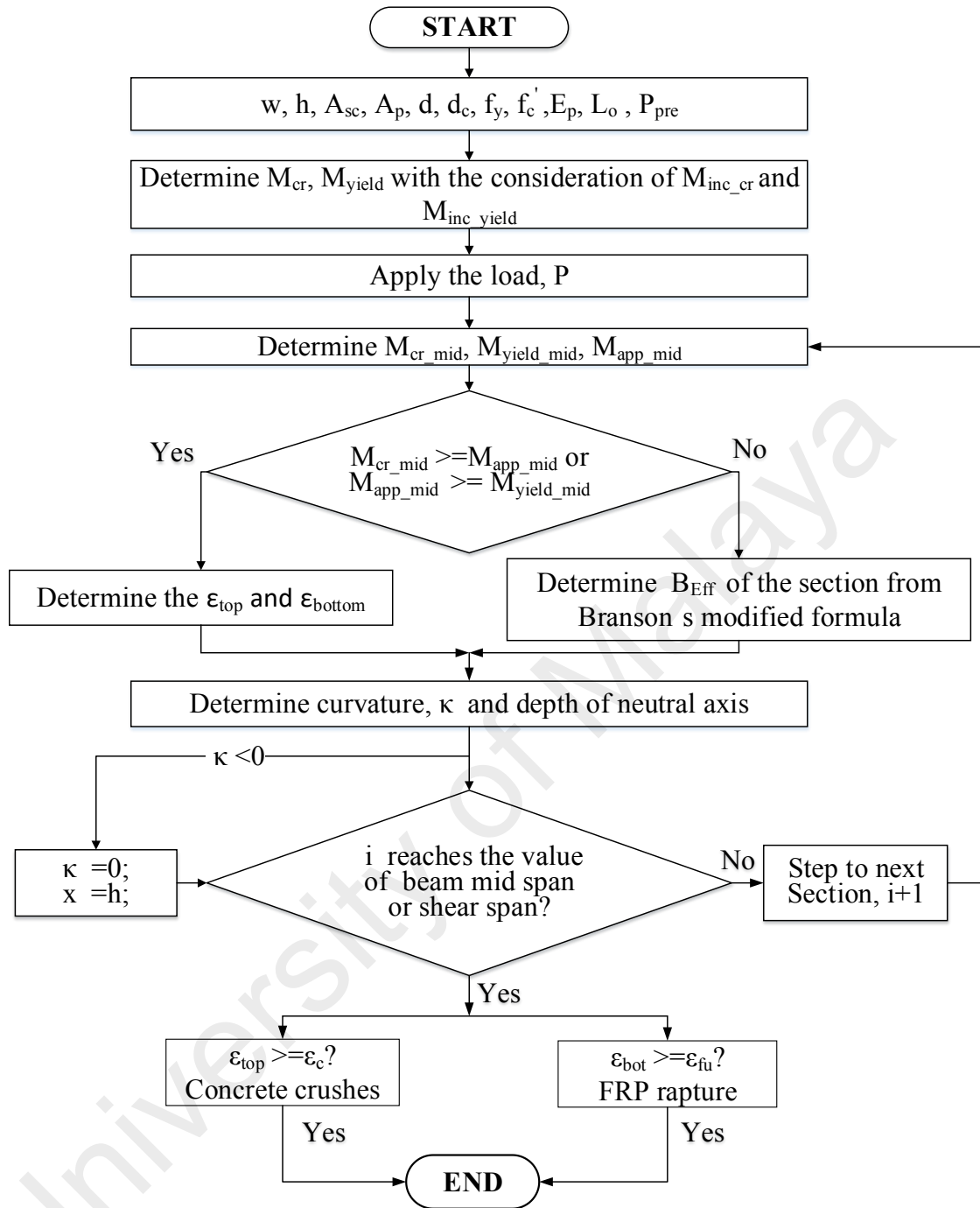


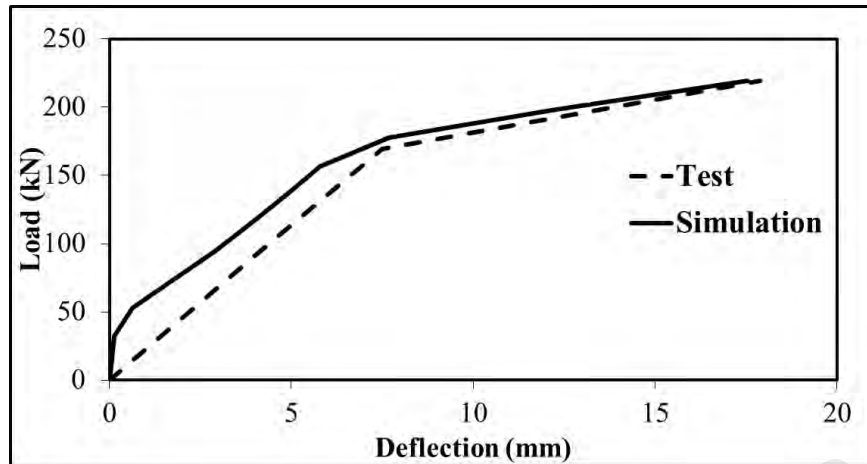
Figure 3.19: Flow chart of moment-curvature for prestressed FRP strengthened beam

After determining strain and curvature, the deflection value at the midspan can be determined using the classical moment area theorem (Hibbeler, 2012). The whole procedure of moment-curvature analysis is summarized in Figure 3.19.

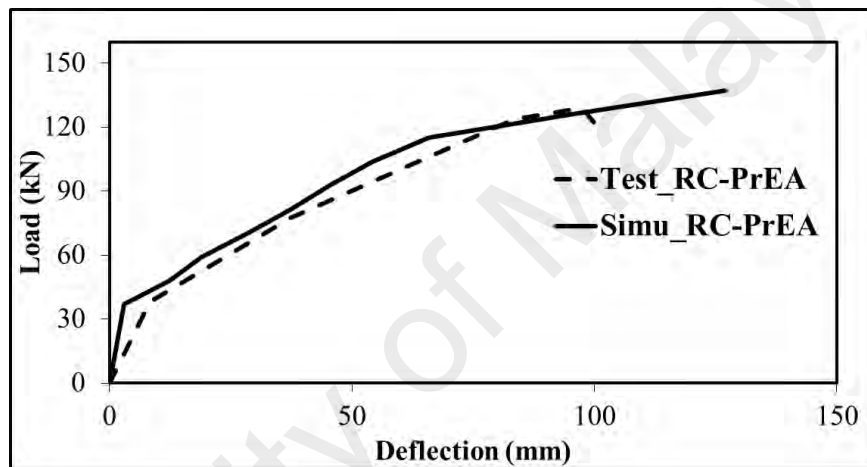
Comparison between experimental load versus deflection plot and load versus FRP strain plot for several prestressed beams strengthened using EBR and NSM techniques

are shown in Figure 3.20 to Figure 3.23 respectively. The figure shows that the agreement between experimental and simulated load versus deflection and load versus FRP strain. Load versus deflection, as well as load versus FRP strain curve for both beams, strengthened using EBR and NSM techniques are quite realistic. This proves the suitability of the moment-curvature model proposed to be used for beams strengthened using prestressed FRP.

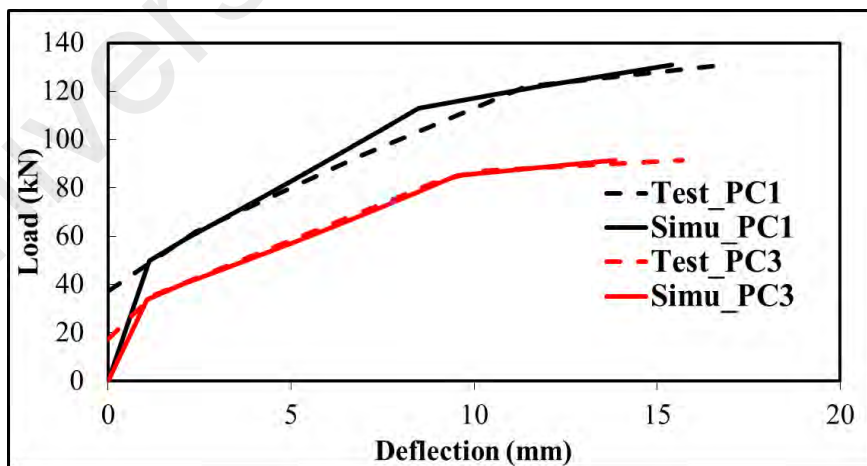
Comparison between the experimental load versus deflection plot and load versus FRP strain plot for several prestressed beams strengthened using EBR and NSM techniques are shown in Figure 3.20 to Figure 3.23, respectively. It shows that the experimental and simulated load versus deflection and load versus FRP strain are in excellent agreement. Load versus deflection and load versus FRP strain curves for beams, strengthened using both EBR and NSM techniques, are quite realistic. This confirms the suitability of the moment-curvature model proposed for strengthened beams using prestressed FRP.



(a) 15% prestressing (Yu et al., 2008)

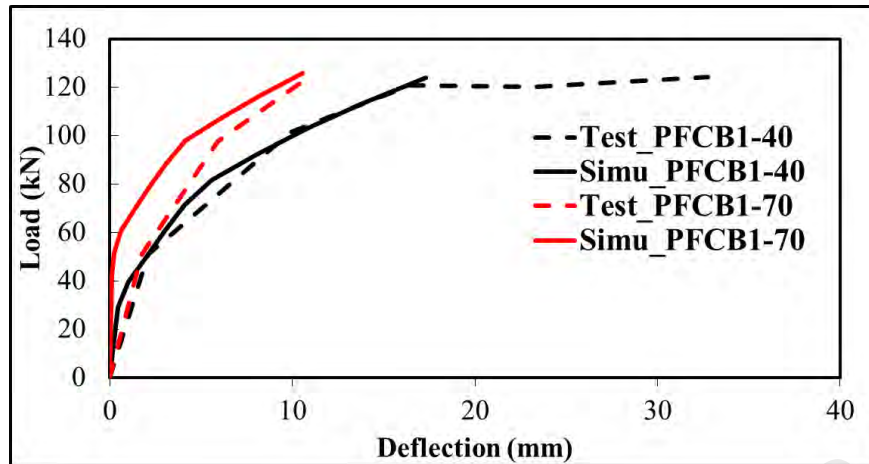


(b) 35% prestressing (Pelligrino et al., 2009)

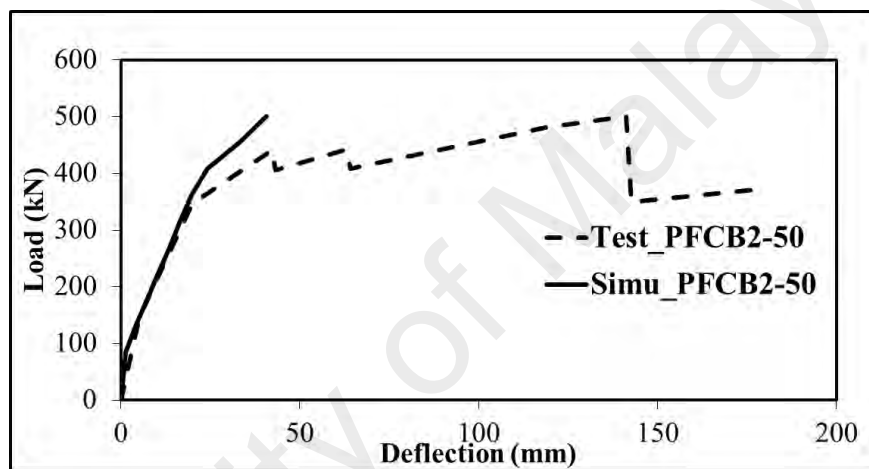


(c) PC-1 and PC-3 (Xue et al., 2010)

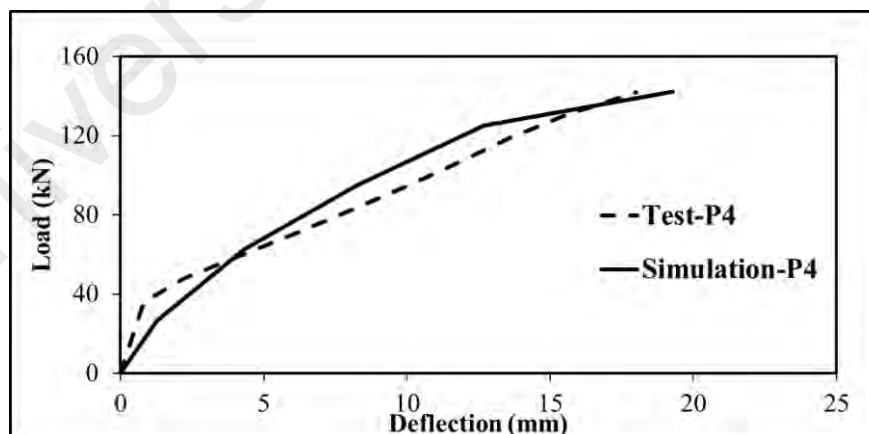
Figure 3.20: Load versus deflection curve for prestressed EBR beam



(d) PCFCB1-40 and PCFCB1-70 (You et al. ,2012)

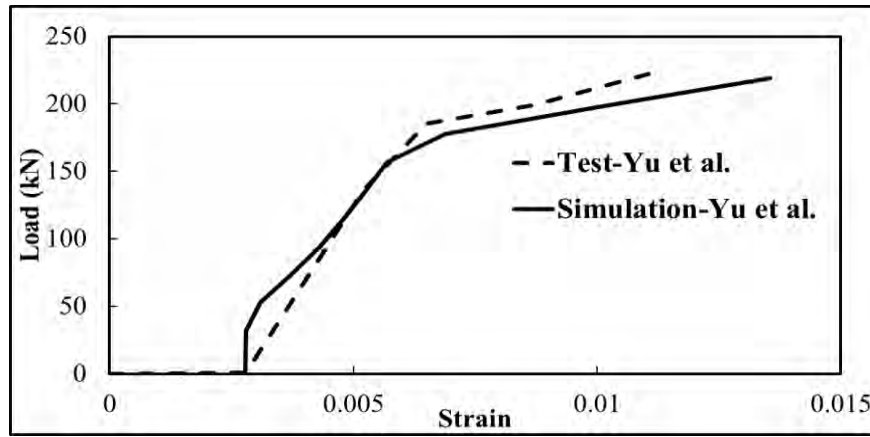


(e) PCFCB2-50 (You et al. ,2012)

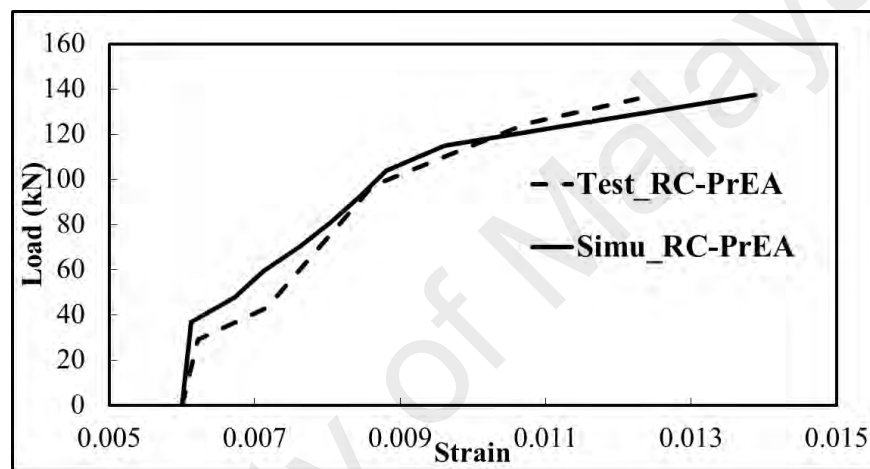


(f) P4 (Quantrill and Hollaway 1998)

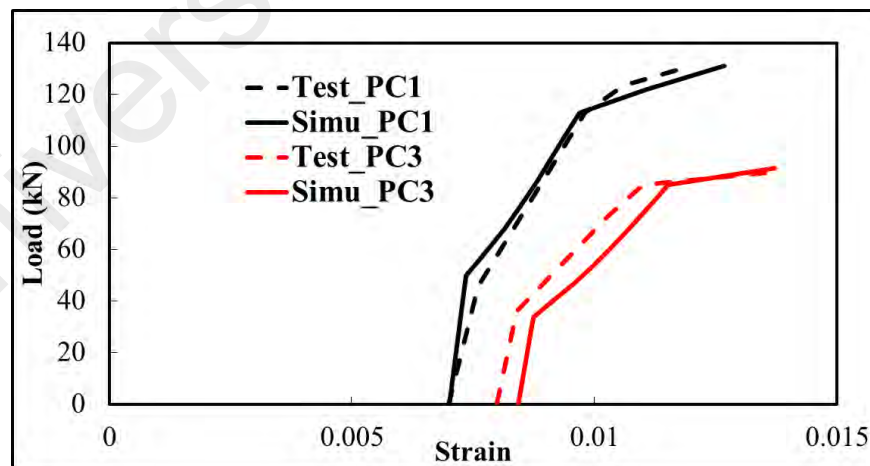
Figure 3.20, Continued



(a) 15% prestressing tested by (Yu et al. 2008)

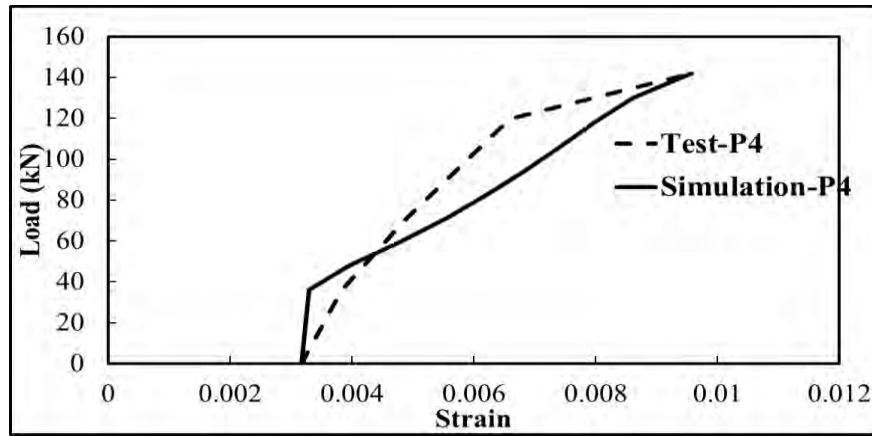


(b) 35% prestressing (Pelligrino et al.,2009)

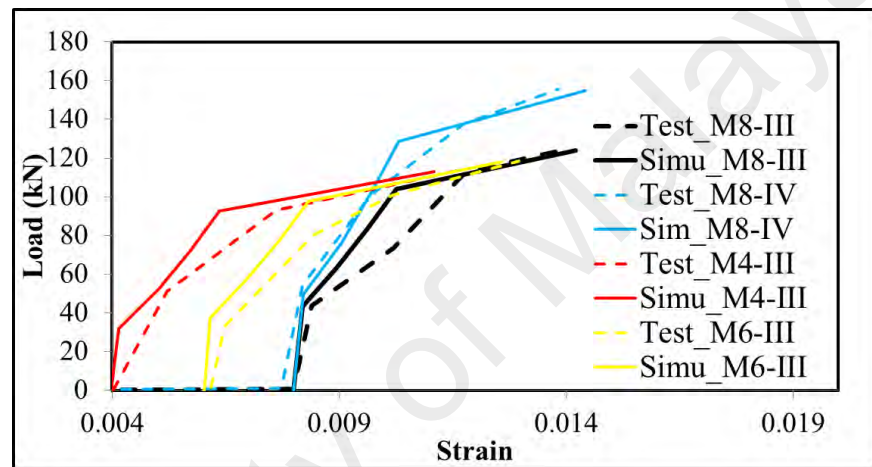


(c) PC-1 and PC-3 (Xue et al.,2010)

Figure 3.21: Load versus FRP strain curve for prestressed EBR beam

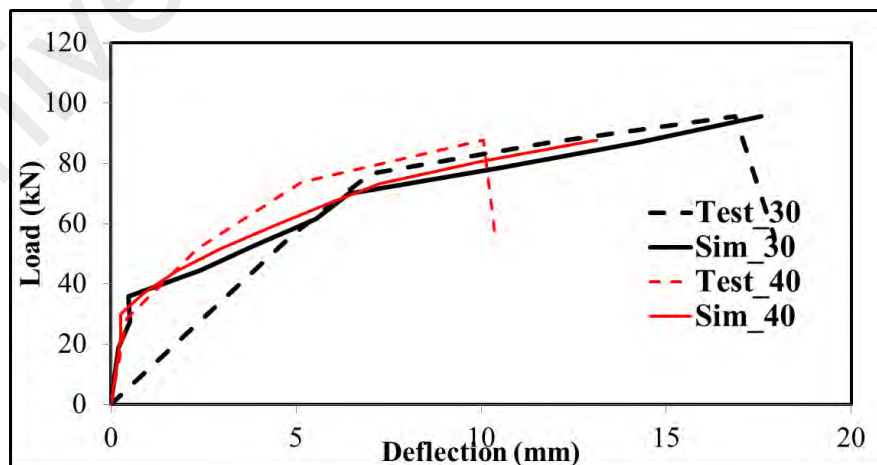


(d) P4 (Quantrill and Hollaway,1998)



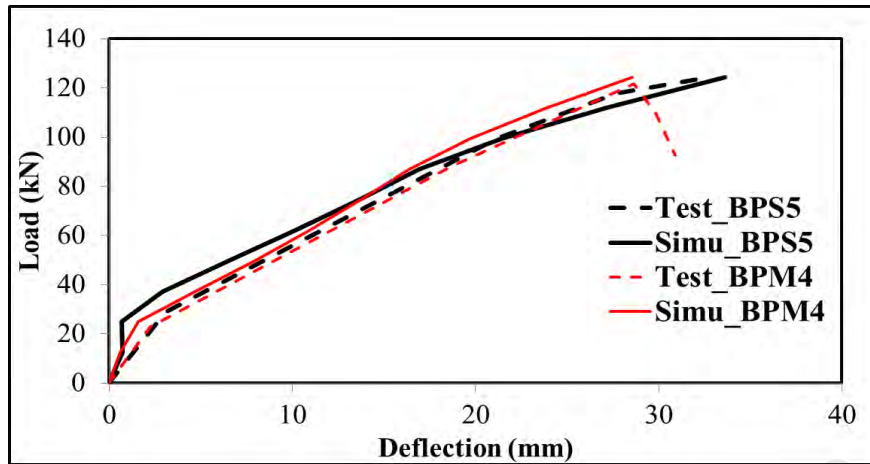
(e) Different Beams (Woo et al. 2008)

Figure 3.21, Continued

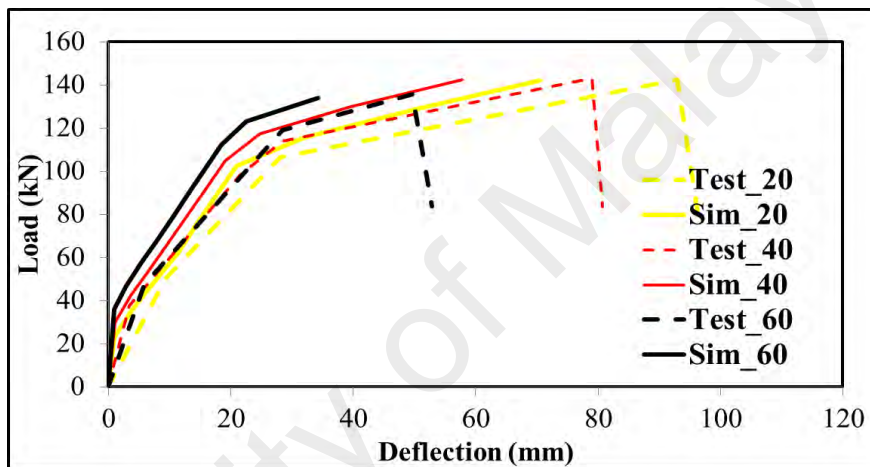


(a) 30 and 40 % prestressing (Rezazadeh et al., 2014)

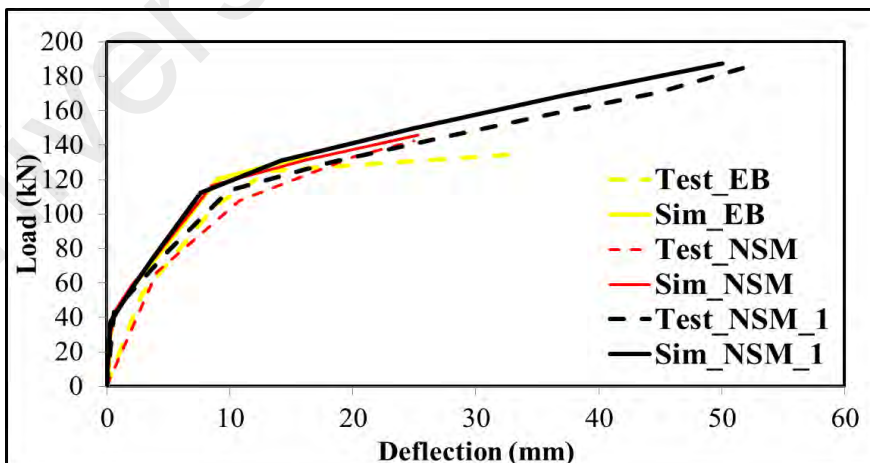
Figure 3.22: Load versus deflection curve for prestressed NSM beam



(b) BPS5 & BPM4 with 20 % prestressing (Nordin and Taljsten,2006)

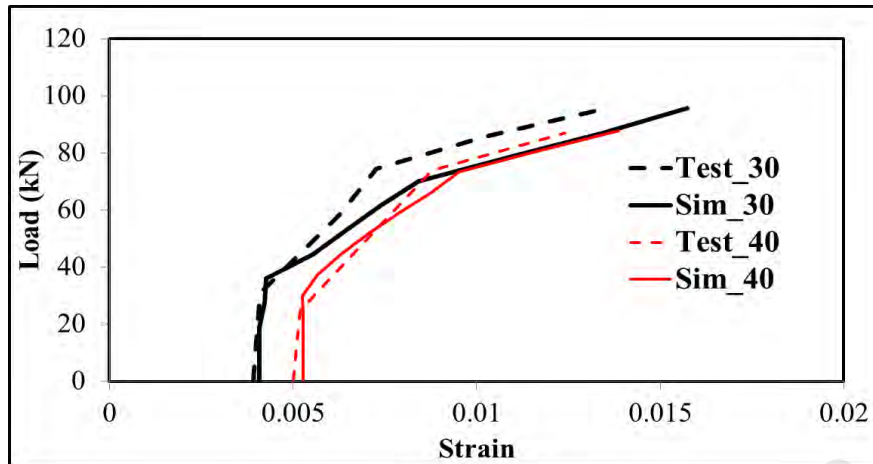


(c) beam with 20,40 and 60 % prestressing (Raafat & Mohamed (2011))

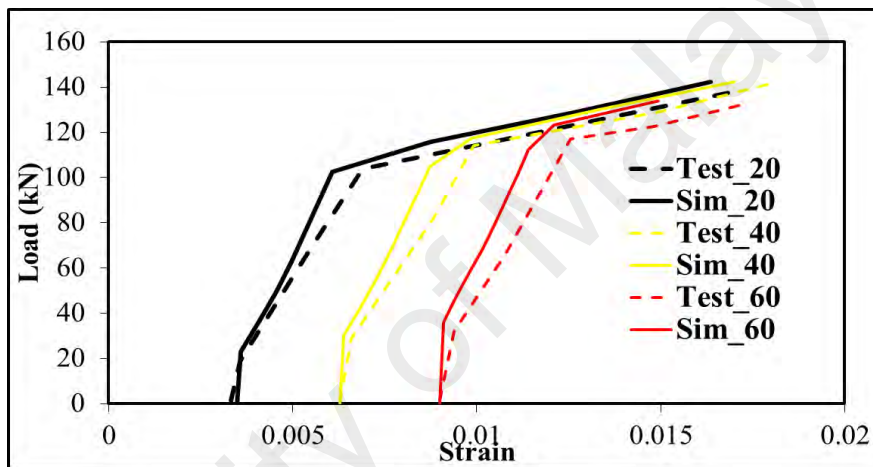


(d) PRS-EB and PRS-2N20 (Peng et al. (2014))

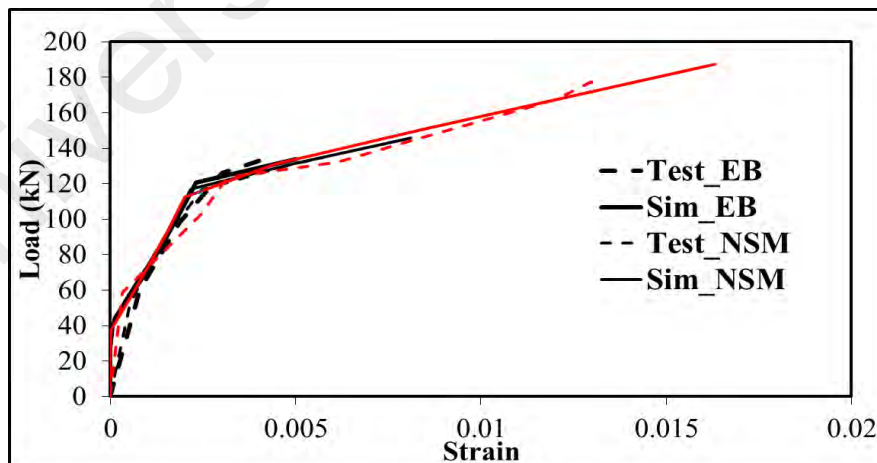
Figure 3.22, Continued



(a) 30 and 40 % prestressing (Rezazadeh et al., 2014)



(b) BPS5 and BPM4 with 20 % prestressing (Nordin and Taljsten 2006)



(c) PRS-EB and PRS-2N20 (Peng et al. (2014)

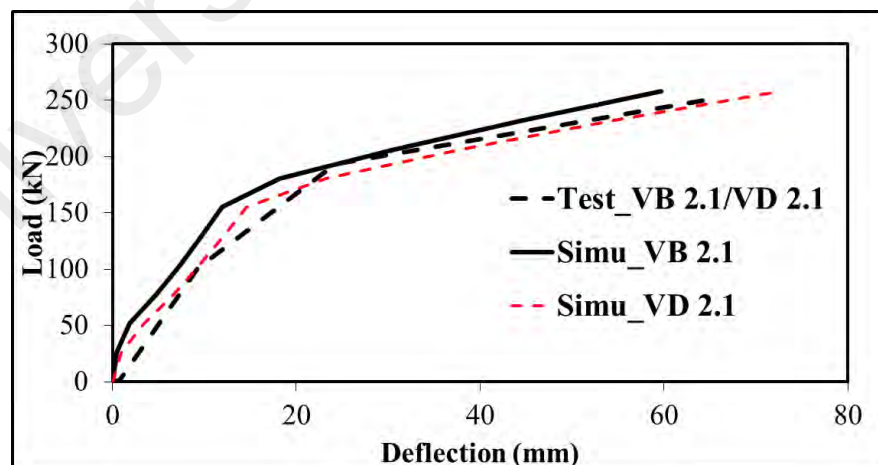
Figure 3.23: Load versus FRP strain curve for prestressed NSM beam

The determination of the centroidal axis and ERR for the prestressed beams are similar to the ones detailed in section 3.2.5 and section 3.6.5 to 3.5.7.

3.8 Analysis of T-beams

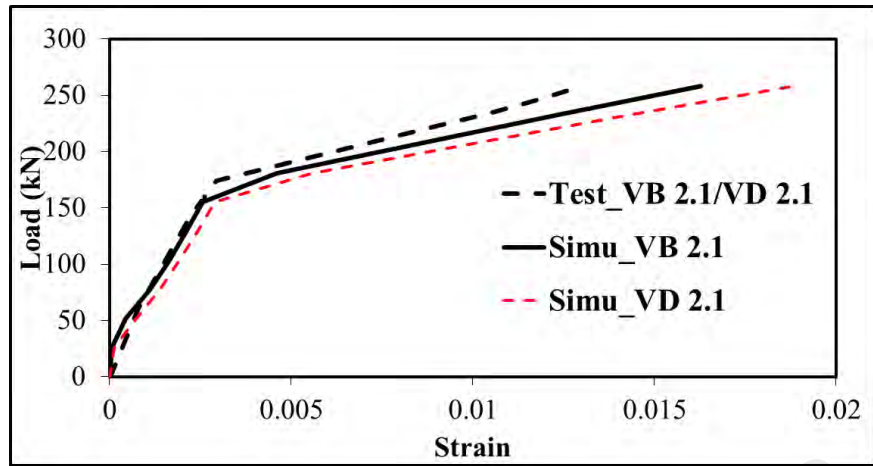
Analysis has been so far conducted for beam with rectangular cross section. Some researchers also tested beams with T-section, which resemble the original beam section in a practical field (Castro, Melo, & Nagato, 2007; Choi, West, & Soudki, 2010; Hassan & Rizkalla, 2004). This section discusses the debonding analysis for beams with T-section.

In the case of a T-beam, first, an assumption will be made if the neutral axis depth is within the flange or in the web part of the T-section. Depending on this assumption, the beam will be regarded to be a rectangular section or a T-section. If the neutral axis falls within the beam flange, the procedure will be the same to the one reported for the rectangular section only, while the beam width in Equations (3.28) and (3.29) will be used as the total flange width.

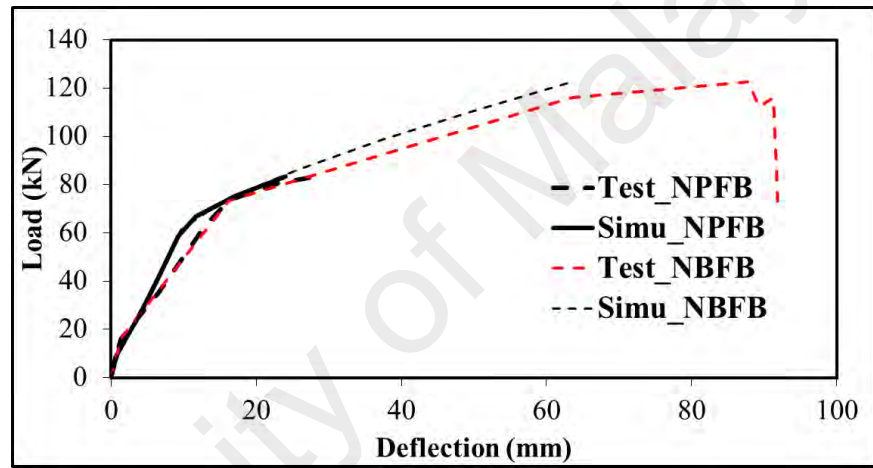


(a) Load versus deflection Castro et al. (2007)

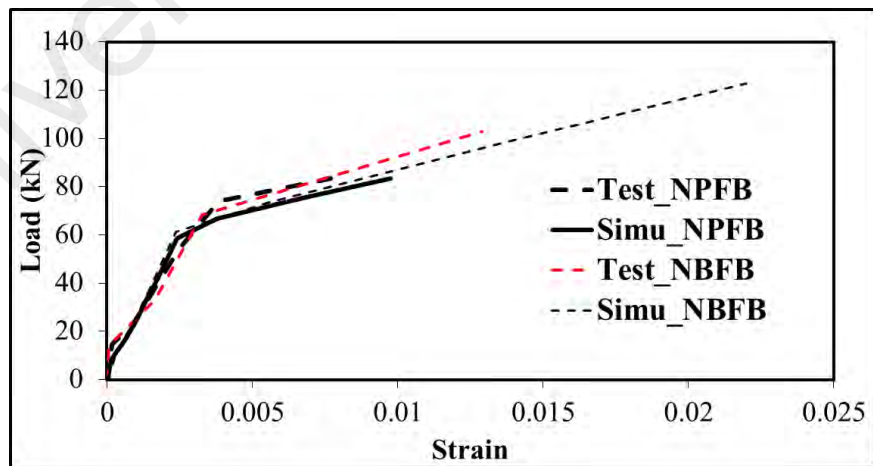
Figure 3.24: Load versus deflection and Load versus FRP strain plot for T-beam



(b) Load versus FRP strain plot for Castro et al. (2007)



(c) Load versus deflection Choi et al. (2010)



(d) Load versus FRP strain plot for Choi et al. (2010)

Figure 3.24, Continued

Figure 3.24 shows the load versus deflection curve for few T-beams using the moment-curvature analysis described in this thesis. The T-beams found in literature are mostly strengthened using the NSM technique.

After establishing the moment-curvature, the ERR will be calculated using the procedure described in section 3.3.2.4.

3.9 Summary

This chapter reported the application of the GEBA model for determining the debonding loads for FRP strengthened RC beams: NSM beam, hybrid beam, beams precracked before strengthening, beams strengthened using prestressed FRP, and the beam with T-section. The developed moment-curvature model for the aforementioned types of the beam is presented. Use of force and moment equilibrium for the uncracked and fully cracked part of the beams and classical and modified Branson formula proposed by Achintha and Burgoyne (2008) for the sections that are partially cracked provided a realistic estimation of the beam response under static load for the NSM strengthened beam. For the hybrid beam, the effects of the two layers of strengthened reinforcement are included in the model. The $M-\kappa$ model developed in this thesis for the precracked beam is realistic because it included the effect of plastic strain and strength degradation post-unloading in the moment-curvature. The $M-\kappa$ analysis for the prestressed beam has been performed by considering the external force applied to the beam due to prestressing. The model is also applicable to the rectangular and T-sections.

The proposed $M-\kappa$ analysis has been validated by comparing the load versus deflection and load versus FRP strain curve. The results are found to be in reasonable agreement with published experimental data. It shows the adequacy of the current moment-curvature analysis for practical purpose. Moreover, this chapter also presents

the steps for determining the ERR of the beams systems. ERR and the safe curtailment length at different loads for end debonding of the NSM strengthened beam can be computed by accounting for the fact that ERR takes place in the transition zone. The length of the transition zone can be obtained from interfacial stress analysis. The width of the fracture surface is taken as the beam width from the observation of failure surface in the experimental work. The analysis is also performed using different possible fracture surfaces. Debonding analysis with beam width taken as the width of fracture surface results in a realistic estimation of failure load. ERR and the debonded zone length at different loads for IC debonding can be computed by assuming that energy changes occur only at the partly debonded zone. It also gives a good approximation of failure.

University of Malaya

CHAPTER 4: VALIDATION OF PROPOSED MODEL

4.1 Introduction

The validation of the GEBA model using the experimental data obtained from literatures for the NSM strengthened beams, hybrid strengthened beams, beams precracked before strengthening, beams strengthened using prestressed FRP and T-beams are presented here. Then, a parametric study, considering the effect of concrete, steel reinforcement, FRP reinforcement, beam geometry, precracking level, prestressing level is performed to elucidate a better understanding of the effects of these parameters on debonding and to close the gaps present in this field.

4.2 Steps for validation of test beams

The steps involved in predicting debonding loads are:

The shear capacity of the strengthened beam, $P_{\text{shear_ACI}}$ can be determined using the ACI-code (2008).

The load corresponding to the rupture of FRP, $P_{\text{frp_rup}}$ can be computed from the moment corresponding to the rupture strain of FRP using Equations (3.28) and (3.29).

PE debonding analysis is executed in MATLAB for different loads, starting from the theoretical yield load, P_{yield} . A safe curtailment length from the beam end can be determined for that particular load using the methodology detailed in Chapter 3.

At the simulated load, if the value of safe curtailment length is greater than the provided curtailment length and shear capacity is within the ACI limit, then flexure or IC debonding failure is assumed for that beam.

At the simulated load, if the value of safe curtailment length is greater than the provided curtailment length but the shear capacity exceeds the ACI limit, then the beam is assumed to have failed in shear.

If the value of safe curtailment length is equal to the distance from the beam end, PE failure will occur at that specific load.

IC debonding analysis can be executed in MATLAB for different loads greater than P_{yield} ; the critical debonded zone length can be determined, where ERR is equal to G_f . If the debonded zone length at the simulated load is less than or equal to 10 mm; failure is assumed to occur at that load.

Appendices A and B show the important calculation steps and MATLAB code for the simulation, respectively.

The steps are shown in the form of a flowchart in Figure 4.1.

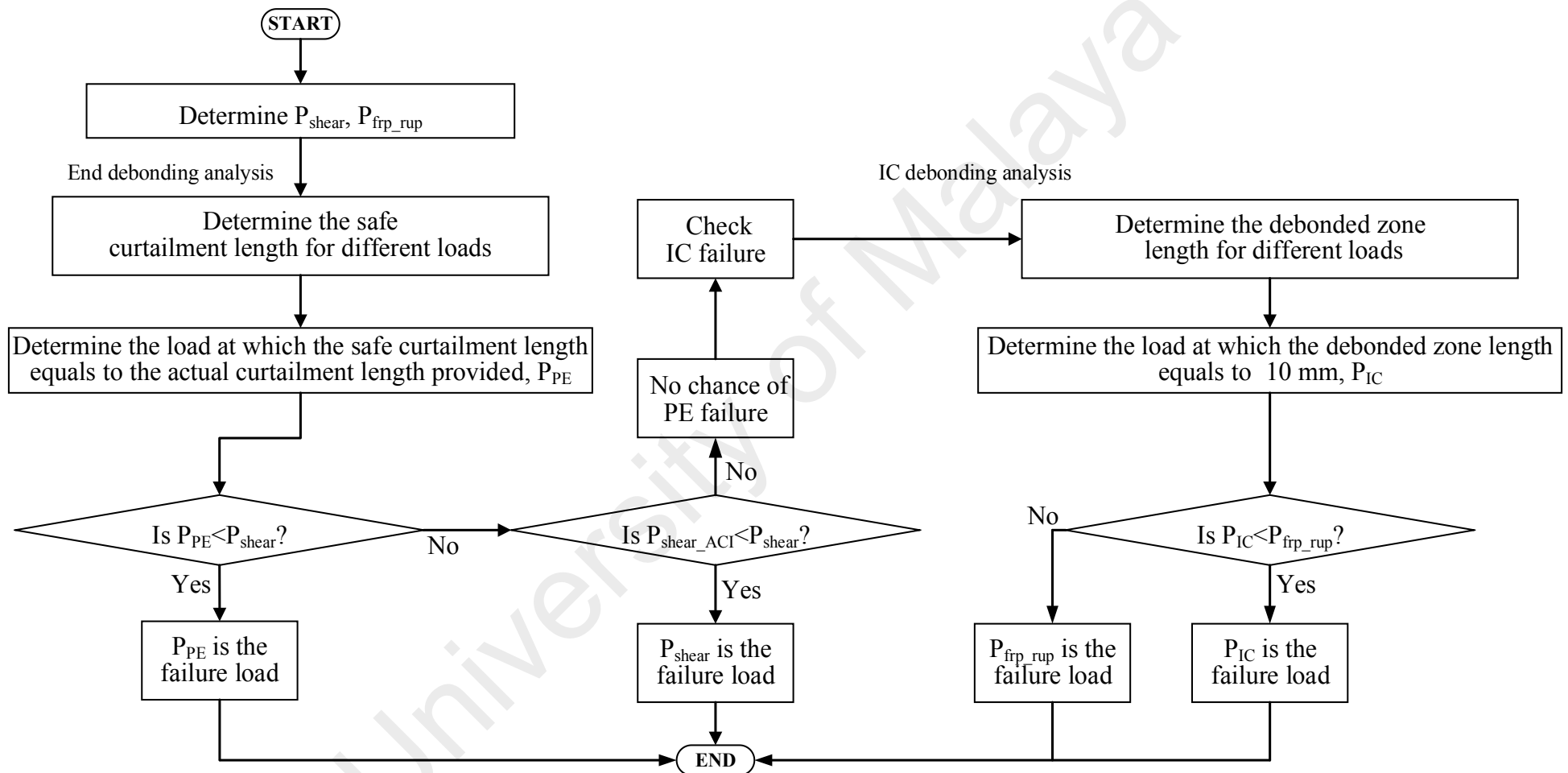


Figure 4.1: Flowchart showing calculating debonding load

The validation of the GEBA model for different types of beams have been carried out against a database of the test results collected from literature, encompassing all possible types of debonding failure in strengthened beam with concrete compressive strength, ranging from 20 - 50 MPa, precracking levels ranged between 15 - 100%, and prestressing level in FRP 30-70%.

All the beams considered for the analyses were tested as a simply supported beam, either under three-point bending or four-point bending, with equal shear spans. The load versus deflection curves and FRP strain versus load curves of unstrengthened and strengthened beams are checked against the reported curves prior to debonding. In instances where the aggregate data are missing, acceptable values of fracture energy are assumed. Karihaloo et al. (2003) reported a fracture energy value of 0.15 N/mm for coarse aggregate measuring 20 mm. The values of fracture energy for the 10 mm crushed and rounded aggregates are set to be 0.10 and 0.07 N/mm, respectively.

4.3 Validation of NSM strengthened beam

The material and geometric properties of the NSM strengthened beams used for validation are tabulated in Tables (4.1) and (4.2).

Table 4.1: Identification and geometric data of the beams used in the analysis

Source	Specimen	Failure Load (kN)	Failure Mode	Rebar type	Rebar Material	Total span l_{span} , mm	Shear span l_{shear} , mm	Unsupp orted len. L_o , mm	Wid. b, mm	Ht., mm	Eff. dep. d, mm	Eff. Dep. d_c , mm	Groove size (width X depth)
Al-Mahmoud et al. (2010)	SC210	109	PE	Bar	CFRP	2800	800	350	150	280	250	30	12x12
	SC270	133.1	IC										
Khalifa (2016)	B-S-2	72.26	IC	Strip	CFRP	2200	950	100	150	260	225	25	–
	B-N-2-2	91.57	IC										15x25
	B-N-2-4	105.56	PE/IC										
Carolin (2003)	E3	140	PE	Square bar	CFRP	3600	1300	300	200	300	262	38	16x16
	C3	123.5	PE										
Teng et al. (2006)	B1200	63	PE	Strip	CFRP	3000	1200	900	150	300	270	30	8x22
	B1800	91	PE					600					
Soliman et al. (2008)	A1	231	PE	Bar	CFRP	2600	800	686	200	300	265	25	19x19
	A2	231	PE					629					
	A3	235	PE					572					
	A4	255	PE					344					
Sharaky et al. (2014)	LB2C1	117.2	PE	Bar	CFRP	2400	800	200	160	280	244	36	16x16
	LB2G1	112	IC		GFRP								
Hosen et al. (2014)	NSM 1	80	Flexure	Bar	Steel	2000	650	50	125	250	220	30	9x9
	NSM 2	101.3											12x12
	NSM 3	114											18x18
Wu et al. (2013)	B11	256.7	CC	Bar	CFRP	1800	600	50	150	300	270	30	20x20
	B21	260.9	IC										
Bilotta et al. (2013)	NSM_c_2	32.51	CCD	Strip	CFRP	2100	925	100	120	160	115	30	5x15
	NSM_c_3	33.7	CCD										

Table 4.2: Reinforcement details of the beams used in the analysis.

Source	Specimen	Ten. steel area A_{st} , mm ²	Top steel area A_{sc} , mm ²	Comp. strength f'_c , MPa	Yield Str., $f_{y_{st}}$, MPa	Yield Str., $f_{y_{sc}}$, MPa	FRP Thck. /dia. t_p , mm	FRP area A_p , mm ²	FRP Mod. E_p , GPa	Adhesive Mod. E_a , GPa
Al-Mahmoud et al. (2010)	SC210	226.2	56.5	36.5	600	600	6	56.6	146	5
	SC270									
Khalifa (2016)	B-N-1-2	226.2	226.2	35	400	400	1.2	60	165	7*
	B-N-2-2							60		
	B-N-2-4							120		
Carolin (2003)	E3	402.1	402.1	64	515	515	10	200	230	7
	C3									
Teng et al. (2006)	B1200	226.2	100.5	42	532	375	4	64	151	2.6
	B1800									
Soliman et al. (2008)	A1	800	200	30	470	454	9.5	70.9	124	1.5
	A2									
	A3									
	A4									
Sharaky et al. (2014)	LB2C1	226.2	100.5	32	540	540	8	101	170	8
	LB2G1								65	
Hosen et al. (2014)	NSM 1	226.2	157.1	40	520	550	6	28.3	200	19
	NSM 2						8	50.3		
	NSM 3						10	113.1		
Wu et al. (2013)	B11	461.8	56.54	34.4	340	240	7.9	49.01	170	3.5
	B21							98.03		
Bilotta et al. (2013)	NSM_c_2	157.1	157.1	21	540	540	1.4	28	171	6
	NSM_c_3							42		

*assumed

4.3.1 A detailed Example of debonding load prediction for NSM beam

An example of predicting debonding load using the proposed model is shown for two beams; SC210 and SC270, tested by Al-Mahmoud et al. (2010) having similar materials, as well as geometric properties. For those beams, the FRP was curtailed at a distance of 350 mm and 50 mm from the support, respectively. Beam SC210 is reported to fail due to PE debonding, whereas beam SC270 failed due to IC debonding at the mid-section of the beam. Steps for debonding load prediction is shown in the following paragraphs, where all the values are taken from Tables (4.1) and (4.2).

- i. Determining the shear capacity of the beam according to ACI guideline:

Shear capacity of a beam contains two components: contribution from concrete and contribution from steel stirrup. Shear capacity of the beam due to concrete can be computed using the empirical relation provided by ACI-code (2008):

$$V_c = 2\sqrt{f'_c}bd = 36.9 \text{ kN} \quad (4.1)$$

The aforementioned beams are reinforced with 6 mm diameter stirrup @ 150 mm with a yield capacity of 400 MPa. The shear capacity of the beam due to stirrup can be computed using the following expression:

$$V_s = \frac{f_{vy}A_vd}{s} = 37.6 \text{ kN} \quad (4.2)$$

Where f_{vy} is the elastic modulus of the stirrup, A_v is the area of stirrup leg, and s is the spacing provided.

Therefore, the total shear capacity for the said beams is:

$$V_c + V_s = 36.9 + 37.6 \text{ kN} = 74.5 \text{ kN}$$

Hence, the maximum load that can be applied without shear failure:

$$P_{\text{shear_ACI}} = 74.5 * 2 = 149 \text{ kN.}$$

- ii. Failure load due to FRP rupture or concrete crushing or steel yielding.

The ultimate capacity (f_u) of FRP used in the strengthening of the beam is 1875 MPa.

$$\text{So, rupture strain of FRP} = \frac{f_u}{E_p} = 0.0128$$

E_p can be found from Table (4.2).

Using this value in Equations (3.28) and (3.29) the moment found is:

$$M_{\text{frp_rup}} = 5.6E4 \text{ kN.mm}$$

$$P_{\text{frp_rup}} = \frac{M_{\text{frp_rup}} * 2}{l_{\text{shear}}} = 140 \text{ kN} \quad (4.3)$$

Using Equations (3.28) and (3.29), the moment causing steel yield can be determined and the load causing steel yield can be determined.

$$M_{\text{steel_yield}} = 3.5E4 \text{ kN.mm}$$

$$\text{Load}_{\text{steel_yield}} = \frac{M_{\text{steel_yield}} * 2}{l_{\text{shear}}} = 87.5 \text{ kN} \quad (4.4)$$

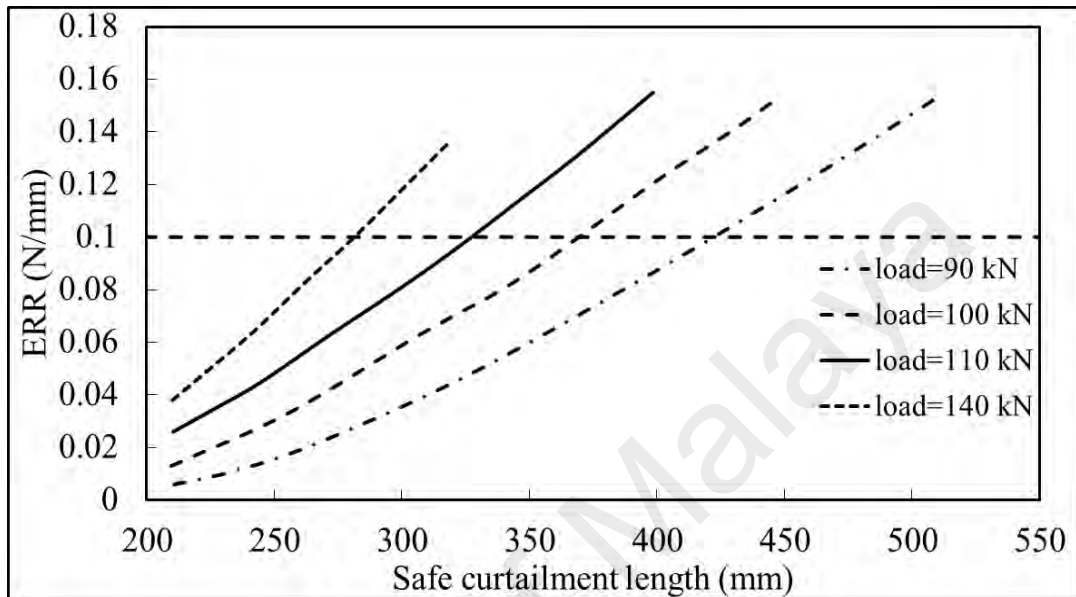
The strain at the top fiber of concrete at the load of 140 kN is equal to 0.002; which is less than the concrete crushing strain, 0.003 (determined from moment-curvature analysis)

Therefore, the chance of concrete crushing is not dominant at the load causing FRP-rupture. As a result of this, the possibility of concrete crushing can be excluded.

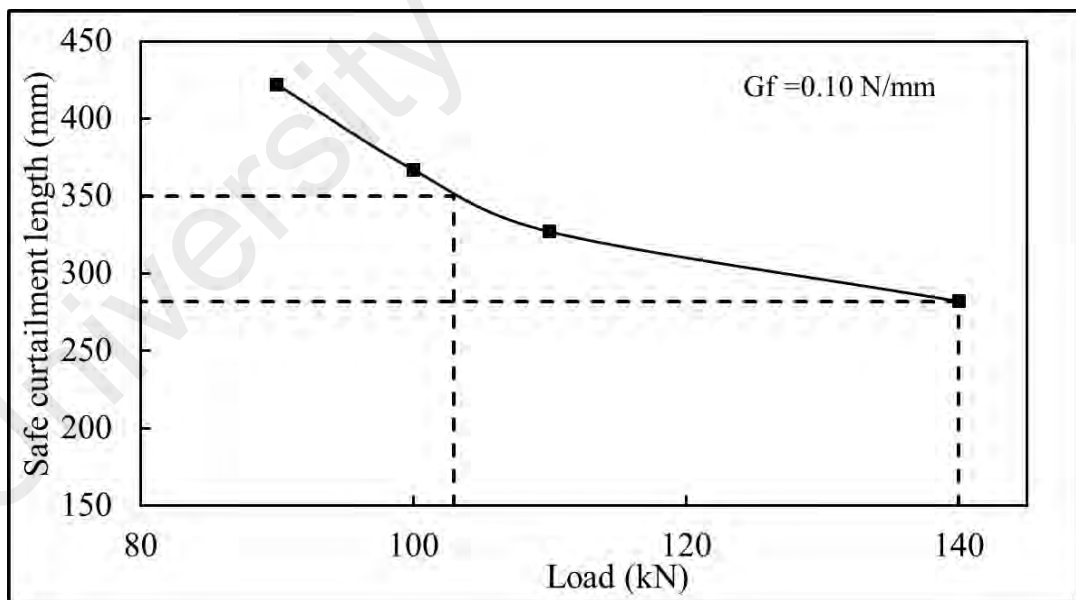
- iii. The next step is finding the load found from PE debonding analysis:

Figure 4.2a plots the ERR versus safe curtailment length found for PE debonding analysis for different loads. The plot has been presented as safe curtailment length versus load plot, as per Figure 4.2b for ERR equal to 0.10 N/mm, because in this case,

the critical fracture energy is 0.10 N/mm. The value of G_f can be determined using Equation (3.46), where the water-cement ratio is 0.62 and the aggregate size is 10 mm, as reported by the author for these particular beams.



(a) ERR versus Safe curtailment length



(b) Debonded zone length versus load

Figure 4.2: Plotting for the beam configuration by Al-Mahmoud et al. (2010)

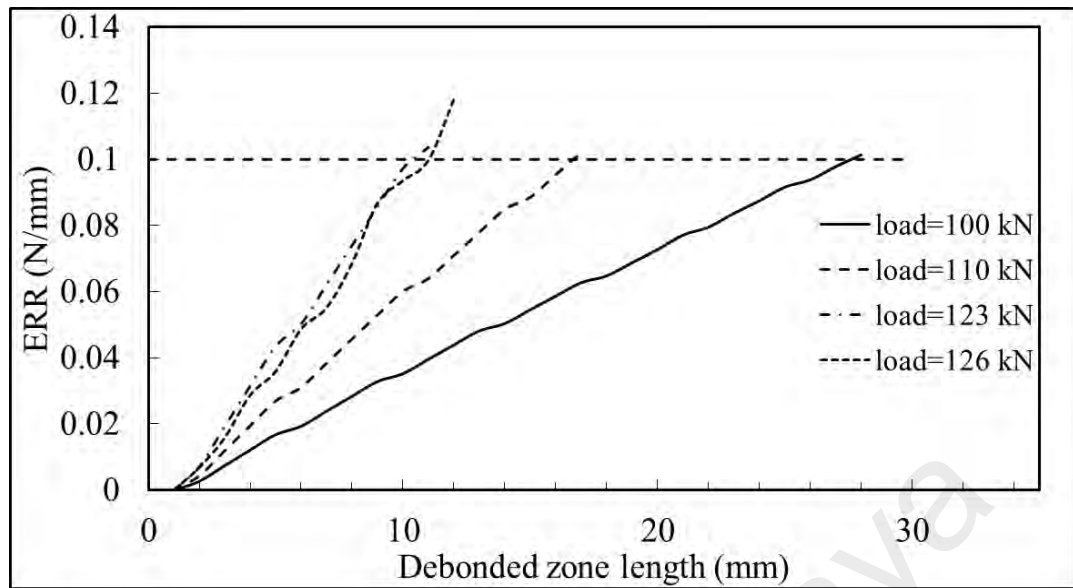
It can be seen from Figure 4.2b that, at a load of 103.5 kN, the beam reaches the value of critical energy at a distance of 350 mm. So, for beam SC210, the failure is expected to occur at a load of 103.5 kN (P_{PE}), since the provided curtailment location for this beam is 350 mm from the beam end.

Figure 4.2b also shows that the safe curtailment length is suggested to be 283 mm for the load of 140 kN (FRP rupture load). The provided curtailment location for the beam, SC270, is 50 mm, which is much less than the suggested length from the analysis at the expected rupture load. Therefore, it can be said that the end failure is not critical for beam SC270.

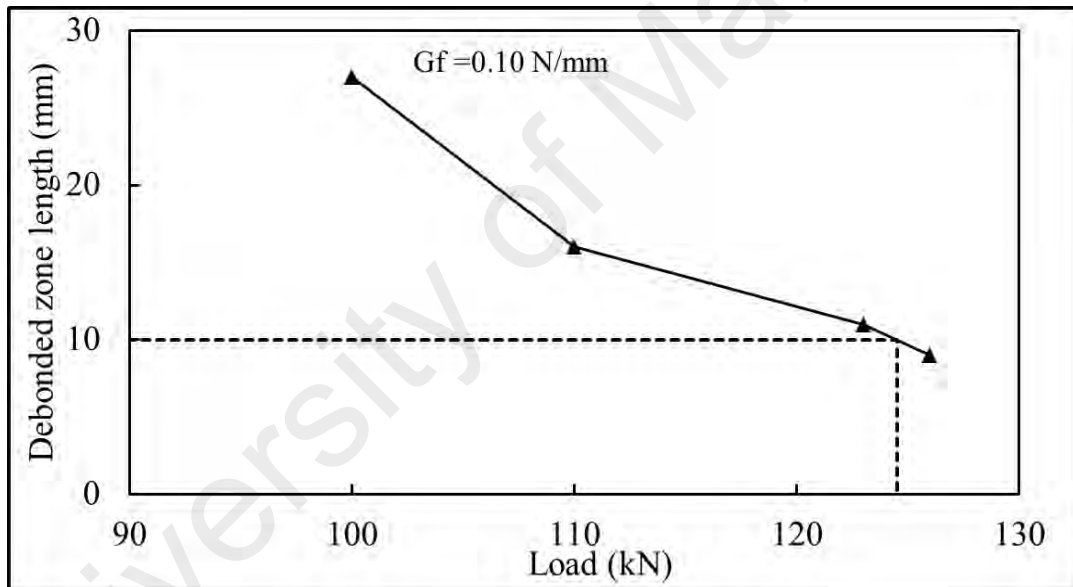
- iv. Since PE failure is not dominant, it is required to check whether or not there is a chance of IC debonding. Figure 4.3a shows a plot of ERR versus debonded zone length for IC debonding analysis. The plot has been presented in the form of debonded zone length versus load plot, as per Figure 4.3b, for ERR equals to the critical fracture energy of 0.10 N/mm. Figure 4.3b shows that the load causing IC debonding failure is 124.5 kN.

In the case of PE debonding, 103.5 kN load is required to cause failure for a safe curtailment length of 350 mm. So, as per the model, PE debonding failure will occur at a load of 103.5 kN for beam SC210. The load required to cause failure at a location of 50 mm is greater than the load causing FRP fracture i.e. 140 kN.

In the case of IC debonding, the beam fails by IC type failure for loads greater than 124.5 kN (P_{IC}) according to analysis. Therefore, according to the model, beam SC270 will fail at the load of 124.5 kN and the predicted failure type would be IC debonding.



(a) ERR versus debonded zone length



(b) Debonded zone length versus load

Figure 4.3: Plotting for the beam configuration by Al-Mahmoud et al. (2010)

From the previous discussions, it can be said that for these two beams (SC210 and SC270) tested by Al-Mahmoud et al. (2010), FRP rupture, and shear failure are not critical.

The validation shown in the following section utilizes the steps shown above for predicting the debonding load. Appendix C contains the energy release rate curve for different beams.

4.3.2 Study on different strengthening technique: EBR and NSM

The designed model has been employed to confirm its effectiveness in determining the IC debonding load for two beams strengthened using EBR and NSM techniques for sample B-S-2 and B-N-2-2, respectively (Khalifa (2016)). The debonded zone length versus load plots from GEBA model for these beams is shown in Figure 4.4 for a G_f value of 0.09 N/mm. It can be seen that the simulated failure load for B-S-2 is 65.6 kN, which is close to experimental failure load of 72.3 kN. It can be seen that the simulation result from the model is 10% lower than the experimental results. It should also be pointed out that the prediction of IC debonding is done for a debonded zone length of 10 mm, which provides a safe estimation. Therefore, it can be said that the model has the ability to predict the failure load for EBR strengthened beam quite efficiently with a safe margin. Contrarily, Figure 4.3 also shows that the estimated debonding load is 80.5 kN for B-N-2-2, which is equivalent to 88% of the reported experimental failure load of 91.6 kN.

The difference in NSM and EBR analysis is mainly the length of the transition zone and the width of fracture surface b_p , as per Equation (3.1). Therefore, from the analysis, it is obvious that the model can capture the IC debonding failure of the NSM strengthened beam with acceptable accuracy. Moreover, from the experimental results, it is obvious that for beams with the same configuration, the beam strengthened using NSM strengthening failed at a higher load than the beams strengthened using EBR technique, and the model also can simulate this phenomenon.

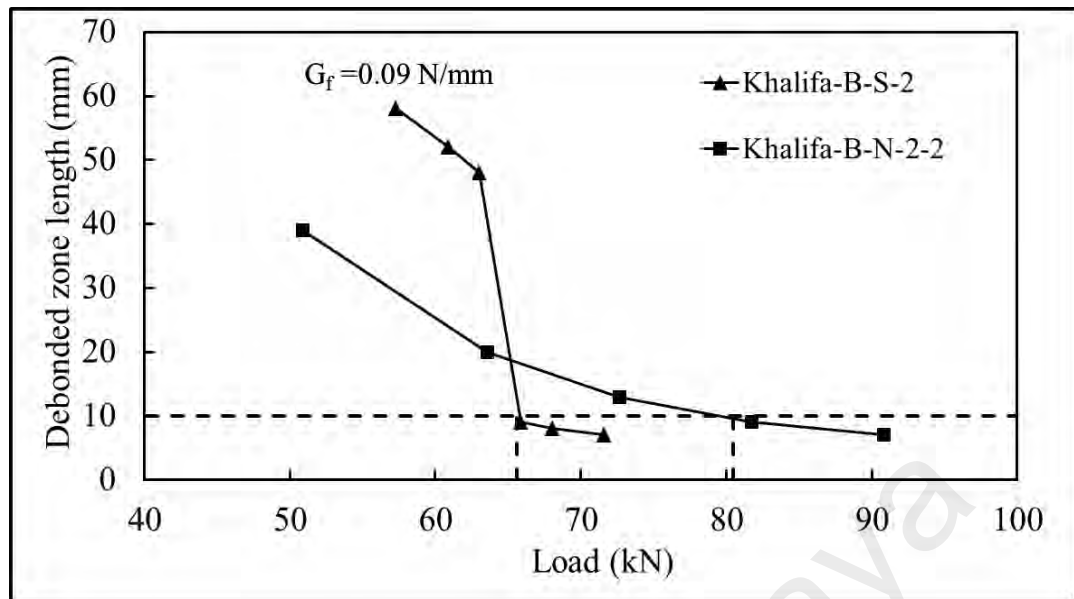


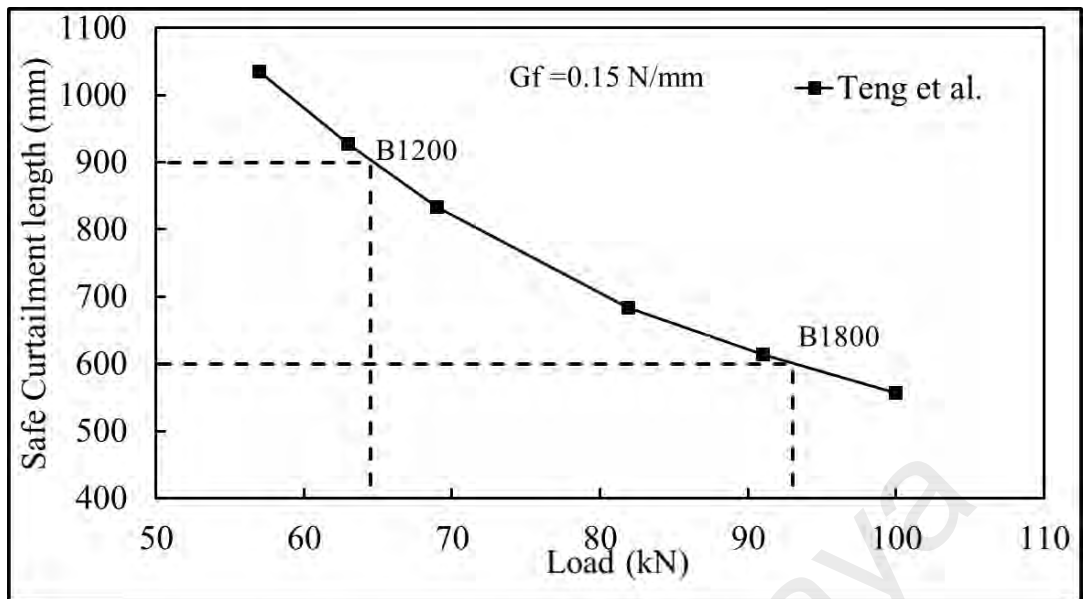
Figure 4.4: Debonded zone length versus load plot for beam tested Khalifa (2016)

4.3.3 Study on Beams with different NSM lengths

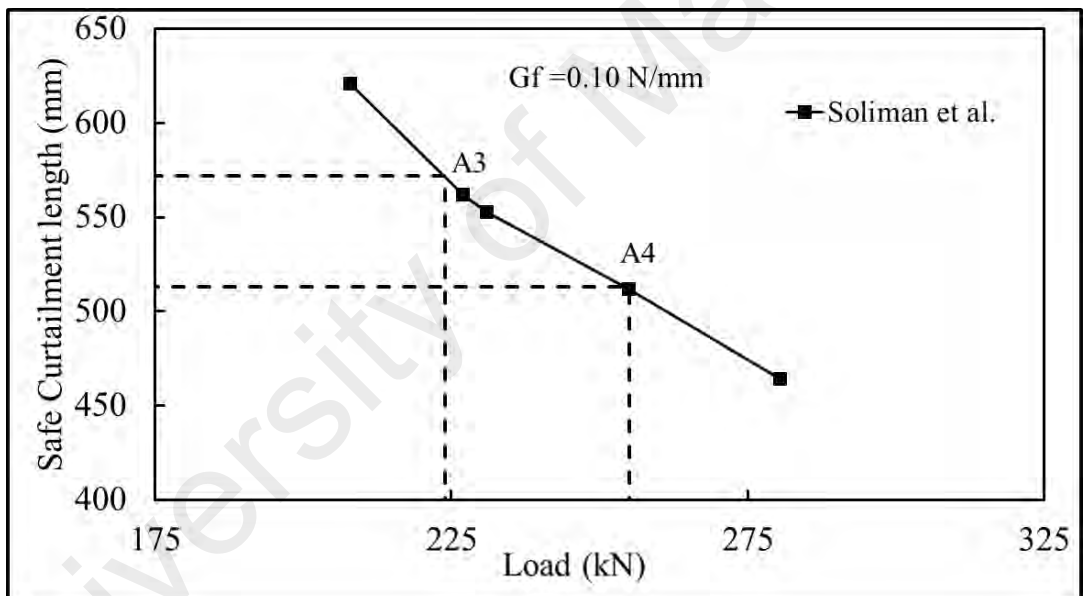
This section shows some analysis for the beams having different NSM length, but all the other properties remain similar. The beams considered for analysis are:

Two beams B1200 and B1800 tested by Teng et al.(2006) having a total FRP length of 1200 mm and 1800 mm, respectively.

Beam series 'A' tested by Soliman et al. (2010) with different FRP length are considered for analysis. The curtailment length for beam A1 to A4 measured from beam end are 686, 629, 572 and 344 mm, respectively, as tabulated in Table 4.1.



(a) B1200 and B1800 by Teng et al. (2006)



(b) A3 and A4 by Soliman et al. (2010)

Figure 4.5: Safe curtailment length versus load plot

Figure 4.5a shows the graphical representation of safe curtailment length versus load found from the GEBA simulation for the beam tested by Teng et al.(2006). It can be seen from Figure 4.5a that, the failure load corresponding to the provided curtailment length for beam B1200 is 64.5kN, which is very close to the experimental value of 63 kN. On the other hand, the failure load corresponding to the safe curtailment length for B1800 is 93 kN, which is also very close to the experimental value of 91 kN. It can be

seen that simulation results are 2% higher than the experimental results for both the beams B1200 and B1800. Hence, it can be said that the proposed model can predict the debonding load for end debonding quite efficiently in this case.

Interestingly, in the case of the beams tested by Soliman et al. (2010), three tested beams of the series A1, A2, and A3 failed pretty much around the same failure load though the FRP length is different. The beams are designed to fail at the NSM end location by providing FRP bonding at the shear span only. Therefore, there is no chance of IC debonding or FRP rupture. According to the analysis, for beams A1 and A2, PE debonding and shear failure are not critical, so both will fail via steel yielding at the mid-span, which can be easily computed from the moment-curvature analysis.

Safe curtailment length versus load for beams A3 and A4, found from the simulation, are presented in Figure 4.5b. Figure 4.5b shows that the simulated failure load corresponding to the given curtailment length for beam A3 is 224 kN, which is quite close to the reported experimental failure load of 231.kN. It can be seen that the simulation result of the model is 3% less than the experimental result for beam A3. However, Figure 4.5b shows that for beam A4, the simulated failure load is 255 kN, which implies the safe curtailment length would be 513 mm. However, the safe curtailment length provided in the experiment is 344 mm. It indicates the availability of insufficient energy at the curtailment location to trigger debonding. As a result of this, there is less chance of PE failure according to the analysis. It should be mentioned here that for strengthened beam configuration the shear capacity, as per ACI code (2008), exceeds the shear load of the strengthened beam A4 at the load of 270 kN, which is 5% higher than the reported failure load of 255 kN for A4. Therefore, according to the analysis, beam A4 actually failed due to the insufficient shear capacity of the beam.

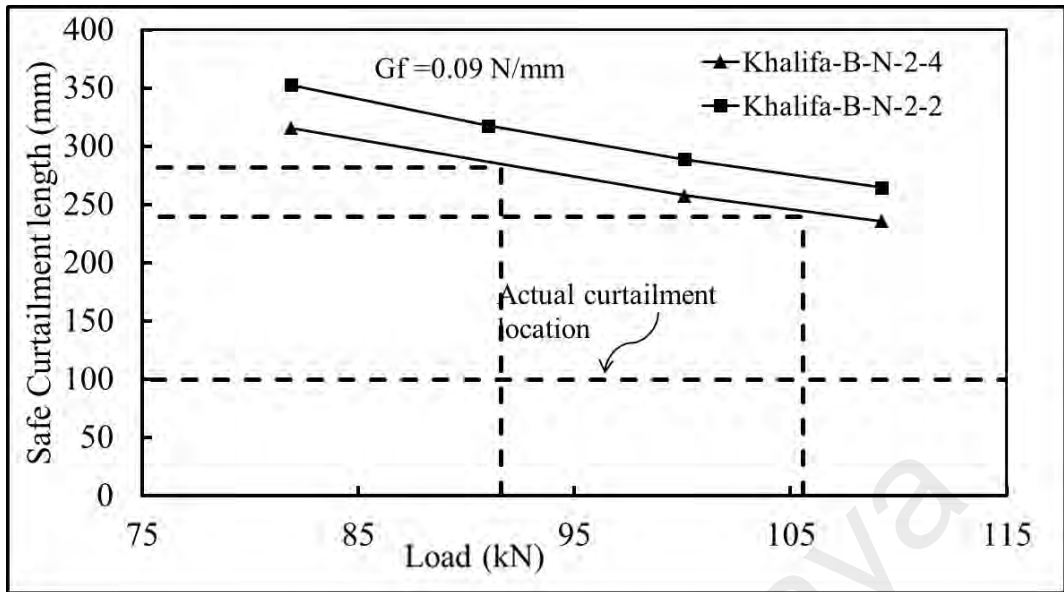
It can be concluded from the analysis that the NSM end location has to be extended more towards the beam's end to increase the load carrying capacity of the beam, and this is obvious both in the experiment as well as the simulation.

4.3.4 Study on beams with different reinforcement percentages

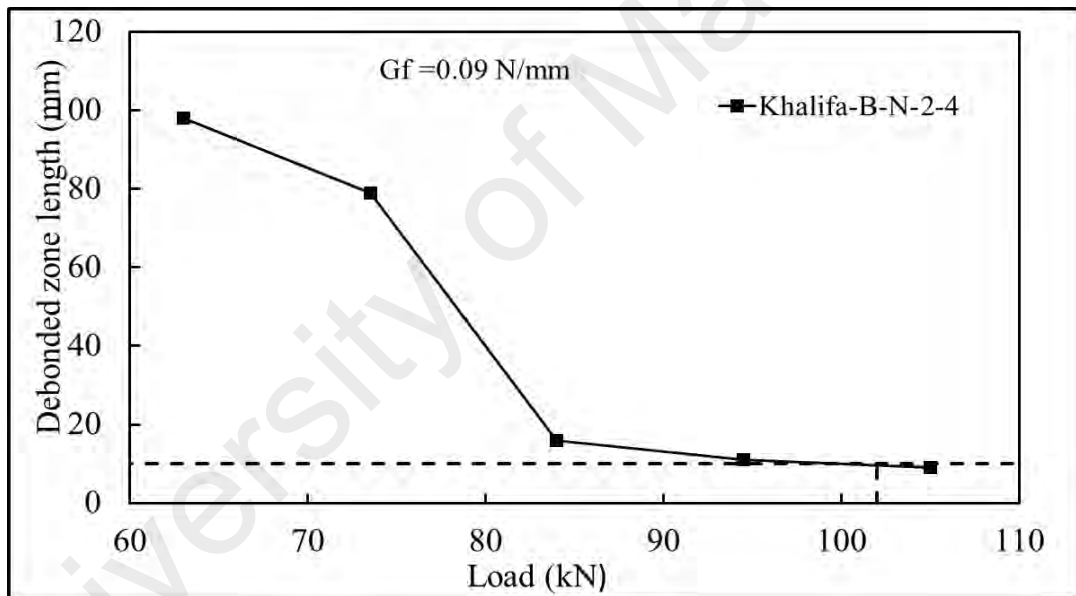
This section shows some analysis for the beams, tested by various researchers, having different reinforcement percentage, but all the other properties remain similar.

Khalifa et al. (2016) reported two beams; namely: B-N-2-2 and B-N-2-4, with different reinforcement percentages. It has already been pointed out that beam B-N-2-2 failed in IC debonding. However, beam B-N-2-4 failed due to peeling, as per Khalifa et al. (2016). However, the authors did not mention whether the peeling starts from the beam end or from the midspan. Hence, an investigation is carried out to determine the chance of PE debonding for both beams. Figure 4.6a shows the safe curtailment length versus load for the beams B-N-2-2 and B-N-2-4 found from the end debonding simulation. As seen from the figure, the curtailment length is suggested to be 282 mm and 240 mm at the reported failure loads of B-N-2-2 and B-N-2-4, respectively. These are pretty large than the actual curtailment location of 100 mm, as shown in the figure. So, the end failure is not critical for these two beams, according to GEBA analysis.

Figure 4.6b shows the debonded zone length versus load found from simulation for beam B-N-2-4 for IC debonding. It can be seen from Figure 4.6b that the simulated failure load in the case of IC debonding is 102 kN for beam B-N-2-4, which is very close to the experimental failure load of 105.6 kN. The simulated result is only 3% less than the experimental result.



(a) Safe curtailment length versus load plot for beam B-N-2-2 and B-N-2-4



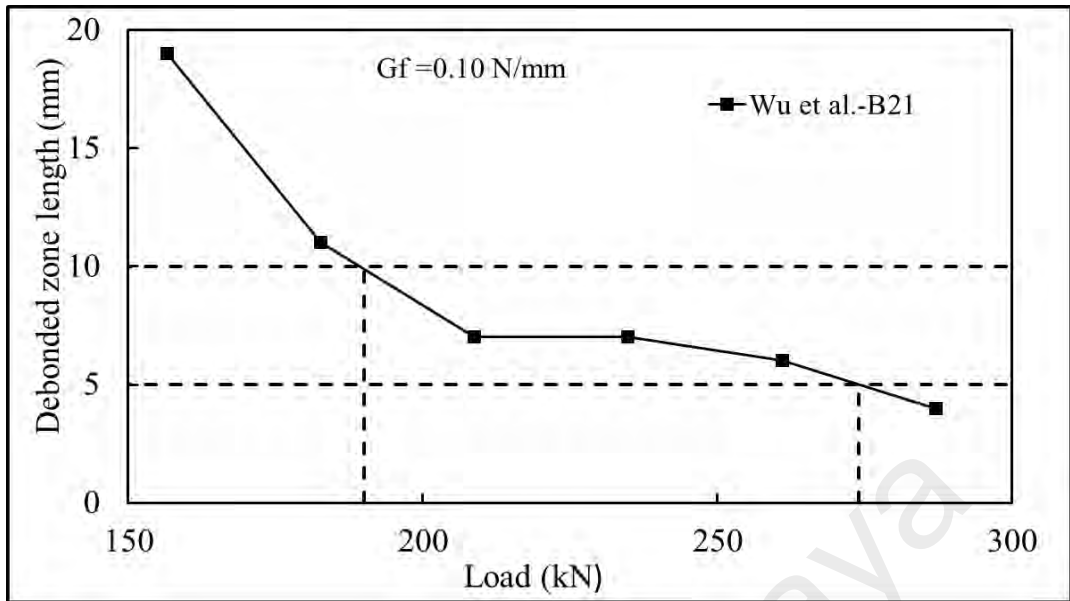
(b) Debonded zone length versus load plot for beam B-N-2-4

Figure 4.6: Plotting of simulation results for beams tested by Khalifa (2016)

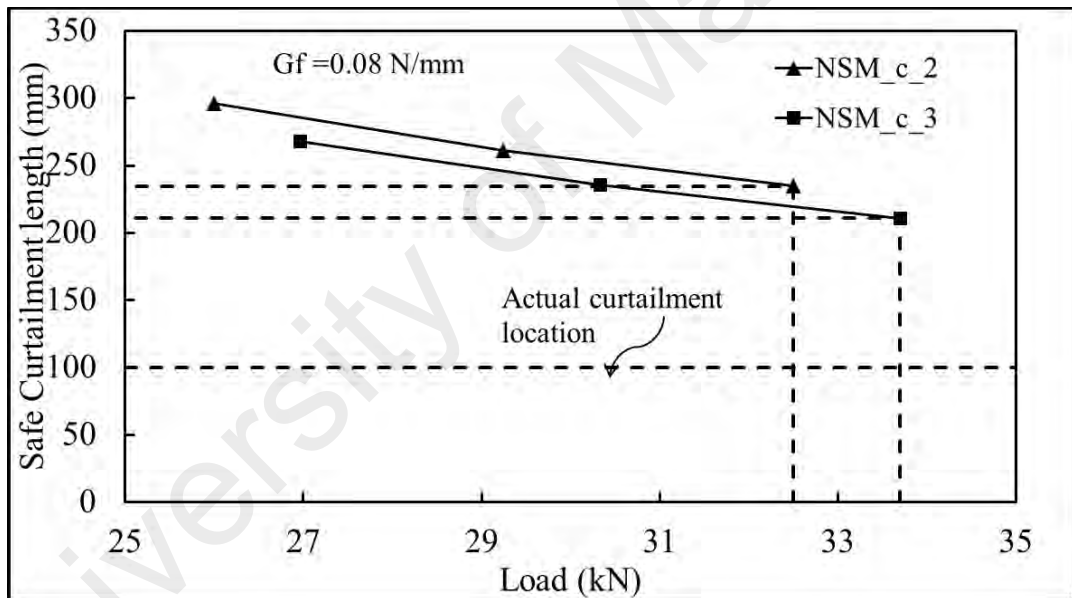
Two NSM strengthened beams, tested by Wu et al. (2013) with different reinforcement percentages are used for simulation. The beam with less reinforcement, B11, shows concrete compression type failure during the experiment, which is also confirmed by the GEBA simulation. The NSM end debonding analysis using GEBA model is conducted for both beams, and it shows that the ERR at the NSM end location is low at the reported failure load to trigger debonding. On the other hand, the

experimental failure mode of beam B21, with a reinforcement ratio twice higher than B11 is IC debonding. The debonded zone length versus load of the beam B21 found from the simulation is shown in Figure 4.7, which shows that the failure load is 190 kN. However, Wu et al. (2013) reported that the failure load for the beam B21 is 260.9 kN, which means that the simulation result is 28% less than the experimental result. It should be mentioned here that the selected failure criterion for IC debonding in GEBA analysis (debonded zone length of 10 mm at the critical fracture energy) is supposed to provide a safe estimation. This may be the reason of this scatter between simulation and reported failure load. For example, it is obvious from Figure 4.7a that if the critical debonded zone length is assumed to be 5 mm, then the failure load would be 274 kN, which is 4% higher than the reported experimental value. It can be seen that in this case, the model would overestimate the failure load. Based on this observation, the debonded zone length of 10 mm is proposed as the failure criteria in this thesis to provide a safe prediction, however, in some cases; this margin of safety is too high.

Another two beams; NSM_c_2 and NSM_c_3, strengthened using NSM CFRP strip, was tested by Bilotta et al. (2015), and is included in this section for comparison purposes. The reinforcement ratios for these two beams differ. Both of the beams NSM_c_2 and NSM_c_3 experienced critical diagonal crack debonding, starting at the NSM end. An investigation is carried out to check the chance of PE debonding for both beams. Figure 4.6b shows the safe curtailment length versus load for the beams NSM_c_2 and NSM_c_3 found from the end debonding simulation. As seen from the figure, the curtailment length is suggested to be 235 mm and 211 mm at the reported failure loads of NSM_c_2 and NSM_c_3, respectively. These are larger than the actual curtailment location of 100 mm, as seen in the figure. Therefore, end failure is not critical for both beams according to the GEBA analysis.



(a) Debonded zone length versus load plot for beam B21 by Wu et al. (2013)



(b) Safe curtailment length versus load plot for beam NSM_c_2 and NSM_c_3 by Billotta et al. (2015)

Figure 4.7: Plotting of simulation results for beams tested with different FRP percentage

The shear analysis, as per Equations (4.1) and (4.2), according to the ACI code (2008), agrees with the experimental finding. According to ACI code (2008), the shear stress caused by the failure load is greater than the shear capacity of the beam. Hence, shear failure is obvious for beams NSM_c_2 and NSM_c_3.

It should be noted that in the case of Wu et al. (2013) and Bilotta et al. (2015), the reinforcement is increased ~ 2 and 1.6 times, respectively, but no significant changes occur in the ultimate load capacity. Therefore, increasing steel ratio does not guarantee increasing load capacity, and the model can also effectively capture this phenomenon.

Three beams tested by Hosen et al (2014), strengthened using steel have been included in this section to confirm the usefulness of the model for steel. The beams tested by Hosen et al. (2014) were identical, except for the diameter of the strengthening bar i.e. the reinforcement ratio. Figure 4.8 shows a graphical representation of simulation results from the model i.e. the safe curtailment length versus load with respect to the assumed G_f (0.10 N/mm) for beams NSM 1, NSM2 and NSM 3 tested by Hosen et al. (2014). It can be seen from Figure 4.8 that the safe curtailment length found from GEBA analysis for the reported failure load are 435 mm, 260 mm, and 135 mm, respectively, for NSM1, NSM2, and NSM3. These are much higher than the actual curtailment location of 75 mm. So, according to the analysis, PE failure is not critical for these beams. Shear reinforcement is also adequate to prevent shear failure. These beams will fail by yielding of strengthening steel, which agrees with the experimental observation. Normal flexure failure due to yielding of strengthening steel was reported for those beams, and the reported failure load is close to the steel yield loading, computed using Equation (4.4).

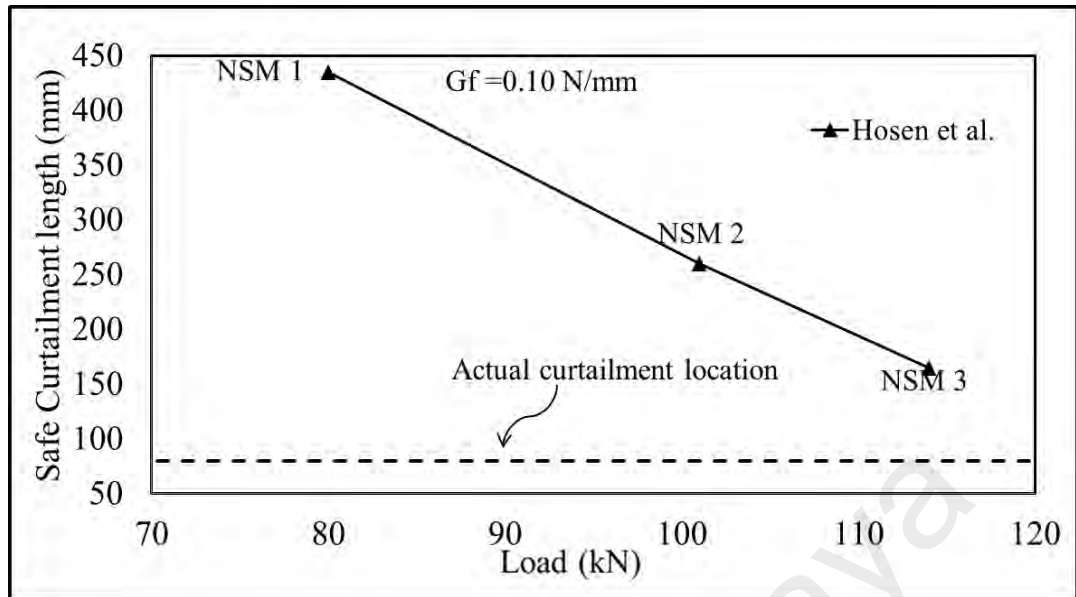


Figure 4.8: Safe curtailment length versus load plot for beams NSM 1, NSM2 and NSM 3 by Hosen et al. (2014)

4.3.5 Study on beams with different adhesive properties

Caroline (2003) tested two beams with the same configuration but with dissimilar adhesive properties. Beams E3 and C3 were tested using epoxy and cement paste as the adhesive, respectively. Figure 4.9 shows the plotting of the model results of safe curtailment length versus load for beams E3 and C3, and this figure can help determine the safe NSM length that can be used in practice. It is obvious from the figure that for beam E3, the failure occurs at a load of 145 kN, which is 3% higher than the reported load of 140 kN. However, for beam C3, the simulated failure load is 150kN, which is ~20 % higher than the reported experimental load of 123.5 kN. This is probably due to the cement paste adhesive for beam C3, and the model does not consider stiffer adhesive such as cement paste. However, for beam E3, the adhesive is epoxy, and the prediction is quite reasonable. Hence, it can be said that the proposed GEBA model is applicable for only epoxy type adhesive.

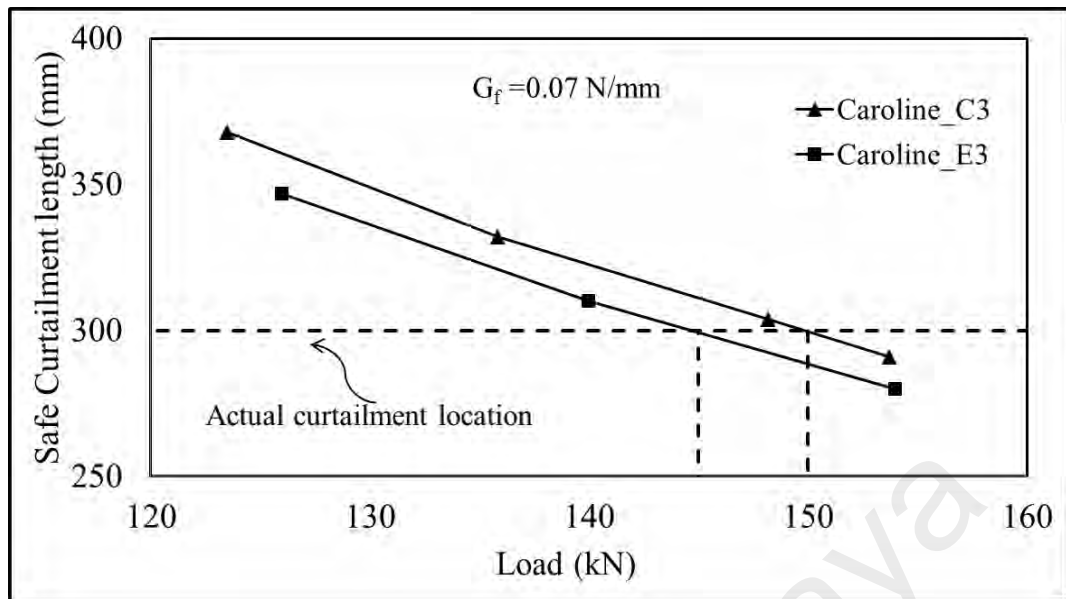


Figure 4.9: Safe curtailment length versus load plot for beam E3 and Beam C3 by Caroline (2003)

4.3.6 Study on beams with different strengthening materials

The efficiency of two different strengthening materials, namely CFRP (beam named LB2C1) and GFRP (beam name LB2G1), had been investigated by Sharaky et al. (2014). Beam LB2C1 shows the PE type of failure at the load of 129 kN, which is 10% greater than the experimental failure load of 117.2 kN. The safe curtailment length versus load plot for the beam is shown in Figure 4.10. The other beam LB2G1 had the same property as the beam LB2C1 except for the use of low modulus GFRP rod instead of the CFRP. The failure type reported for that beam was not PE, rather it was FRP rupture failure though the curtailment length provided is similar for both beams. The failure load due to the FRP-rupture can be computed using Equation (4.3), and it is found to be 119.1 kN, which 6% higher than the reported failure load of 112 kN.

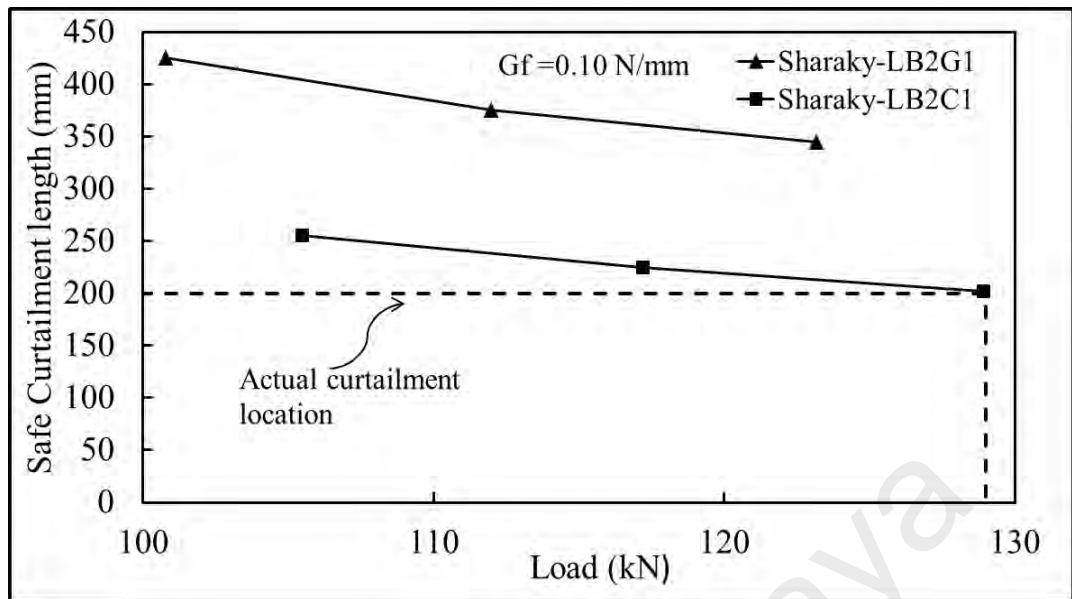


Figure 4.10: Safe curtailment length versus load plot for beam configuration of Sharaky et al. (2014)

This phenomenon could be explained from the safe curtailment length versus load in Figure 4.10, where it is clearly evident that the curtailment length at the reported failure load is quite large for LB2G1, which means insufficient energy is available to trigger debonding at the actual NSM curtailment location. Another point that should be outlined is that beam LB2G1 did not fail at the NSM cut-off location though the modulus is lower than the beam LB2C1. This confirms the assumption of higher peeling stress developed at that location due to high modulus for beam LB2C1, which causes the end peeling. Therefore, the model can also effectively capture the change in elastic modulus.

4.4 Validation of test beams for Hybrid strengthened beam

The material and geometric properties of the beams validated using the model for hybrid beams are tabulated in Table 4.3 and Table 4.4. Very few data are available for beams strengthened using the combination of NSM and EBR technique i.e. hybrid technique. The beams selected for simulation are strengthened using both steel and CFRP material.

Table 4.3 Identification and geometric data of the Hybrid beams used in the analysis

Source	Sample	Failure load P_f (kN)	Material	Failure mode	Total span l_{span} , mm	Shear span l_{shear} , mm	Unsupport ed len. L_o , mm	Wid. b, mm	Ht. h, mm	Eff. Dep. d, mm	Eff. Dep. d_c , mm
Jumaat et al.(2016)	CBC10P2	87	CFRP	IC	3000	1250	50	125	250	215	35
Rahman et al. (2015)	HS1	132	Steel	PE+ shear	2000	650	50	125	250	215	35
	HS2	105.6					175				
	HS3	102					175				
	HS5	109					50				
	HS6	130					50				

Table 4.4: Reinforcement Details of the beams used in the analysis.

Source	Sample	Area of tension steel A_{st} , mm^2	Area of top steel A_{sc} , mm^2	Yield of tension steel f_{y_s} , MPa	Yield of top steel $f_{y_{sp}}$, MPa	Comp. str of conc. f'_c , MPa	Thc. of EBR FRP t_p , mm	Area of EBR FRP A_p , mm^2	Dia. of NSM FRP t_p , mm	Area of NSM FRP A_p , mm^2	Mod. of FRP E_p , (EBR) GPa	Mod. of FRP E_p , (NSM) GPa
Jumaat et al.(2016)	CBC10P2	226.2	157	529	521	50.1	0.17	42.5	10	78.5	230	165
Rahman et al. (2015)	HS1	226.2	-	551	-	30	2	146	8	50.3	200	2001
	HS2								8			
	HS3								6	28.3		
	HS5								6	56.6		
	HS6							209.8	6	56.5		

bg

4.4.1 Study on hybrid beam with steel as strengthening material

Beam HS1 tested by Rahman et al. (2015) was reported to fail by PE debonding, followed by shear failure. The simulation result of the safe curtailment length versus load for the beam HS1 is shown in Figure 4.11. According to the simulation results in Figure 4.11, at an experimental failure load of 132 kN, the suggested curtailment length is 92 mm, which is higher than the actual curtailment length of 50 mm. Therefore, the beam will not fail due to PE debonding, according to the analysis. Rather, the simulated failure load is found to be 140 kN, using Equations (4.1) and (4.2), which is 5% higher than the reported experimental load. Therefore, according to the analysis, the beam failed due to shear. Results of few other beams are also shown in Table 4.11.

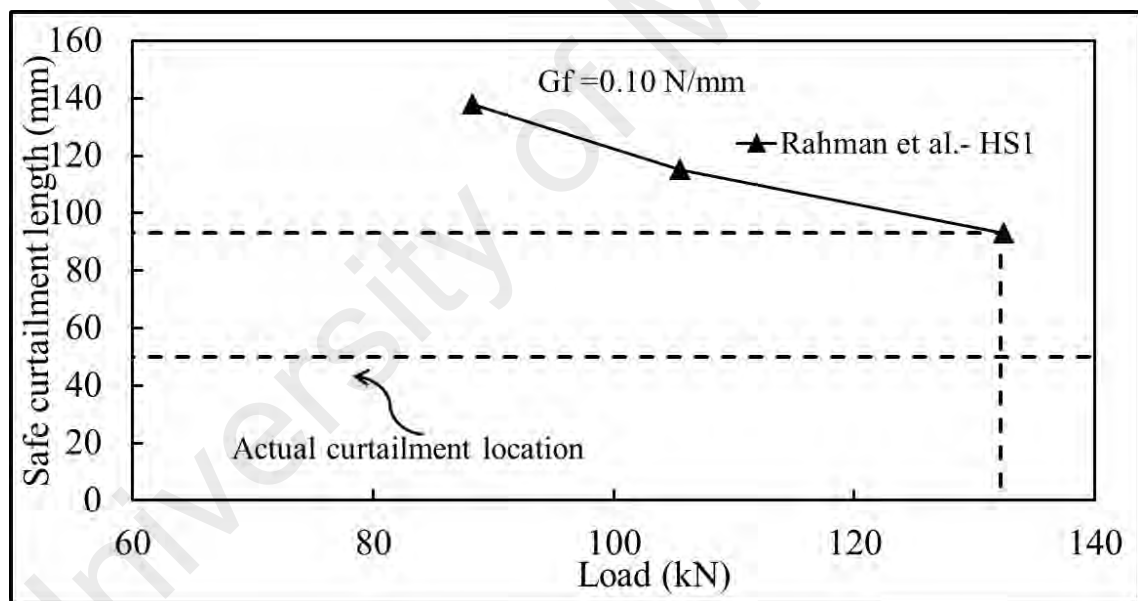


Figure 4.11: Safe curtailment length versus load plot for hybrid beam HS1 tested by Rahman et al. (2015)

4.4.2 Study on hybrid beam with CFRP as strengthening material

Beam CBC10P2 tested by Jumaat et al. (2016) exhibit IC debonding. The debonded zone length versus load reported by the simulation result is shown in Figure 4.12, which reveals that the predicted failure load from the simulation of the GEBA model is 69.6 kN. The simulation result is 80% of the reported failure load, which is 87 kN. This

underestimation of the failure load is possibly due to the chosen failure criterion, which will provide a safe prediction, which has already been discussed previously.

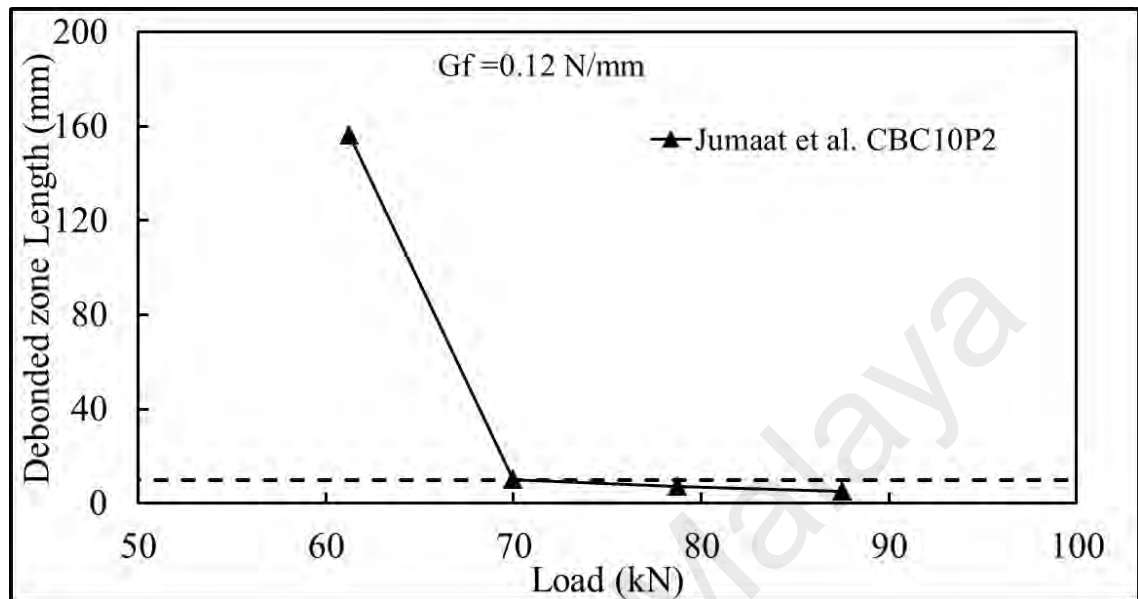


Figure 4.12: Debonded zone length versus load plot for beam CBC10P2 by Jumaat et al. (2016)

4.5 Validation of beams precracked before strengthening

Several precracked beams are validated to confirm the efficiency of the model. Only beams strengthened using the EBR technique are available in literature, so this type of beams are considered for validation. As a result of this, it is not possible to investigate the applicability of the model for precracked beams with NSM strengthening. The precracking level varies between 15 to 100% for the beams, which are selected for validation. This percentage refers to the ratio of the load applied to the beam prior to strengthening and the flexural capacity of the beam.

The geometric and material properties of the validated precracked beams are tabulated in Table 4.5 and Table 4.6. It was pointed out that the effect of precracking is more prominent in beams with precracking greater than 80%, as per literature and as discussed in Chapter 2. The presentation of the analysis of precracked beams is divided into subsections based on the percentages of precracking.

Table 4.5: Beam property for precracked beams failed due to IC debonding

Source	Specimen	Failure load (kN)	Failure mode	Precrack (%)	Material	Total Span l_{span} , mm	Shear span l_{shear} , mm	Unsupported len., L_o , mm	Wid. b, mm	Ht. h, mm	Eff. Dep. d, mm
Wu et al. (2007)	3-C1-40	90.6	IC	40	CFRP strip	1800	900	50	150	200	160
	3-C1-60	87.8	IC	60							
Al-Zaid et al. (2014)	B-0.3-0.5	177	IC	50	CFRP Plate	5000	2000	100	500	250	215
	B-0.6-0.9	233	IC	90							
Dong (2003)	B1	148.2	PE	20	CFRP	2896	991	381	152.4	304.8	253
	B2	157.9	PE	20				305			
	B3	189.1	IC	15				76			
Matthys (2000)	BF4	372	IC	60	CFRP strip	3800	1250	75	200	450	409
Sharif et al. (1994)	P2	68	IC	60	GFRP	1180	393	75	150	150	114
	P3	66	IC								
Arduini & Nanni (1997)	SM3	112	IC	30	CFRP	1100	420	50	320	160	110
Gunes et al. (2009)	S1PF1M	131.9	IC	75	CFRP plate	1300	450	50	150	180	150
	S2PF7M	148.3	IC								

Table 4.6: Reinforcement details for precracked beams failed due to IC debonding

Source	Specimen	Ten. Steel Area A_{st} , mm ²	Com. Steel Area A_{sc} , mm ²	Comp. str. f'_c , MPa	Yield Str. f_{y_s} , MPa	FRP Thck /dia. t_p , mm	FRP area A_p , mm ²	FRP mod. E_p , GPa
Wu et al. (2007)	3-C1-40	265.5	265.5	50.3	358	0.11	49.5	230
	3-C1-60						49.5	
Al-Zaid et al. (2014)	B-0.3-0.5	804.3	452.4	30	562	1.4	336	165
	B-0.6-0.9						480	
Dong (2003)	B1	402.1	141.8	38.2	410	1.11	152.4	73.1
	B2							
	B3							
Matthys (2000)	BF4	804.2	402.1	35	590	1.2	120	159
Sharif et al. (1994)	P2	157.1	56.5	37.7	450	2	200	14
	P3					3	300	
Arduini & Nanni (1997)	SM3	226.2	226.2	36	550	0.17	51	235
Gunes et al. (2009)	S1PF1M	397.1	141.8	41.4	440	1.2	45.6	165
	S2PF7M							

4.5.1 Study on beams with precracking beyond 80 %

Figure 4.13 shows a beam tested by Zaid et al. (2014), with 90% precracking and simulation reveals that the predicted load is 229 kN, which is 2% lower than the reported failure load of 233 kN.

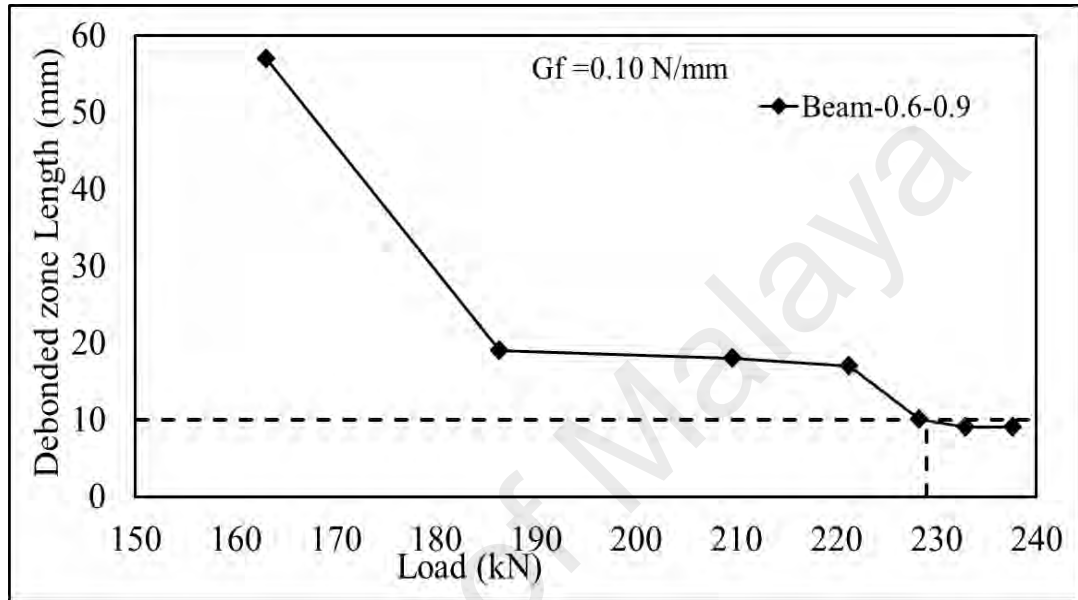


Figure 4.13: Plotting of debonded zone length versus load plot for beams by Zaid et al. (2014)

Sharif et al. (1994) reported PE debonding for beams FP2 and FP3, however, the ERR calculation at the plate end location shows that for these beams, the value of critical ERR is low for triggering debonding. The failure mode is not PE debonding, as per this analysis. The failure trend seems to be IC debonding, which is also confirmed by GEBA analysis, where the small critical flaw can trigger debonding close to the reported failure load, as shown in Figure 4.14. The figure shows that IC debonding is taking place for both beams at 89% of the reported failure load. The beam is analyzed without this cracking effect as well, but no significant changes are detected because, in this test program, the FRP used for strengthening was low strength FRP with a modulus of elasticity of $\sim 15 \text{ GPa}$.

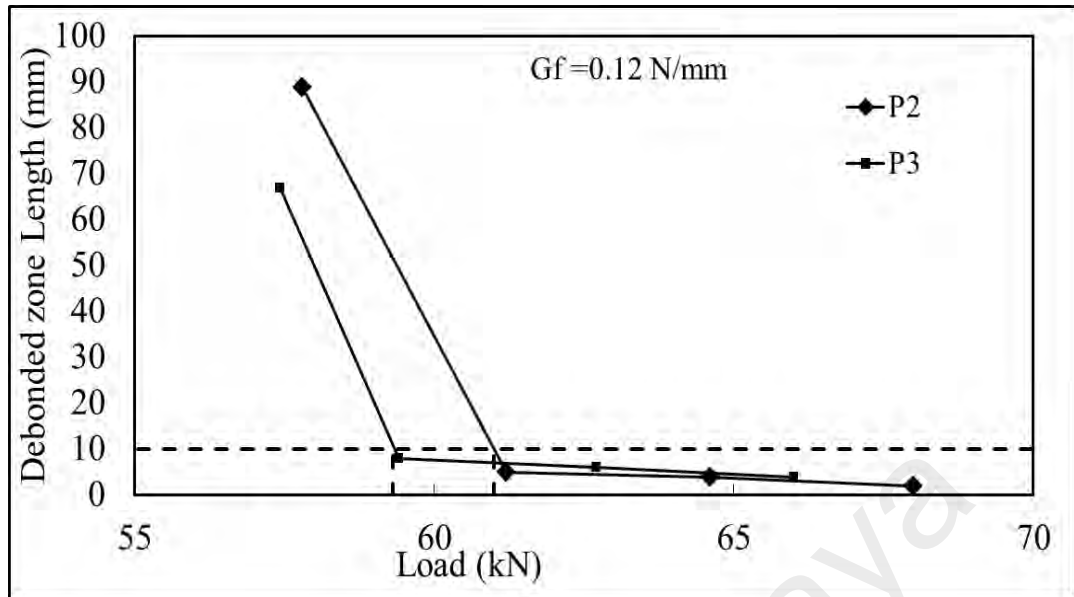


Figure 4.14: Plotting of debonded zone length versus load plot for beams tested by Sharif et al. (Sharif et al., 1994)

From the discussion and analysis in this section, it can be said that the proposed GEBA model can predict the failure due to IC debonding for highly damaged beams prior to strengthening efficiently.

4.5.2 Study on beams with precracking less than or equal to 80%

This section illustrates the debonded zone length versus load plot for some of the beams that were preloaded with a precracking force of less than 80% of the yield capacity of the unstrengthened beam.

Two beams at 40% and 60% precracking was tested by Wu et al. (2007). The beams were simulated to estimate the debonding load, and the simulation results are shown in Figure 4.15. It is clearly evident from Figure 4.15 that the predicted failure load from the analysis is 83 kN and 80 kN for the beams, which is 99% and 95% of the reported failure loads, respectively.

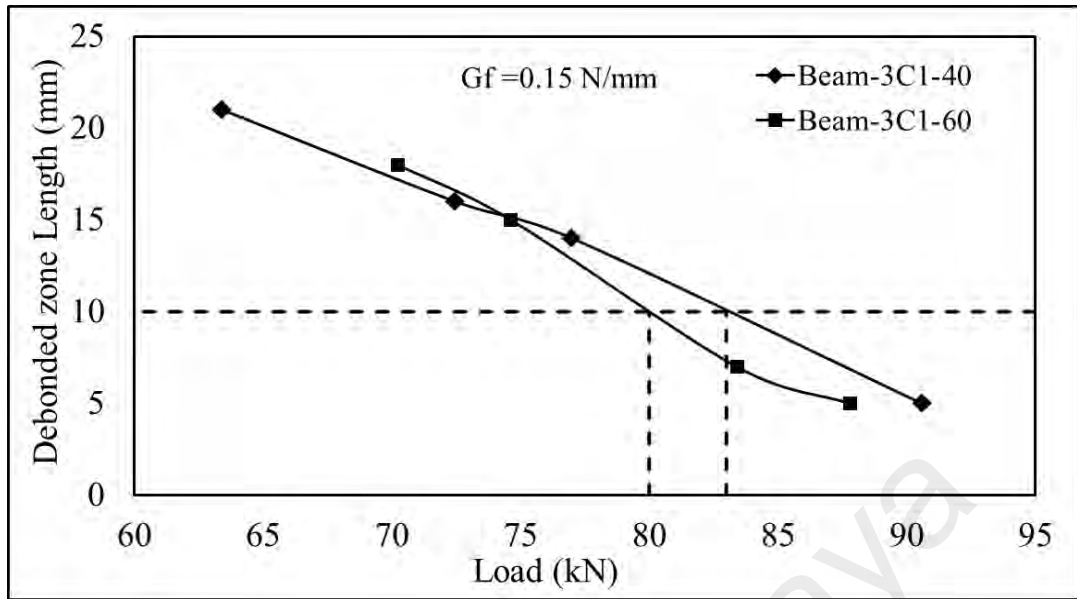
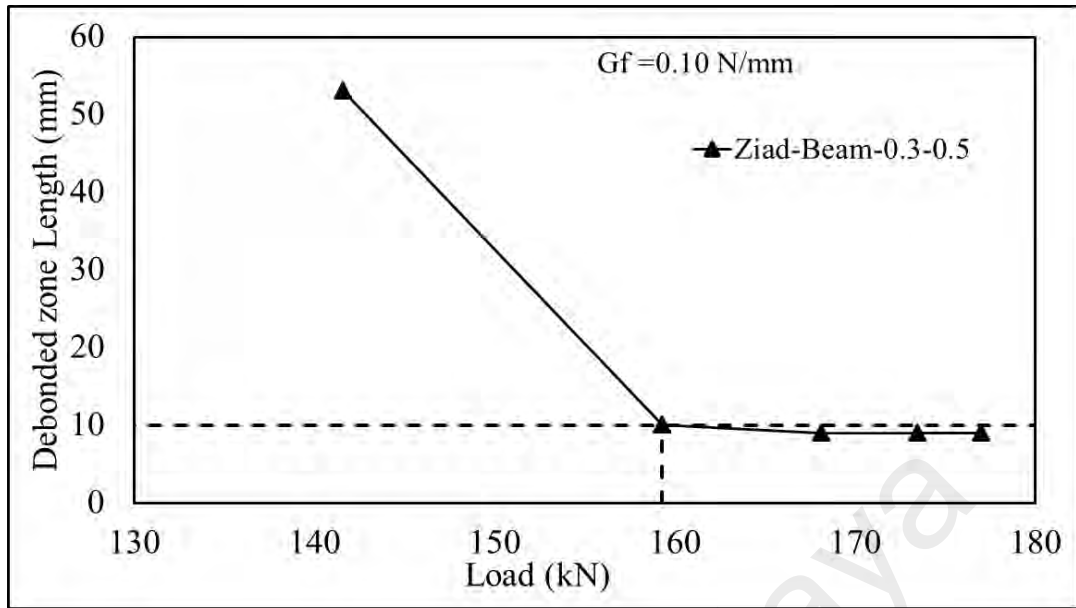


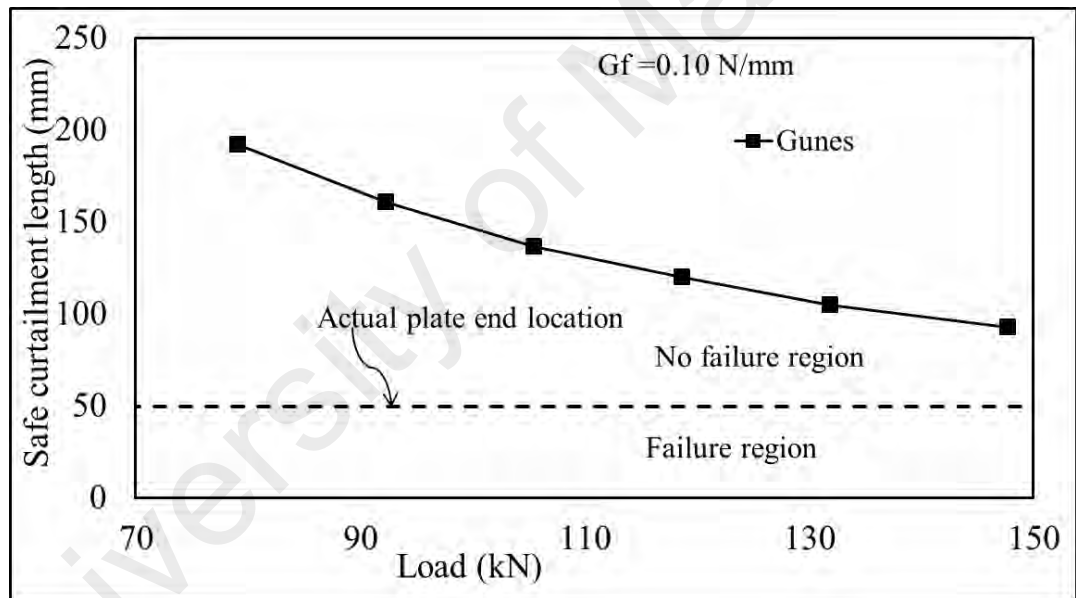
Figure 4.15: Plotting of debonded zone length versus load for beams by Wu et al. (2007)

Zaid et al. (2014) tested precracked beams with different precracking levels. The beams tested by Zaid et al. (2014) are simulated, and Figure 4.16a shows the results. It is evident from Figure 4.16a that for the beam at 50% precracking, the predicted load is 159.3 kN, which is equivalent to 90% of the reported experimental failure load of 177 kN.

Beam S2PF7M tested by Gunes et al. (2009) is simulated in this work. The authors reported that the beam failed by IC type debonding. PE debonding simulation for the beam configuration shows that the ERR near plate end location is pretty low, as per Figure 4.16b. Therefore, according to the simulation results, the interface flaw developed at the curtailment location is incapable of triggering PE debonding. On the other hand, Figure 4.16c shows the debonded zone length versus load plot from the IC debonding analysis for the same beam configuration and confirms that the predicted load is 127.5 kN which is 86% of the experimental failure load of 131.9 kN.

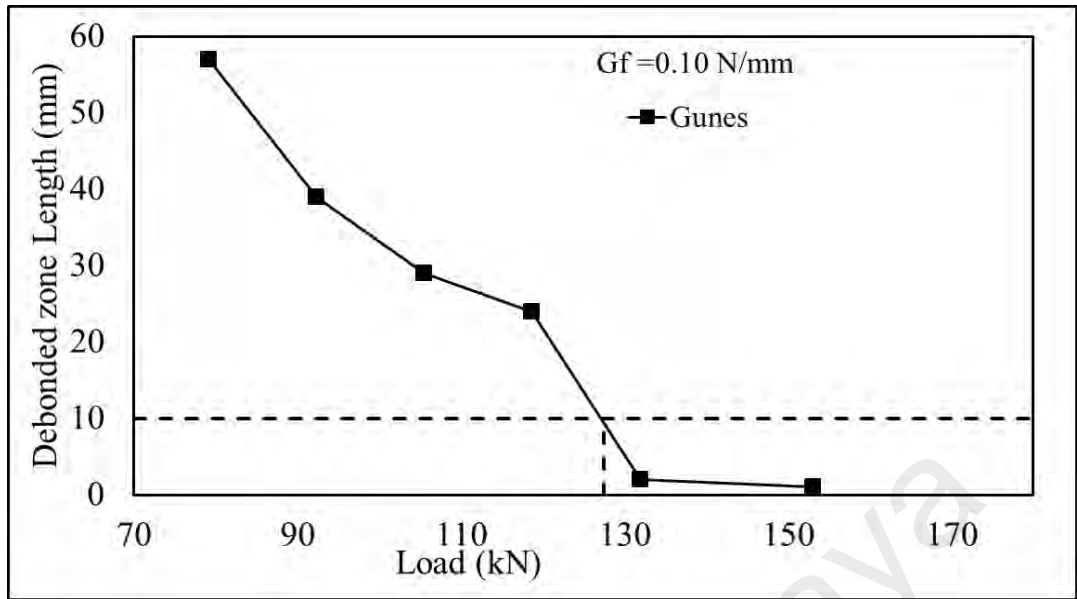


(a) Debonded zone length versus load plot for beams by Zaid et al. (2014)

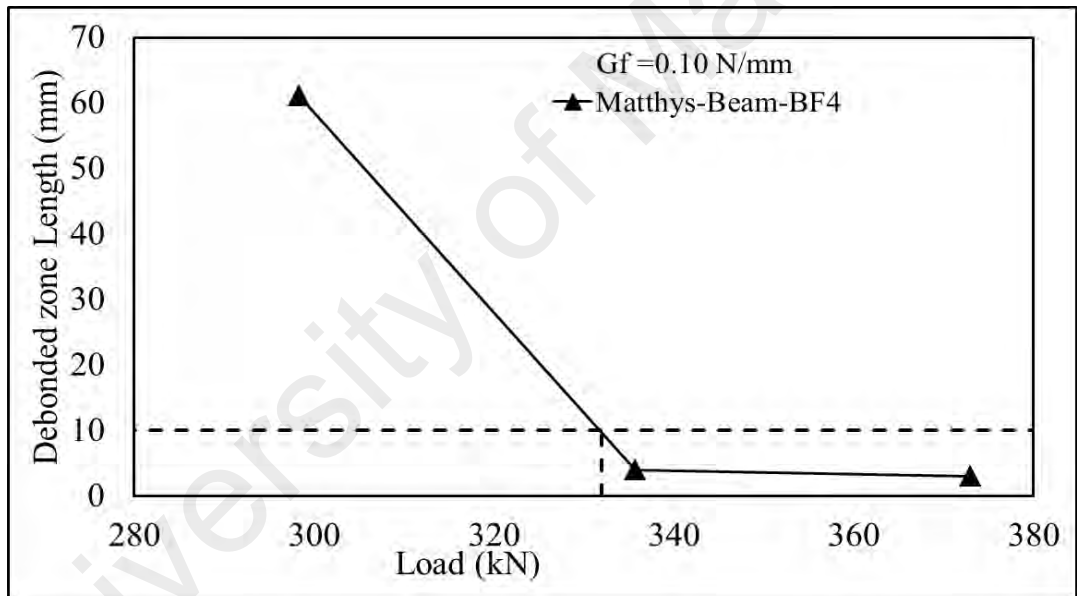


(b) Safe curtailment length versus load plot for beams by Gunes et al. (2009)

Figure 4.16: Plotting of simulation results



(c) Debonded zone length versus load plot for Beams by Gunes et al. (2009)



(d) Debonded zone length versus load plot for beam by Matthys (2000)

Figure 4.16, Continued

Matthys (2000) tested one RC beam that was precracked prior to strengthening. From the report and observation of the failure mode of that beam, it is quite evident that the beam failed due to IC debonding failure. The simulation result from the model for this beam in Figure 4.16d also complies with the experimental result, and shows that the predicted failure load is 332 kN, which is 90% of the reported experimental failure load of 372 N.

A precracked beam of SM series tested by Arduini et al. (1997) (SM3 beam) is selected for simulation. Arduini et al. (1997) reported that for beam SM3, failure initiated from one of the flexural cracks in the constant moment region, and moved towards the sheet end until the complete delamination, making it viable to IC debonding failure. Figure 4.17 shows the debonded zone length versus load plot for beam SM3, and it is obvious that the predicted load is 121 kN. However, the experimental failure load for this beam is 112.kN, and simulation result is 8% higher than the experimental result.

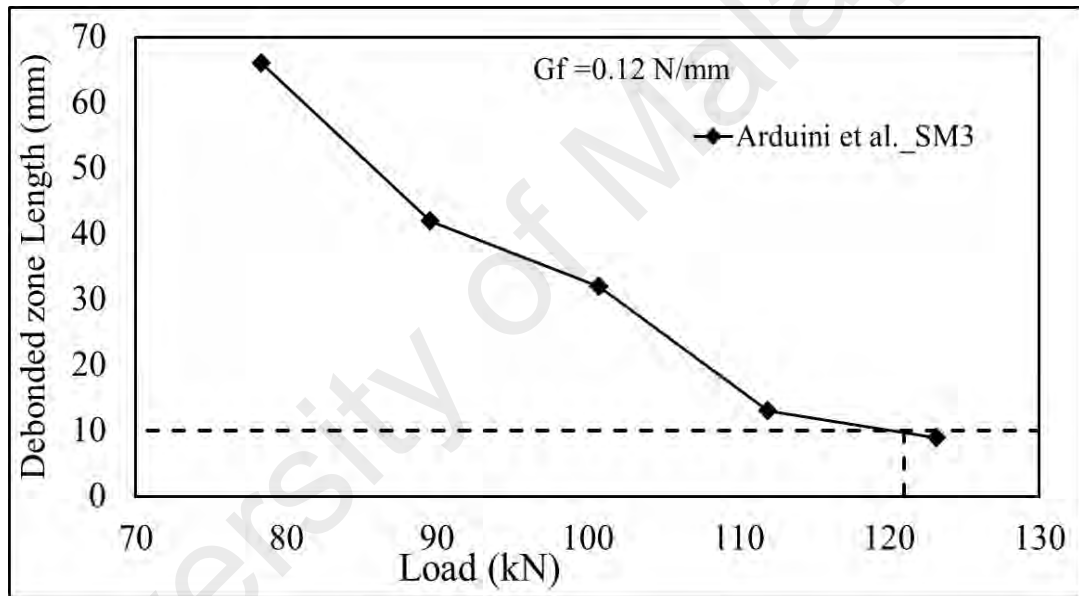


Figure 4.17: Plotting of debonded zone length versus load plot for beam SM3 tested by Arduini et al. (1997)

In the case of the beam B3 tested by Dong (2003) as shown in Figure 4.18, the predicted load in IC debonding, according to GEBA analysis, is 150 kN, which is 80% of the reported experimental load of 187.5 kN.

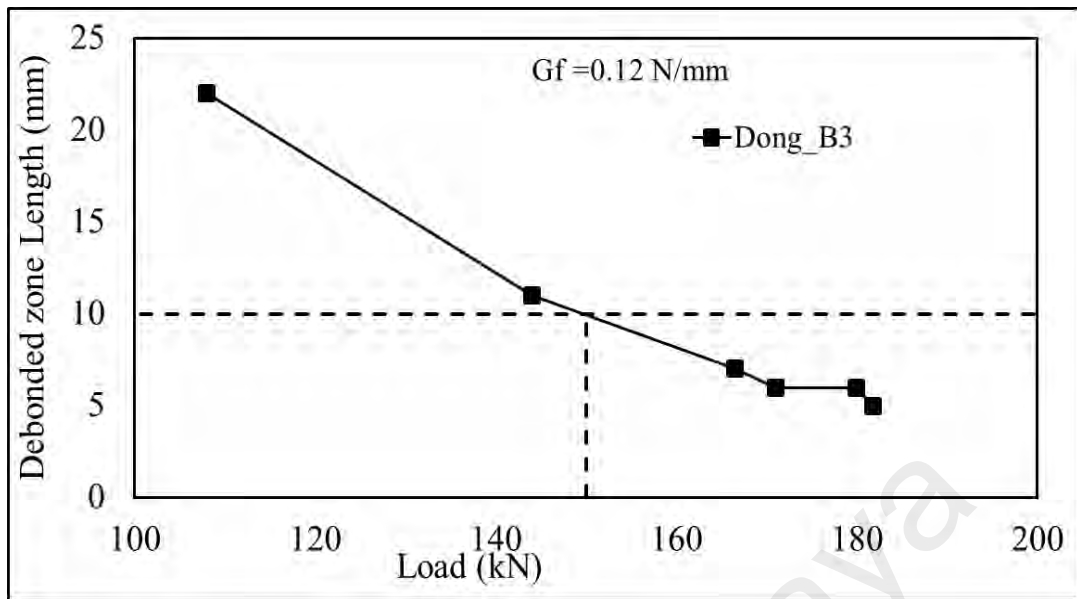


Figure 4.18: Plotting of debonded zone length versus load plot for beam B3 tested Dong (2003)

This section provides debonding prediction using GEBA analysis for precracked beams that is less damaged prior to strengthening. It can be concluded from this section that the GEBA analysis can predict the debonding in this cases with 10% tolerance, mostly with few exceptions. Therefore, the prospect of GEBA method for debonding prediction of the precracked beam is excellent.

4.6 Validation of test beams for prestressed FRP strengthened beam

Several beams strengthened with prestressed FRP from literature are validated in this thesis in order to predict the debonding of the beams. The properties of those beams are tabulated in Table 4.7 and Table 4.8.

Table 4.7: Details of EBR strengthened prestressed beam

Source	Specimen	P _f (kN)	Failure mode	Pr _{ini} %	Material	Total span l _{span} , mm	Shear span l _{shear} , mm	Wid. b, mm	Ht. h, mm	Eff. Dep. d, mm
Pelligrino & Modena (2009)	RC-PrEA	137.3	IC	30	CFRP Laminate	9000	3200	300	500	425
Xue et al. (2010)	PC-1	131.1	IC	42	CFRP plate	2500	950	150	250	210
	PC-3	91.6	IC	50						
You et al. (2012)	PCFCB1-40	120	IC	40	CFRP strips	2400	1200	200	300	249
	PCFCB1-60	119.6	IC	60		6400	2300	400	600	549
	PFCB2-50	450	IC	50						
Quantrill & Hollaway (1998)	P3	142.5	IC	40	CFRP plate	2200	845	130	230	180
Yu et al.(2008)	C	212	IC	15	CFRP sheet	2130	710	203	305	265
Peng et al. (2014)	PRS-EB	146.4	IC	30	CFRP Plate	3300	1200	150	350	314
	PRS-2N20	141.7	IC	50	CFRP Strip					

Table 4.8: Reinforcement details of EBR strengthened prestressed beam

Author	Specimen	Ten. steel area Ast, mm ²	Top steel area Asc, mm ²	Comp. str. fc', MPa	Yield Str. fy_s, MPa	FRP Thck. /dia tp, mm	FRP area Ap, mm ²	FRP mod. Ep, GPa
Pelligrino & Modena (2009)	RC-PrEA	708	307	71	375	1.2	96	166
Xue et al. (2010)	PC-1	420	56.5	52.3	350	1.2	70	150
	PC-3	339.2					28	
You et al. (2012)	PCFCB1-40	235.6	398	18	420	1.4	65	165
	PCFCB1-60						140	
	PFCB2-50	1906	850.5					
Quantrill & Hollaway (1998)	P4	314.15	100.5	45	556	1.3	117	135
Yu et al.(2008)	C	402.1	157.1	39	510	0.16	31.6	228
Peng et al. (2014)	PRS-EB	402.1	760.2	26.4	400	1.2	60	165
	PRS-2N20					2	64	131

4.6.1 Study on beams with prestressing in EBR technique

The failure of the prestressed beam C tested by Yu et al. (2008) started from intermediate flexural cracks in the constant moment region and a final failure occurred by the rupture of CFRP sheet at the end of CFRP sheets. The results of IC debonding analysis are plotted in Figure 4.19. Figure 4.19 illustrates the debonded zone length versus load plot for beam C, and the simulation result shows the predicted failure load is 189.5 kN. The predicted load is 90% of the reported experimental failure load, which is 212 kN.

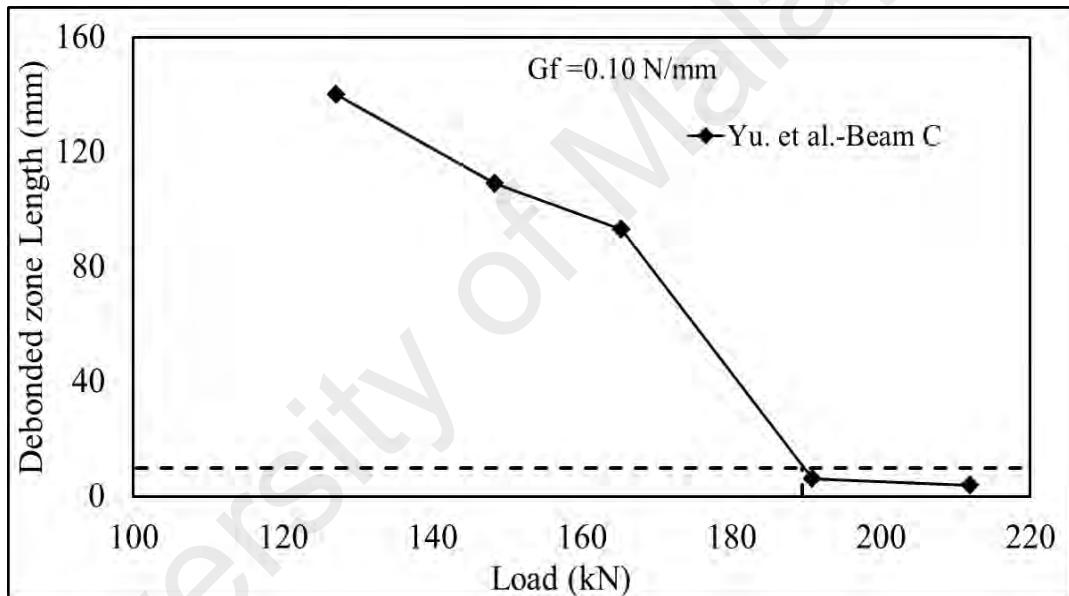


Figure 4.19: Debonded zone length versus load plot for beam C by Yu et al. (2008)

Pelligrino and Modena (2009) tested a beam series to check the usefulness of strengthening with and without prestressed FRP laminate. The beam with prestressed FRP laminate delaminated from the beam soffit. The plot in Figure 4.20 shows the debonded zone length versus load, found from the simulation result, for the beam. The predicted failure load is 130 kN. The predicted load is 95% of the reported experimental failure load, which is 137.3 kN.

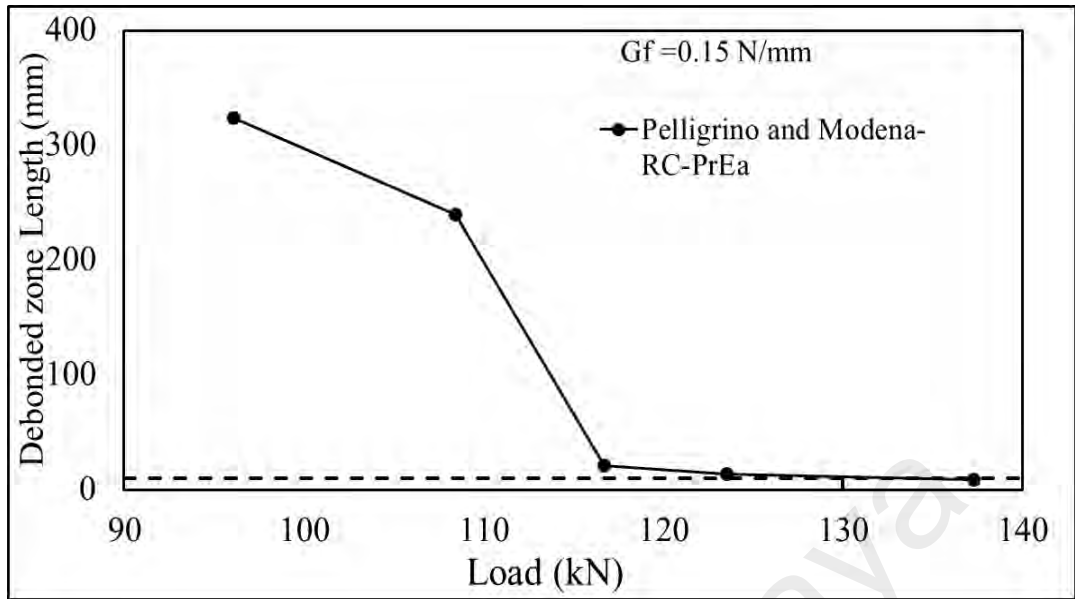


Figure 4.20: Debonded zone length versus load plot for beams tested by Pelligrino and Modena (2009)

Two RC beams strengthened with prestressed CFRP plates, tested by Xue et al. (2010), are simulated for debonding prediction. Figure 4.21 shows the simulation results. For beam PC-1, sudden debonding of the FRP sheet was reported by Xue et al. (2010). The simulated failure load is 85% of the reported experimental failure load and the values of simulation and experimental load are 112.5 kN and 131.1 kN, respectively. On the other hand, in the case of beam PC-3, it can be seen from the plot that the predicted failure load is 88.6 kN, which is 97% of the reported experimental failure load of 91.6 kN.

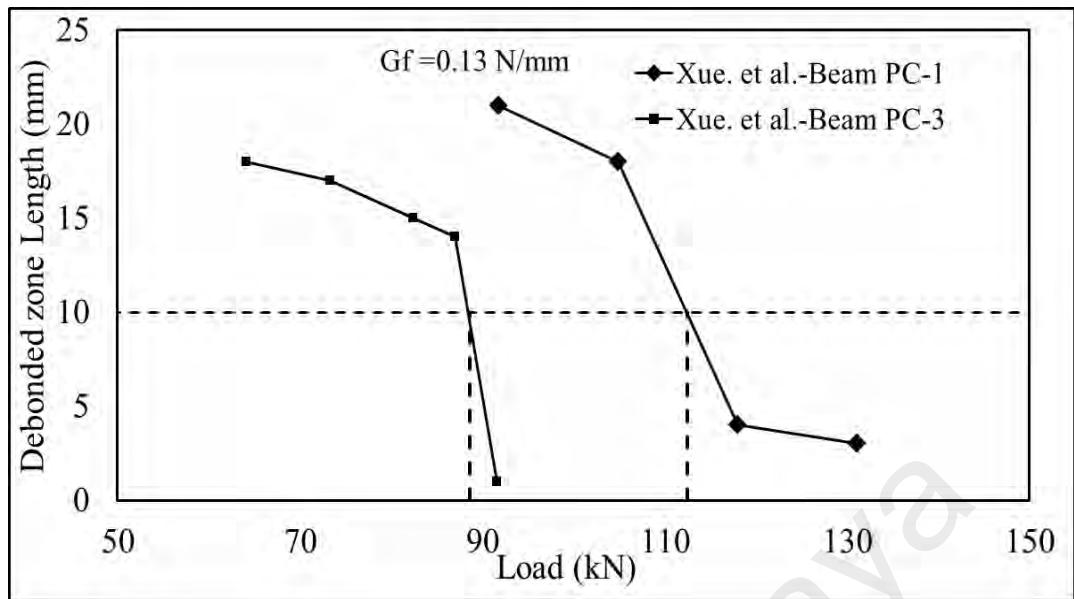
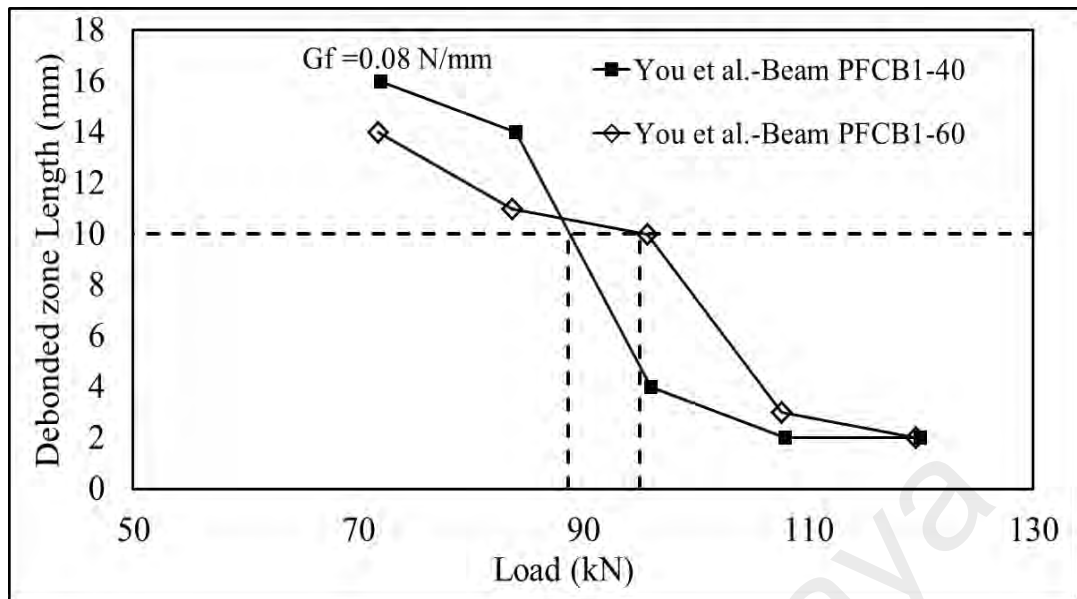
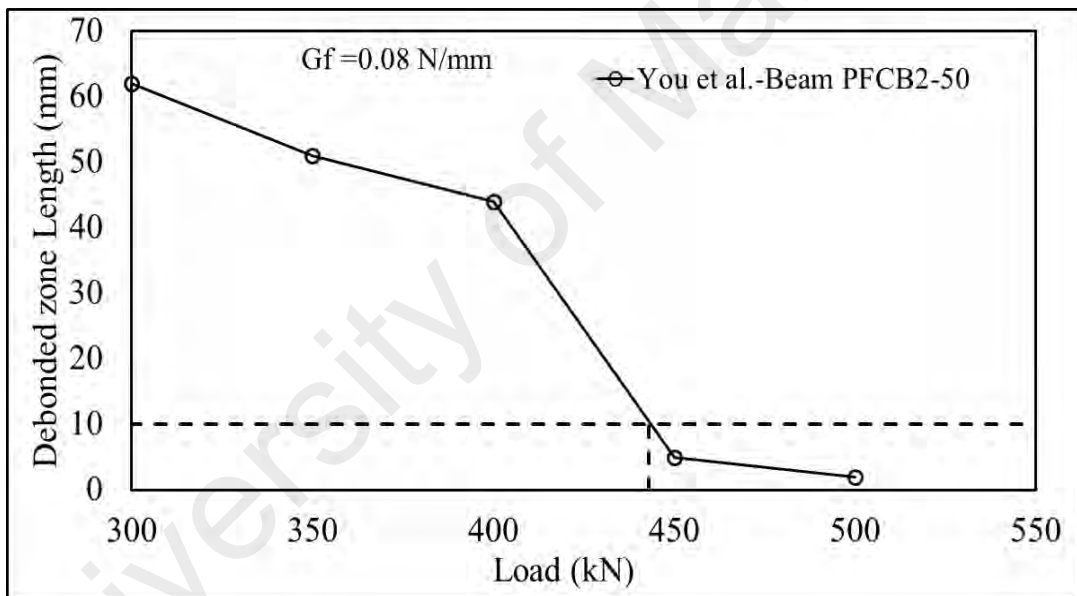


Figure 4.21: Debonded zone length versus load plot for beams tested by Xue et al. (2010)

Beams with 40%, 60%, and 70% prestressing, tested by You et al. (2012), are simulated for debonding prediction. It can be seen from the experimental results that the maximum load carried by the beam with 70% prestressing is not very different from the beam with 40% or 60% prestressing. As discussed earlier, an increase in prestressing force is supposed to increase the load for IC debonding failure. However, in that case, the beam with 70% prestressing fails in FRP rupture prior to the occurrence of IC debonding, which is obvious from the strain value at the FRP found from the moment-curvature analysis. Small scale beams with a prestressing level less than 70% show debonding of the FRP sheet, followed by FRP rupture. Debonded zone length versus load plot is shown in Figure 4.22a for beam PFCB1-40 with 40% prestressing. The plot shows that the predicted failure load of 88.7 kN is 73% of the reported debonding load of 120 kN. For beam PFCB1-60, the predicted failure load is 112.6 kN, which is 94% of the reported load of 119.6 kN, while for beam PFCB2-50, shown in Figure 4.22b, the predicted debonding load is 443 kN, which is 98% of the reported debonding load of 450 kN.



(a)



(b)

Figure 4.22: Debonded zone length versus load plot for beams tested by You et al. (2012)

The prestressed beam P3, tested by Quantrill and Hollaway (1998) failed in shear span. The plot of debonded zone length versus load, as per Figure 4.23, shows that at a load of 138.3 kN, the debonded zone length is 10 mm. The predicted load, in this case, is therefore 97% of the reported failure load of 142.5 kN.

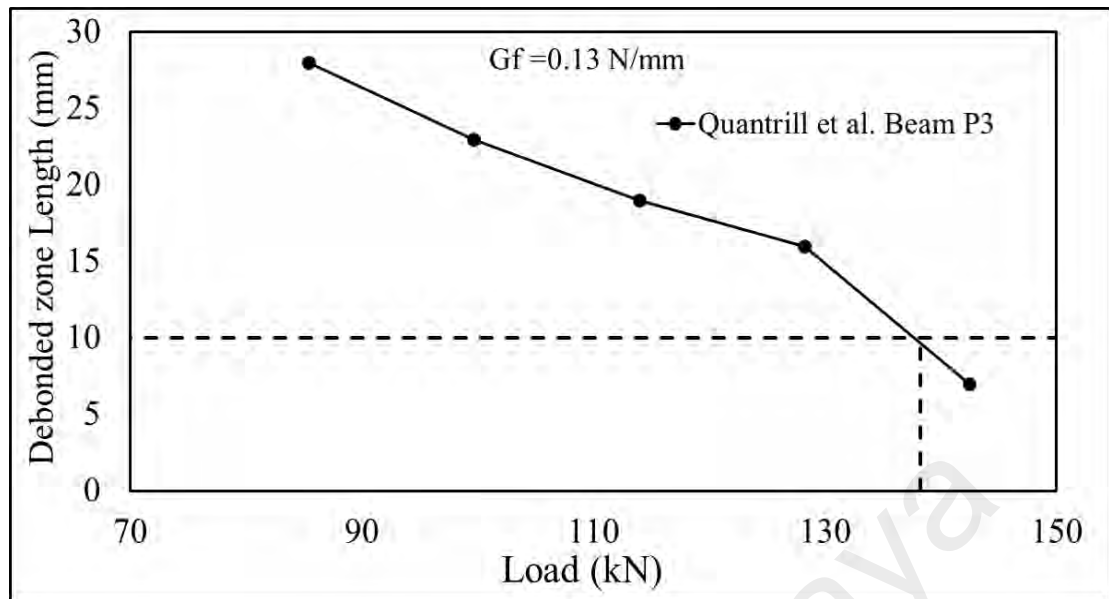


Figure 4.23: Debonded zone length versus load plot for beams tested by Quantrill and Hollaway (1998)

4.6.2 Comparison of beams with prestressing in EBR and NSM

Two beams tested by Peng et al. (2014) are selected for simulation. The beams, namely PRS-EB and PRS-2N20, reported similar amounts of strengthening reinforcement percentage, but strengthened with different strengthening techniques, i.e. EBR and NSM.

The failure of EBR strengthened beam is initiated from the midspan of the beam. Therefore, the simulation result of IC debonding analysis is shown in Figure 4.24. It is clear from the figure that the predicted failure load, 125.5 kN, is 85% of the reported failure load of 141.4 kN. For the NSM strengthened beams, the predicted failure load is found to be 126 kN, which is 89% of the experimental failure load of 146.7 kN.

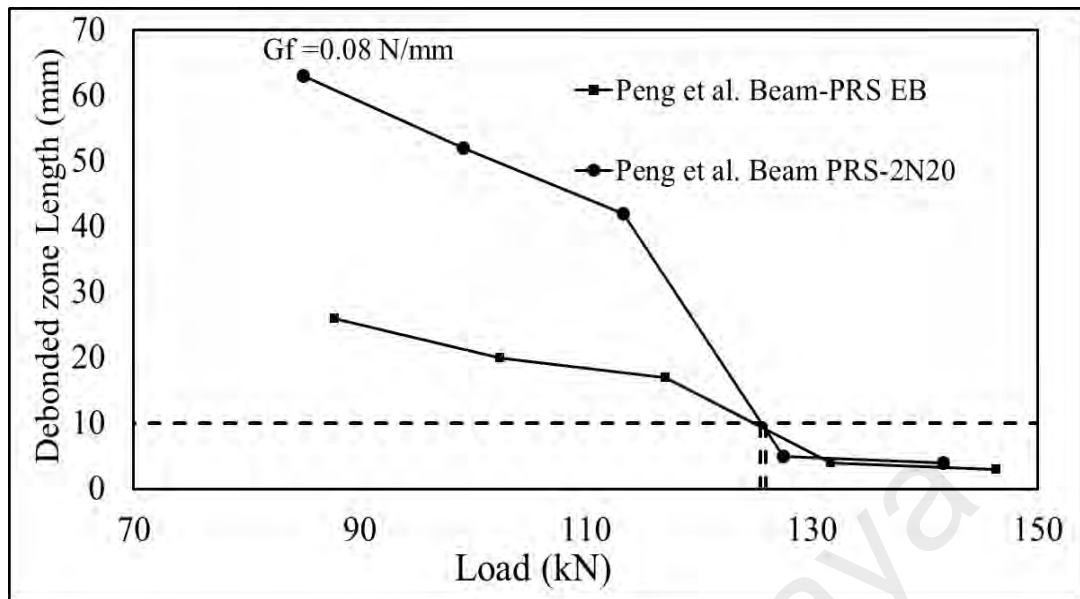


Figure 4.24: Debonded zone length versus load plot for beams tested by Peng et al. (2014)

4.7 Validation of test beams for T- Beam

The simulation of T-beam for debonding are conducted on the few reported beams in literature. These beams were strengthened using the NSM technique, and their corresponding properties are tabulated in Table 4.9 and Table 4.10

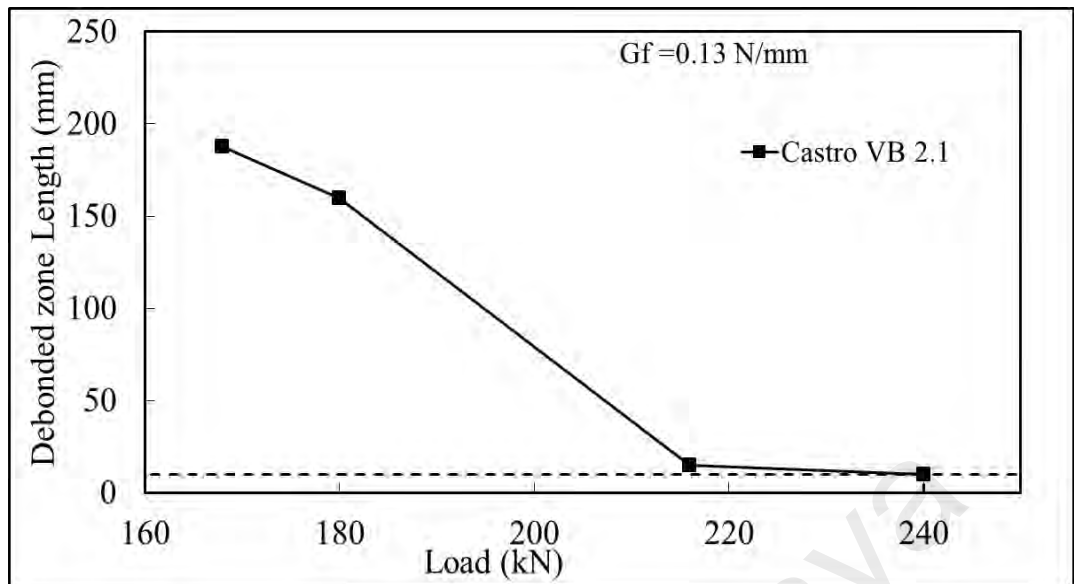
Table 4.9: Identification and geometric data of the T-beams used in the analysis

Source	Sample	P_f (kN)	Failure mode	Total Span l_{span} , mm	Shear Span l_{shear} , mm	Flange Wid. b_f , mm	Web Wid. b_w , mm	Ht. h , mm	Eff. Dep. d , mm
Choi et al. (2010)	NPFB	83.9	IC	3300	1500	400	150	300	250
Castro et al. (2007)	VB 2.1	240	IC	4000	1500	550	150	400	365

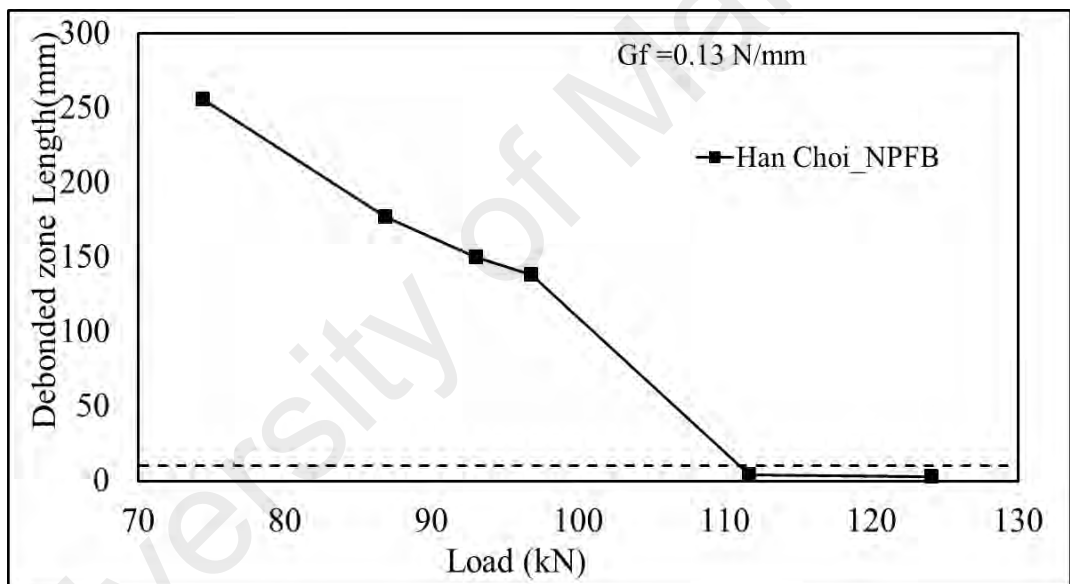
Table 4.10: Reinforcement details of the beams used in the analysis

Source	Sample	Ten. steel area A_{st} , mm ²	Comp. steel area A_{sc} , mm ²	Comp. str. f_c , MPa	Yield Str. $f_{y,s}$, MPa	FRP Thck. /dia. t_p , mm	FRP area A_p , mm ²	FRP mod. E_p , GPa
Choi et al. (2010)	NPFB	402.1	285.1	52.5	473	1.2	36	165
Castro et al. (2007)	VB 2.1	628.3	113	50	558	2	96	131

T-beams tested by Castro et al. (2007) and Choi et al. (2010) are simulated in this work. The beams failed due to IC debonding, and the debonded zone length versus load plots are shown in Figure 4.25. For beam VB 2.1, tested by Castro et al., the predicted failure load from GEBA analysis is 240 kN, which is 100% of the reported failure load. For beam NPFB, tested by Choi et al., the predicted load is 75 kN, which is 89% of the experimental load of 83.9 kN.



(a)



(b)

Figure 4.25: Debonded zone length versus load plot for beam tested by a) Castro (2007) and b) Choi et al. (2010)

4.8 Comparison of simulation versus experimental results

A summary of the simulated and experimental load, failure mode, and ratio between theoretical to experimental loads are tabulated in Table 4.11 and Table 4.12 by adopting the mode I fracture energy as the limiting failure criteria. The graphical comparison of the experimental and simulated failure loads shown in Table 4.11 and Table 4.12 are presented in Figures 4.26a and b. The plots show excellent agreement of the simulated load with the experimental results.

In case of NSM strengthening the mean is 0.99 with a standard deviation of 0.09. For hybrid strengthening the mean is 0.95 with a standard deviation of 0.08. For precracked beams, the mean is 0.97 with a standard deviation of 0.09. For beams strengthened using prestressed FRP the mean is 0.93 with a standard deviation of 0.09. For T-beams, the mean is 0.94 with a standard deviation of 0.07. The overall mean of the ratio between the simulated and experimental failure load is 0.96, with a standard deviation of 0.09 which is good for practical implication of the model.

Table 4.11: Summary of results for beams strengthened using different technique

Beam type	Beam ID	EFM	SFM	P _{failure}	P _{theo}	P _{theo} /P _{failure}	Mean	St.dev.
NSM	B-S-2	IC	IC	72.3	65.6	0.90	0.99	0.09
	B-N-2-2	IC	IC	91.6	80.5	0.87		
	B-N-2-4	PE	PE	105.6	102	0.97		
	E3	PE	PE	140	145	1.03		
	C3	PE	PE	123.5	150	1.21		
	B1200	PE	PE	63	64.5	1.02		
	B1800	PE	PE	91	93	1.02		
	A1	PE	PE+	231	232.8	1.01		
	A2	PE	PE+	231	232.8	1.01		
	A3	PE	PE	231	224	0.97		
	A4	PE	S	255	270	1.06		
	SC210	PE	PE	109	103.5	0.95		
	SC270	IC	IC	133.1	124.1	0.94		
	LB2C1	PE	PE	117.2	129	1.10		
	LB2G1	IC	F-rup	112	119.6	1.06		
	NSM 1	Flexu ral	F	80	84.9	1.06		
	NSM 2		F	101.3	94.1	0.93		
	NSM 3		F	114	119.5	1.04		
	B11	CC	CC	256.7	228.5	0.89		
	B21	IC	IC	260.9	190	0.73		
NSM_c_2	CC	S	32.5	31.1	0.96			
NSM_c_3	CC	S	33.7	35	1.03			
Hybrid	CBC10P2	IC	IC	87	69.6	0.8	0.95	0.08
	HS1	PE+S	S	132.4	140	1.05		
	HS2	PE+S	PE	105.6	105	0.99		
	HS3	PE+S	PE	102	99	0.97		
	HS5	PE+S	PE	109	108	0.99		
	HS6	PE+S	PE	130	119	0.92		

*EFM: experimental failure mode; *SFM: simulated failure mode

PE: Plate end; IC: Intermediate crack induced debonding; Y: Yield failure; S: Shear failure; F: Flexure; CC: Concrete crushing, F-rup: FRP rupture; CDCD: Critical diagonal crack debonding.

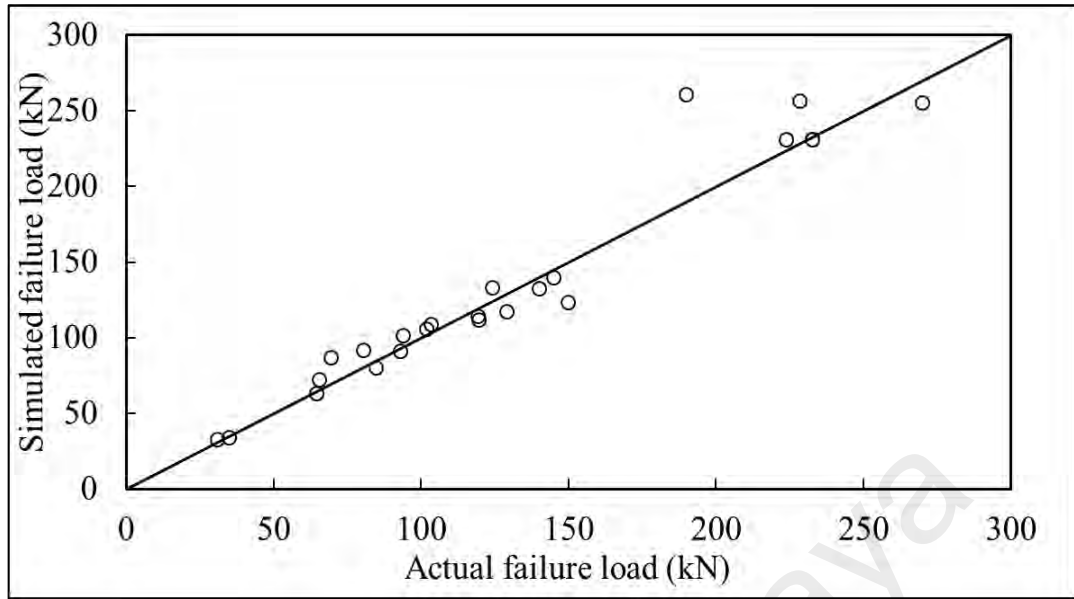
Table 4.12: Summary of results for different types of strengthened beams

Beam type	Beam ID	EFM	SFM	P _{failure}	P _{theo}	P _{theo} /P _{failure}	Mean	St.dev
Precracked	3-C1-40	IC	IC	83.4	83	0.99	0.97	0.09
	3-C1-60	IC	IC	81.2	80	0.95		
	B-0.3-0.5	IC	IC	177	159.3	0.9		
	B-0.6-0.9	IC	IC	233	229	0.98		
	B1	PE	PE	148.2	142.1	0.96		
	B2	PE	PE	157.9	177.4	1.13		
	B3	IC	IC	189.1	150	0.79		
	RB4	PE	PE	30.8	34.7	1.12		
	RB3	PE	PE	32.1	34.4	1.07		
	RB2	PE	PE	37.7	35.4	0.94		
	BF4	IC	IC	373	332	0.89		
	P2	IC	IC	68	61	0.89		
	P3	IC	IC	66	59.3	0.89		
	SM3	IC	IC	112	121	1.08		
	S1PF1M	IC	IC	131.9	127.5	0.97		
Prestressed FRP	RC-PrEA	IC	IC	137.3	135	0.98	0.93	0.09
	PC-1	IC	IC	131.1	112.5	0.86		
	PC-3	IC	IC	91.6	88.6	0.97		
	PCFCB1-40	IC	IC	120	88.7	0.74		
	PCFCB1-60	IC	IC	112.6	95	0.84		
	PB2-50	IC	IC	450	443	0.98		
	P3	IC	IC	142.5	138.3	0.97		
	C	IC	IC	212	189.5	0.89		
	PRS-EB	IC	IC	146.4	125.5	0.86		
	PRS-2N20	IC	IC	141.7	126	0.89		
	Rezazadeh et al.-30%	FR	FR	142	143.6	1.01		
	Rezazadeh et al.-40%	FR	FR	143	143.1	1.00		
	Hacha et al. 20%	FR	FR	135	143.3	1.06		
	Hacha et al. 40%	FR	FR	137.3	135	0.98		

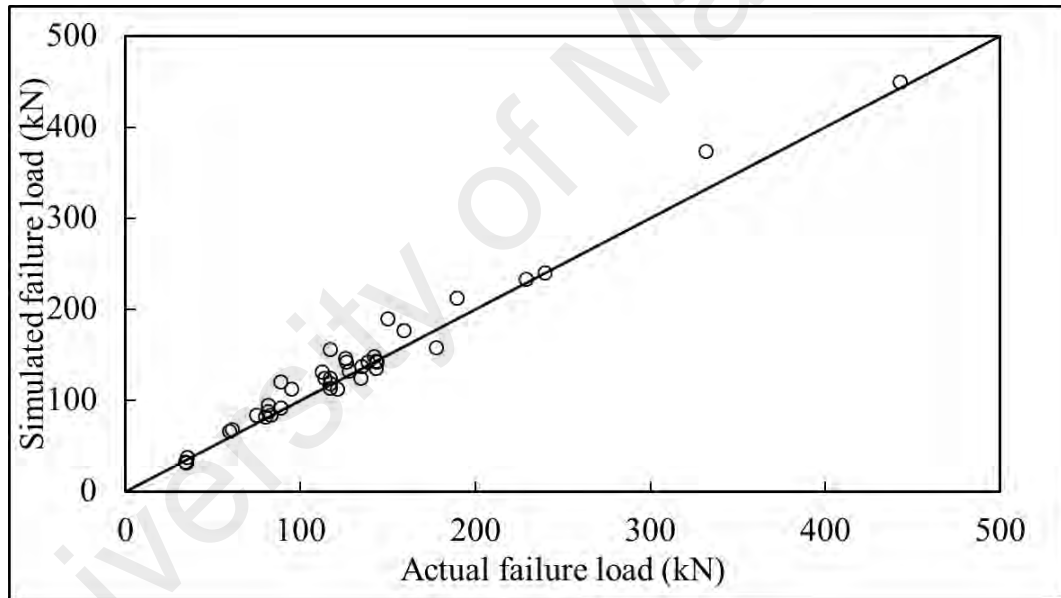
Table 4.12, continued

Beam	Beam ID	EFM	SFM	P _{failure}	P _{theo}	P _{theo} / P _{failure}	Mean	St.dev
	Hacha et al.	FR	FR	113.2	117	1.03		
	Sang- M4-III	FR	FR	118.3	117	0.99		
	Sang-M6-III	FR	FR	155.6	117	0.75		
	Sang-M8-4	FR	FR	124.0	117	0.94		
	Sang-M8-3	FR	FR	94.8	81.63	0.86		
	Nordin-BPS5	FR	FR	87.8	81.63	0.93		
	Nordin-	FR	FR	124.2	113.8	0.92		
T-beam	NPFB	IC	IC	83.9	75	0.89	0.94	0.07
	VB 2.1	IC	IC	240	240	1		

It can be seen that, for few beams the EFM and SFM is not the same and it occurs for beams where the reported failure mode is plate end debonding or critical diagonal crack debonding (CDCD). In those cases, the simulated failure mode is found to be shear failure. It should be noted here that the shear failure and plate end failure in some cases cannot be distinguished due to the failure nature as already mentioned in literature review. So it is quite possible that the experimental failure mode is reported to be PE or CDCD though the computation of shear capacity confirms that the failure actually occurs due to inadequate shear capacity of the beam due to strengthening.



(a) NSM and Hybrid technique



(b) Beams with precracking, prestressed FRP and T-shape

Figure 4.26: Comparison of simulated and experimental failure load

4.9 Parametric study

After validating the proposed model against available test data reported in the literature, the parametric analysis is carried out using the model. To illustrate the application of the model, RC beams strengthened with a carbon fiber reinforced polymer (CFRP) plate with the geometric details as shown in Figure 4.27 has been analyzed.

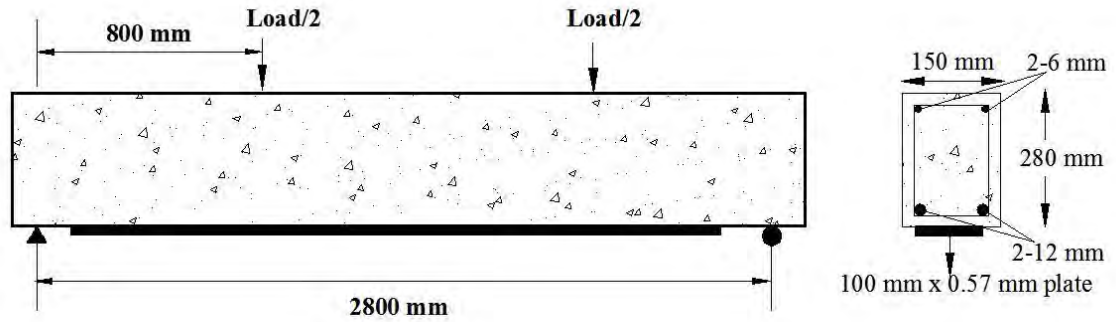
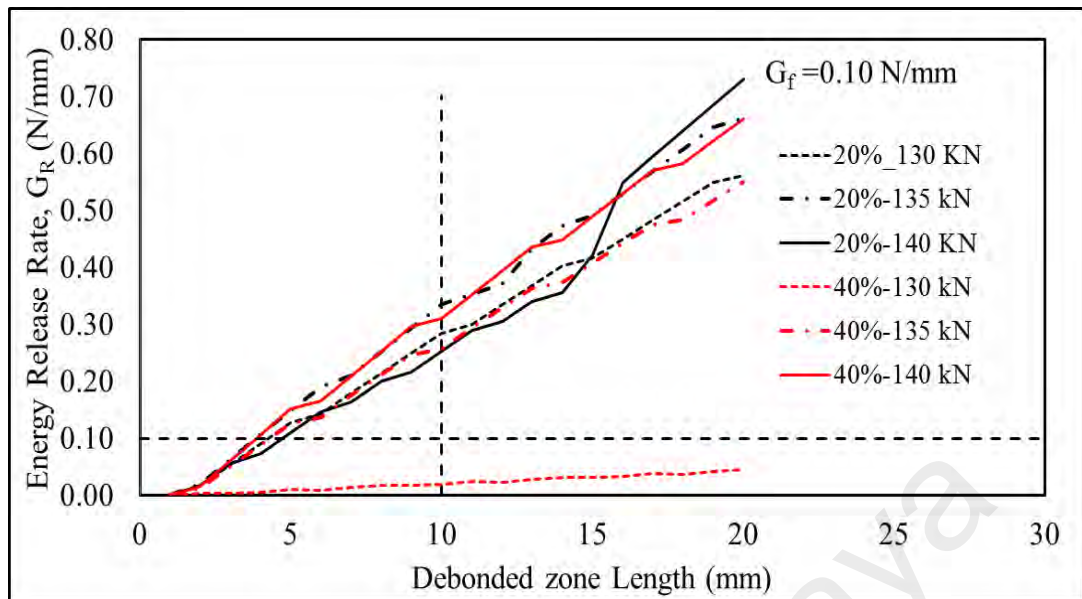


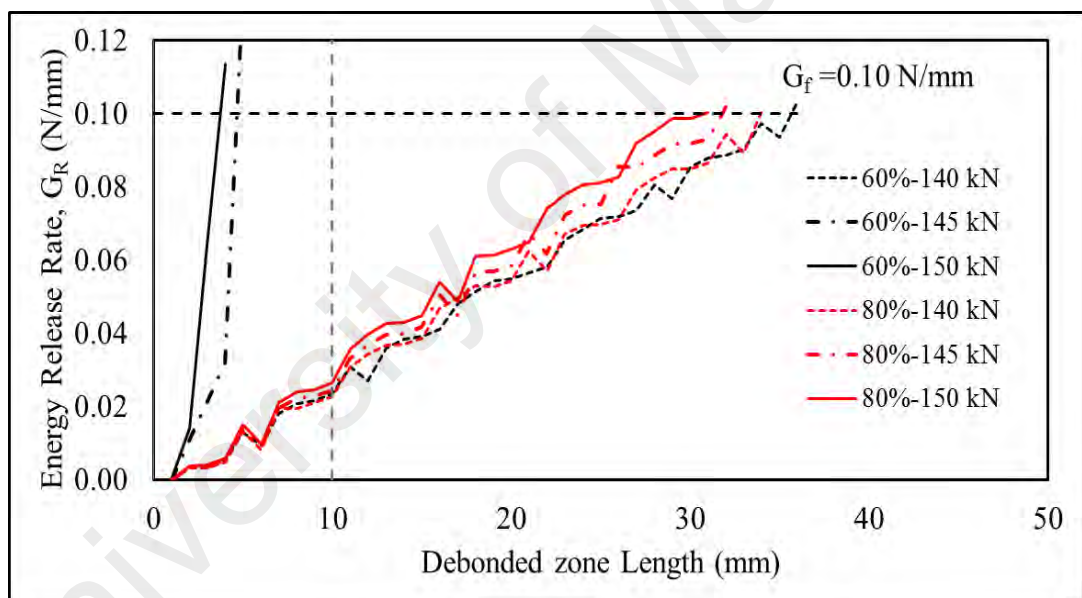
Figure 4.27: Geometric details of assumed example beam

The compressive and tensile strength of concrete is taken as 35 MPa and 2.8 MPa respectively. The Young's modulus and steel stress of steel are taken as 200GPa and 600 MPa respectively. The Young's modulus of CFRP is taken as 145 MPa with a tensile strength of 2200 MPa. The ultimate theoretical capacity of the unstrengthened beam is 75 kN for steel yielding and the ultimate theoretical capacity for strengthened beam is 158 kN for FRP rupture.

Two cases are investigated; i.e.(i): FRP is prestressed and (ii): the beam is precracked. Since the primary premature failure of the prestressed beam occurs in IC debonding mode, so for case 1, the beam is analyzed with different prestressing level and checked how prestressing effect the IC debonding. Figure 4.28a shows the plotting of ERR versus debonded zone length at different load near the ultimate theoretical strengthened capacity with prestressing level of 20 and 40%. Figure 4.28b shows the same features for the prestressing level of 60 and 80%. The figure reveals that as the load increases, the ERR increases to cause the same debonded zone length. On the other-hand for the same load as the prestressing increases, the ERR decreases, which means increase in failure load.



(a) 20% and 40% prestressing



(b) 60 % and 80% prestressing

Figure 4.28: ERR versus debonded zone length for prestressed beam a) and b) with different level of prestressing

So according to Figure 4.28 reveals that as the prestress level increases the debonded zone length for a certain force also increases, which means failure load will also increase based on the assumption of failure criteria used in the analysis.

Figure 4.29 shows the plotting of ERR versus debonded zone length at different load for a strengthened beam, that has been precracked before strengthening to 100% of its flexural capacity. The figure shows that the debonding failure is critical for a load of 95 kN. That means, the ultimate capacity of the strengthened beams increases only 30 % than the unstrengthened capacity of the beam due to precracking.

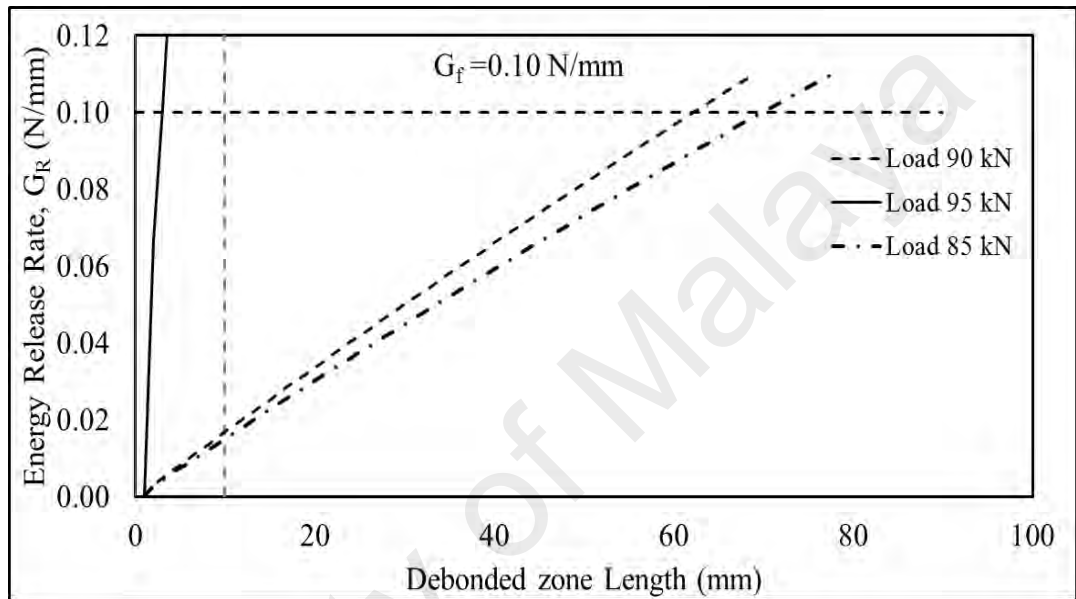
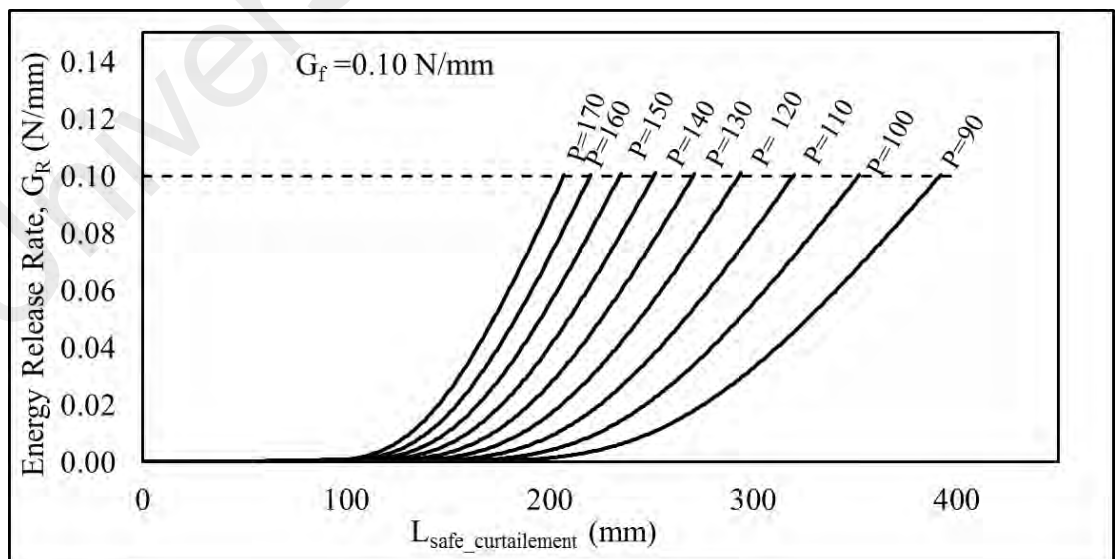
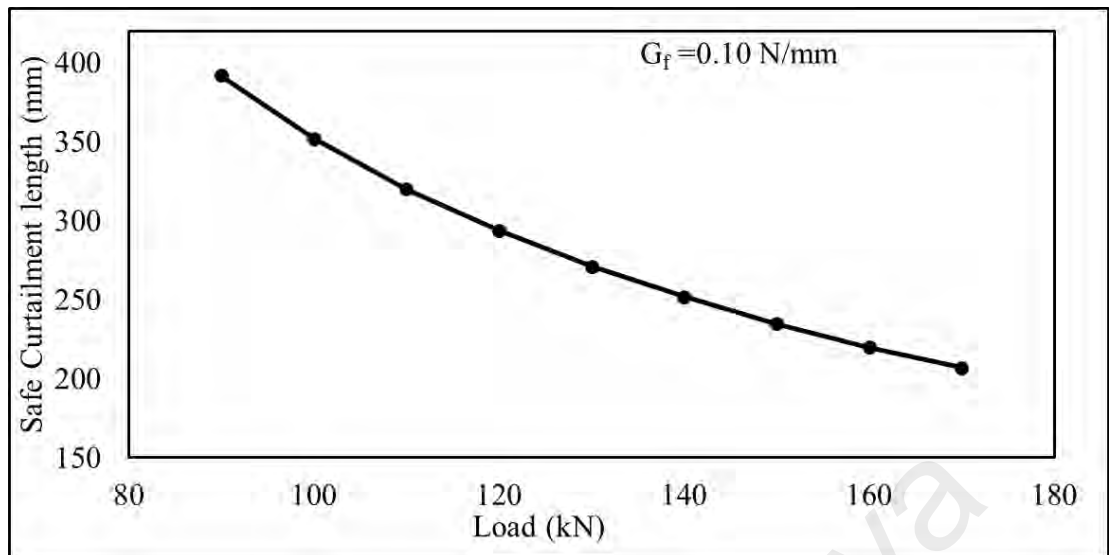


Figure 4.29: ERR versus debonded zone length for IC debonding failure for 100 % precracked beam

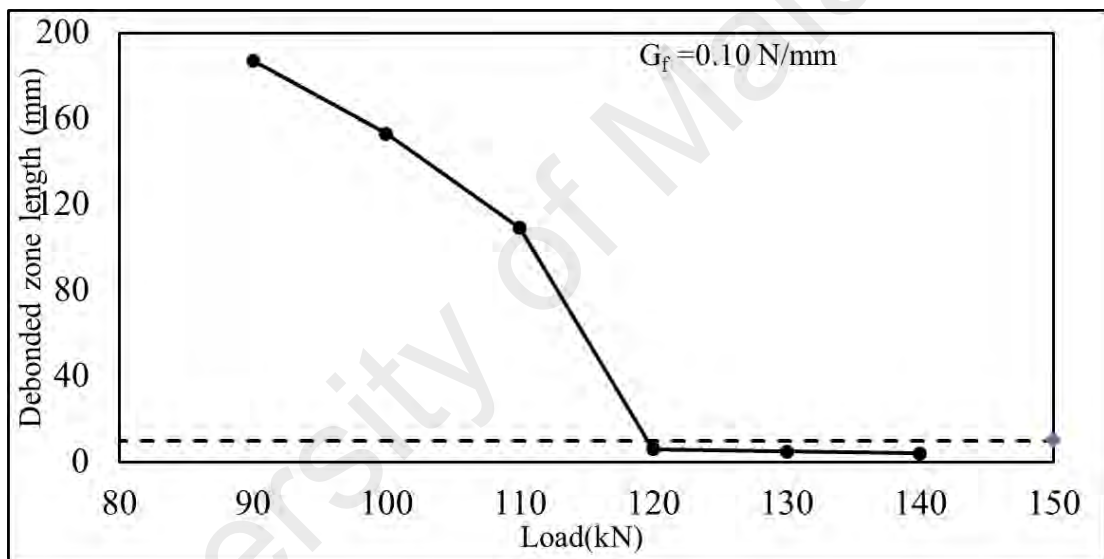


(a) ERR versus plate curtailment location

Figure 4.30: Plotting of simulated results for NSM strengthened beam



(b) Safe curtailment length location versus load plot for PE failure



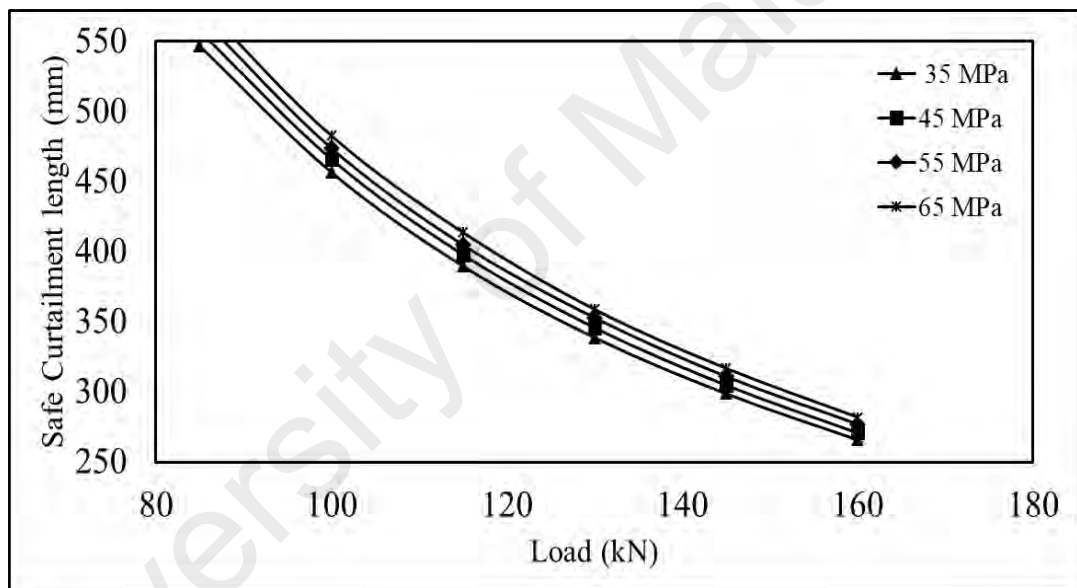
(c) Debonded zone length versus load

Figure 4.30, Continued

Figure 4.30 presents the debonding analysis for NSM strengthened beam found from GEBA analysis. Figure 4.30a illustrates the ERR versus safe curtailment length (as mentioned in 3.3.2.4) at different load in case of end debonding, for the aforementioned beam with same FRP percentage but strengthened using NSM technique. The plotting simply implies that if the expected load capacity is higher, the curtailment length needs to be shortened to avoid failure. The same results can be plotted as shown in Figure 4.30b as a design chart where one can simply read the safe curtailment length for a

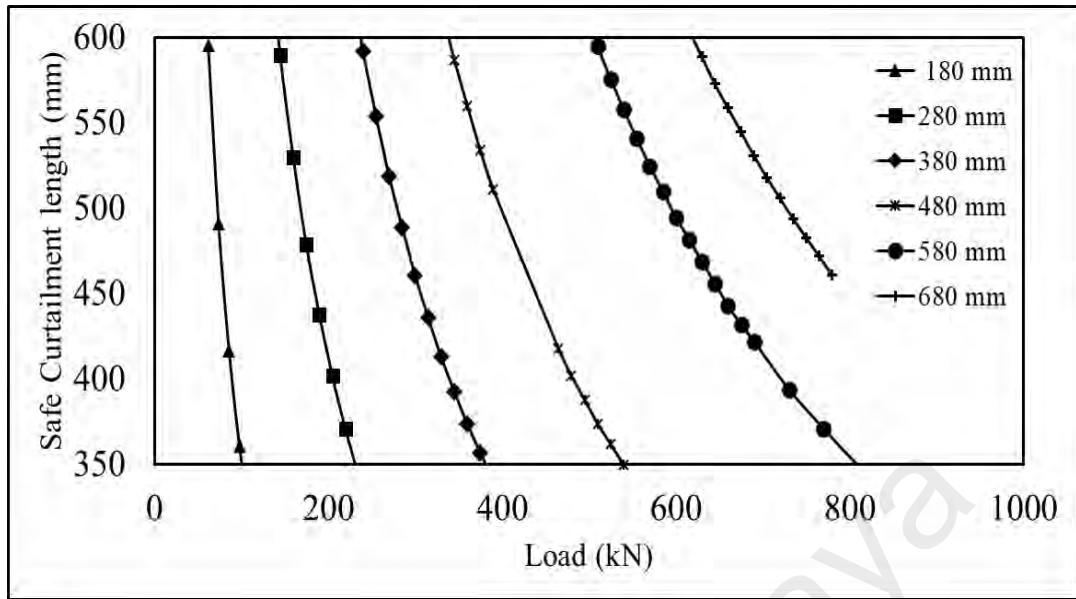
specific load for certain fracture energy. Figure 4.30c shows the debonded zone length required to trigger IC debonding for different loads for the same beam configuration. The plotting implies that IC debonding is not possible at lower loads and as the load increases the chance of IC debonding increases.

Different parameters are related with the debonding analysis, such as material properties, geometric properties. The effect of different parameters on the safe curtailment length of NSM strengthened beam such as concrete compressive strength, beam height, steel percentage and FRP percentage are shown in this part of the thesis.

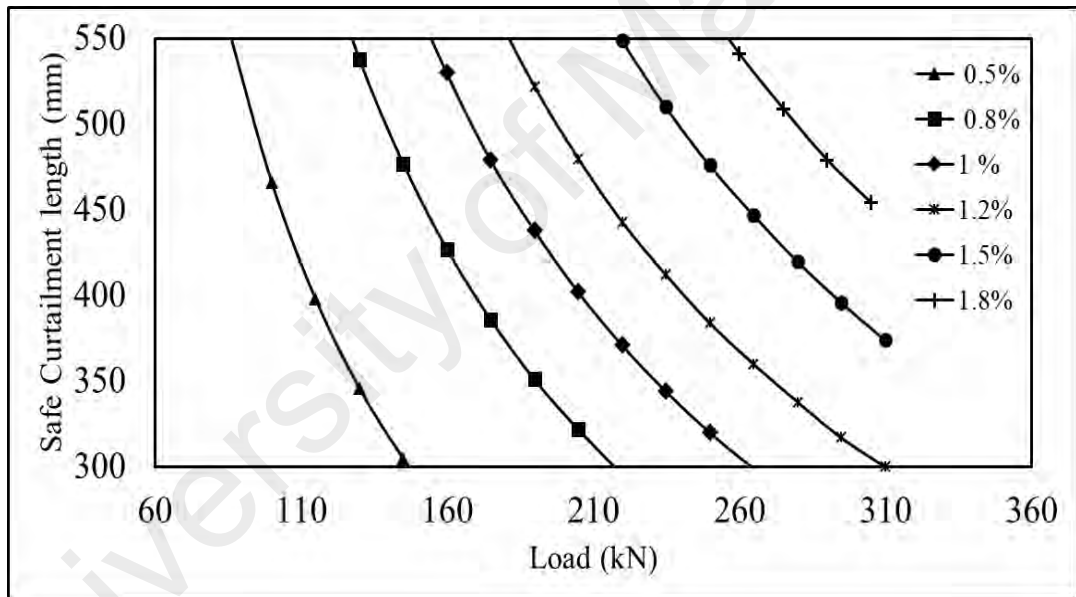


(a) Change in compressive strength

Figure 4.31: Safe curtailment length from (a) to (d) and debonded zone length versus load of from (e) to (f)

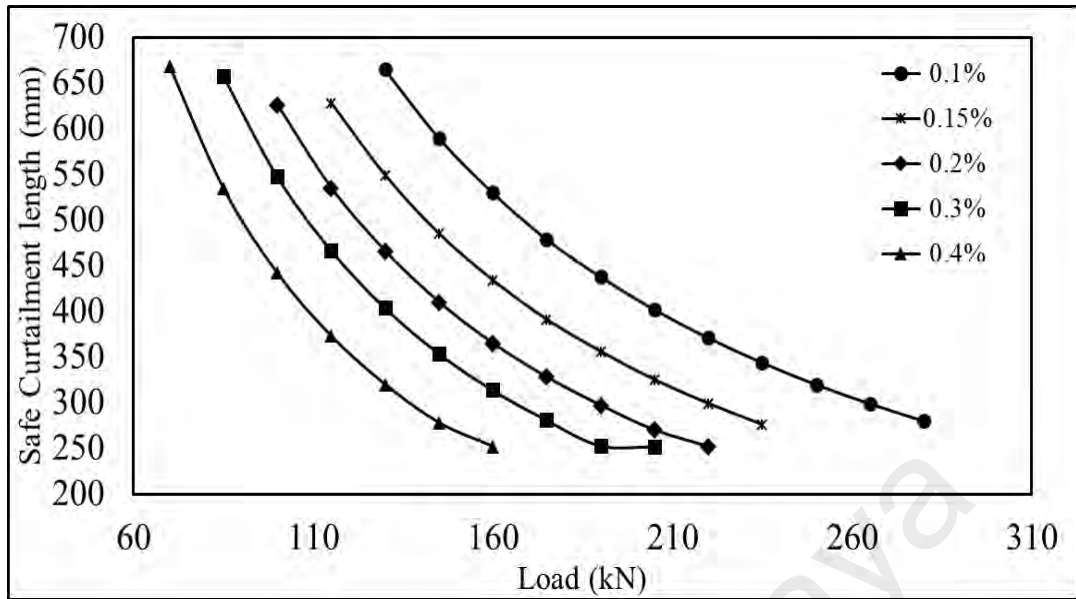


(b) Change in beam height

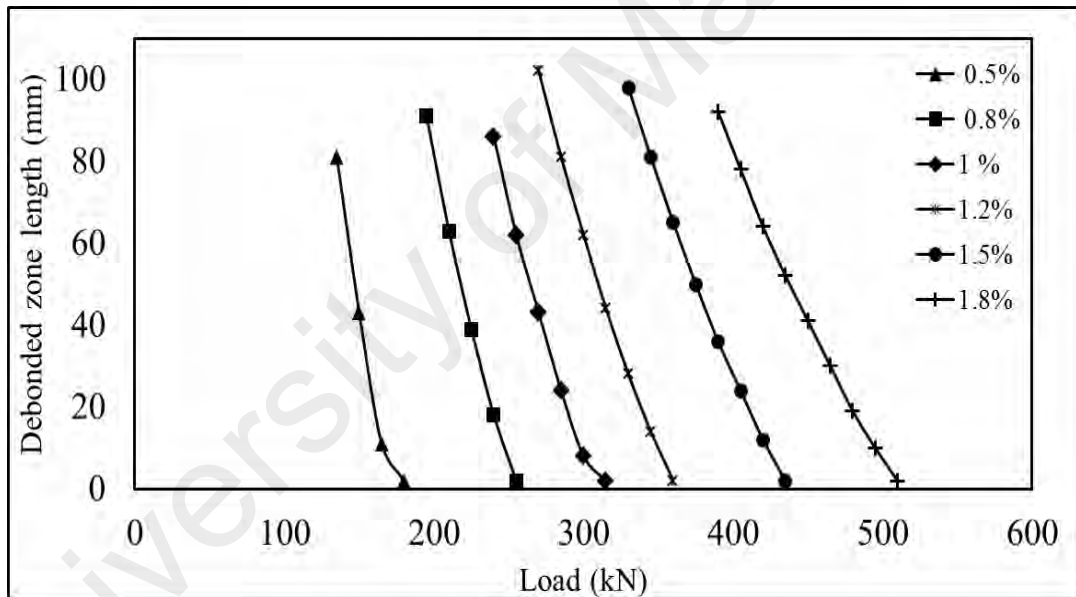


(c) Change in steel percentage

Figure 4.31, Continued

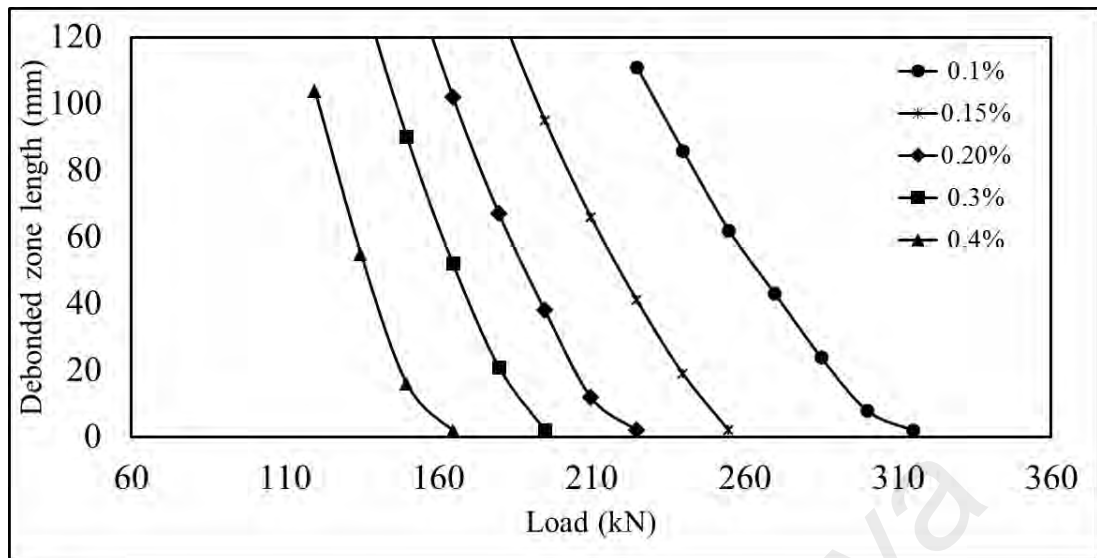


(d) Change in FRP percentage



(e) Change in reinforcement percentage

Figure 4.31, Continued



(f) Change in FRP percentage

Figure 4.31, Continued

Figure 4.31 presents the results of the parametric analysis for NSM strengthened beam both for PE as well as for IC debonding. Figure 4.31a shows that the change in compressive strength marginally affects the safe curtailment length. Actually, the effect of compressive strength in the case of debonding is mainly due to the change in tensile strength. This change alters the first cracking moment and the energy state of the section. A beam with higher strength concrete renders the section stiffer, which lowers the curvature and strain energy of the beam. However, increased beam height increases the safe curtailment length, as shown in Figure 4.31b, and debonding is less likely to occur, as the tension steel ratio increases due to the increase in steel contributing into an increase in the stiffness of the section, as shown in Figure 4.31c and e for end debonding and IC debonding, respectively. This reduces its curvature, which in turn reduces the strain energy that is available for release, meaning that the ERR is small and the chance of debonding is decreased. Another noteworthy point is that the change due to steel is relatively even. This is due to the fact that the tension steel is always fully bonded with the RC section, and the flexural capacity provided by the steel transfers to the section effectively without any loss. However, as the FRP percentage increases, the

safe curtailment length decreases due to the high peeling force, causing earlier debonding failure due to the high FRP percentages, as shown in Figure 4.31d and f for end debonding and IC debonding, respectively. Increased FRP percentage means more energy is being stored in the FRP prior to debonding, and more ERR while fracturing. Sections with a small amount of FRP shows less risk of debonding, because in that case, the FRP carries less load, which limits the amount of energy released.

4.10 Summary

This chapter provided the comparison between the experimental to simulated debonding failure load of beams gathered from literature, encompassing NSM, hybrid, precracked EBR beam, EBR, as well NSM beams strengthened beam using prestressed FRP and beam with T-section. The comparison between the experimental and simulated results showed that the GEBA based debonding analysis can estimate the debonding load with appreciable accuracies. Therefore, this analysis can be used in practical applications for predicting the failure of strengthened beams. This chapter also provided a brief parametric study for the aforementioned types of beams, showing the effect of different geometrical or material parameters on debonding.

CHAPTER 5: FUZZY LOGIC APPROACH FOR DETERMINING THE SAFE CURTAILMENT LENGTH USING ENERGY BALANCE

5.1 Introduction

The GEBA based model proposed by Achintha and Burgoyne (2008) for EBR and its extension for different other types of beams, as presented in this thesis, shows the efficiency of the model for predicting failures. However, this model is too complex for design purpose. Therefore, it is required to develop a method using the results of GEBA analysis so that it can be incorporated into the design. This chapter presents a method to deal with PE debonding of the EBR strengthened beam. Similar technique can be extended to include the effect of NSM and hybrid techniques, including the effect of precracking and prestressing. A similar technique can also be developed for IC debonding.

The estimation of PE debonding is a complex event, as it relies on several parameters, such as beam dimension and material properties. It is therefore next to impossible to realize debonding location based on individual values of variables involved in the phenomena. This drawback can be mitigated via the application of dimensional analysis to the numerical results obtained from the parametric analysis of Achintha and Burgoyne (2009) model. Guan et al. (2014) proposed a parametric study for PE debonding modifying GEBA and fracture based method proposed by Achintha and Burgoyne to predict the debonding load. The study created the foundation for the application of the model for design purpose by the use of groups of the chart for multiple combinations of material properties. However, the proposed method still lacks simplicity. The current study will apply this simple but effective approach of dimensional analysis in EBR FRP strengthened RC beams to predict the safe curtailment length, depending on several variables. The purpose of the dimensional

analysis, in this case, is to reduce the dependable parameter or group them into dimensionless numbers to simplify the problem. If the variable involved in the debonding process is reduced using dimensional analysis to some non-dimensional number, the prediction of critical curtailment length will still not be as simple, because it involves a series of charts, as proposed by Guan et al. (2014) for different dimensionless group. Therefore, there is a need for a simple and rapid, yet reliable and accurate alternative technique.

Based on the aforementioned research gaps, this study proposed an innovative approach based on FLES to predict PE debonding i.e. the critical curtailment length of EBR FRP strengthened RC beams. The procedure for determining the critical curtailment length for FRP strengthened EBR beam consists of following steps:

- i. The first step is to conduct a parametric analysis of the EBR strengthened beam. From the results of the parametric study, non-dimensional load and non-dimensional length can be plotted.
- ii. These plots help to identify the parameters influencing the curtailment length, which helps to reduce the number of dependent variables.
- iii. FLES is developed in MATLAB using if-then rules. In order to determine the debonding length for any beam, one has to determine the equivalent value of a variable using nondimensional numbers.
- iv. These numbers are provided as inputs in FLES, which gives the nondimensional length number that can be converted to the actual critical curtailment length.

5.2 Development of the FLES for EBR beam

Three types of PE debonding failures commonly found in experimental work as are shown in Figure 5.1 (Achintha, 2009).

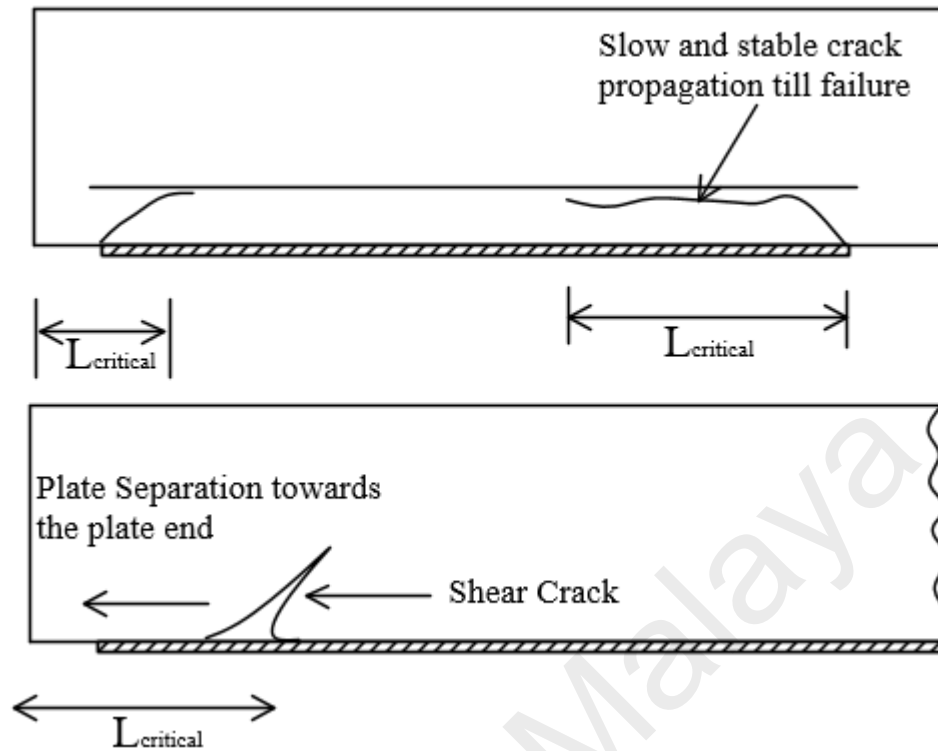


Figure 5.1: Types of critical interface flaw at plate end failure (Achintha, 2009)

Achintha and Burgoyne (2009) proposed the method for determining the critical length of curtailment, $L_{critical}$, using the GEBA with fracture mechanics. In case, where the FRP is curtailed at a considerable distance from the beam support, as soon as a dominant shear crack evolves near the plate end, it triggers debonding immediately. The critical crack development could be avoided by extending the FRP till the support. However, this does not prevent the slow crack growth rate of the original crack which ultimately leads to failure. Another possibility might be the initiation of debonding at the toe of shear crack. The analysis developed by Achintha and Burgoyne (2008) predicts the critical location for plate end anchoring device covering all likely form of plate end debonding.

However, this approach is quite complicated for modeling debonding as it involves a large number of parameters such that it becomes too cumbersome for design purpose. To overcome this, a combined method of dimensional analysis and Fuzzy logic is

proposed in this thesis. Dimensional analysis reduces the number of variables and then the Fuzzy method is applied to predict the failure load for a particular combination of parameters.

5.2.1 Dimensional analysis

The concept of dimensional analysis can be introduced, which involves combining the response of dimensionless groups of the variables involved in the system rather than their actual values. This allows a simple prediction system of critical debonded zone length for EBR strengthened beam to be created. Dimensional analysis is a useful tool which allows scaling the model parameters precisely in order to simulate the behaviour of a real structure at the laboratory scale. As for example, if it is required to find the curtailment length for a 5 m long and 1 m high beam and other material properties by means of an experimental test on a beam scaled 1:10 ($h = 0.1$ m), dimensional analysis suggests that this is possible only if the values of the dimensionless numbers of the original beams are kept similar to that of the scaled specimen.

5.2.2 Dimensional analysis and its application to the present problem

The fundamental principle of dimensional analysis is to express any physical expression in such a way that the relationship between the actual physical quantities remains valid and independent of the magnitude of the major component. So, dimensional analysis cut any system to a minimum dimension space, which can study the behaviour of a specific system by relating and ordering the assumed governing variables $(Q) = (Q_1, Q_2, Q_3, \dots, Q_n)$ containing independent primary dimensions $(D) = (D_1, D_2, D_3, \dots, D_m)$. The system is then reduced to $N = n - m$ dimensionless groups namely $(\Pi_1, \Pi_2, \Pi_3, \dots, \Pi_N)$ where N is less than n (Butterfield, 1999).

The basic of dimensional analysis and Buckingham's π theory is briefly described here. The idea of dimensional analysis is that any physically significant equation can be

represented in such a manner that the relationship between the actual physical quantities remains valid though the independent values may vary. The logical theories of this idea can be derived from Dimensional analysis. Suppose Q_0 is any physical quantities which is dependent on other variables. The first step in dimensional analysis is to identify the independent variables, Q_1, Q_2, \dots, Q_n that determine the value of Q_0 . So

$$Q_0 = f(Q_1, Q_2 \dots \dots Q_n); \quad (5.1)$$

The next step is listing the dimension of dependent as well as independent variables using the basic three dimensions: length(L), mass(m) and time(t). So all quantities will have dimension of the form

$$Q_i = L^a M^b T^c; \quad (5.2)$$

Where the exponent a, b and c are dimensionless numbers that follow from each quantities definition.

The next step is to pick from the complete set of physically independent variables, a complete dimensionally independent subset $Q_1 \dots \dots Q_k$ and expressing all the other dependent and independent variables as the product of powers of the set of base dimension. After choosing the dimensionally independent subset, the dimensions of Q_0 and remaining independent quantities $Q_{k+1} \dots \dots \dots Q_n$ will be expressed as follows

$$[Q_i] [Q_1^{N_{i1}} Q_2^{N_{i2}} \dots \dots \dots Q_k^{N_{ik}}]; \quad (5.3)$$

Where $i > k$ or $i = 0$;

The exponent N_{ij} are dimensionless real numbers which can be determined by inspection or by using the formal algebraic method.

Now the remaining n-k independent variables can be expressed in dimensionless form by dividing each one by the product of the power of $Q_1 \dots \dots Q_k$ having the same dimension.

$$P_i = \frac{Q_{k \ i}}{Q_1^{N_{(k \ i)1}} Q_2^{N_{(k \ i)2}} \dots \dots Q_k^{N_{(k \ i)k}}}, \quad (5.4)$$

Where $i=1,2,\dots,n-k$; and a dimensionless form of the dependent variable Q_o

$$P_o = \frac{Q_o}{Q_1^{N_{o1}} Q_2^{N_{o2}} \dots \dots Q_k^{N_{ok}}}, \quad (5.5)$$

Now Equation (5.1) can be expressed alternatively in the following form

$$\Pi_o = f(Q_1, Q_2, \dots \dots Q_k; \Pi_1, \Pi_2 \dots \dots \Pi_{n-k}) \quad (5.6)$$

In which all quantities are dimensionless except $Q_1 \dots Q_k$, and they cannot be put into dimensionless form since they are by definition independent of each other. So from the principal that any physically meaningful equation must be dimensionally homogeneous, it can be said that Equation (5.6) will not contain $Q_1 \dots Q_k$ and will take the following form

$$\Pi_o = f(\Pi_1, \Pi_2 \dots \dots \Pi_{n-k}) \quad (5.7)$$

This is the final results of dimensional analysis and contains Buckingham's Π theorem which states that 'when a complete relationship between dimensional physical quantities is expressed in dimensionless form, the number of independent quantities that appear in it is reduced from the original n to $n-k$, where k is the maximum number of the original n that are dimensionally independent'.

In studying the debonding phenomena the initial step in the dimensional analysis is to fix a complete set of independent quantities that might affect the debonding load. Equation (5.8) comprises all the prospective parameter that might affect the debonding load in a strengthened beam:

$$P = f(G_c, f'_c, E_c, f_y, \rho_t, E_p, \rho_p, h, \frac{b}{h}, L_{us-safe}) \quad (5.8)$$

Where P is the debonding load, G_c is the concrete mode I fracture energy, f'_c is the concrete compressive strength, E_c is the concrete modulus of elasticity, f_y is the yield strength of steel, ρ_t is the tension steel ratio, E_p is the modulus of elasticity of FRP steel, ρ_p is the FRP steel ratio, b is the width of the beam, h is the height of the beam, b/h represent the geometry of the sample and $L_{us-safe}$ is the safe curtailment length for FRP. Since b and h cannot be changed randomly, so the effect of these two parameters has been included by taking the aspect ratio, b/h and height, h .

However, parametric analysis run by the author showed that f'_c can be excluded from the analysis since they have insignificant influence in debonding load as shown in Figure 5.2.

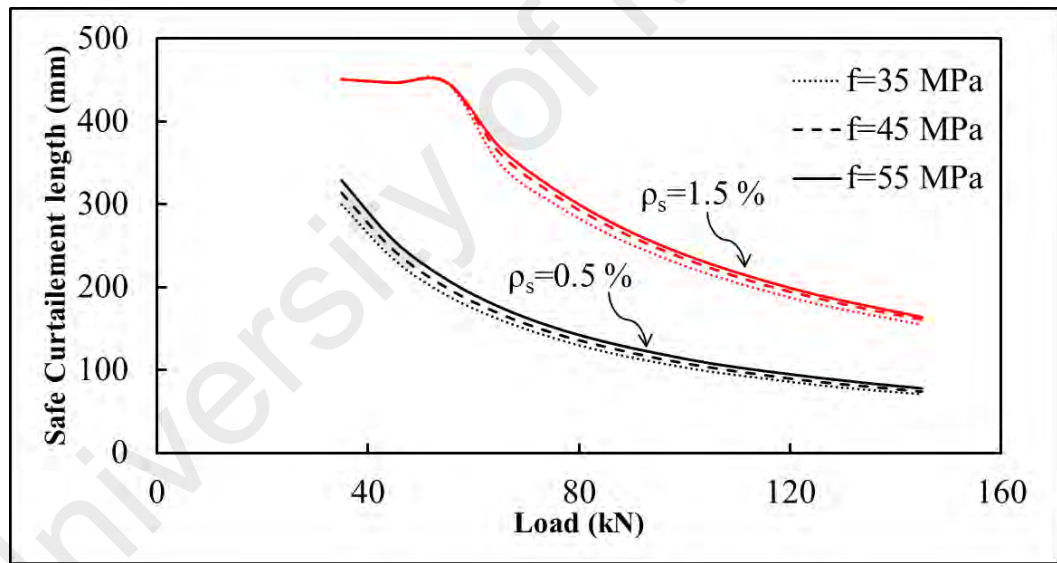


Figure 5.2: Load versus debonding load comparison for various compressive strengths

According to PI rules, the variables which are already dimensionless (such as steel and FRP ratio) cannot contribute to formulating the remaining PI groups. So, they are combined with their corresponding material properties steel yield and FRP modulus in the PI group.

On the other hand, only beam depth, h , is considered for further analysis since the geometrical ratio b/h is assumed to be constant in the present analysis. And for a fixed ratio the effect of beam width is also insignificant. So, based on these observations the set of prospective variables in Equation (5.8) can be reduced to

$$P = f(G_c, E_c, f_y, \rho_t, E_p, \rho_p, h, L_{us-safe}) \quad (5.9)$$

Application of Buckingham's Π Theorem to Equation (5.9) gives the following relationship in Equation (5.10).

$$\frac{P}{\sqrt{G_c E_c} h^{1.5}} = \phi_1\left(\frac{\rho_t f_y h^{0.5}}{\sqrt{G_c E_c}}, \frac{\rho_p E_p h^{0.5}}{\sqrt{G_c E_c}}, \frac{L_{us-safe} E_c}{\sqrt{G_c E_c} h}\right) \quad (5.10)$$

G_c, E_c, h are assumed as the dimensionally independent variables since they contains very basic dimensions. It is worth mentioning here that the independent dimension ' h ' is the representative of the size scale of the specimen and $\sqrt{G_c E_c}$ is the material property. As a result, the dimensionless functional relationship for the proposed model becomes

$$P'' = \phi_1(N_s, N_p, L''_{us-safe}) \quad (5.11)$$

$$N_s = \frac{\rho_t f_y h^{0.5}}{\sqrt{G_c E_c}} \quad (5.12)$$

$$N_p = \frac{\rho_p E_p h^{0.5}}{\sqrt{G_c E_c}} \quad (5.13)$$

$$P'' = \frac{P}{\sqrt{G_c E_c} h^{1.5}} \quad (5.14)$$

N_s and N_p are the governing dimensionless number i.e. normalized steel ratio and normalized FRP ratio.

P'' is the normalized force and

$$L''_{us-safe} = \frac{L_{us-safe} E_c}{\sqrt{G_c E_c} h} \quad (5.15)$$

$L''_{us-safe}$ is the normalized safe curtailment length.

Equation (5.11) implies that the structural reaction, in terms of nondimensional force – normalized safe curtailment length is a function of only the dimensionless number N_s representing the contribution of tension steel and N_p representing the contribution of strengthened steel. In other words, when the dimensionless parameters are kept constant physical resemblance is assumed though particular mechanical and geometrical properties might vary.

5.2.3 Interpretation of numerical results based on dimensional analysis

This section provides an interpretation of numerical results to obtain the exhaustive description of the effect of materials and geometrical properties on the curtailment length of FRP strengthened RC beams. As the evidence of analytical results obtained through the dimensional analysis, numerical simulations have been carried out on beams characterized by the values of $N_s=1.89$; $N_p=80.3$; although different geometrical and material properties have been assigned, as reported in Table 5.1.

Table 5.1 Mechanical and geometric properties of beam characterized by the same dimensionless value

Beam	b	h	f_y	ρ_t (%)	ρ_p (%)	E_p (GPa)	N_s	N_p
A	120	170	627	1.5	0.19	210	1.89	80.3
B	150	215		1.34	0.17		1.89	80.3
C	178	250		1.23	0.21		1.89	80.3

As expected the obtained numerical results expressed by the nondimensional load versus normalized safe curtailment length as shown in Figure 5.3 converge to a single graph. Such a result evidenced a physical similarity in the curtailment length by varying structural dimensions but keeping the nondimensional number constant. This implies that plate curtailment length can be predicted based on the two nondimensional numbers instead of separate geometric and mechanical properties.

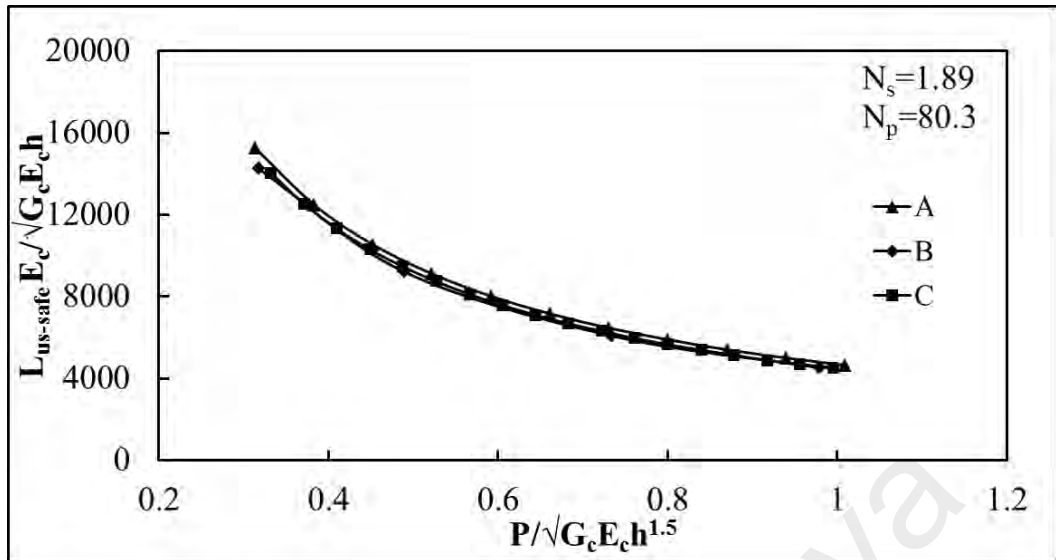
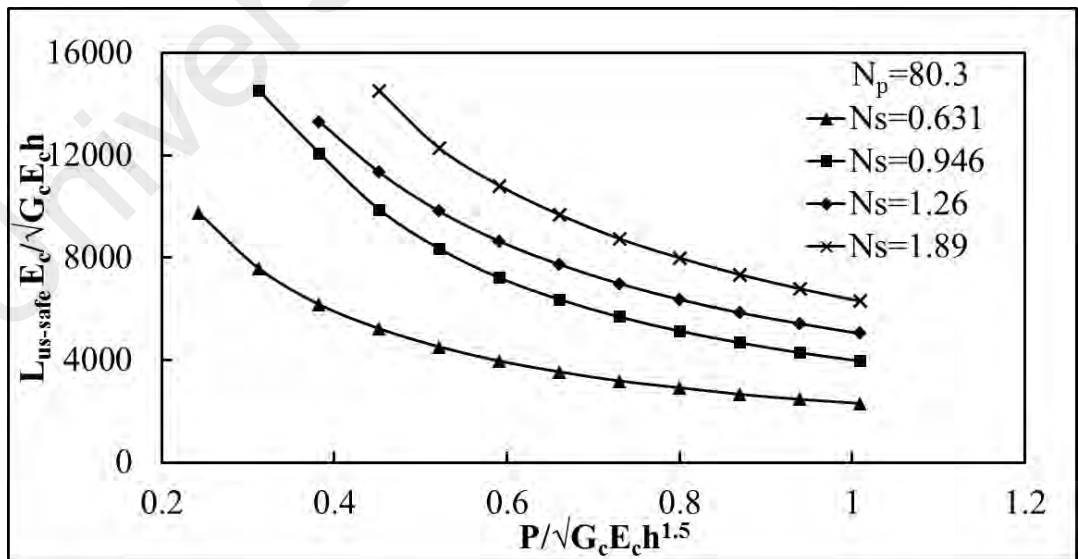


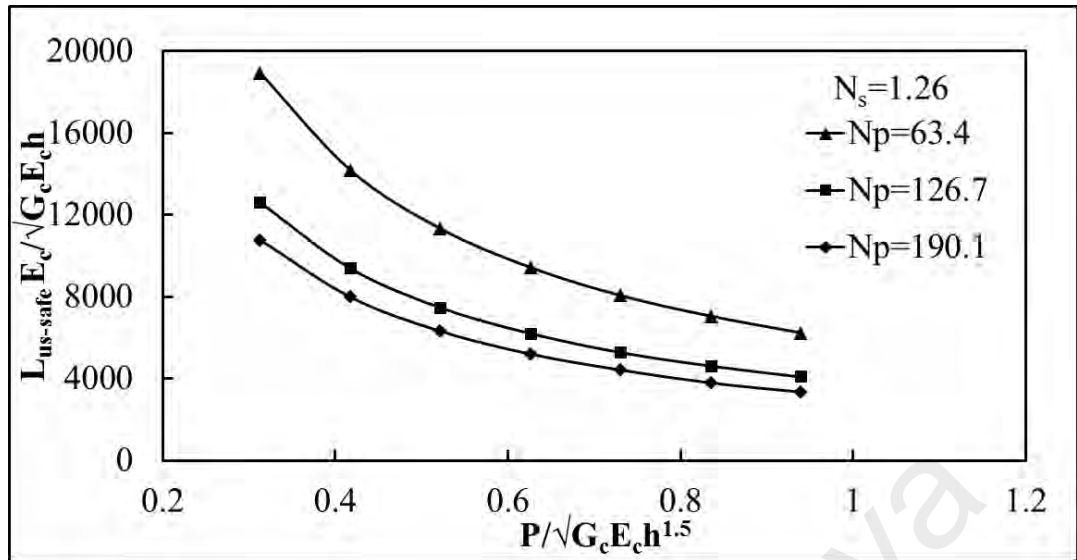
Figure 5.3: Nondimensional load versus normalized safe curtailment length

A numerical simulation for values of N_s ranging from 0.631 to 1.89 with N_p being fixed and N_p ranging from 63.4 to 190 with N_s being fixed are shown in Figure 5.4a and b. A clear increase in curtailment length is observed with the increasing N_s and decrease in curtailment length is observed with increasing N_p . This trend can be easily interpreted as the increase in steel percentage and FRP percentage captured in the terms N_s or N_p .



(a) Fixed N_p , Different N_s

Figure 5.4: Nondimensional load versus normalized safe curtailment length



(b) Fixed N_s , Different N_p

Figure 5.4, Continued

5.3 Implementation of Fuzzy

The previous section implies that critical section found for a particular beam can be interpreted for other beam combination if the dimensionless numbers are kept the same, but a procedure must be developed to use the results obtained from the parametric analysis as an actual design tool. One possible solution is the development of a series of curves for different values of characteristic numbers as shown in Figure 5.4. This however still requires a large number of dimensionless numbers combinations. So, a fuzzy logic expert system, FLES is used to find the nondimensional curtailment length for any combination of mechanical and geometric properties parameters.

The concept of Fuzzy has been first perceived in the year 1965 (Zadeh, 1965). Since then, it has been used by design engineers to develop a simple and intuitive control system for complicated systems. The superiority of Fuzzy operator than another operator is its capability of conceiving human perception. This thesis presents the construction of fuzzy knowledge-based model by if-then rules based on Mamdani approach using the fuzzy toolbox in MATLAB.

Application of Fuzzy logic in control process requires the following elements:

(a) Fuzzification- receiving the crisp numeric input and making them compatible for fuzzy decision-making logic.

(b) Rule base- preserve a set of if-then rules which encompasses the knowledge gathered by human expertise regarding solving the problem. It is composed of a set of logical statement for the linguistic variables used in the FLES with the membership function generated from previous expertise. Every fuzzy rule is the effect of an individual fuzzy set of input signals on the individual fuzzy set of the output signal.

(c) Inference- the numerical procedure of determining this effect. The influence produced by all rules for an individual set of the output signal are combined together to obtain the total output

(d) Defuzzification- the process of finding only a single crisp value that summarizes the fuzzy set.

Every linguistic input and output consist of a set of the membership function. There are various types of membership function available in MATLAB such as triangular, trapezoidal, Gauss et cetera. However triangular function is computationally more effective. The triangular curve is a function of a vector x and depends upon three scalar parameters a, b, c and can be represented as follows:

$$f(x; a, b, c) = \begin{cases} 0, & x \leq a \\ \frac{x-a}{b-a}, & a \leq x \leq b \\ \frac{c-x}{c-b}, & b \leq x \leq c \\ 0, & c \leq x \end{cases} \quad (5.16)$$

The general form of the fuzzy if-then rule is:

$$IF I_i THEN O_i = f_i(x_1, x_2, \dots, x_n) \quad (5.17)$$

Where I_i is the relation between fuzzy sets of input parameters defined using fuzzy operators, O_i is the output, f_i is the function and x_1, x_2, \dots, x_n - numerical value of input

There are two types of controller available, when the function f_i is polynomial it is called Takagi-Sugeno model, whereas when this function is reduced to constant value a zero order fuzzy controller is obtained and this is called Mamdani model. In this case, Fuzzy rule can be formulated as

$$IF I_i THEN O_i = A_{jk} \quad (5.18)$$

A_{jk} - is singular fuzzy set of output value j

Due to its simplicity Mamdani model is used in the analysis used in this thesis.

Centroid defuzzification is the most common among these as it gives quite accurate results and it can be expressed using following relation (Kozłowska, 2012)

$$z_o = \frac{\int \mu_i(x) x dx}{\int \mu_i(x) dx} \quad (5.19)$$

Where z_o is the Defuzzified output, x is the Output variable and μ_i is the membership function.

5.3.1 Fuzzy model development for EBR strengthened beam

Determination of safe curtailment length for EBR depends on five parameters: load, steel ratio, steel yield value, FRP ratio and FRP modulus as found from the previous section of the dimensional analysis. This could be further reduced to load, steel ratio and FRP ratio only by using the dimensionless numbers in Equations (5.12) and (5.13), which will incorporate the effect of steel yield f_y and FRP modulus E_p . Curtailment lengths are determined for different combination of load, steel ratio and FRP ratio for

the beam shown in Figure 5.5 using complete debonding analysis in MATLAB environment. These simulated values are recorded and subdivided into groups with specific ranges and linguistic variables such as VL, L, LM, M, HM, H, VH, VVH for creating the membership function for developing fuzzy modeling as shown in Table 5.2. The steps required for developing Fuzzy modeling are described in the subsequent section.

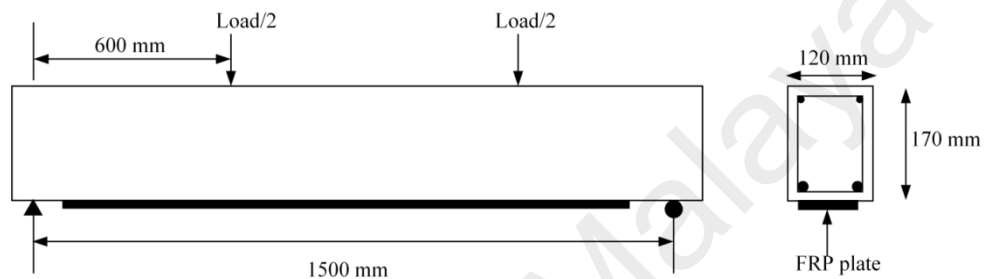
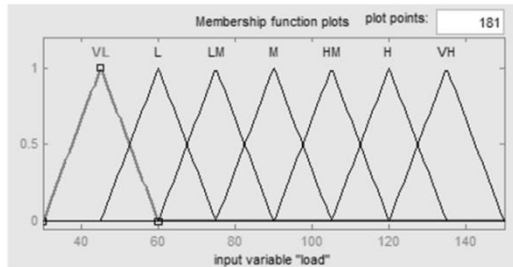


Figure 5.5: Beam specification for parametric analysis.

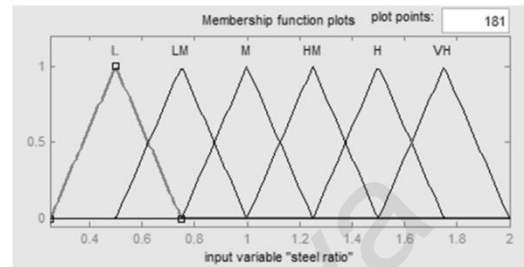
5.3.2 Fuzzify inputs

Fuzzification is the process of transforming the input data with the rule condition to determine how well the condition of each rule matches that particular input instance. The preliminary step is defining inputs and hence determining the degree by which each linguistic term fits each of the suitable fuzzy sets through membership function. According to dimensional analysis, the input in this study comprises of three input parameters with safe curtailment length as one output. The corresponding fuzzy sets in this study are quantitatively defined by a membership function. In order to create discrete membership functions, a necessary step is to specify the ranges of values and value at each point as presented in Table 5.2. System accuracy increases with the increase in a number of the overlapping membership function. The widths are chosen in such a way that each value represents a member of at least two sets. Among various types of membership function, the triangular function is computationally more effective.

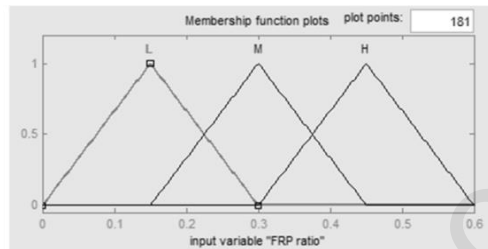
So this work adopted triangular member function. Figure 5.6 a to d shows the triangular overlapping membership functions developed for all three factors and safe curtailment length in the fuzzy system.



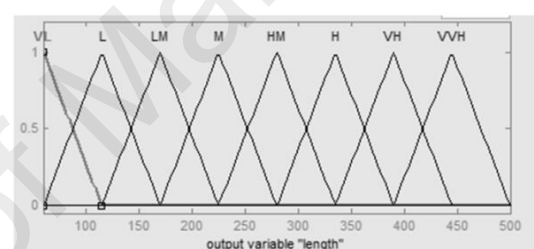
(a) membership function for P



(b) membership function for ρ_s

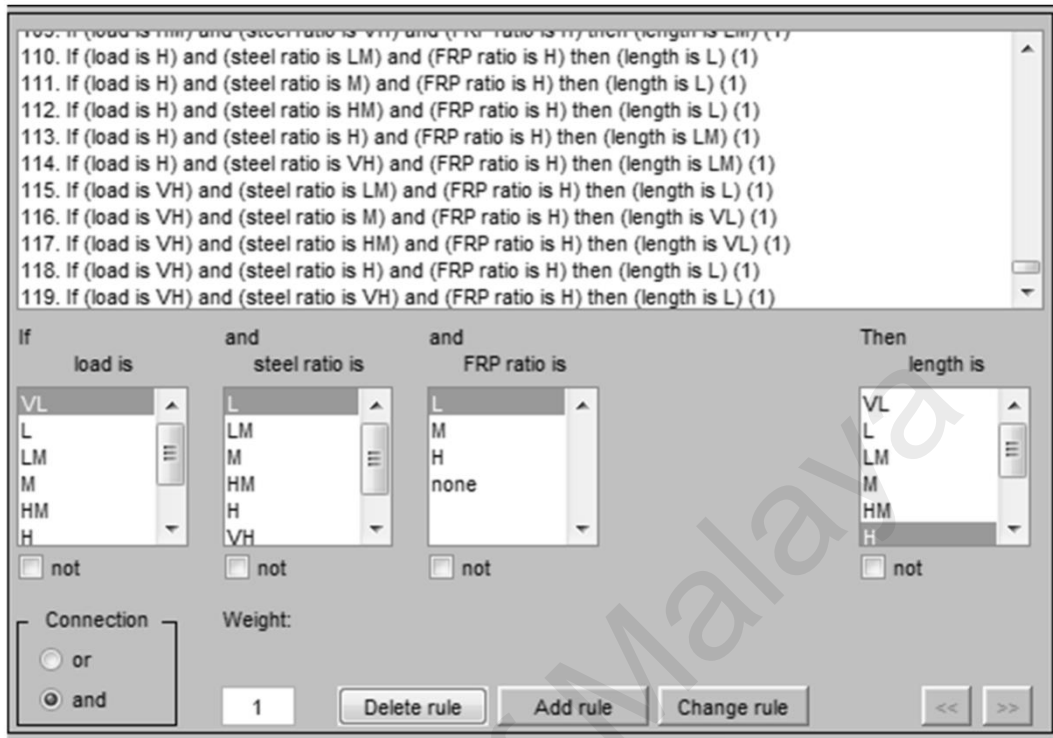


(c) membership function for ρ_p



(d) membership function for $L_{us-safe}$

Figure 5.6: Membership functions and rules created in fuzzy inference engine



(e) Rules created in fuzzy

Figure 5.6, Continued

5.3.3 Creating rule base

The next step in FLES is to map an input space to an output space in terms of if-then statements known as rules. The rule order is unimportant in this case and all rules are actually triggered simultaneously for a particular condition. Total 119 rules are formed from Table 5.2 based on the simulation results. Some rules are omitted due to their insignificance within the framework. The rules used in this fuzzy system are shown in Figure 5.6e.

Table 5.2 Membership function for different parameter

Fuzzy set label	Load (kN)	Steel ratio (%)	FRP ratio (%)	Curtailement Length (mm)
Very low (VL)	30 – 60	–	–	60 – 115
Low (L)	45 – 75	0.25 – 0.75	0 – 0.3	60 – 170
Low medium(LM)	60 – 90	0.5 – 1.0	–	115 – 225
Medium (M)	75– 105	0.75 – 1.25	0.15 – 0.45	170 – 280
High Medium(HM)	90– 120	1 – 1.5	–	225 – 335
High (H)	105 – 135	1.25 – 1.75	0.3 – 0.6	280 – 390
Very High (VH)	120 – 150	1.5 – 2	–	335 – 445
Very Very High (VVH)	–	–	–	390-500

5.3.4 Aggregation of truncated conclusions

The next step is the aggregation or rule fulfillment. In this process, fuzzy sets representing the output of each rule are combined into a single fuzzy set. In fuzzy inference engine rules are formed in the if-then format as shown here:

If P is VH and ρ_s is LM and ρ_p is H, then $L_{us-safe}$ is L. (VH, LM, H and L are fuzzy set labels representing very high, low medium, high and low respectively.)

The developed rules then generate fuzzy membership values corresponding to each input. Aggregation implies combining these three membership values in a unit output, correspondingly for other rules also.

5.3.5 Defuzzification

The last step in FLES is called defuzzification, which involves defuzzifying the fuzzy sets given to a control variable and transforming them into a single crisp value.

Various mathematical techniques are available for defuzzification process i.e. the process which yields only a single crisp value that summarizes the fuzzy set, such as centroid, bisector, mean, maximum and weighted average.

Among various methods of calculating output signal, COG (center of gravity) method is the most prevalent and appealing defuzzification method which has been used in this work.

To comprehend fuzzification, an example is considered here. For crisp input of $P=85$; $\rho_s=1.13$; $\rho_p=0.25$ the rules 15, 16, 21, 22, 57, 58, 63, 64, 101 and 102 are fired. The firing strength, α (truth value) of the eight rules are obtained as:

$$\alpha_{15} = \min \{ \mu_{LM}(P), \mu_M(\rho_s), \mu_L(\rho_p) \} = \min (0.34, 0.48, 0.34) = 0.34$$

$$\alpha_{16} = \min \{ \mu_{LM}(P), \mu_{HM}(\rho_s), \mu_L(\rho_p) \} = \min (0.34, 0.52, 0.34) = 0.34$$

$$\alpha_{21} = \min \{ \mu_M(P), \mu_M(\rho_s), \mu_L(\rho_p) \} = \min (0.67, 0.48, 0.34) = 0.34$$

$$\alpha_{22} = \min \{ \mu_M(P), \mu_{HM}(\rho_s), \mu_L(\rho_p) \} = \min (0.67, 0.52, 0.34) = 0.34$$

$$\alpha_{57} = \min \{ \mu_{LM}(P), \mu_M(\rho_s), \mu_M(\rho_p) \} = \min (0.34, 0.48, 0.67) = 0.34$$

$$\alpha_{58} = \min \{ \mu_{LM}(P), \mu_{HM}(\rho_s), \mu_M(\rho_p) \} = \min (0.34, 0.52, 0.67) = 0.34$$

$$\alpha_{63} = \min \{ \mu_M(P), \mu_M(\rho_s), \mu_M(\rho_p) \} = \min (0.67, 0.48, 0.67) = 0.48$$

$$\alpha_{64} = \min \{ \mu_M(P), \mu_{HM}(\rho_s), \mu_M(\rho_p) \} = \min (0.67, 0.52, 0.67) = 0.52$$

Therefore the membership functions for the conclusion achieved by rule (15), (16), (21), (22), (57), (58), (63) and (64) can be obtained as follows:

$$\begin{aligned}\mu_{15}(\text{length}) &= \min \{0.34, \mu_{HM}(\text{length})\}; & \mu_{16}(\text{length}) &= \min \{0.34, \mu_H(\text{length})\}; \\ \mu_{21}(\text{length}) &= \min \{0.34, \mu_{HM}(\text{length})\}; & \mu_{22}(\text{length}) &= \min \{0.34, \mu_H(\text{length})\}; \\ \mu_{57}(\text{length}) &= \min \{0.34, \mu_{LM}(\text{length})\}; & \mu_{58}(\text{length}) &= \min \{0.34, \mu_M(\text{length})\}; \\ \mu_{63}(\text{length}) &= \min \{0.48, \mu_{LM}(\text{length})\}; & \mu_{64}(\text{length}) &= \min \{0.52, \mu_{LM}(\text{length})\};\end{aligned}$$

Now $\text{length}^{\text{crisp}}$ can be obtained using Equation (5.19). This is the defuzzification step.

$$\text{Length} = \left(\frac{0.34*280+0.34*335+0.34*280+0.34*335+0.34*170+0.34*225+0.48*170+0.52*170}{0.34*6+0.48+0.52} \right) = 238$$

Figure 5.7 shows the results obtained from MATLAB for the same input values. Two sample fuzzy control surfaces for a set of associations described in the earlier section are shown in Figure 5.8, where output variable length is developed from the corresponding rules base for two inputs of load and steel ratio for two different fixed FRP ratios. The surface plots actually depict the impacts of the beam parameters on the FRP curtailment length.

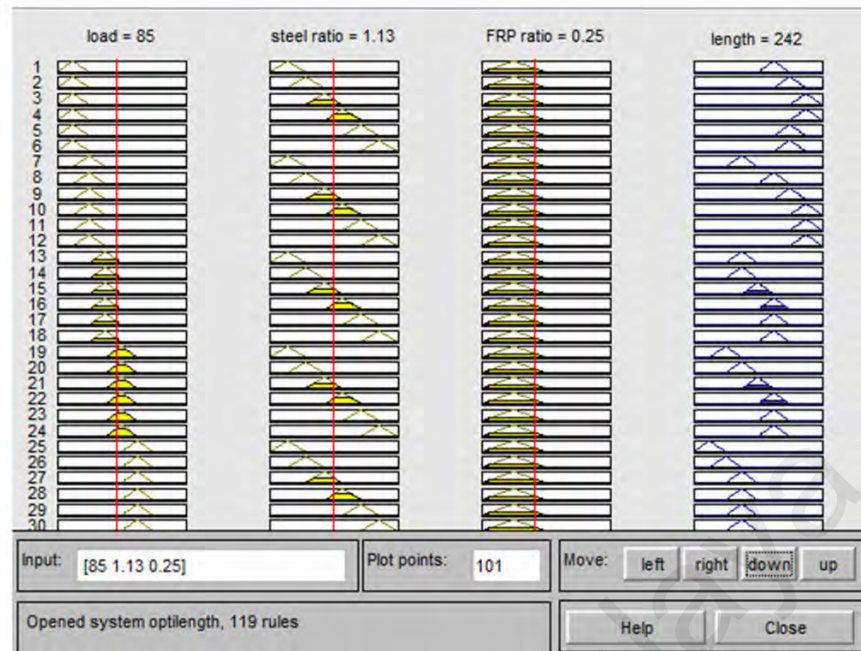


Figure 5.7: Fuzzy rule viewer in MATLAB

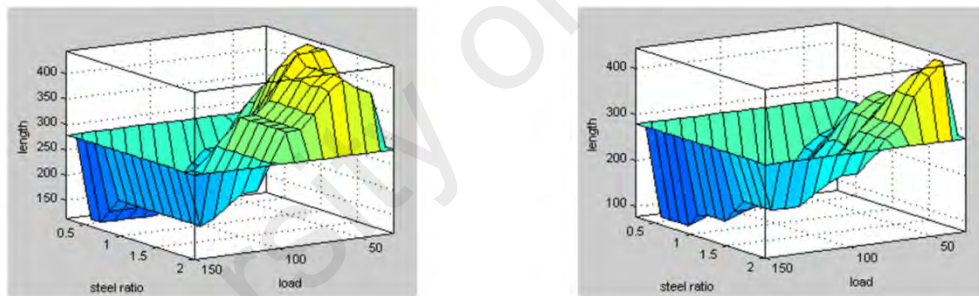


Figure 5.8: Example of control surfaces of fuzzy inferring system for length

5.4 Validation of the proposed model

Once the system is developed the critical length for any beam can be found from the Fuzzy system. This requires the equivalent steel ratio, equivalent FRP ratio and equivalent load using Equations (5.12) to (5.14). This equivalency ensures that the nondimensional numbers: N_s , N_p and P'' are the same. Then curtailment length L can be determined from fuzzy using the equivalent input. Hence the this curtailment length found from Fuzzy, can be converted to actual safe using Equation (5.15), with actual

' G ', ' h ' and ' E_c ' values of the beam in question. It should be mentioned here that the fuzzy is developed here for a G value of 0.15 N/mm.

5.4.1 Comparison of predicted failure load

Eleven sets of values are taken arbitrarily to compare fuzzy and actual simulation results. The process involves

- i. Determining the equivalent load, steel ratio, and FRP ratio from the geometric and material properties of the beam using dimensionless numbers, as per Equations (5.12) to (5.14).
- ii. Using the equivalent values as the input in fuzzy and determine the curtailment length.
- iii. Finding the actual length using Equation (5.15).

An example of obtaining the safe curtailment length for a beam at certain load is shown in Table 5.3 for beam B2, tested by Dong (2003).

Table 5.3 Obtaining safe curtailment length from F-dim analysis

Term	Value	Unit
Steel area, A_s	402.1	mm ²
Width, b	152.4	mm
Effective depth, d	253	mm
FRP area, A_{frp}	152.4	mm ²
Steel ratio, ρ_s	1.04	-
FRP ratio, ρ_f	0.395	-
FRP modulus, E_{frp}	73.1	MPa
Beam height, h	304.8	mm
Steel yield, f_y	410	MPa
load	148.2	kN
converted load using Equation(5.14)	61.73	kN
converted steel ratio using Equation(5.12)	0.91	-
converted FRP ratio using Equation(5.13)	0.18	-
length found using converted load, steel ratio and FRP ratio	349	mm
converted length using Equation (5.15)	381.6≈382	mm

The model predicted values are pretty close to the actually simulated values obtained using actual beam data as shown in Figure 5.9 which indicates the satisfactory implementation of the fuzzy model developed.

Table 5.4: Comparison of safe curtailment length: Actual versus fuzzy

Beam ID	Length _{Actual}	Length _{Fuzzy}	Length _{Fuzzy} / Length _{Actual}
Arduini et al.(1997)	120	115	0.96
Maalej & Bian(2001)	155	150	0.97
Nguyen (2001)	165	188	1.14
Pham & Al-Mahaidi (2006)	238	247	1.04
Fanning (2001)	326	333	1.02
Ceroni (2010)	344	309	0.90
Dong (2003)	369	381	1.03
	345	381	1.10
Benjeddou et al. (2007)	129	145	1.12
	158	146	0.92
	170	144	0.85

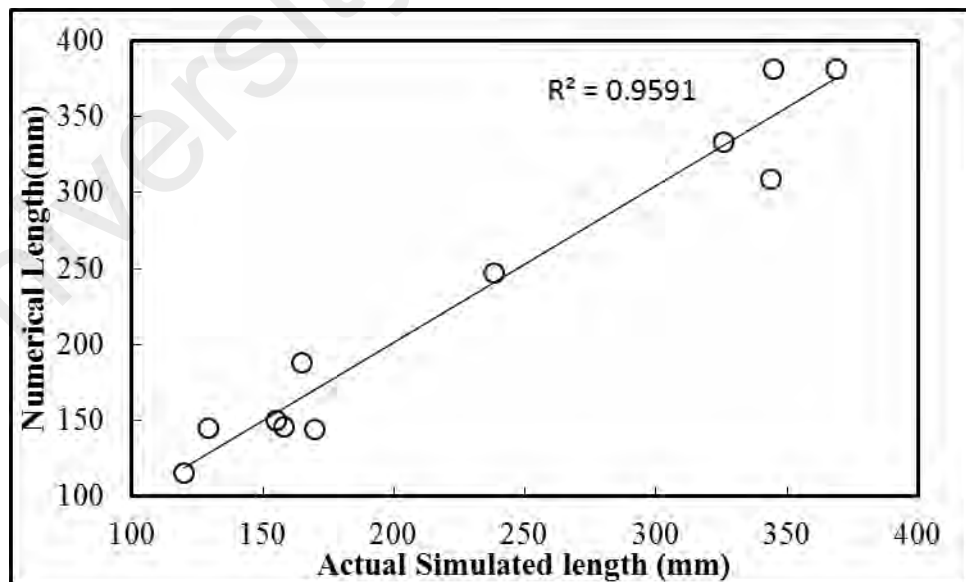


Figure 5.9: Comparison of actual and numerically predicted value

The prediction ability of the developed system has been assessed by evaluating the coefficient of efficiency (η). The value of η ranges from minus infinity (poor model) to 1.0 (perfect model), and can be computed using:

$$\eta = 1 - \frac{\sum_{i=1}^N (Q_{ac} - Q_{pre})^2}{\sum_{i=1}^N (Q_{ac} - Q_{ac_m})^2} \quad (5.20)$$

Where Q_{ac} and Q_{pre} are the values found from actual simulation and Fuzzy-Dimensional analysis model, respectively, for event i , and Q_{ac_m} is the mean of actual values. The value of η is computed to be equal to 0.96, which is close to 1, implying the successful training of the fuzzy model.

The relative error of the model can be computed using following equation

$$\varepsilon = \sum_{i=1}^N \left| \frac{Q_{ac} - Q_{pre}}{Q_{ac}} \right| \frac{100\%}{n}, \quad (5.21)$$

The value of ε is computed as 7.9% which is reasonable also.

5.4.2 Application of fuzzy model in Design

The debonding analysis presented in this thesis can provide the curtailment length location from the beam end for any beam at any load that would cause end debonding failure, as discussed previously. It can also provide the load value that would cause IC debonding failure. The allowable FRP strain at the mid-section of the beam can be determined from the load value. A complete fuzzy system has to be developed based on the results obtained from the detailed parametric analysis of beams with different combination of steel ratio, FRP ratio, beam dimension, to obtain the safe curtailment location from beam end and the allowable FRP strain at the mid-section for IC debonding. After the formation of the fuzzy system, the safe curtailment length can be determined from the fuzzy system alongside the dimensional analysis using the

procedure illustrated in Table 5.3. Similarly, limiting strain can be determined using the same procedure for IC debonding. This safe curtailment length and limiting strain value obtained from the proposed FRP debonding failure model can be easily integrated into the design using the following approach:

i. Let us consider a beam of length 2.9 m, with a shear span of 1 m. The factored moment capacity M_u of the beam has to be determined first. For the dead load and the design live load it is assumed that the factored moment capacity is equal to 65 kN-m.

ii. Obtaining the beam dimensions, the material properties of the beam to be designed for strengthening purposes. In this case following properties are assumed: beam width=152.4 mm; Beam height=305 mm; steel rebar=2 No. 16; concrete compressive strength $f=38$ Mpa; $f_y=500$; $t_p=1$ mm; $B_{frp}=152.4$ mm (one ply); $E_{frp}=73.1$ Mpa.

iii. Computing the steel rebar area and FRP area. $A_s=402.1$ mm²; $A_{frp}=152.1$ mm²

iv. Calculating the maximum load allowed in the beam without IC debonding by applying the model using the procedure described in 4.3.1. The load is found to be 157 kN.

v. Computing the moment capacity M_n of the beam for that load.

$$M_n=157*1/2=78.5;$$

vi. If the factored moment M_n is greater than or equal to M_u , then the design is sufficient with the assumed FRP without causing debonding failure. Otherwise, the FRP area has to be revised, and the analysis from steps 4 to 6 will be repeated until the criteria are met. Here, M_n is greater than M_u , so the section is sufficient for that load;

vii. Once the FRP area is fixed for the beam, the next step is to fix the curtailment location from the beam's end.

viii. The maximum force corresponding to M_u is determined; hence the safe curtailment location can be determined from the Fuzzy-dim system, which can then be implemented in the beam.

5.5 Summary

This study represents a model to predict safe curtailment length for end debonding of FRP strengthened RC beam to be used for design purpose. The analysis is based on the GEBA and fracture mechanics approach which is an effective but lengthy process to be used in design directly. The results demonstrate that the combination of dimensional analysis with the fuzzy method is capable of predicting critical debonding length for PE debonding failure with reasonable accuracies for any strengthened RC beam with various dimensions and property.

CHAPTER 6: CONCLUSIONS

6.1 General

A GEBA-based debonding prediction model with fracture energy as the failure criteria is developed and validated against published experimental data for beams strengthened using different techniques. The moment-curvature relationships of the types of beams studied in this thesis are simulated. The debonding loads for prior stated types of strengthened beams are predicted. Finally, a fuzzy dimensional analysis-based model is developed for the field applications of the model. The following important conclusions are drawn on the basis of the objectives of the research work.

6.2 Development of GEBA based model for strengthened beams using NSM and hybrid technique

The validity of the moment-curvature model proposed in this thesis is evaluated by comparing the load-versus-deflection and load-versus-FRP strain plots for the beams strengthened using NSM and hybrid techniques, as presented in Chapter 3. The results of the proposed model demonstrate a realistic agreement with the published experimental data. The strain, curvature, neutral axis depth, centroidal depth, and deflection can be determined from this moment-curvature analysis with sufficient accuracy.

For end debonding, the model provides a safe curtailment length, which can be used in beams with anchorage devices without causing failure. The model proposes a failure criterion for estimating IC debonding failure. On the basis of the analysis, the model proposes that the debonding load for IC type failure is the load beyond yield capacity, which gives a debonded zone length of 10 mm, at the critical fracture energy. In practical applications, the strain value obtained from the debonding analysis model can be used as a limiting strain value in design.

The comparison of debonding loads obtained from the model for EBR and NSM strengthened beams shows that, with all the other parameters remaining the same, the model can capture the change in the technique quite efficiently with a 10% tolerance.

For beams strengthened using various curtailment lengths from the beam end, the prediction is quite efficient with a 5% tolerance. The types of failure obtained from predictions are PE, combined PE and shear, or simply flexure failure, which goes well with the actual failure mode in most cases. Increasing the curtailment length does not always ensure increased capacity. The analysis can also capture this trend and predict how much curtailment can be done to reach the maximum capacity of the beam.

The efficiency of the model is checked through validation of beams strengthened using different percentages of reinforcement. The results demonstrate that the developed GEBA-based model can predict the debonding load with a 5% tolerance in most cases. However, the disparity between the predicted and actual debonding load is sometimes as high as 28%. Increasing the steel ratio does not mean increased capacity in the same ratio, which is also supported by experiments and analyses.

The effectiveness of the developed GEBA-based model is evaluated for different adhesive properties. The model is capable of predicting failure for an epoxy adhesive with good accuracy. However, the model gives a more scattered prediction for a beam with cement paste as adhesive than the experiment, thereby indicating the limitation of the model when used for beams with cement-type adhesives. This finding is due to the consideration of the adhesive as an elastic material during the formulation of the model.

The developed GEBA-based model is validated for beams strengthened using different FRP materials (CFRP and GFRP), and the results show that the model can predict the debonding load with a 10% tolerance.

The study also presents the applicability of the model for beams strengthened using hybrid technique, i.e., combined NSM and EBR techniques, which is discussed in only a few studies. The model is validated for beams strengthened using the hybrid technique. The prediction is good in PE debonding. However, for IC debonding, the model underestimates the IC debonding load in the experiment by 20%.

On average, the simulated result is 1% lower than the experimental results with a standard deviation of 0.09 for the NSM-strengthened beam and 5% lower than experimental with a standard deviation of 0.09 for hybrid strengthened beam.

6.3 Application of the GEBA-based model for precracked and prestressed FRP and T-beams

The load-versus-deflection and load-versus-FRP strain plots for the aforementioned types of beams are compared and show reasonable agreement with the published experimental data, as shown in Chapter 3.

The application of the GEBA-based model is employed for predicting the IC debonding of FRP-strengthened RC beams that are precracked before strengthening. The model can predict the failure load in precracked beams within 5% to 10% of the experimental load. On average, the model underestimates the results by 3% with a standard deviation of 9%.

The simulations of beams that are strengthened using prestressed FRP comprise EBR and NSM-strengthened beams. Prediction using the GEBA-based model in beams strengthened with prestressed FRP varies from 2% to 27% with an average underestimation of 3% from the experiment and a standard deviation of 9%.

The analysis yields a good approximation with a 10% tolerance of failure load for T-beams relative to the data available in the literature.

6.4 GEBA based model: Overall performance and parametric study

The average value of the ratio of theoretical (obtained using model) versus experimental failure load is 0.96 with a standard deviation of 0.09, thereby implying that the model is good in approximating debonding load for the types of beams discussed in this thesis.

A parametric study is performed for NSM-strengthened beams. The study shows that the parameters that affect the safe curtailment length in end debonding and debonded zone length in case of IC debonding, for beams strengthened using the NSM technique, are mainly the steel and FRP percentages and beam dimension. The effect of compressive strength is minimal.

The curtailment length or debonded zone length increases with the steel percentages and beam height. This finding is probably due to the increased stiffness of the beam, which causes delays in yielding and consequently in debonding. Conversely, an increase in FRP percentage decreases the curtailment length and debonded zone length.

6.5 Fuzzy method and dimensional analysis for practical application

Estimating debonding load using GEBA and fracture mechanics is an exhaustive numerical procedure. Therefore, this study develops a model for predicting the critical debonding length for PE debonding of FRP-strengthened EBR RC beam, as presented in Chapter 5, by using dimensional analysis and fuzzy approach. This work aims to evaluate the applicability of the GEBA-based model in practical design. The conclusions drawn from Chapter 5 are summarized below:

Dimensional analysis reduces the number of parameters and converts specific values for a specific combination of geometric properties of the beam to a normalized number.

The affecting parameters in debonding analysis can be combined with two nondimensional numbers N_s (normalized steel ratio) and N_p (normalized FRP ratio). This hypothesis can be used efficiently to determine the accurate value of experimental results. As far as the curtailment length is concerned, the normalized length is a decreasing function of N_s or N_p , provided that one is constant while the other being changed.

By using MATLAB fuzzy environment, the results of parametric analysis using GEBA with fracture mechanics are incorporated in the fuzzy tool in rule forms. From this normalized length, the value can be determined for equivalent N_s , N_p , and normalized load.

The proposed model is validated against published experimental results, and the simulation and experimental results agree. The goodness of the fuzzy model is checked using the coefficient of efficiency, and is found to be 0.96, thereby implying the successful training of the fuzzy model.

6.6 Recommendation for future works

- i. The database on detailed failure of IC debonding of strengthened RC beams is rather limited. An exhaustive experimental work for IC debonding should be performed using digital image correlation and microscopic observation of IC debonding failure.
- ii. The GEBA-based method can be extended for indeterminate beams setup.
- iii. The proposed fuzzy dimensional model can be extended for estimating IC debonding failure, NSM strengthening, and precracked and prestressed beams. Hence, a complete design package using the GEBA-based method should be developed.

- iv. Further experimental works are required to increase the efficiency of the model for beams strengthened using the hybrid technique.
- v. The applicability of the GEBA-based method for fatigue loading should be investigated.

University of Malaya

REFERENCES

- Achintha, M. (2009). *Fracture Analysis of Debonding mechanism of FRP plate*. (Doctor of Philosophy), University of Cambridge. , United Kingdom.
- Achintha, M., & Burgoyne, C. (2008). Fracture mechanics of plate debonding. *Journal of Composites for Construction*, 12(4), 396-404.
- Achintha, M., & Burgoyne, C. (2013). Fracture energy of the concrete–FRP interface in strengthened beams. *Engineering Fracture Mechanics*, 110, 38-51.
- Achintha, M., & Burgoyne, C. J. (2009). Moment-curvature and strain energy of beams with external fiber-reinforced polymer reinforcement. *ACI Structural Journal*, 106(1).
- Achintha, M., & Burgoyne, C. J. (2012). Prediction of FRP debonding using the global-energy-balance approach. *Magazine of Concrete Research*, 64(11), 1033.
- ACI-4402R-08. (2008). *Guide for the design and construction of externally bonded FRP systems for strengthening concrete structures*. Retrieved from Farmington Hill, Mich.:
- ACI-CODE. (2008). *Building Code requirements for Structural Concrete*. Retrieved from Detroit, :
- Ahmed, O., Van Gemert, D., & Vandewalle, L. (2001). Improved model for plate-end shear of CFRP strengthened RC beams. *Cement and Concrete Composites*, 23(1), 3-19.
- Al-Mahmoud, F., Castel, A., & François, R. (2012). Failure modes and failure mechanisms of RC members strengthened by NSM CFRP composites–Analysis of pull-out failure mode. *Composites Part B: Engineering*, 43(4), 1893-1901.
- Al-Mahmoud, F., Castel, A., François, R., & Tourneur, C. (2010). RC beams strengthened with NSM CFRP rods and modeling of peeling-off failure. *Composite Structures*, 92(8), 1920-1930.
- Al-Saadi, N. T. K., & Al-Mahaidi, R. (2016). Modelling of near-surface mounted carbon fibre reinforced polymer strips embedded in concrete with cement-based adhesive. *Construction and Building Materials*, 127, 383-393.
- Al-Zaid, R. A., El-Sayed, A. K., Al-Negheimish, A. I., Shuraim, A. B., & Alhozaimy, A. M. (2014). Strengthening of structurally damaged wide shallow RC beams

using externally bonded CFRP plates. *Latin American Journal of Solids and Structures*, 11(6), 946-965.

Alfano, G., De Cicco, P. D., Fiorenzo, & Prota, A. (2011). Intermediate debonding failure of RC beams retrofitted in flexure with FRP: Experimental results versus prediction of codes of practice. *Journal of Composites for Construction*, 16(2), 185-195.

Ali-Ahmad, M., Subramaniam, K., & Ghosn, M. (2006). Experimental investigation and fracture analysis of debonding between concrete and FRP sheets. *Journal of engineering mechanics*, 132(9), 914-923.

Almassri, B., Kreit, A., Al Mahmoud, F., & François, R. (2014). Mechanical behaviour of corroded RC beams strengthened by NSM CFRP rods. *Composites Part B: Engineering*, 64, 97-107.

Altun, F., Tanrıöven, F., & Dirikgil, T. (2013). Experimental investigation of mechanical properties of hybrid fiber reinforced concrete samples and prediction of energy absorption capacity of beams by fuzzy-genetic model. *Construction and Building Materials*, 44, 565-574.

Amarasinghe, N., & Gamage, J. (2016). *Experimental study on integrated method of NSM and EBR techniques for flexural strengthening of Concrete Beams using CFRP*. Paper presented at the 6th International Conference on Structural Engineering and Construction Management 2015, Kandy, Sri Lanka, 11th-13th December 2015.

Arduini, M., Di Tommaso, A., & Nanni, A. (1997). Brittle failure in FRP plate and sheet bonded beams. *ACI Structural Journal*, 94(4).

Arduini, M., & Nanni, A. (1997). Behavior of precracked RC beams strengthened with carbon FRP sheets. *Journal of Composites for Construction*, 1(2), 63-70.

Aslani, F., & Jowkarmeimandi, R. (2012). Stress-strain model for concrete under cyclic loading. *Magazine of Concrete Research*, 64(8), 673-685.

Asplund, S. (1949). *Strengthening bridge slabs with grouted reinforcement*. Paper presented at the Journal Proceedings.

Baluch, M., Ziraba, Y., Azad, A., Sharif, A., Al-Sulaimani, G., & Basunbul, I. (1995). Shear strength of plated RC beams. *Magazine of Concrete Research*, 47(173), 369-374.

- Barros, J. A., & Fortes, A. (2005). Flexural strengthening of concrete beams with CFRP laminates bonded into slits. *Cement and Concrete Composites*, 27(4), 471-480.
- Barros, J. A., Taheri, M., Salehian, H., & Mendes, P. J. (2012). A design model for fibre reinforced concrete beams pre-stressed with steel and FRP bars. *Composite Structures*, 94(8), 2494-2512.
- Bashir, R., & Ashour, A. (2012). Neural network modelling for shear strength of concrete members reinforced with FRP bars. *Composites Part B: Engineering*, 43(8), 3198-3207.
- Bazant, Z. (1992). *Fracture mechanics of concrete structures* (Z. P. Bazant Ed.). England: Elsevier Science Publisher Limited.
- Bažant, Z. (2002). Concrete fracture models: testing and practice. *Engineering Fracture Mechanics*, 69(2), 165-205.
- Bažant, Z. P., & Becq-Giraudon, E. (2002). Statistical prediction of fracture parameters of concrete and implications for choice of testing standard. *Cement and Concrete Research*, 32(4), 529-556.
- Benjeddou, O., Ouezdou, M. B., & Bedday, A. (2007). Damaged RC beams repaired by bonding of CFRP laminates. *Construction and building materials*, 21(6), 1301-1310.
- Bilotta, A., Ceroni, F., Nigro, E., & Pecce, M. (2015). Efficiency of CFRP NSM strips and EBR plates for flexural strengthening of RC beams and loading pattern influence. *Composite Structures*, 124, 163-175.
- Branson, D. E. (1968). Design procedures for computing deflections. *ACI Journal Proceedings*, 65(9), 730-742.
- Bruno, D., Greco, F., Feudo, S. L., & Blasi, P. N. (2016). Multi-layer modeling of edge debonding in strengthened beams using interface stresses and fracture energies. *Engineering structures*, 109, 26-42.
- Bull, J. W. (2012). *Precast concrete raft units*: Springer Science & Business Media.
- Butterfield, R. (1999). Dimensional analysis for geotechnical engineers. *Geotechnique*, 49(3), 357-366.

- Buyukozturk, O., Gunes, O., & Karaca, E. (2004). Progress on understanding debonding problems in reinforced concrete and steel members strengthened using FRP composites. *Construction and Building Materials*, 18(1), 9-19.
- Capozucca, R., Blasi, M., & Corina, V. (2015). NSM technique: Bond of CFRP rods and static/dynamic response of strengthened RC beams. *Composite Structures*, 127, 466-479.
- Capozucca, R., & Magagnini, E. (2016). Vibration of RC beams with NSM CFRP with unbonded/notched circular rod damage. *Composite Structures*, 144, 108-130.
- Carolin, A. (2003). *Carbon fiber reinforced polymers for strengthening of structural elements*. (PhD), Luleå Univ. of Technology, Luleå, Sweden.
- Carpinteri, A., & Corrado, M. (2010). Dimensional analysis approach to the plastic rotation capacity of over-reinforced concrete beams. *Engineering Fracture Mechanics*, 77(7), 1091-1100.
- Castro, E. K., Melo, G. S., & Nagato, Y. (2007). *Flexural strengthening of RC "T" beams with near surface mounted (NSM) FRP reinforcements*. Paper presented at the Proceedings of International Symposium on FRP Reinforcement of Concrete Structures (FRPRCS-8), Patras, Greece.
- CEB-FIP. (2010). *CEB-FIP Model Code*. Retrieved from Lausanne, Switzerland.:
- Ceroni, F. (2010). Experimental performances of RC beams strengthened with FRP materials. *Construction and Building Materials*, 24(9), 1547-1559.
- Ceroni, F., & Pecce, M. (2009). Design provisions for crack spacing and width in RC elements externally bonded with FRP. *Composites Part B: Engineering*, 40(1), 17-28.
- Chen, G., Teng, J., Chen, J., & Xiao, Q. (2015). Finite element modeling of debonding failures in FRP-strengthened RC beams: A dynamic approach. *Computers & Structures*, 158, 167-183.
- Chen, Y., Ashour, A., & Garrity, S. (2007). Modified four-hinge mechanism analysis for masonry arches strengthened with near-surface reinforcement. *Engineering structures*, 29(8), 1864-1871.
- Choi, H. T., West, J. S., & Soudki, K. A. (2010). Effect of partial unbonding on prestressed near-surface-mounted CFRP-strengthened concrete T-beams. *Journal of Composites for Construction*, 15(1), 93-102.

- Choi, K.-K., Sim, W.-C., & Kim, H.-S. (2015). Shear strength prediction of reinforced-concrete beams based on fuzzy theory. *Proceedings of the Institution of Civil Engineers-Structures and Buildings*, 169(5), 357-372.
- Committee, A., Institute, A. C., & Standardization, I. O. f. (2008). *Building code requirements for structural concrete (ACI 318-08) and commentary*.
- Coronado, C. A., & Lopez, M. M. (2006). Sensitivity analysis of reinforced concrete beams strengthened with FRP laminates. *Cement and Concrete Composites*, 28(1), 102-114.
- Dalfré, G. M., & Barros, J. A. (2013). NSM technique to increase the load carrying capacity of continuous RC slabs. *Engineering structures*, 56, 137-153.
- Daouadji, T. H. (2013). Analytical analysis of the interfacial stress in damaged reinforced concrete beams strengthened by bonded composite plates. *Strength of Materials*, 45(5), 587-597.
- Daouadji, T. H., Rabahi, A., Abbes, B., & Adim, B. (2016). Theoretical and finite element studies of interfacial stresses in reinforced concrete beams strengthened by externally FRP laminates plate. *Journal of Adhesion Science and Technology*, 30(12), 1253-1280.
- Darain., K. M. U., Jumaat, M. Z., Hossain, M. A., Hosen, M. A., Obaydullah, M., Huda, M. N., & Hossain, I. (2015). Automated serviceability prediction of NSM strengthened structure using a fuzzy logic expert system. *Expert Systems with Applications*, 42(1), 376-389.
- Darain., K. M. U., Shamshirband, S., Jumaat, M. Z., & Obaydullah, M. (2015). Adaptive neuro fuzzy prediction of deflection and cracking behavior of NSM strengthened RC beams. *Construction and Building Materials*, 98, 276-285.
- De Lorenzis, L. (2004). Anchorage Length of Near-Surface Mounted Fiber-Reinforced Polymer Rods for Concrete Strengthening? Analytical Modeling. *ACI Structural Journal*, 101(3).
- De Lorenzis, L., & Teng, J. (2007). Near-surface mounted FRP reinforcement: An emerging technique for strengthening structures. *Composites Part B: Engineering*, 38(2), 119-143.
- de Sena Cruz, J. M., & Oliveira de Barros, J. A. (2004). Bond between near-surface mounted carbon-fiber-reinforced polymer laminate strips and concrete. *Journal of Composites for Construction*, 8(6), 519-527.

- Dong, Y. (2003). *Static and fatigue performance of reinforced concrete beams retrofitted with external CFRP composites*. (PhD), University of Illinois.
- Ebead, U., & Saeed, H. (2013). Hybrid shear strengthening system for reinforced concrete beams: An experimental study. *Engineering structures*, 49, 421-433.
- El-Gamal, S., Al-Nuaimi, A., Al-Saidy, A., & Al-Lawati, A. (2016). Efficiency of near surface mounted technique using fiber reinforced polymers for the flexural strengthening of RC beams. *Construction and Building Materials*, 118, 52-62.
- El-Hacha, R., & Rizkalla, S. H. (2004). Near-surface-mounted fiber-reinforced polymer reinforcements for flexural strengthening of concrete structures. *ACI Structural Journal*, 101(5).
- El-Mihilmy, M. T., & Tedesco, J. W. (2000). Deflection of reinforced concrete beams strengthened with fiber-reinforced polymer (FRP) plates. *ACI Structural Journal*, 97(5).
- El-Hacha, R., Wight, R., & Green, M. (2001). Prestressed fibre-reinforced polymer laminates for strengthening structures. *Progress in Structural Engineering and Materials*, 3(2), 111-121.
- Fanning, P. J., & Kelly, O. (2001). Ultimate response of RC beams strengthened with CFRP plates. *Journal of Composites for Construction*, 5(2), 122-127.
- Fernandes, P. M., Silva, P. M., & Sena-Cruz, J. (2015). Bond and flexural behavior of concrete elements strengthened with NSM CFRP laminate strips under fatigue loading. *Engineering structures*, 84, 350-361.
- Firmo, J., & Correia, J. (2015). Fire behaviour of thermally insulated RC beams strengthened with NSM-CFRP strips: Experimental study. *Composites Part B: Engineering*, 76, 112-121.
- Fossetti, M., & Papia, M. (2012). Dimensionless analysis of RC rectangular sections under axial load and biaxial bending. *Engineering structures*, 44, 34-45.
- Fukuzawa, K., Numao, T., Wu, Z., & Mitsui, M. (1997). *Critical strain energy release rate of interface debonding between carbon fiber sheet and mortar*. Paper presented at the 3rd International symposium on non metallic reinforcement for concrete structures, Sapporo, Japan.
- Garden, H., & Hollaway, L. (1997). A preliminary evaluation of carbon fibre reinforced polymer plates for strengthening reinforced concrete members. *Proceedings of the ICE-Structures and Buildings*, 122(2), 127-142.

- Garden, H., & Hollaway, L. (1998). An experimental study of the failure modes of reinforced concrete beams strengthened with prestressed carbon composite plates. *Composites Part B: Engineering*, 29(4), 411-424.
- Garden, H., Quantrill, R., Hollaway, L., Thorne, A., & Parke, G. (1998). An experimental study of the anchorage length of carbon fibre composite plates used to strengthen reinforced concrete beams. *Construction and Building Materials*, 12(4), 203-219.
- Gopinath, S., Murthy, A. R., & Patrawala, H. (2016). Near surface mounted strengthening of RC beams using basalt fiber reinforced polymer bars. *Construction and Building Materials*, 111, 1-8.
- Guan, G., & Burgoyne, C. (2013). Determination of Debonding Fracture Energy Using Wedge-Split Test. Retrieved from <http://www-civ.eng.cam.ac.uk/cjb/papers/cp99.pdf>
- Guan, G., & Burgoyne, C. (2013.). *Determination of Debonding Fracture Energy Using Wedge-Split Test*. Paper presented at the FRPRCS-11, Guimaraes, Portugal, .
- Guan, G., Burgoyne, C., & Achintha, M. (2014). Parametric study of FRP plate debonding using global energy balance. *Journal of Composites for Construction*, 18(6), 04014020.
- Guinea, G., Planas, J., & Elices, M. (1992). Measurement of the fracture energy using three-point bend tests: Part 1—Influence of experimental procedures. *Materials and Structures*, 25(4), 212-218.
- Güler, K., Demir, F., & Pakdamar, F. (2012). Stress–strain modelling of high strength concrete by fuzzy logic approach. *Construction and Building Materials*, 37, 680-684.
- Gunes, O. (2004). *A fracture based approach to understanding debonding in FRP bonded structural members*. (Doctor of Philosophy in Structures an Materials), Massachusetts Institute of Technology, United States of America.
- Gunes, O., Buyukozturk, O., & Karaca, E. (2009). A fracture-based model for FRP debonding in strengthened beams. *Engineering Fracture Mechanics*, 76(12), 1897-1909.
- Hajihashemi, A., Mostofinejad, D., & Azhari, M. (2011). Investigation of RC beams strengthened with prestressed NSM CFRP laminates. *Journal of Composites for Construction*, 15(6), 887-895.

- Hassan, T. K., & Rizkalla, S. H. (2004). Bond mechanism of near-surface-mounted fiber-reinforced polymer bars for flexural strengthening of concrete structures. *ACI Structural Journal*, 101(6).
- Hawileh, R., Abdalla, J., Naser, M., & Tanarlan, M. (2015). Finite element modeling of shear deficient RC beams strengthened with NSM CFRP rods under cyclic loading. *Spec. Publ*, 301, 1-18.
- Hawileh, R. A. (2012). Nonlinear finite element modeling of RC beams strengthened with NSM FRP rods. *Construction and Building Materials*, 27(1), 461-471.
- Hearing, B. P. (2000). *Delamination in reinforced concrete retrofitted with Fiber Reinforced plastics*. (Doctor of Philosophy in Civil Engineering), Massachusetts Institute of Technology, United States of America.
- Hibbeler, R. C. (2012). *Structural Analysis*. Upper Saddle River, NJ: Pearson.
- Hillerborg, A. (1983). *Concrete fracture energy test performed by 9 laboratories according to a draft RILEM recommendation*. Retrieved from Lund, Sweden:
- Hillerborg, A. (1985). The theoretical basis of a method to determine the fracture energy G_f of concrete. *Materials and Structures*, 18(106), 291-296.
- Hognestad, E. (1951). Study of combined bending and axial load in reinforced concrete members. *University of Illinois. Engineering Experiment Station. Bulletin; no. 399*.
- Hosen, M., Jumaat, M. Z., Islam, A., Darain, K., & Rahman, M. (2016). Flexural Performance of Reinforced Concrete Beams Strengthened by a New Side Near-Surface Mounted Technique Using Carbon Fibre-Reinforced Polymer Bars: Experimental and Analytical Investigation. *Science of Advanced Materials*, 8(4), 726-740.
- Hosen, M. A., Jumaat, M. Z., Alengaram, U. J., Islam, A., & bin Hashim, H. (2016). Near surface mounted composites for flexural strengthening of reinforced concrete beams. *Polymers*, 8(3), 67.
- Hosen, M. A., Jumaat, M. Z., Darain, K. M. U., Obaydullah, M., & Islam, A. S. (2014). *Flexural Strengthening of RC Beams with NSM Steel Bars*. Paper presented at the International Conference on Food, Agriculture and Biology (FAB-2014) Kuala Lumpur (Malaysia)
- Hutchinson, J. W. (1990). Mixed mode fracture mechanics of interfaces. *Metal and Ceramic interfaces*, 295-306.

- Irwin, G. R. (1957). Analysis of stresses and strains near the end of a crack traversing a plate. *J. appl. Mech.*
- Jansze, W. (1997). *Strengthening of reinforced concrete members in bending by externally bonded steel plates-design for beam shear and plate anchorage.*
- Jenq, Y., & Shah, S. P. (1985). Two parameter fracture model for concrete. *Journal of engineering mechanics*, 111(10), 1227-1241.
- Jones, R., Swamy, R., & Charif, A. (1988). Plate separation and anchorage of reinforced concrete beams strengthened by epoxy-bonded steel plates. *Structural Engineer*, 66(5).
- Jumaat, M. Z., Shukri, A. A., Obaydullah, M., Huda, M. N., Hosen, M. A., & Hoque, N. (2016). Strengthening of RC Beams Using Externally Bonded Reinforcement Combined with Near-Surface Mounted Technique. *Polymers*, 8(7), 261.
- Kaiser, H. P. (1989). *Strengthening of Reinforced concrete with epoxy bonded carbon fiber plastics.* (Doctor of Philosophy), ETH, Swiss Federal Institute of Technology Zurich Switzerland. (Diss. ETH Nr.8918)
- Kara, I. F. (2011). Prediction of shear strength of FRP-reinforced concrete beams without stirrups based on genetic programming. *Advances in Engineering Software*, 42(6), 295-304.
- Kara, I. F., Ashour, A. F., & Koroğlu, M. A. (2016). Flexural performance of reinforced concrete beams strengthened with prestressed near-surface-mounted FRP reinforcements. *Composites Part B: Engineering*, 91, 371-383.
- Karbhari, V., & Engineer, M. (1996). Investigation of bond between concrete and composites: use of a peel test. *Journal of Reinforced Plastics and Composites*, 15(2), 208-227.
- Karihaloo, B. L., Abdalla, H., & Imjai, T. (2003). A simple method for determining the true specific fracture energy of concrete. *Magazine of Concrete Research*, 55(5), 471-481.
- Karsan, I. D., & Jirsa, J. O. (1969). Behavior of concrete under compressive loadings. *Journal of the Structural Division*, 95(12), 2543-2564.
- Kent, D. C., & Park, R. (1969). *Inelastic behaviour of reinforced concrete members with cyclic loading.* Citeseer.

- Khalifa, A. M. (2016). Flexural performance of RC beams strengthened with near surface mounted CFRP strips. *Alexandria Engineering Journal*.
- Khshain, N. T., Al-Mahaidi, R., & Abdouka, K. (2015). Bond behaviour between NSM CFRP strips and concrete substrate using single-lap shear testing with epoxy adhesive. *Composite Structures*, 132, 205-214.
- Kim, Y. J. (2015). Modeling of Near-Surface-Mounted Carbon Fiber-Reinforced Polymer for Strengthening Reinforced Concrete Beams in Sustained Load. *ACI Structural Journal*, 112(6), 805.
- Kim, Y. J., & Khan, F. (2015). Creep-Induced Distress on Flexural Behavior of Reinforced Concrete Beams Retrofitted with Near-Surface-Mounted Carbon Fiber-Reinforced Polymer. *ACI Structural Journal*, 112(4), 493.
- Kimpara, I., Kageyama, K., Suzuki, T., Osawa, I., & Yamaguchi, K. (1999). Characterization of debonding energy release rate of FRP sheets bonded on mortar and concrete. *Advanced Composite Materials*, 8(2), 177-187.
- Kozłowska, E. (2012). Basic principles of fuzzy logic. Retrieved from <http://access.feld.cvut.cz/view.php?cislocianku=2012080002>
- Leung, C. K. (2001). Delamination failure in concrete beams retrofitted with a bonded plate. *Journal of Materials in Civil Engineering*, 13(2), 106-113.
- Leung, C. K., & Yang, Y. (2006). Energy-based modeling approach for debonding of FRP plate from concrete substrate. *Journal of engineering mechanics*, 132(6), 583-593.
- Liang, M.-T., Wu, J.-H., & Liang, C.-H. (2000). Applying fuzzy mathematics to evaluating the membership of existing reinforced concrete bridges in Taipei. *Journal of Marine Science and Technology*, 8(1), 16-29.
- Lorenzis, L. D. (2002). *Strengthening of RC structures with near surface mounted FRP rods*. (Ph.D. thesis), Department of Innovation,Engineering, Univ. of Lecce, Lecce, Italy.
- Lu, X., Teng, J., Ye, L., & Jiang, J. (2007). Intermediate crack debonding in FRP-strengthened RC beams: FE analysis and strength model. *Journal of Composites for Construction*, 11(2), 161-174.
- Maalej, M., & Bian, Y. (2001). Interfacial shear stress concentration in FRP-strengthened beams. *Composite Structures*, 54(4), 417-426.

- Mahal, M., Täljsten, B., & Blanksvärd, T. (2016). Experimental performance of RC beams strengthened with FRP materials under monotonic and fatigue loads. *Construction and Building Materials*, 122, 126-139.
- Makris, N., & Black, C. J. (2004). Dimensional Analysis of Yielding Structures.
- Malek, A. M., Saadatmanesh, H., & Ehsani, M. R. (1998). Prediction of failure load of R/C beams strengthened with FRP plate due to stress concentration at the plate end. *ACI Structural Journal*, 95(2).
- Mander, J. B., Priestley, M. J., & Park, R. (1988). Theoretical stress-strain model for confined concrete. *Journal of Structural Engineering*, 114(8), 1804-1826.
- Martínez-Rueda, J. E., & Elnashai, A. (1997). Confined concrete model under cyclic load. *Materials and Structures*, 30(3), 139-147.
- Matthys, S. (2000). *Structural behaviour and design of concrete members strengthened with externally bonded FRP reinforcement*. (PhD), Ghent University.
- Matuszak, A. (2015). Dimensional analysis can improve equations of the model. *Procedia Engineering*, 108, 526-535.
- Meier, U., Deuring, M., Meier, H., & Schwegler, G. (1993). Strengthening of structures with advanced composites. *Alternative materials for the reinforcement and prestressing of concrete*, 1.
- Mohammed, A., Al-Saadi, N., & Al-Mahaidi, R. (2016). Bond behaviour between NSM CFRP strips and concrete at high temperature using innovative high-strength self-compacting cementitious adhesive (IHSSC-CA) made with graphene oxide. *Construction and Building Materials*, 127, 872-883.
- Morsy, A. M., El-Tony, E.-T. M., & El-Naggar, M. (2015). Flexural repair/strengthening of pre-damaged RC beams using embedded CFRP rods. *Alexandria Engineering Journal*, 54(4), 1175-1179.
- Na, U., Park, T., Feng, M. Q., & Chung, L. (2009). Neuro-fuzzy application for concrete strength prediction using combined non-destructive tests. *Magazine of Concrete Research*, 61(4), 245.
- Nanni, A., Alkhrdaji, T., Barker, M., Chen, G., Mayo, R., & Yang, X. (1999). *Overview of testing to failure program of a highway bridge strengthened with FRP composites*. Paper presented at the Proceedings of fourth international symposium on non-metallic (FRP) reinforcement for concrete structures (FRPRCS-4).

- Nasrollahzadeh, K., & Basiri, M. M. (2014). Prediction of shear strength of FRP reinforced concrete beams using fuzzy inference system. *Expert Systems with Applications*, 41(4), 1006-1020.
- Nehdi, M., El Chabib, H., & Said, A. (2006). Evaluation of shear capacity of FRP reinforced concrete beams using artificial neural networks. *Smart Structures and Systems*, 2(1), 81-100.
- Nguyen, D. M., Chan, T. K., & Cheong, H. K. (2001). Brittle failure and bond development length of CFRP-concrete beams. *Journal of Composites for Construction*, 5(1), 12-17.
- Niu, H., & Wu, Z. (2001). Interfacial debonding mechanism influenced by flexural cracks in FRP-strengthened beams. *Journal of Structural Engineering*, 47, 1277-1288.
- Nordin, H., & Täljsten, B. (2006). Concrete beams strengthened with prestressed near surface mounted CFRP. *Journal of Composites for Construction*, 10(1), 60-68.
- Oehlers, D. J. (1992). Reinforced concrete beams with plates glued to their soffits. *Journal of Structural Engineering*, 118(8), 2023-2038.
- Ombres, L. (2010). Prediction of intermediate crack debonding failure in FRP-strengthened reinforced concrete beams. *Composite Structures*, 92(2), 322-329.
- Oudah, F. (2011). *Fatigue Performance of RC Beams Strengthened using Prestressed NSM CFRP*. (Masters), University of Calgary, Calgary, Alberta.
- Oudah, F., & El-Hacha, R. (2013). Research progress on the fatigue performance of RC beams strengthened in flexure using Fiber Reinforced Polymers. *Composites Part B: Engineering*, 47, 82-95.
- Pakdamar, F., & Güler, K. (2012). Evaluation of Flexible Performance of Reinforced Concrete Structures Using a Nonlinear Static Procedure Provided by Fuzzy Logic. *Advances in Structural Engineering*, 15(12), 2173-2190.
- Pellegrino, C., & Modena, C. (2009). Flexural strengthening of real-scale RC and PRC beams with end-anchored pretensioned FRP laminates. *ACI Structural Journal*, 106(3), 319.
- Peng, H., Zhang, J., Cai, C., & Liu, Y. (2014). An experimental study on reinforced concrete beams strengthened with prestressed near surface mounted CFRP strips. *Engineering structures*, 79, 222-233.

- Pešić, N., & Pilakoutas, K. (2003). Concrete beams with externally bonded flexural FRP-reinforcement: analytical investigation of debonding failure. *Composites Part B: Engineering*, 34(4), 327-338.
- Petersen, R. B., Masia, M. J., & Seracino, R. (2009). Bond behavior of near-surface mounted FRP strips bonded to modern clay brick masonry prisms: Influence of strip orientation and compression perpendicular to the strip. *Journal of Composites for Construction*, 13(3), 169-178.
- Petersson, P.-E. (1981). Crack growth and development of fracture zones in plain concrete and similar materials.
- Pham, H. B., & Al-Mahaidi, R. (2006). Prediction models for debonding failure loads of carbon fiber reinforced polymer retrofitted reinforced concrete beams. *Journal of Composites for Construction*, 10(1), 48-59.
- Phatak, D., & Deshpande, N. (2005). Prediction of 28 days compressive strength of 53-grade cements using dimensional analysis. *Journal of Materials in Civil Engineering*, 17(6), 733-735.
- Phatak, D., & Dhonde, H. (2003). Dimensional analysis of reinforced concrete beams subjected to pure torsion. *Journal of Structural Engineering*, 129(11), 1559-1563.
- Planas, J., Elices, M., & Guinea, G. (1992). Measurement of the fracture energy using three-point bend tests: Part 2—Influence of bulk energy dissipation. *Materials and Structures*, 25(5), 305-312.
- Quantrill, R., & Hollaway, L. (1998). The flexural rehabilitation of reinforced concrete beams by the use of prestressed advanced composite plates. *Composites Science and Technology*, 58(8), 1259-1275.
- Raafat, E.-H., & Mohamed, G. (2011). Flexural strengthening of reinforced concrete beams using prestressed, near-surface-mounted CFRP bars. *PCI JOURNAL*, 56(4), 134-151.
- Rahimi, H., & Hutchinson, A. (2001). Concrete beams strengthened with externally bonded FRP plates. *Journal of Composites for Construction*, 5(1), 44-56.
- Rahman, M. M., Jumaat, M. Z., Rahman, M. A., & Qeshta, I. M. (2015). Innovative hybrid bonding method for strengthening reinforced concrete beam in flexure. *Construction and Building Materials*, 79, 370-378.

- Rasheed, H. (2014). Externally Bonded GFRP and NSM Steel Bars for Improved Strengthening of Rectangular Concrete Beams Hayder Rasheed, Augustine Wuertz, Abdelbaset Traplsi, Hani Melhem, and Tarek Alkhrdaji.
- Reda, R., Sharaky, I., Ghanem, M., Seleem, M., & Sallam, H. (2016). Flexural behavior of RC beams strengthened by NSM GFRP Bars having different end conditions. *Composite Structures*, 147, 131-142.
- Rezazadeh, M., Barros, J., & Costa, I. (2015). Analytical approach for the flexural analysis of RC beams strengthened with prestressed CFRP. *Composites Part B: Engineering*, 73, 16-34.
- Rezazadeh, M., Cholostiakow, S., Kotynia, R., & Barros, J. (2016). Exploring new NSM reinforcements for the flexural strengthening of RC beams: Experimental and numerical research. *Composite Structures*, 141, 132-145.
- Rezazadeh, M., Costa, I., & Barros, J. (2014). Influence of prestress level on NSM CFRP laminates for the flexural strengthening of RC beams. *Composite Structures*, 116, 489-500.
- RILEM. (1985). Determination of the fracture energy of mortar and concrete by means of three-point bend tests on notched beams. *Materials and Structures*, 18(106), 285-290.
- Ritchie, P. A., Thomas, D. A., Lu, L.W., & Conelly, G. M. (1991). External reinforcement of concrete beams using fiber reinforced plastics. *ACI Structural Journal*, 88(4).
- Roberts, T. (1989). Approximate analysis of shear and normal stress concentrations in the adhesive layer of plated RC beams. *The Structural Engineer*, 67(12), 229-233.
- Rosenboom, O., & Rizkalla, S. (2008). Modeling of IC debonding of FRP-strengthened concrete flexural members. *Journal of Composites for Construction*, 12(2), 168-179.
- Saadatmanesh, H., & Ehsani, M. R. (1991). RC beams strengthened with GFRP plates. I: Experimental study. *Journal of Structural Engineering*, 117(11), 3417-3433.
- Sebastian, W. M. (2001). Significance of midspan debonding failure in FRP-plated concrete beams. *Journal of Structural Engineering*, 127(7), 792-798.
- Seko, E. V. (2014). Optimization and the Dimensional Analysis in Structural Engineering Problems. *Advanced Materials Research*.

- Seo, S.-Y., Lee, M. S., & Feo, L. (2016). Flexural analysis of RC beam strengthened by partially de-bonded NSM FRP strip. *Composites Part B: Engineering*, 101, 21-30.
- Seracino, R., Jones, N. M., Ali, M., Page, M. W., & Oehlers, D. J. (2007). Bond strength of near-surface mounted FRP strip-to-concrete joints. *Journal of Composites for Construction*, 11(4), 401-409.
- Shafabakhsh, G., & Tanakizadeh, A. (2015). Investigation of loading features effects on resilient modulus of asphalt mixtures using Adaptive Neuro-Fuzzy Inference System. *Construction and Building Materials*, 76, 256-263.
- Shahawy, M., & Beitelman, T. (1996). *Flexural behavior of reinforced concrete beams strengthened with advanced composite materials*. Retrieved from
- Sharaky, I., Torres, L., Comas, J., & Barris, C. (2014). Flexural response of reinforced concrete (RC) beams strengthened with near surface mounted (NSM) fibre reinforced polymer (FRP) bars. *Composite Structures*, 109, 8-22.
- Sharif, A., Al-Sulaimani, G., Basunbul, I., Baluch, M., & Ghaleb, B. (1994). Strengthening of initially loaded reinforced concrete beams using FRP plates. *ACI Structural Journal*, 91(2).
- Shukri, A., & Jumaat, M. (2016). Simulating concrete cover separation in RC beams strengthened with near-surface mounted reinforcements. *Construction and Building Materials*, 122, 1-11.
- Sima, J. F., Roca, P., & Molins, C. (2008). Cyclic constitutive model for concrete. *Engineering Structures*, 30(3), 695-706.
- Sinha, B., Gerstle, K. H., & Tulin, L. G. (1964). *Stress-strain relations for concrete under cyclic loading*. Paper presented at the ACI Journal Proceedings.
- Smith, S. T., & Teng, J. (2001). Interfacial stresses in plated beams. *Engineering Structures*, 23(7), 857-871.
- Smith, S. T., & Teng, J. (2002). FRP-strengthened RC beams. I: review of debonding strength models. *Engineering structures*, 24(4), 385-395.
- Sobhani, J., & Ramezaninpour, A. (2009). *Modeling the corrosion of reinforced concrete structures based on fuzzy systems*. Paper presented at the Proceedings of the 3rd International Conference on Concrete and Development.

- Soliman, S. M., El-Salakawy, E., & Benmokrane, B. (2010). Flexural behaviour of concrete beams strengthened with near surface mounted fibre reinforced polymer bars. *Canadian Journal of Civil Engineering*, 37(10), 1371-1382.
- Sun, R., Sevillano, E., & Perera, R. (2015). A discrete spectral model for intermediate crack debonding in FRP-strengthened RC beams. *Composites Part B: Engineering*, 69, 562-575.
- Täljsten, B. (1996). Strengthening of concrete prisms using the plate-bonding technique. *International journal of Fracture*, 82(3), 253-266.
- Täljsten, B. (1997). Strengthening of beams by plate bonding. *Journal of Materials in Civil Engineering*, 9(4), 206-212.
- Tang, W., Balendran, R., Nadeem, A., & Leung, H. (2006). Flexural strengthening of reinforced lightweight polystyrene aggregate concrete beams with near-surface mounted GFRP bars. *Building and environment*, 41(10), 1381-1393.
- Teng, J., De Lorenzis, L., Wang, B., Li, R., Wong, T., & Lam, L. (2006). Debonding failures of RC beams strengthened with near surface mounted CFRP strips. *Journal of Composites for Construction*, 10(2), 92-105.
- Teng, J., Lu, X., Ye, L., & Jiang, J. (2004). *Recent research on intermediate crack debonding in FRP-strengthened RC beams*. Paper presented at the 4th International Conference on Advanced Composite Materials in Bridges and Structures Calgary, Alberta, Canada.
- Teng, J., Smith, S. T., Yao, J., & Chen, J. (2003). Intermediate crack-induced debonding in RC beams and slabs. *Construction and Building Materials*, 17(6), 447-462.
- Teng, J., Zhang, J., & Smith, S. T. (2002). Interfacial stresses in reinforced concrete beams bonded with a soffit plate: a finite element study. *Construction and Building Materials*, 16(1), 1-14.
- TR-55. (2012). *The Concrete Society (UK): Technical Report No. 55 – Design guidance for strengthening concrete structures using fibre composite materials*. Retrieved from United Kingdom:
- Triantafillou, T. C., & Deskovic, N. (1991). Innovative prestressing with FRP sheets: mechanics of short-term behavior. *Journal of engineering mechanics*, 117(7), 1652-1672.
- Triantafillou, T. C., & Plevris, N. (1992). Strengthening of RC beams with epoxy-bonded fibre-composite materials. *Materials and Structures*, 25(4), 201-211.

- Vilnay, O. (1988). The analysis of reinforced concrete beams strengthened by epoxy bonded steel plates. *International Journal of Cement Composites and Lightweight Concrete*, 10(2), 73-78.
- Wang, B., Man, T., & Jin, H. (2015). Prediction of expansion behavior of self-stressing concrete by artificial neural networks and fuzzy inference systems. *Construction and Building Materials*, 84, 184-191.
- Wang, C., & Ling, F. (1998). *Prediction model for the debonding failure of cracked RC beams with externally bonded FRP sheets*. Paper presented at the Second International Conference on Composites in Infrastructure.
- Wenwei, W., & Guo, L. (2006). Experimental study and analysis of RC beams strengthened with CFRP laminates under sustaining load. *International Journal of Solids and Structures*, 43(6), 1372-1387.
- Wight, R., Green, M., & Erki, M. (2001). Prestressed FRP sheets for poststrengthening reinforced concrete beams. *Journal of Composites for Construction*, 5(4), 214-220.
- Woo, S.-K., Nam, J.-W., Kim, J.-H. J., Han, S.-H., & Byun, K. J. (2008). Suggestion of flexural capacity evaluation and prediction of prestressed CFRP strengthened design. *Engineering structures*, 30(12), 3751-3763.
- Wu, G., Dong, Z.-Q., Wu, Z.-S., & Zhang, L.-W. (2013). Performance and parametric analysis of flexural strengthening for RC beams with NSM-CFRP bars. *Journal of Composites for Construction*, 18(4), 04013051.
- Wu, Z., Shao, Y., Iwashita, K., & Sakamoto, K. (2007). Strengthening of preloaded RC beams using hybrid carbon sheets. *Journal of Composites for Construction*, 11(3), 299-307.
- Xue, W., Tan, Y., & Zeng, L. (2010). Flexural response predictions of reinforced concrete beams strengthened with prestressed CFRP plates. *Composite Structures*, 92(3), 612-622.
- Yankelevsky, D. Z., & Reinhardt, H. W. (1987). Model for cyclic compressive behavior of concrete. *Journal of Structural Engineering*, 113(2), 228-240.
- You, Y.-C., Choi, K.-S., & Kim, J. (2012). An experimental investigation on flexural behavior of RC beams strengthened with prestressed CFRP strips using a durable anchorage system. *Composites Part B: Engineering*, 43(8), 3026-3036.

- Yu, P., Silva, P. F., & Nanni, A. (2008). Description of a mechanical device for prestressing of carbon fiber-reinforced polymer sheets-Part I. *ACI Structural Journal*, 105(1), 3.
- Zadeh, L. A. (1965). Fuzzy sets. *Information and control*, 8(3), 338-353.
- Zhang, S., Raoof, M., & Wood, L. (1995). Prediction of peeling failure of reinforced concrete beams with externally bonded steel plates. *Proceedings of the ICE-Structures and Buildings*, 110(3), 257-268.
- Zhang, S. S. (2011). *Behaviour and modelling of RC beams strengthened in flexure with near surface mounted FRP strips*. (Doctor of Philosophy), The Hongkong Polytechnic University, Hongkong.
- Zheng, S.-j., Li, Z.-q., & Wang, H.-t. (2011). A genetic fuzzy radial basis function neural network for structural health monitoring of composite laminated beams. *Expert Systems with Applications*, 38(9), 11837-11842.
- Zhu, H., Wu, G., Zhang, L., Zhang, J., & Hui, D. (2014). Experimental study on the fire resistance of RC beams strengthened with near-surface-mounted high-T g BFRP bars. *Composites Part B: Engineering*, 60, 680-687.
- Zidani, M. h. B., Belakhdar, K., & Tounsi, A. (2015). Finite element analysis of initially damaged beams repaired with FRP plates. *Composite Structures*, 134, 429-439.
- Ziraba, Y., Baluch, M., Basunbul, I., Sharif, A., Azad, A., & Al-Sulaimani, G. (1994). Guidelines toward the design of reinforced concrete (RC) beams with external plates. *ACI Structural Journal*, 91(6).

LIST OF PUBLICATIONS

Manuscript accepted/under preparation/submission

Sl.No.	Title	Authors	Journal	Status
1	Critical curtailment location of EBR FRP bonded RC beams using Dimensional analysis and Fuzzy logic expert system.	Hoque, N., Jumaat, M.Z, Shukri, A.A.	Composite Structures (ISI WOS Q1)	Published
2	Prediction of IC debonding failure of precracked FRP strengthened RC beams using global energy balance.	Hoque, N., Jumaat, M.Z, Shukri, A.A.	Materials and Structures (ISI WOS Q1)	Accepted for publication
3	Debonding failure analysis of Prestressed FRP Strengthened RC beams.	Hoque, N., Jumaat, M.Z.	Structural Engineering and mechanics (ISI WOS Q3)	Accepted for publication
4	Fracture mechanics based debonding analysis of near surface mounted reinforcement concrete beam.	Hoque, N., Jumaat, M.Z, Sulong, NHR.,	Journal of Composite for Construction (ISI WOS Q1)	Under Review.
5	A Critical Review of Fracture Energy Based FRP Debonding Models for Externally Reinforced Beams.	Hoque, N., Achintha, M., Jumaat, M.Z, Sulong, NHR.,		Under preparation